SANDIA REPORT
SAND2010-0363
Unlimited Release
Printed February 2010

On the Detection of Crevasses in Glacial Ice with Synthetic-Aperture Radar

Billy C. Brock

Prepared by
Sandia National Laboratories
Albuquerque, New Mexico 87185 and Livermore, California 94550

Sandia is a multiprogram laboratory operated by Sandia Corporation,
a Lockheed Martin Company, for the United States Department of Energy's
National Nuclear Security Administration under Contract DE-AC04-94AL85000.

Approved for public release; further dissemination unlimited.

Sandia National Laboratories

Issued by Sandia National Laboratories, operated for the United States Department of Energy by Sandia Corporation.

NOTICE: This report was prepared as an account of work sponsored by an agency of the United States Government. Neither the United States Government, nor any agency thereof, nor any of their employees, nor any of their contractors, subcontractors, or their employees, make any warranty, express or implied, or assume any legal liability or responsibility for the accuracy, completeness, or usefulness of any information, apparatus, product, or process disclosed, or represent that its use would not infringe privately owned rights. Reference herein to any specific commercial product, process, or service by trade name, trademark, manufacturer, or otherwise, does not necessarily constitute or imply its endorsement, recommendation, or favoring by the United States Government, any agency thereof, or any of their contractors or subcontractors. The views and opinions expressed herein do not necessarily state or reflect those of the United States Government, any agency thereof, or any of their contractors.

Printed in the United States of America. This report has been reproduced directly from the best available copy.

Available to DOE and DOE contractors from
U.S. Department of Energy
Office of Scientific and Technical Information
P.O. Box 62
Oak Ridge, TN 37831

Telephone: (865) 576-8401
Facsimile: (865) 576-5728
E-Mail: reports@adonis.osti.gov
Online ordering: http://www.osti.gov/bridge

Available to the public from
U.S. Department of Commerce
National Technical Information Service
5285 Port Royal Rd.
Springfield, VA 22161

Telephone: (800) 553-6847
Facsimile: (703) 605-6900
E-Mail: orders@ntis.fedworld.gov
Online order: http://www.ntis.gov/help/ordermethods.asp?loc=7-4-0#online

SAND2010-0363
Unlimited Release
Printed February 2010

On the Detection of Crevasses in Glacial Ice with Synthetic-Aperture Radar

Billy C. Brock
SAR Sensor Technologies Department
Sandia National Laboratories
P.O. Box 5800
Albuquerque, NM 87185-0529

Abstract

The intent of this study is to provide an analysis of the scattering from a crevasse in Antarctic ice, utilizing a physics-based model for the scattering process. Of primary interest is a crevasse covered with a snow bridge, which makes the crevasse undetectable in visible-light images. It is demonstrated that a crevasse covered with a snow bridge can be visible in synthetic-aperture-radar (SAR) images. The model of the crevasse and snow bridge incorporates a complex dielectric permittivity model for dry snow and ice that takes into account the density profile of the glacier. The surface structure is based on a fractal model that can produce sastrugi-like features found on the surface of Antarctic glaciers. Simulated phase histories, computed with the Shooting and Bouncing Ray (SBR) method, are processed into SAR images. The viability of the SBR method for predicting scattering from a crevasse covered with a snow bridge is demonstrated. Some suggestions for improving the model are given.

This Page Intentionally Blank

Contents

Introduction 7
Brief history 7
Dielectric properties of ice and snow 9
  Density profiles for Antarctic snow and glacial ice 14
Crevasse geometric model 19
Simulated SAR images 23
  Trihedral array 24
  Transparency of the Antarctic snow and glacial ice 26
  Simulated images of the crevasse and snow bridge 34
    Snow bridge only, without crevasse walls 37
    Optimum radar band for imaging crevasses 38
    Effect of depression angle 39
    Effect of non-monotonic density profile 40
Conclusions and recommendations 43
Appendix I – Building a fractal surface 45
Appendix II – Shooting and Bouncing Ray (SBR) Method 49
  Relationship between MoM and SBR 50
  The Xpatch® implementation of the SBR method 51
Appendix III – Some validation tests for Xpatch® 53
  Perfectly conducting circular disk 53
  Rectangular dielectric slab 57
    Finite-integral time-domain model – normal incidence 59
    Method of Moments and Multilevel Fast Multipole Algorithm 60
  Dielectric slab covering a PEC corner reflector 61
Appendix IV – Considerations for computing SAR phase histories with Xpatch® 63
  Maximum-bounce limit 63
  Multi-look field compensation 64
  Sampling the reflection / transmission coefficient table 67
Appendix V – SAR images of the crevasse and snow bridge 69
  Crevasse with snow bridge, Siple Dome model, 0.5-m depth 72
    Monochrome, snow-bridge depth is 0.5 m 72
    Square root of magnitude (4th root of power), crevasse with snow bridge, 0.5-m depth 82
    Color, snow-bridge depth is 0.5 m 92
  Crevasse with snow bridge, Siple Dome model, 2-m depth 102
    Monochrome, snow-bridge depth is 2.0 m 102
    Square root of magnitude (4th root of power), crevasse with snow bridge, 2-m depth 112
    Color, snow-bridge depth is 2.0 m 122
  Snow bridge only, Siple Dome model, 2-m depth 132
    Monochrome, snow-bridge depth is 2.0 m 132
    Square root of magnitude (4th root of power), snow bridge only, 2-m depth 136
    Color, snow bridge only, 2-m depth 140
  Snow bridge only, Siple Dome model, 4-m depth 144
    Monochrome, snow-bridge depth is 4.0 m 144
    Square root of magnitude (4th root of power), snow bridge only, 4-m depth 148
    Color, snow-bridge depth is 4.0 m 152
  Snow bridge only, Newall Glacier model, 4-m depth 156
    Monochrome, snow-bridge depth is 4.0 m 156
    Square root of magnitude (4th root of power), snow bridge only, 4-m depth 160
    Color, snow-bridge depth is 4.0 m 164
References 169

This page intentionally blank

Introduction

This study provides an analysis of the scattering from a crevasse in ice, utilizing a physics-based model for the scattering process. After a brief historical review of some earlier attempts to see crevasses with radar, a discussion of the physical model is provided. The model for the dielectric properties of ice and Antarctic fern (partially compacted granular snow on the surface of a glacier) is given in some detail. This model depends on several parameters, including location. Models for three locations are given, but only the Siple Dome and Newall glacier models are used in generating the simulated synthetic-aperture-radar (SAR) images of the crevasse and snow bridge.

Because the size of a crevasse in a glacier is extremely large when measured in wavelengths of the radar signal, an *exact* physical model is not practical. The geometric model for the crevasse must be limited in extent to allow the computation of the scattering to be tractable, so only a limited section of a crevasse is modeled. A fractal-surface model is used to account for the surface features. The fractal model is capable of including sastrugi-like features, produced by winds blowing over the Antarctic ice. The method of computing the fractal surface is described in Appendix I.

The radar-scattering model is based on numerical calculation, but even with the power of modern computers, it is necessary to use approximations in the physics to achieve a practical solution. The physics approximation allows the size of the crevasse model, though small in comparison to a real crevasse, to be sufficiently large so that formation of meaningful images is possible. The electromagnetic scattering phenomena will be modeled with a method called the Shooting and Bouncing Ray method (SBR), which is an extension of the Physical Optics method (PO) [1, 2, 3]. Appendix II provides a description of the SBR method. Results from some validation tests for the specific implementation of SBR used here are discussed in Appendix III.

Finally, the simulated SAR images are discussed. Creating SAR images with the SBR method can introduce some artifacts, if the method is not applied appropriately. These are discussed in Appendix IV, where the artifacts are demonstrated along with the method used to mitigate their effects. The approach described there is used for all images of the crevasse and ice bridge. The first part of the discussion addresses the transparency of the Antarctic snow and glacial ice. Then the geometry of the crevasse and snow-bridge model is described. An appropriate set of simulated SAR images are presented and compared. A more complete set of images is included in Appendix V, along with a table providing a key to the relevant parameters for each figure.

The total surface area of the model measures over 250,000 square wavelengths and contains a volume of over 6,800,000 cubic wavelengths at X-band. Thus, each SAR image requires a considerable amount of computer time, even though the SBR method is an efficient, yet reasonably accurate, approximation to the physics of electromagnetic scattering. As a consequence, this study only allowed for modeling one geometry for the crevasse. The features and limitations of this single geometry are addressed. Future work should include variations of this geometry. Additional recommendations are stated in the conclusion.

Brief history

The detection of crevasses in glacial ice has proven difficult when the top of the crevasse is bridged with snow. In this case, the crevasse can be virtually indistinguishable visually from nearby solid portions of the glacier which are also covered with snow. Attempts to detect crevasses with electromagnetic or electrostatic methods date to as early as 1956 [4]. Typical methods involve dragging an apparatus over the snow in an attempt to detect changes in the electrical properties when the hollow crevasse is traversed. In 1987, an X-band pulsed radar system demonstrated that Antarctic snow and fern could be penetrated [5].

In 1992, the synthetic-aperture radar carried by the European Research Satellite 1 (ERS-1) was used to image the Greenland Ice Sheet [6]. In 1993, the same SAR was used to image the Columbia Glacier in Prince William Sound, Alaska [7]. The ERS-1 SAR, operated at C-band (5.3 GHz) and produced a resolution of 25-30 m. The Greenland data showed distinguishable zones in the ice sheet, based on variations in amounts of surface accumulation and melting. Dry-zone areas produced low backscatter, while refrozen zones, where surface-melt water percolates down into the ice, showed higher backscatter, apparently due to the increased surface roughness. The wet-snow zones produced intermediate backscatter. The bare-ice zones also produced relatively low backscatter. Rough zones, containing crevasses, were bright. The 30-m resolution allowed the boundaries of the different zones to be seen. Zones with heavy crevassing could be distinguished, but it appears that the resolution was not adequate to map individual crevasses.

The Columbia Glacier began a rapid retreat in 1985, was known to be calving icebergs, and was also known to contain numerous crevasses. The ERS-1 SAR, providing a resolution of 25 m, was able to distinguish large crevasses, which were visible in optical photos [7]. The data show that crevasse patterns are most visible when the crevasses are aligned normal to the radar look direction. It is likely that backscatter from the opposite wall of the crevasse is the dominant component. Crevasses oriented at diagonal angles to the look direction are barely visible in the SAR images. The course resolution is apparently a limiting factor here.

Recently, ground-penetrating radar has successfully located crevasses covered by snow bridges [8]. The instrumentation consisted of a pulsed radar operating at 400 MHz, the antenna of which was suspended a few centimeters above the surface and pushed at low speeds with a tracked vehicle. The range resolution was about 35 cm. The reflections from snow layers were very weak, but reflections were absent in the region of the crevasse void. It was noted that moving the radar parallel and offset from the crevasse made detection difficult. However, when the radar path crossed a crevasse, detection was possible.

In December of 2006, Sandia National Laboratories collected data near McMurdo Station and Pegasus in Antarctica with the X-band Miniature Synthetic-Aperture Radar (MiniSAR) [9]. The Pegasus wreck site, where an LC-130 aircraft encountered a crevasse hidden by a snow bridge after landing, was one of the sites where image data were collected. However, the higher-priority image data were collected for a trio of crevasses covered with snow bridges (named Tres Hermanas). From the air, these crevasses were difficult to discern optically from the relatively flat glacier surface. The crevasses were about twelve feet wide at the top, with snow-bridge depth of about six feet. The data show that detection of a crevasse with 1-m resolution is difficult when the range direction is along the length of the crevasse, but that detection improves at the finer 12-inch and 8-inch resolutions. When the range direction moves away from the direction of the crevasse length, even slightly, the crevasse appears wider in the SAR image, and is easier to discern. The data imply that both resolution and crevasse orientation affect the appearance of the crevasse, but that resolution is more important than the geometry. The finer resolutions provide the most easily discernable images of the crevasses. The data also show that contrast between the glacier surface and the crevasse is better at lower grazing angles compared to higher grazing angles. The signature of a crevasse appears to be a narrow line of low radar return accompanied by bright returns, which presumably originate from the far wall of the crevasse. The line corresponding to the bright return appears somewhat broken, or at least consists of returns of significantly varying intensity along its length. The darker, low-return line appears to be more continuous for greater lengths.

The Sandia National Laboratories X-band miniSAR data [9] provide very convincing evidence that synthetic-aperture radar, operating at X-band, can detect crevasses even in the presence of snow bridges. The often-presumed mechanism is that a low-level return is obtained from the snow bridge itself, while a brighter return is obtained from the far (down-range) wall of the crevasse. The low-

return component is darker than the adjacent surface scattering. The brighter return exceeds that of the adjacent surface over much of the length of the crevasse. It is assumed that the far wall is illuminated by energy which penetrates the snow bridge.

However, in the December 2006 Antarctica mission, 8-inch resolution data was collected from a simulated crevasse with buried corner reflectors. A reflector buried two feet below the surface was not visible in the image, but one buried four feet below the surface was apparent. Contrast between returns from deeper corners was insufficient to distinguish them from the surface clutter. This data seems to indicate that penetration to at least four feet is possible, but even so, penetration to two feet is not guaranteed.

While it is difficult to argue with the demonstrated success of the Sandia National Laboratories miniSAR images in detecting the crevasses, it is also important to understand the physical process of scattering from a crevasse in the presence of a snow bridge. An understanding of the scattering process can improve understanding of the advantages and possible limitations of using synthetic-aperture radar to locate crevasses in the Antarctic ice.

The visibility of the crevasse arises from two simple scattering processes:

- Different reflection coefficients resulting from different dielectric permittivity (index of refraction) of adjacent materials, and
- Different backscatter reflection arising from surfaces with different geometry.

While this much is obvious, it is desirable to quantify the processes in order to understand if conditions can arise that would tend to obscure the crevasses and prevent their detection in a SAR image. The Pegasus wreck site and the experiences of the Sandia team [9] are sufficient to show that such conditions can occur at optical wavelengths, but the question is whether such conditions can occur at centimeter wavelengths, too.

Dielectric properties of ice and snow

Propagation through ice and snow depends on its complex permittivity,

$$\varepsilon = \varepsilon' - j\varepsilon'' , \tag{1.1}$$

where the real part, ε', is often called the dielectric constant, and the imaginary part, which contributes to propagation loss, is often described by the loss tangent, $\tan\delta$, as

$$\varepsilon'' = \varepsilon' \tan\delta . \tag{1.2}$$

A model for the complex permittivity of dry snow and ice will be needed for computing the scattering from the crevasse and snow bridge. This section will describe the model used in this study.

Measurements of the dielectric properties of water, ice, and snow are reported by von Hippel [10] for frequencies ranging from 1 kHz to 10 GHz in Table 1. While this data is over 50 years old, it is considered to be of high quality. These data show that the relative dielectric permittivity of ice decreases slightly as the signal frequency increases. The loss tangent also decreases as frequency increases. This behavior for the loss tangent seems to apply to freshly fallen snow as well, and for hard-packed snow after light rain. Although the relative permittivity of liquid water decreases as frequency increases, the loss tangent increases. The decreasing permittivity and loss tangent of ice, as frequency increases, indicates that the loss per wavelength decreases as frequency is increased. However, it will be shown below that the critical parameter, loss per meter, actually increases as frequency increases.

Table 1 Dielectric Properties of Water and Ice (from von Hippel [10])

	Temp °C		1 kHz	10 kHz	100 kHz	1 MHz	10 MHz	300 MHz	3 GHz	10 GHz
Ice	−12	ε_r			4.8	4.15	3.7		3.20	3.17
		tan δ			0.8000	0.1200	0.0180		0.0009	0.0007
Freshly fallen snow	−20	ε_r	3.33	1.82	1.24	1.20	1.20	1.20	1.20	
		tan δ	0.4920	0.3420	0.1400	0.0215	0.0040	0.0012	0.00029	
Freshly fallen snow	−6	ε_r								1.26
		tan δ								0.00042
Hard-packed snow after light rain	−6	ε_r			1.9	1.55			1.5	
		tan δ			1.5300	0.2900			0.0009	
water	1.5	ε_r			87.0	87.0	87.0	86.5	80.5	38.0
		tan δ			0.1900	0.0190	0.0020	0.0320	0.3100	1.0300
water	5	ε_r				85.5		85.2	80.2	41.0
		tan δ				0.0220		0.0273	0.2750	0.9500
water	15	ε_r				81.7		81.0	78.8	49
		tan δ				0.0310		0.0210	0.2050	0.7000
water	25	ε_r			78.2	78.2	78.2	77.5	76.7	55
		tan δ			0.4000	0.0400	0.0046	0.0160	0.1570	0.5400
water	55	ε_r				68.2		68	67.5	60
		tan δ				0.0720		0.0092	0.0890	0.3600
water	85	ε_r			58	58	58	57	56.5	54
		tan δ			1.2400	0.1240	0.0125	0.0073	0.0547	0.2600

The permittivity of pure liquid water at frequency *f* in the microwave region is given by the Debye formula [11],

$$\varepsilon'_{H_2O} = \varepsilon_\infty + \frac{\varepsilon_{static} - \varepsilon_\infty}{1 + \omega^2\tau^2} \tag{1.3}$$

and

$$\varepsilon''_{H_2O} = \frac{\left(\varepsilon_{static} - \varepsilon_\infty\right)\omega\tau}{1 + \omega^2\tau^2} \tag{1.4}$$

where

$$\varepsilon_{H_2O} = \varepsilon'_{H_2O} - j\varepsilon''_{H_2O} \tag{1.5}$$

and $\omega = 2\pi f$, and at $0°\,\mathrm{C}$, $\varepsilon_{static} = 87.90$, $\varepsilon_\infty = 5.7$, and $\tau = 17.67\ \mathrm{ps}$.

Mätzler [12] described what appear to be very accurate measurements of the real part of the permittivity for dry snow (no quasi-liquid layer) at 1 GHz as a function of ice density. This data, measured at temperatures between $-8°\ \mathrm{C}$ and $-1°\ \mathrm{C}$, cover the range of ice volume fraction from about 0.05 to 0.5. Over this range of ice density, the measured real part of the relative permittivity, ε' , ranges from about 1.1 to about 1.9. The real part of the permittivity is essentially constant to at least 10 GHz. Mätzler concluded that the Polder- van Santen mixing formula [13] provides an extremely good fit to this data. His model for the real part of the dielectric constant of dry snow is

$$\varepsilon = 1 + \frac{v\left(\varepsilon_s - 1\right)\sum_{i=1}^{3}\frac{\varepsilon_a}{\varepsilon_a + A_i\left(\varepsilon_s - 1\right)}}{3 - v\left(\varepsilon_s - 1\right)\sum_{i=1}^{3}\frac{A_i}{\varepsilon_a + A_i\left(\varepsilon_s - 1\right)}} \tag{1.6}$$

with

$$\begin{aligned} \varepsilon_a &= 1 + a\left(\varepsilon - 1\right) \\ a &= 1 - A_i \end{aligned} \tag{1.7}$$

where $\varepsilon_s = 3.185$ for ice (slightly higher than given by von Hippel [10]), and v is the volume fraction of ice. For dry snow, the best fit to the carefully measured data has

$$A_1 = A_2 = A$$
$$A_3 = 1 - 2A \tag{1.8}$$
$$A = \begin{cases} 0.1 + 0.5v & 0 < v < 0.33 \\ 0.18 + 3.24(v - 0.49)^2 & 0.33 \le v < 0.71 \\ 1/3 & v \ge 0.71 \end{cases}$$

The standard deviation from the measured data in [12] is 0.0064. Note that (1.6) must be iterated to find the effective dielectric constant, since ε appears on both the left- and right-hand sides. When the volume fraction of ice is $v = 0$, (1.6) gives $\varepsilon = 1$ as expected. When the mixture is entirely ice, $v = 1$, then $\varepsilon = \varepsilon_s$, as expected.

Koizumi and Sato *et al* measured the dielectric constant and loss tangent ($\tan\delta$) for snow and shaved ice at several temperatures at 9.5 GHz [14]. Their data show that both dielectric constant and loss tangent are nearly constant versus temperature when the temperature $T < -1°\text{ C}$. While there is some small variation near $T = -1°\text{ C}$, the variation increases rapidly as T approaches zero and beyond. The increased slope of both dielectric constant and loss tangent are apparently due to a liquid water component that is present at the higher temperatures. Since the dielectric constant and loss tangent of liquid water are both higher than that of ice, the mixture properties will be sensitive to the fractional volume of water. However, for dry snow at temperatures below $T = -1°\text{ C}$, the temperature dependence of both can be ignored. Koizumi *et al* report the dielectric constant as a function of density at $T = -5°\text{ C}$, giving 7% – 8% higher values than reported by Mätzler [12] near 1 GHz. Although they report that the error in measuring the loss tangent is large, they report a value of $\tan\delta \sim 0.001$. This is larger than von Hippel [10] reports for ice at 3GHz and 10 GHz (see Table 1), which might imply very slight water content in their snow samples. Unfortunately, the variations in the measured data were too large to draw conclusions about the variation of the loss tangent with density. Koizumi and Sato *et al* [14] suggest Wiener's mixing formula for dry snow

$$\frac{\varepsilon_{snow} - 1}{\varepsilon_{snow} + u} = v_{air}\frac{\varepsilon_{air} - 1}{\varepsilon_{air} + u} + v_{ice}\frac{\varepsilon_{ice} - 1}{\varepsilon_{ice} + u} + v_{water}\frac{\varepsilon_{water} - 1}{\varepsilon_{water} + u} \tag{1.9}$$

where v_{air}, v_{ice}, and v_{water} are the volumetric fractions of air, ice, and water, respectively. The parameter u is a polarity factor that depends on the shape and features of the particles. For their model of dry snow,

$$\begin{aligned} v_{water} &= 0 & v_{ice} &= v & v_{air} &= 1 - v \\ \varepsilon_{air} &= 1 & \varepsilon_{ice} &= 3.17 & u &= 5 \end{aligned} \tag{1.10}$$

Putting (1.10) into (1.9), their model for the real part of the dielectric constant depends only on the volumetric fraction of ice as follows:

$$\varepsilon_{dry\ snow} = \frac{3.765 + 5v}{3.765 - v}. \tag{1.11}$$

Tiuri and Sihvola *et al* considered both the real and imaginary parts of the dielectric permittivity [15]. Based on measurements of dry snow in a cylindrical cavity, they report the following second-order fit for the real part, $\varepsilon'_{dry\ snow}$,

$$\varepsilon'_{dry\ snow} = 1 + 1.7\rho + 0.7\rho^2 \tag{1.12}$$

where ρ is the density of snow relative to water. (1.13)

The models for the permittivity use either volume fraction of ice or density as the parameter describing the snow. The relation between volume fraction v and density ρ is

$$\rho = v\rho_{ice}. \tag{1.14}$$

The three models for the real part of the dielectric permittivity given by Mätzler (equations (1.6) – (1.8)), Koizum *et al* (equation (1.11)), and Tiuri *et al* (equation (1.12)) are compared in Figure 1 as a function of volume fraction of ice, ν. The models are very similar, with the largest disagreement occurring at volume fractions between about 0.2 and 0.45.

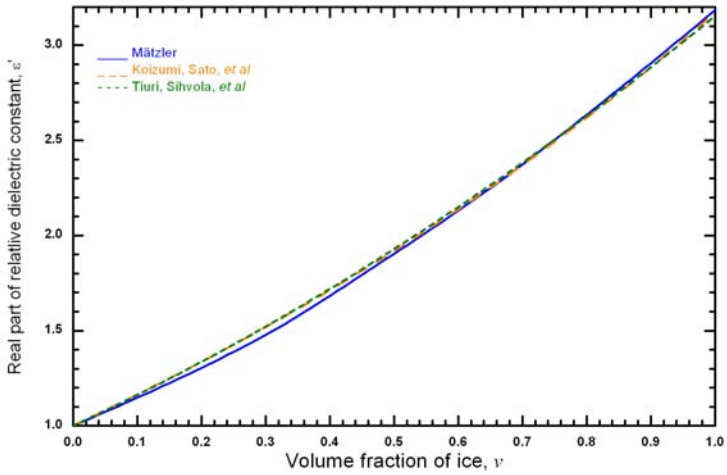

Figure 1 Real part of dielectric constant for dry snow for three models.

For the loss tangent, Tiuri and Sihvola *et al* give [15]

$$\tan\delta = -\frac{\varepsilon''_{dry\ snow}}{\varepsilon'_{dry\ snow}} = 1.59\cdot 10^{6}\,\frac{0.52\rho_{ice}+0.62\rho_{ice}^{2}}{1+1.7\rho_{ice}+0.7\rho_{ice}^{2}}\left(\frac{1}{f}+1.23\cdot 10^{-14}\sqrt{f}\right)e^{0.036T}\,, \tag{1.15}$$

where f is the frequency in hertz and T is the temperature in degrees Celsius. Since the medium is lossy, the minus sign is consistent with the time convention $e^{j\omega t}$, which is used here.

The modeling of the loss tangent of ice is complicated by the variations in measured values obtained by different experimenters. While different values are often attributed to varying amounts of impurities in different samples, another possibility has been suggested by Bordonski and Krylov [16]. They suggest that the loss tangent as a function of temperature exhibits a hysteresis effect; the loss tangent depends not only on the current temperature, but also on the temperature history. Although they do not suggest a mechanism to cause this, they do describe a series of measurements at 13.5 GHz and 37.5 GHz on the upper ice layer of the Arakhley Lake of the Chita region of Russia. The data were collected over a span of more than 100 days, starting from the time the ice sample froze, with temperature slowly varying over that time span. The data show a general downward trend as the ice ages, although the loss tangent begins to increase after about 80 days. Of course, the temperature varied from day-to-day and week-to-week. As temperature is thought to be the primary parameter needed to describe the variation of loss tangent at a fixed frequency, the data were plotted as a function of temperature, with time as a parameter along the path joining the data points. The surprising result is that different loss tangent values were obtained with the same sample at the same temperature, but at different times. Bordonski and Krylov conclude that this is due to a hysteresis effect as temperature fluctuates while the ice ages. These measurements were obtained with microwave radiometers, and estimated accuracy of the loss tangent values was 10%.

The density of ice varies slightly with temperature. Some accepted values [11] are listed in Table 2. A quadratic fit to the data in [11] is

$$\rho_{ice}(T) = 0.91692 - 1.6712\cdot 10^{-4}T - 4.5253\cdot 10^{-7}T^{2}\,. \tag{1.16}$$

Table 2 Density of ice [11].

$T\ (°\mathrm{C})$	Density, $\rho_{ice}\ \left(\mathrm{g}/\mathrm{cm}^3\right)$
0	0.9167
–10	0.9187
–20	0.9203
–30	0.9216
–40	0.9228
–50	0.9240
–60	0.9252
–80	0.9274
–100	0.9290

Assuming time dependence of $e^{j\omega t}$, a plane wave propagates as $e^{j(\omega t - kr)}$, where r is the distance along the direction of propagation, and the wave number k is

$$k = \omega \frac{\sqrt{\varepsilon'_{snow}\left(1 - j\tan\delta\right)}}{c} = \beta - j\alpha\,, \tag{1.17}$$

where $\omega = 2\pi f$ and c is the speed of light in vacuum. Since the loss tangent is very small,

$$\beta \simeq \omega \frac{\sqrt{\varepsilon'_{snow}}}{c}\,, \tag{1.18}$$

and

$$\alpha \simeq \omega \frac{\sqrt{\varepsilon'_{snow}}}{c} \frac{1}{2} \tan\delta\,. \tag{1.19}$$

The plane wave propagating in the snow propagates according to $e^{-\alpha r} e^{j(\omega t - \beta r)}$, and thus decays exponentially as it propagates. This means that the propagation loss, measured in decibels, is directly proportional to the propagation distance.

Combining the Mätzler model (1.6) – (1.8) for $\varepsilon'_{dry\ snow}$ and the Tiuri-Sihvola model (1.15) for $\tan\delta_{dry\ snow}$ provides a reasonable model for the complex dielectric constant for dry snow. In this case, $\varepsilon'_{dry\ snow}$ is a function of the volume fraction of ice, and is assumed to be independent of temperature and frequency over the microwave frequencies of interest. However, the loss tangent is characterized as a function of the fraction of ice, the temperature, and the frequency. This is the model for permittivity that will be used in this study.

The propagation loss, in decibels per meter, is plotted in Figure 2 as a function of frequency for T = 0° C, and in Figure 3 for T = –20° C, for various densities, given as the volume fraction of ice. The radar frequency allocation, as designated by the FCC [17], is also indicated for C-, X-, and Ku-bands. The loss roughly doubles (in decibels per meter) from one band to the next higher band. Clearly, greater penetration into the ice can be expected at C-band, but the available bandwidth is limited. The propagation loss also depends on the temperature of the ice. Figure 4 shows the loss in decibels per meter as a function of temperature when the frequency is held constant at 10 GHz. As the temperature approaches the 0° C, the loss begins to rise rapidly, with the slope becoming steeper as the volume fraction of ice increases.

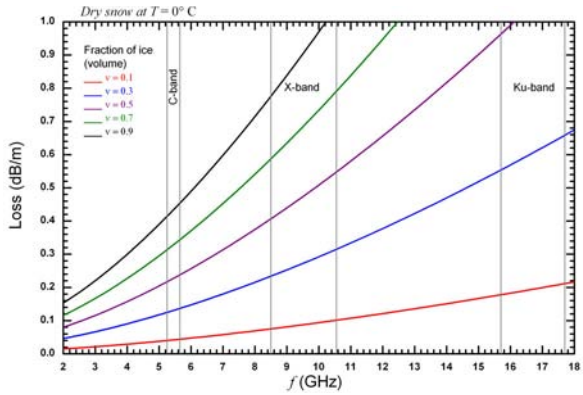

Figure 2 *Propagation loss through dry snow as function of frequency for several fractional volumes of ice at temperature T = 0° C.*

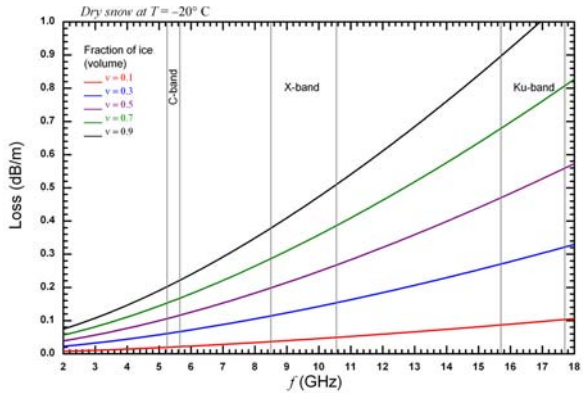

Figure 3 *Propagation loss through dry snow as function of frequency for several fractional volumes of ice at temperature T = –20° C.*

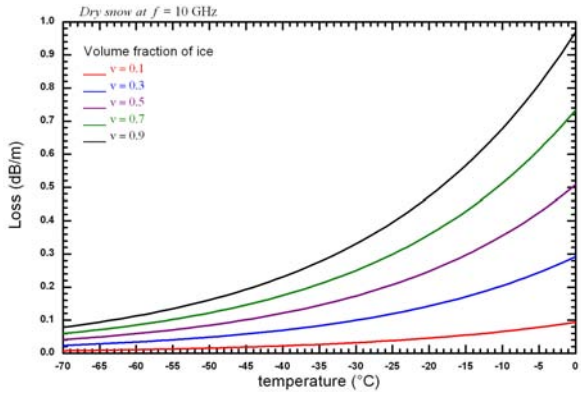

Figure 4 *Propagation loss through dry snow, at f = 10 GHz, as a function of temperature.*

Density profiles for Antarctic snow and glacial ice

Density data has been obtained from core-sample data at three sites, plotted (approximately) on the map of Landsat Image Mosaic of Antarctica [18] in Figure 5, and on the true-color image in Figure 6. The data sets are:

Siple Dome, cores C, E, F at 148° 49´ W 81° 40´ S [19], plotted in Figure 7;
Newall Glacier at 162° 30´ E 77° 35´ S [20], plotted in Figure 8;
Dominion Ridge at 166° 10´ E 85° 15´ S [21], plotted in Figure 9.

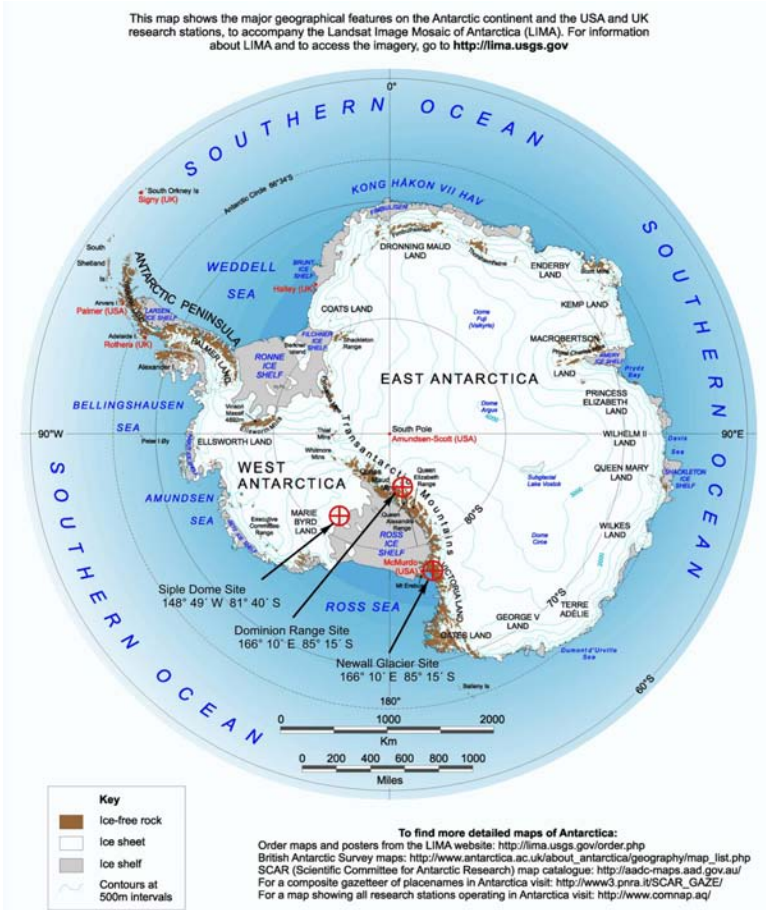

Figure 5 *Approximate locations of the Siple Dome, Dominion Range, and Newall Glacier sites. (Antarctica map is the overview map from the Landsat Image Mosaic of Antarctica, courtesy of the U.S. Geological Survey [18].)*

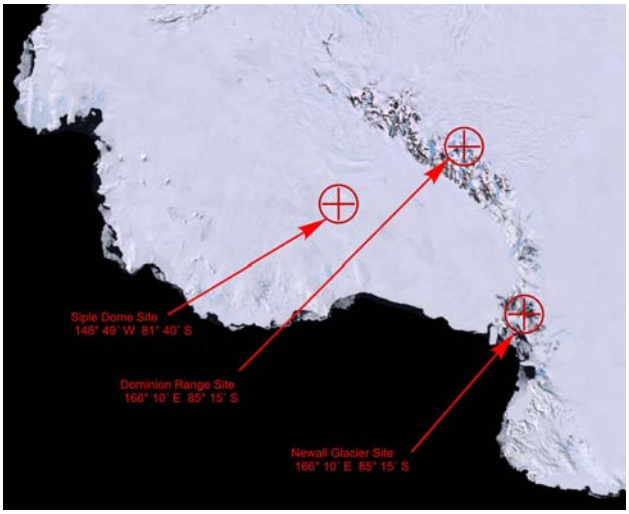

Figure 6 *Approximate locations of the Siple Dome, Dominion Range, and Newall Glacier site plotted on Landsat Image Mosaic of Antarctica. (Landsat Image Mosaic of Antarctica, courtesy of the U.S. Geological Survey [24])*

The Siple Dome data extends from about 4 m below the surface to about 100 m depth. However, the data is plotted in Figure 7 to only a depth of 60 m. The Newall Glacier data extends from the surface to about 129 m depth, but it is plotted to only 60 m depth in Figure 8. There is considerable variation in the first 5 m of depth, and the surface density is about 0.32 g/cm^3. The Dominion Range data is

very shallow, extending from the surface to nearly 1.8 m. Figure 9 shows that the density is quite variable, with a surface density ranging from about 0.35 g/cm^3 to 0.426 g/cm^3. The large variation of the Dominion Range data is consistent with the variation in the first few meters of the Newall Glacier data. It appears that the snow and glacial ice density near the surface is quite variable, but becomes more consistently monotonic as the depth increases. A typical snow and glacial ice density at the surface is 0.35 g/cm^3 [23].

The density can be modeled as a function of depth, *x*, with a rational curve fit to the data. The following rational curve fits have been calculated for the Siple Dome data, and are plotted in Figure 7,

$$\rho_{Siple,C} = \frac{x^2 + 212x + 822}{283x + 2,950} \text{ for core C,} \tag{1.20}$$

$$\rho_{Siple,E} = \frac{x^2 + 491x + 3,800}{553x + 11,200} \text{ for core E,} \tag{1.21}$$

$$\rho_{Siple,F} = -\frac{x^2 - 505x - 5,680}{332x + 16,900} \text{ for core F,} \tag{1.22}$$

and

$$\rho_{Siple} = \frac{x^2 + 969x + 8,560}{945x + 25,500} \text{ for the composite data.} \tag{1.23}$$

In (1.20) through (1.23), *x* is the depth in meters, and ρ is the density in g/cm^3.

For the Newall Glacier, the dip in the density between about 1.6 m and 4 m causes some difficulty. The following rational fit provides a dip in that region,

$$\rho_{Newall,dip} = \frac{x^3 - 2.73x^2 - 1.53x + 6.20}{-0.004x^4 + 1.27x^3 + 1.38x^2 - 19.0x + 23.8}. \tag{1.24}$$

However, if the dip is ignored, the following rational fit is obtained

$$\rho_{Newall} = \frac{x^2 + 13.5x + 8.54}{0.852x^2 + 30.1x + 30.6}. \tag{1.25}$$

In (1.24) and (1.25), as before, *x* is the depth in meters, and ρ is the density in g/cm^3 .The density computed from (1.24) and (1.25) are plotted in Figure 8 with the measured data.

The Dominion Range data was obtained from shallow pits, and extends no more than 2 m deep. The data is quite variable, and appears almost random. A least-squared-error linear fit is

$$\rho_{Dominion} = 0.367 + 1.39 \times 10^{-2} x + \rho_{error}, \tag{1.26}$$

where the units for $\rho_{Dominion}$ are g/cm^3, the depth *x* is in meters, and the standard deviation of the zero-mean error term, ρ_{error}, is 0.044 g/cm^3. To underscore the variability of the density as a function of depth, Figure 10 shows the range of values obtained in November, 2009, in an area known as the Shear Zone [22], located near S 78° 01.9´, E 168° 32.0´.

Since the complex electric permittivity of the snow and glacial ice depends on the density, this data implies that there will be some scattering in the first few meters of depth due to the fluctuating density. This scattering will compete with scattering from surface features and with scattering from buried objects. It will also compete with the scattering from the walls of a crevasse as seen through a snow bridge. The net result will be a loss of contrast of the crevasse image, compared to the image if the snow and glacial ice were more homogeneous.

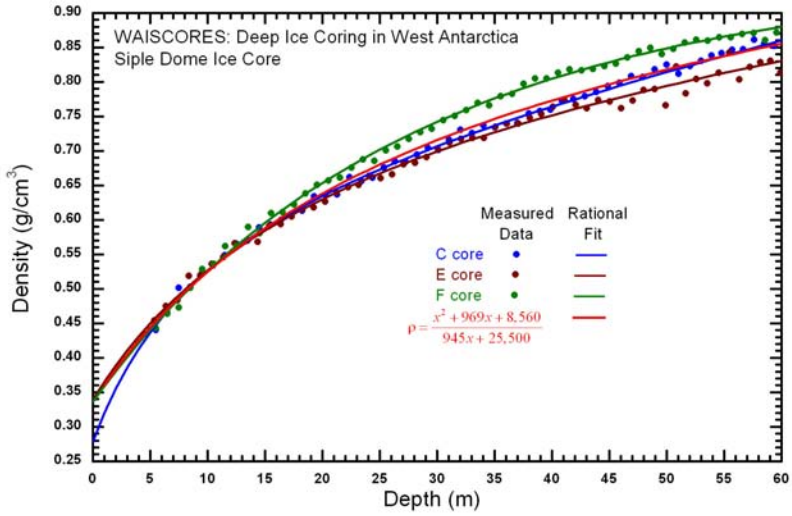

Figure 7 *Siple Dome ice-core density as a function of depth [19].*

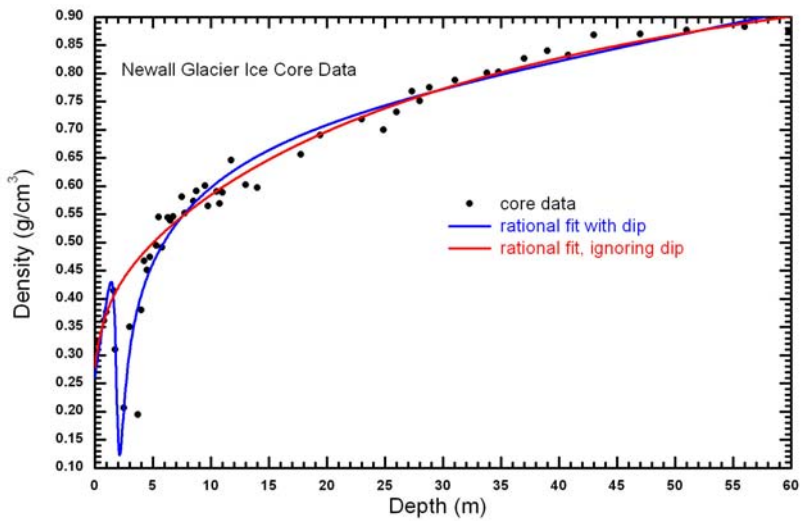

Figure 8 *Newall Glacier ice-core density as a function of depth [20].*

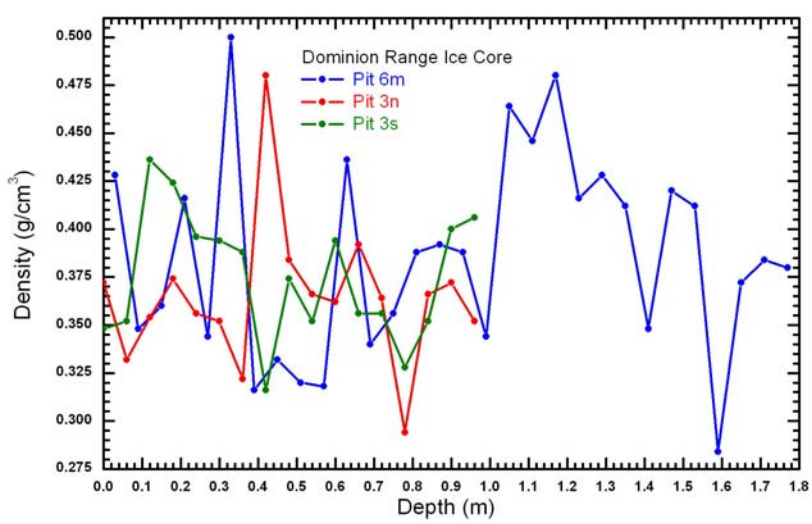

Figure 9 *Dominion Range ice-core density as a function of depth [21].*

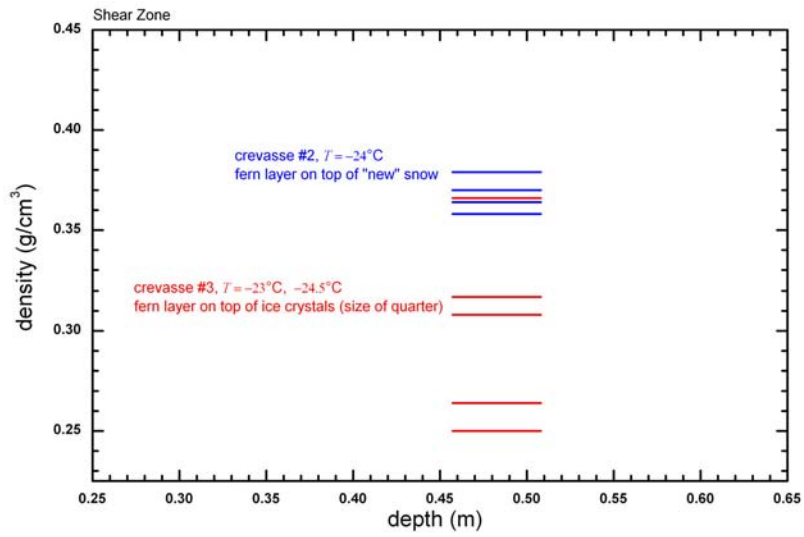

Figure 10 Shear-zone fern density as a function of depth, obtained in November, 2009 [22].

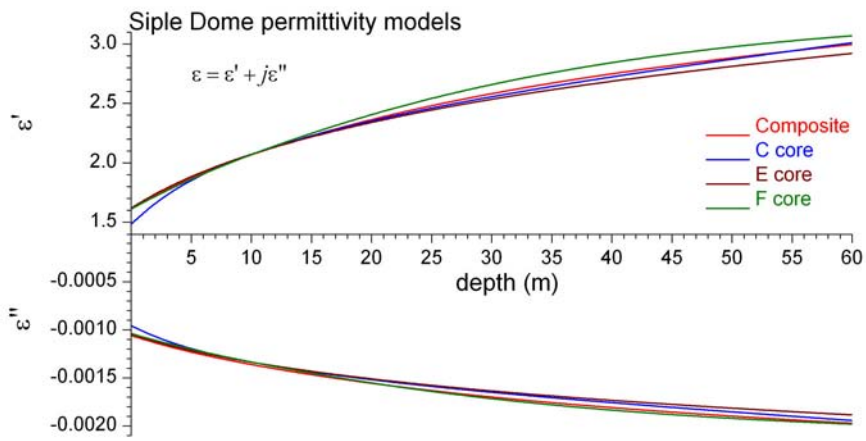

Figure 11 Dielectric permittivity profile at $f = 9.5$ GHz and $T = 0°$ C for the Siple Dome C, E, F cores and composite models for the entire core depth.

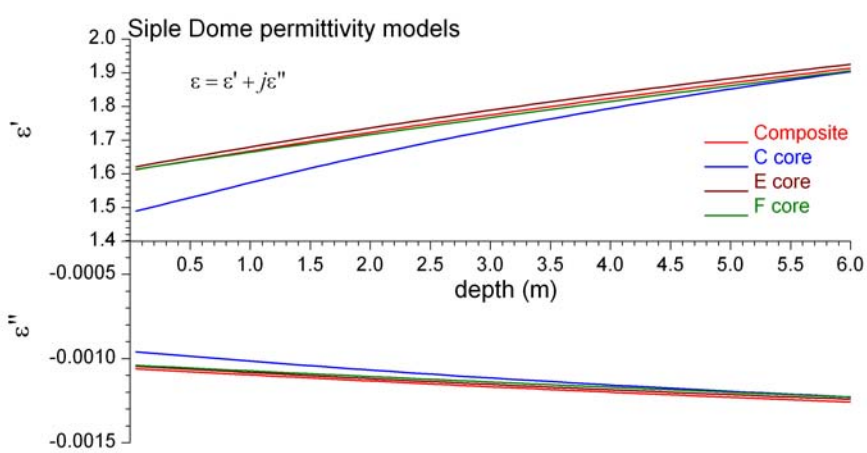

Figure 12 Dielectric permittivity profile at $f = 9.5$ GHz and $T = 0°$ C for the Siple Dome C, E, F cores and composite models for the top 6 m depth.

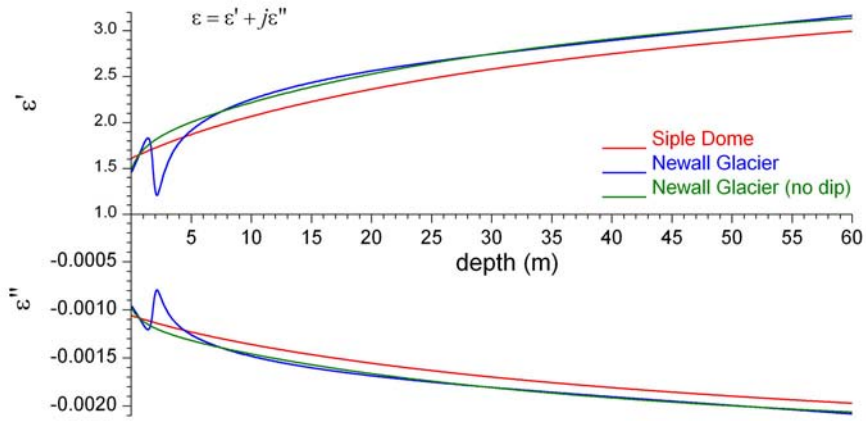

Figure 13 *Dielectric permittivity profile at* $f = 9.5\ \text{GHz}$ *and* $T = 0°\ \text{C}$ *for the Siple Dome composite and Newall Glacier models for the entire core depth.*

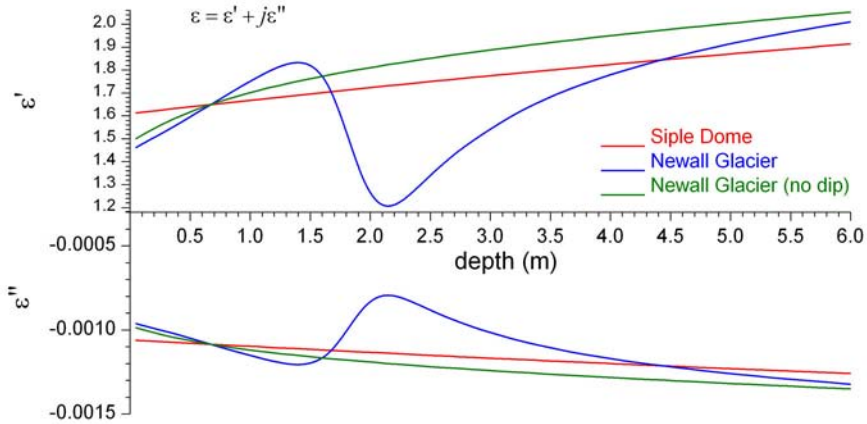

Figure 14 *Dielectric permittivity profile at* $f = 9.5\ \text{GHz}$ *and* $T = 0°\ \text{C}$ *for the Siple Dome composite and Newall Glacier models for the top 6 m core depth.*

Crevasse geometric model

The crevasse will be modeled as a void in the glacier, filled with air. It is assumed that the sides of the crevasse are rough, so the fractal-surface model will be used for the walls. The top of the glacier and snow bridge are also assumed to have rough surfaces, so a fractal surface will be applied to these. A cross section of the geometry is illustrated in Figure 15. Because of the nature of the SBR method, only surfaces are relevant to the model, and the extent of the material beyond the surface is modeled by specifying a material profile.

The top surface will be modeled as layered media, with each layer 2 cm thick. The dielectric properties are obtained from the various models described above. The snow-bridge region will terminate in a region filled with air (the crevasse), while the remaining top surface adjacent to the snow bridge will terminate with a dielectric half-space (the remaining glacier). The dielectric properties of the walls of the crevasse will be modeled with several regions, according to depth, consisting of dielectric half-spaces, each region having dielectric properties associated with the density at the middle of the region. With the SBR method, when an incident ray enters the half space, it terminates. Reflection occurring at the surface is retained, of course.

The geometric crevasse model is created in two steps. The first step creates a smooth solid model for the top layer of snow (including the snow bridge), for the glacier, and for the crevasse structure by extruding the two-dimensional outline illustrated in Figure 15 into a smooth three-dimensional solid. The model has different profiles for the snow bridge and the surface region on either side. The parameter d_{top} is a geometry parameter, while depth represents the thickness of the multilayer dielectric model representing the surface materials. Also, note the initial symmetry of the models.

The second step is to extract the appropriate surfaces and apply the fractal-creation algorithm described in Appendix I. The result of applying the fractal-creation algorithm to the crevasse geometry is illustrated in Figure 16. To avoid anomalous results from the simulation due to the truncation of the surface geometry, an absorbing box is placed around the model. When a ray encounters the absorber, it is terminated. Consequently, no reflection occurs from the surface, and no scattered-field contribution is computed from the surface. This allows the crevasse to be illuminated only through the snow bridge material, and prevents illumination of the crevasse walls from the wrong side.

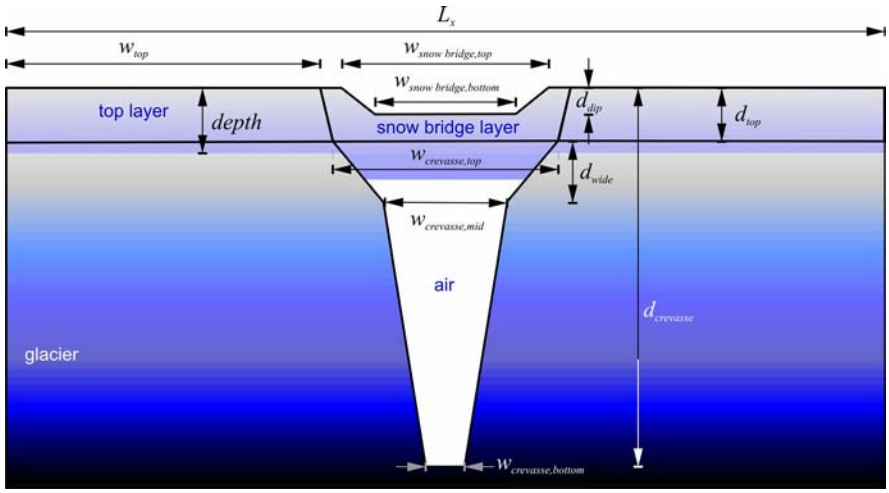

Figure 15 Diagram of the smooth cross section of the crevasse, with parameters, before fractal generation is applied.

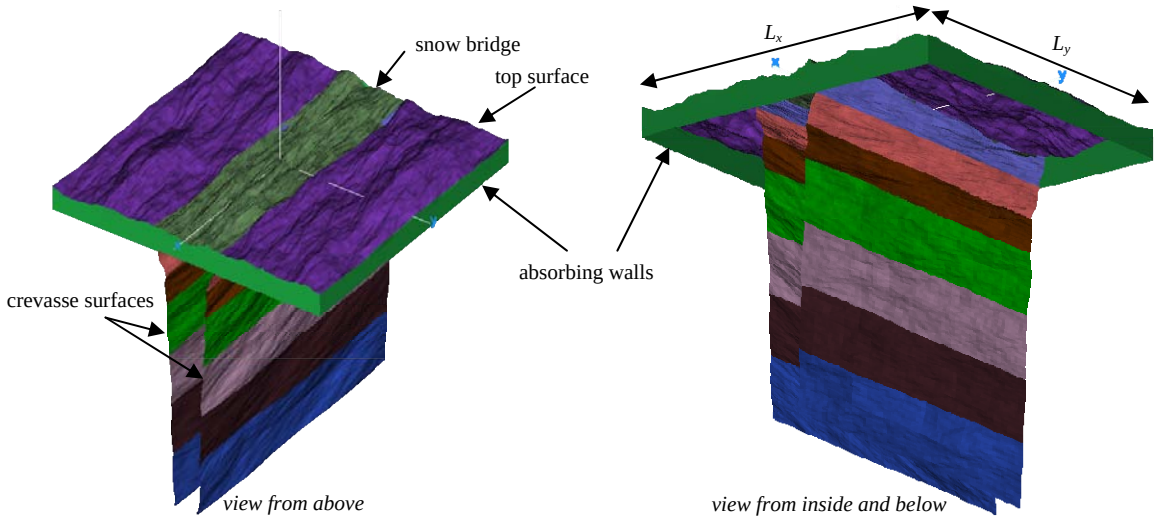

Figure 16 Illustration of the fractal surface geometry, with different colors representing regions with different material properties. The smooth, green sides represent perfect absorber, which, in the complete model, actually extents downward to enclose the interior of the model.

The different regions where the dielectric properties are defined separately are delineated in Figure 16 with different colors. The gray-green region on the top surface represents the snow bridge, and the adjacent purple regions represent the glacier. The smooth green vertical sides at the edges of the top surface represent the absorbing walls that prevent illumination of the crevasse walls from the wrong side. Although the absorbing walls extend only a small depth in the illustration, they extend to the full depth in the computational model and completely shield the crevasse from any illumination, except that entering through the top surface. The absorber is necessary since the surface does not extend indefinitely in all directions, exposing the interior of the model to the incident energy if the absorber were not present.

The dielectric permittivity will be modeled with a series of layers to an appropriate depth for both the top layer and snow-bridge layer. For the images presented here, the top layer and the snow bridge will have identical density profiles, except that the snow-bridge layer is terminated by air and the remainder of the top layer is terminated by a dielectric half-space. Since the permittivity varies with density, the density profile will affect reflection from, propagation into, and propagation through the snow-bridge layer. The variations of the density profile will have the largest effect in the near-surface region, so the permittivity of the top regions will be modeled with 2 cm resolution in depth. The total depth of the top layer varies from 0.5 m to 4 m for different simulations. On the walls of the crevasse, the permittivity will also vary with depth. Since scattering from the crevasse walls will be dominated by the large difference in permittivity between the air inside the crevasse and the ice of the glacier, and will not be strongly affected by small changes in the permittivity of the glacier, only a few regions will be modeled inside the crevasse. The dielectric properties will be appropriate for the depth at the center of each region.

The geometric and fractal parameters for the model used in the simulations are given in Table 3. The geometrical parameters are defined in Figure 15 and Figure 16, except for N_g, which is the number of regions modeled along the crevasse walls. The fractal parameters are described in Appendix I, except for N_{top}, which is the number of rectangular sections (along the $\hat{\mathbf{x}}$ direction) into which the top surfaces on either side of the snow bridge are divided. Starting the fractal-generation process with long, narrow rectangular regions will produce the linear features that mimic the sastrugi produced by winds blowing over the Antarctic ice. That is how the long, linear features visible in Figure 24 and Figure 16 were produced. Note that the snow-bridge region does not slump below the surrounding region in this particular model.

Table 3 Geometric and fractal parameters for crevasse model.

	Top Surface				Snow-bridge definition				Crevasse definition					
Basic geometry	L_x (m)	L_y (m)	w_{top} (m)		d_{top} (m)	d_{dip} (m)	$w_{snow\ bridge,\ top}$ (m)	$w_{snow\ bridge,\ bottom}$ (m)	$d_{crevasse}$ (m)	d_{wide} (m)	$w_{screvassee,top}$ (m)	$w_{screvassee,mid}$ (m)	$w_{screvassee,bottom}$ (m)	N_g
	6.0	6.0	2.25		0.5	0.001	1.5	0.5	6.0	0.50	1.25	0.90	0.50	7
Fractal parameters	*fractal levels*	*peak height* (m)	*scale factor*	N_{top}	*levels*		*peak height* (m)	*scale factor*	*fractal levels*		*peak height* (m)		*scale factor*	
	5	0.125	0.5	2	5		0.125	0.5	5		0.05		0.50	

The top surface, after application of the fractal-surface algorithm, is illustrated in Figure 17. The regions are no longer delineated by color, but the snow-bridge region is still visible due to its finer fractal detail. The mesh is somewhat finer on the snow-bridge surface than on the surrounding surface, as can be easily seen in the wire-grid representation in Figure 18. This will have both positive and negative consequences in the simulated SAR images.

Because the texture of the snow bridge is rougher than the surrounding surface, it will appear brighter at some aspect angles. This will aid the differentiation of the scattering from the top of the snow bridge and the scattering from the bottom within the image. In some cases, these components

of the image overlap, but in others they will be quite distinct. However, this does increase the contrast between the parts of the image due to surface scattering from the snow bridge and the adjacent glacier surface.

Initially, the intent of this study was to include several different geometrical models, with some having the snow-bridge and adjacent regions with more similar structure, much like that in Figure 24. For other models, the snow bridge would slump below the adjacent regions, as allowed by choices of parameters illustrated in Figure 15. Unfortunately, the current study was limited to a single geometric model because of the long computational times required for each phase history, and by the need to examine the performance with respect to variation of a number of parameters. Such a parametric examination requires that a common geometry be used to obtain valid comparisons.

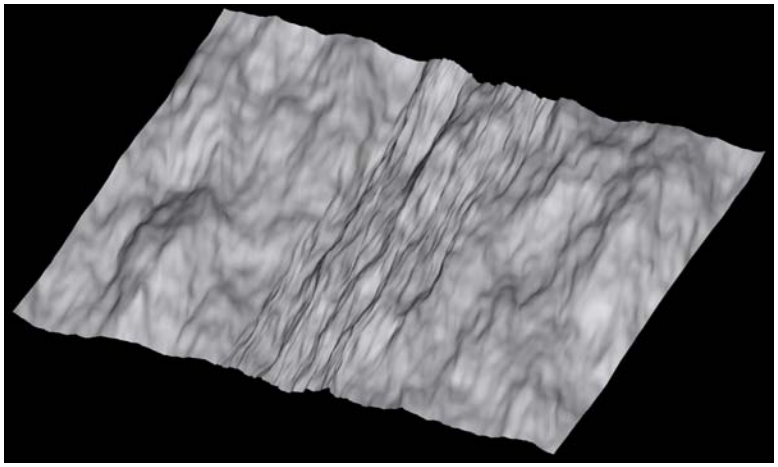

Figure 17 Illustration of the fractal surface geometry of the top layer, without the snow-bridge area differentiated by different color.

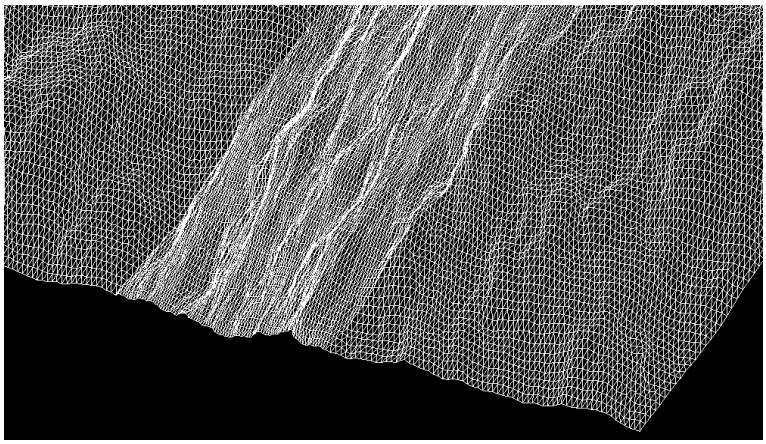

Figure 18 Illustration of the fractal surface geometry of the top layer, showing a smooth rendition on the left, and a wire-frame rendition on the right. The finer resolution of the fractal surface is clearly visible.

Simulated SAR images

The glacial ice and fern exhibit loss at microwave frequencies, and Figure 2 and Figure 3 show that lower frequencies have lower losses. Because of this frequency dependence, images produced in three radar bands will be examined. The FCC frequency-allocation chart [17] shows the following allocations (combining primary and secondary allocations) for radiolocation in C-, X-, and Ku-bands:

C-band: 5.25 to 5.65 GHz
X-band: 8.5 to 10.55 GHz
Ku-band: 15.7 to 17.7 GHz

If the SAR images are processed with Taylor weighting, $\bar{n} = 4$, $SLL = -35\text{ dB}$, then the resolutions that are possible (using up to the entire allocation) are listed in Table 4.

Table 4 Possible resolutions available within the FCC radiolocation allocations.

	Resolution and bandwidth with Taylor weighting ($\bar{n} = 4$, $SLL = -35$ dB)					
	24-inch (0.2912 GHz)	18-inch (0.3882 GHz)	12-inch (0.5824 GHz)	8-inch (0.8735 GHz)	6-inch (1.1647 GHz)	4-inch (1.7471 GHz)
C-band	✓	✓	—	—	—	—
X-band	✓	✓	✓	✓	✓	✓
Ku-band	✓	✓	✓	✓	✓	✓

The simulated synthetic-aperture-radar images will be presented in several forms. When appropriate, the amplitude scale will be radar cross section, σ, usually plotted in decibels relative to a square meter (dBsm). The radar cross section is an effective area that describes how effectively the object scatters the incident radar signal back to the radar. The product of the radar cross section with the incident power density gives the total power scattered in the direction of the radar. Scaling the image to radar cross section is appropriate for objects like trihedral corner reflectors, but is less appropriate for distributed objects, and for this reason it is not often used for SAR images.

When the scattering is from a distributed scatterer, it is appropriate to use a reflection coefficient without units, σ_0, that represents the radar cross section per unit area of the distributed scatterer. The amplitude scale will be labeled in decibels relative to the unit area. Because SAR images typically contain distributed clutter, it is appropriate to measure the image amplitude in terms of σ_0.

A third representation of the image will simply plot the square root of the magnitude of the response at each point. This representation provides different contrast in the printed image, and is typical of the way SAR images are displayed. When used here, there will be no scale given with the plot. This representation is proportional to the fourth root of power.

The logarithmic (decibel), square root, and linear intensity curves are compared in Figure 19. The non-linear curves expand the intensity range for weak responses and compress the intensity for strong responses. The decibel weighting strongly emphasizes the weak responses, while the linear response treats all responses equally. The square root weighting exaggerates the weak responses much less severely than the decibel weighting, but still improves their visibility in the image.

Phase histories for the images are computed with an implementation of the shooting and bouncing ray (SBR) method, called Xpatch® [27, 28]. The SBR is described in Appendix II. Some computations for canonical objects show that Xpatch® is capable of producing reasonably realistic results for scattering from dielectric objects, although it appears that results with polarization perpendicular to the plane of incidence is somewhat more accurate than with polarization parallel to the plane of incidence (see Appendix III). An array of 15 triangular trihedral reflectors was modeled to test the imaging capability of Xpatch®.

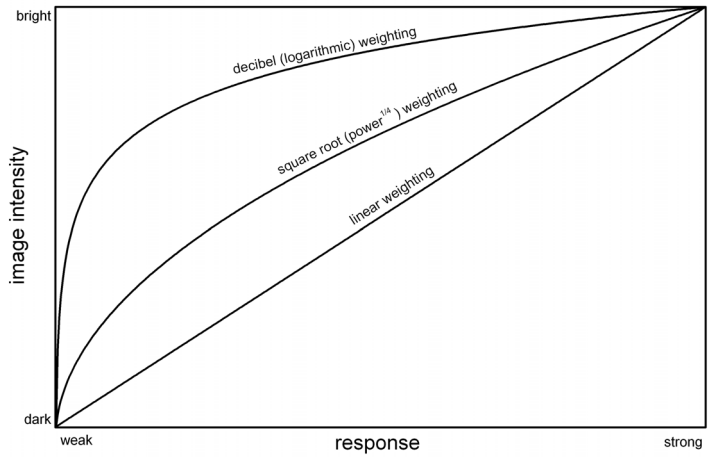

Figure 19 Comparison of different intensity curves used to plot images.

Trihedral array

The corner-seam dimension of each trihedral is 0.200 m. The nominal radar cross section of each trihedral is +8.3 dBsm at 9.5 GHz. The reflectors were placed on the surface $z = 0$ in the pattern illustrated in Figure 20. Note that the dimension *x* is measured positive down and *y* is positive to the right. The location of each reflector is listed in Table 5. The SAR image, based on a phase history computed by Xpatch® at X-band over a 1.75 GHz bandwidth is shown on the right in Figure 20. The elevation angle to the SAR platform is 30°. Each trihedral reflector is clearly visible as a bright spot. To suppress sidelobes, the phase-history data is weighted with a Taylor window in both dimensions, with $\bar{n} = 4$ and the design sidelobe level -35 dB, giving resolution of about 4.0 inches (at the -3 dB points). This Taylor window will be used with all subsequent images. However, as different bandwidths will be used, the resolution will change. The resolution obtained with this weighting will be noted for each SAR image. Figure 21 shows simulated SAR images of the trihedral array for resolutions of 18, 12, 8, and 4 inches. Note that the 18- and 12-inch resolutions are not capable of resolving the most closely spaced reflectors.

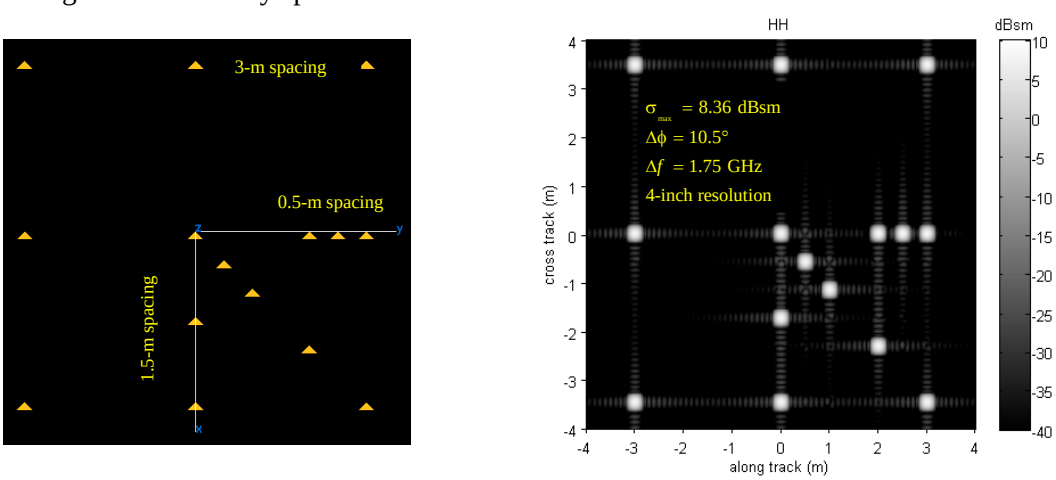

Figure 20 Diagram of the array of 15 trihedral corner reflectors (left) and a synthetic-aperture image of the array (right).

Table 5 Location of the trihedral reflectors in the array illustrated in Figure 20.

	tri-1	tri-2	tri-3	tri-4	tri-5	tri-6	tri-7	tri-8	tri-9	tri-10	tri-11	tri-12	tri-13	tri-14	tri-15
x	–3 m	0 m	3 m	–3 m	0 m	1.5 m	3 m	–3 m	0 m	3 m	0 m	0 m	0.5 m	1 m	2 m
y	–3 m	–3 m	–3 m	0 m	0 m	0 m	0 m	3 m	3 m	3 m	2 m	2.5 m	0.5 m	1 m	2 m

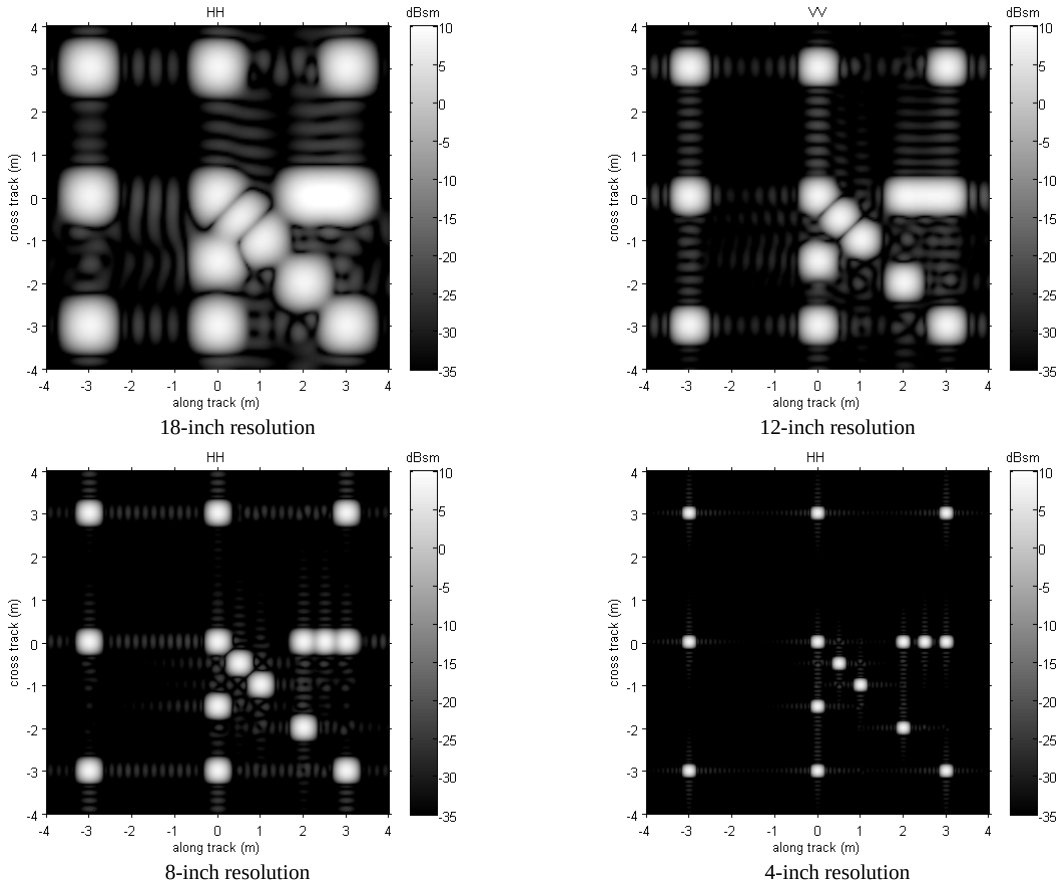

Figure 21 *Images of the trihedral array with resolutions of 18, 12, 8, and 4 inches, at X-band. The 8-inch-resolution image resolves each trihedral, but the 12-inch and 18-inch images cannot completely resolve the closely spaced trihedrals.*

As an example of the ways images will be reproduced here, Figure 22 shows the image of the trihedral array at 8-inch resolution, with each of the different representations. The image on the far right is most representative of a typical SAR image, while the other three representations allow amplitude values to be read more easily. Of these, the color scale is best for reading amplitude values. The two center monochrome images differ in measurement scale. The image at center left is scaled according to the radar cross section (decibels with respsect to a square meter), appropriate for non-distributed scatterers, like corner reflectors. The image at center right is scaled according to reflection coefficient (decibels with respsect to unit area), appropriate for distributed scatterers, like surface clutter. The color images will be scaled as radar cross section or reflection coeffcient, as appropriate. The label for the magnitude scale should be referenced to decern the difference.

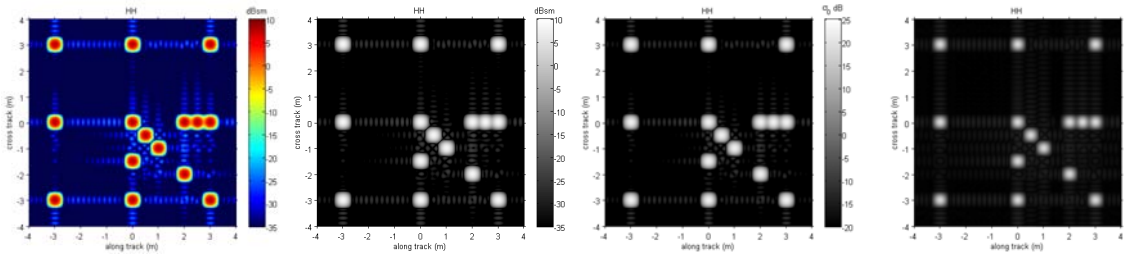

Figure 22 *Illustration of the various image representations: far left is radar cross section, σ in dBsm, with color scale; middle left is radar cross section (dBsm) with gray scale; middle right is cross section per unit area, σ_0 in dB; and far right is square root of the amplitude (no scale given).*

Transparency of the Antarctic snow and glacial ice

For the initial transparency tests, a *flat* surface 12 m x 12 m was placed 1 m above the trihedral array. The dielectric model consisted of 50 layers, each 2.0 cm deep, for a total depth of 1 m. The dielectric profile is based on the composite Siple Dome density profile; the density is given by equation (1.23). Simulated X-band SAR images with 18-, 12-, and 8-inch resolutions are illustrated in Figure 23 for the case where the trihedral array buried under the 1-m deep flat layer, with depression angle of 30°. The array is imaged faithfully, without distortion, except for the image-processing sidelobes associated with the Taylor weighting. However, the HH polarization (on the left) clearly shows the multiple reflections (manifest as a delayed "ghost" image) between the reflector and dielectric layer. This is an expected and potentially important aspect of the scattering from a crevasse. Fortunately, the SBR method as implemented by Xpatch® includes this effect.

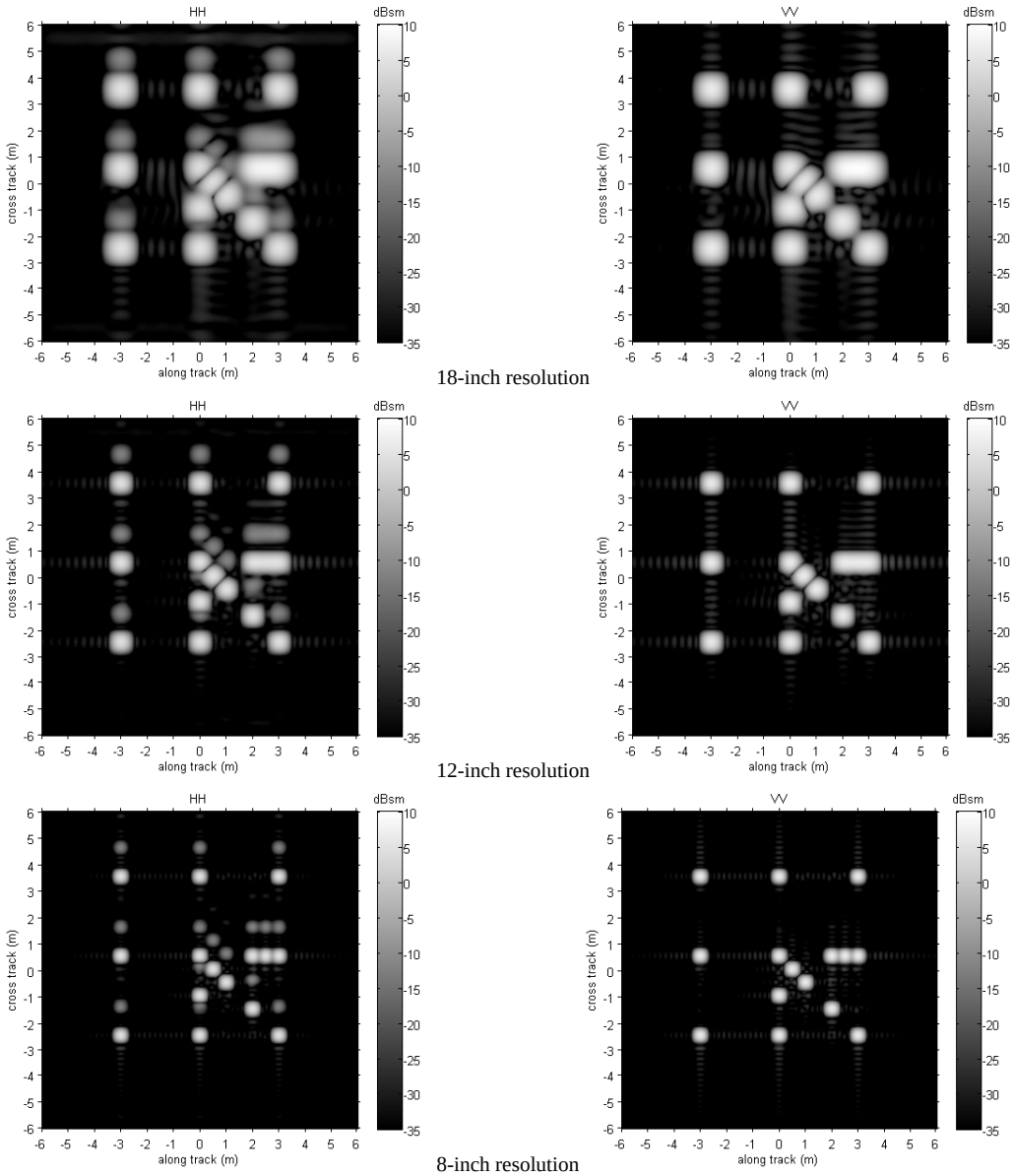

Figure 23 X-band response of trihedral array buried under a perfectly flat, 1 m deep layer of Siple Dome composite snow and glacial ice, for HH (left) and VV (right) polarizations, with three resolution bandwidths.

The Antarctic snow and glacial ice is not perfectly flat, so the model is modified to include a rough surface. The surface roughness is based on a fractal-surface model. A fractal-surface representation of the glacial surface is illustrated in Figure 24. This surface was generated from a perfectly flat surface by applying five levels of the algorithm described in Appendix I. The parameters (see Appendix I for definitions) are $\delta_{max} = 0.1$ m and $\eta = 1/2$. The area represented measures 12 m along each side. The initial surface, before applying the fractal algorithm, was located 1 m above the $\hat{\mathbf{x}}, \hat{\mathbf{y}}$ plane. The level 0 mesh was obtained by dividing the surface into strips 2 m wide in the $\hat{\mathbf{y}}$ direction, and then dividing each strip into two right triangles. By using parallel diagonals to form the triangles in each of the strips, the wind-blown-drift (sastrugi) nature of the surface was obtained. The resulting mesh cells are narrow triangles, elongated in the $\hat{\mathbf{x}}$ direction, as illustrated in Figure 24.

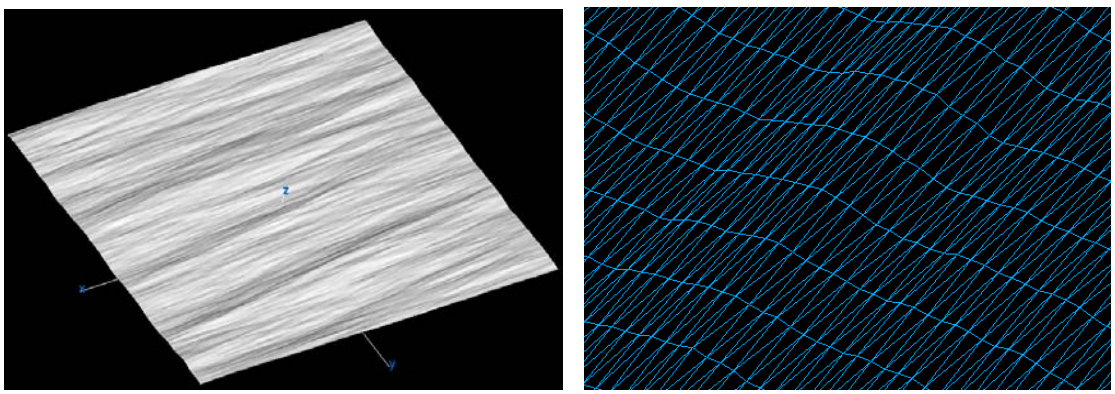

Figure 24 Fractal surface representing the top surface of the Antarctic snow and glacial ice, with the full surface on the left and the mesh detail near center of the fractal surface on the right.

The SAR images of the trihedral array beneath the 1-m deep fractal-surface cover are shown in Figure 25, for resolutions of 18, 12, and 8 inches. The dielectric model consists of 50 layers, each 2 cm thick, based on the profile of the Siple Dome density model. The images of the trihedral array are not quite as crisp as those for the flat-layer covering. There is some additional surface scattering, as expected. There is also a sidelobe on either side of the main lobe of each trihedral response that was not present in the images with the flat layer. The rough surface introduces some phase error which will increase sidelobes, but these sidelobes are at least partially due to an artifact associated with the creating SAR images with the SBR method. This artifact, its cause, and appropriate Xpatch® parameter settings to reduce its effect are discussed in Appendix IV. Parameters for the simulations in this study have been chosen to minimize the artifact.

A side-by-side comparison between X-band images of the uncovered array, the array beneath the perfectly flat cover, and beneath the fractal-surface cover are provided in Figure 26, Figure 27, and Figure 28 for resolutions of 18, 12, and 8 inches, respectively, with the cover thickness of 1 m. The center frequency is $f = 9.5$ GHz. Evidence of multiple reflections is seen clearly in the HH-polarized response when the flat surface is present, and is visible to a lesser degree when the fractal surface is present. With the perfectly flat cover, the response of the reflectors is reduced somewhat, but the image is not substantially different from the image of the uncovered reflectors. However, with the fractal cover, the response of the reflectors is reduced, but not uniformly. The rough surface reduces the response of the reflectors, in addition to the inherent propagation loss of the material.

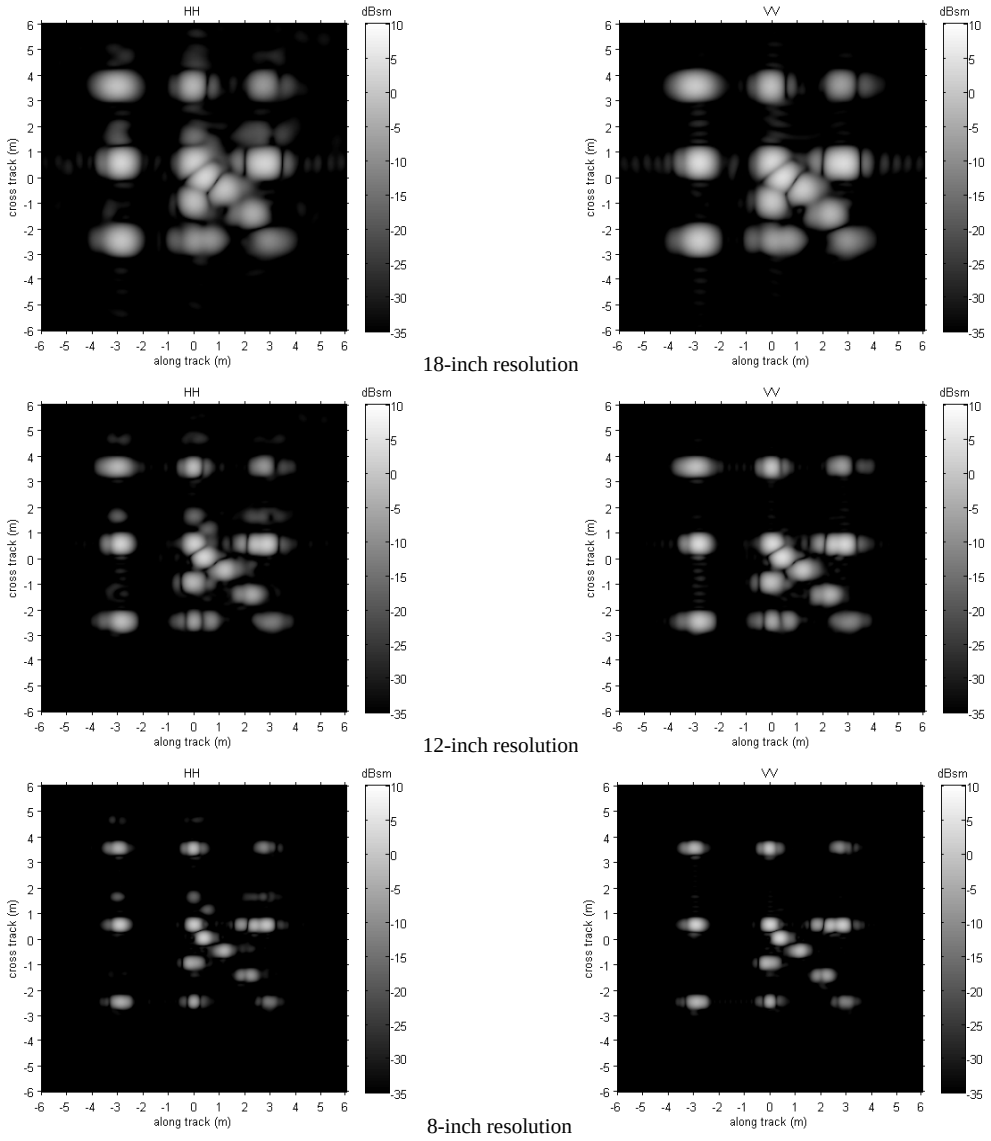

Figure 25 X-band response of trihedral array buried under a rough, 12 m x 12 m x 1 m deep layer of Siple Dome composite snow and glacial ice, for HH (left) and VV (right) polarizations, with three resolution bandwidths. The rough surface is the fractal-based surface illustrated in Figure 24.

Figure 29 compares the response of the trihedral array at C-band (18-inch resolution) when the array is uncovered, covered with a smooth surface, and covered with a rough fractal surface for depths of 1 m, 2 m, and 4 m. Figure 30 and Figure 31 provide the same comparison at X-band and Ku-band, respectively, but with 8-inch resolution. The peak radar cross section is reduced by the presence of the cover, and when surface roughness is introduced, the effect is to increase the loss, and to make the loss nonuniform over the image. With the rough cover in place, most of the reflectors are dimmer than the peak response within the image. The peak radar cross sections in the various images of the trihedral array are listed in Table 6, Table 7, and Table 8 for C-band, X-band, and Ku-band respectively. The minimum loss, defined as the difference between peak radar cross section with no cover and the peak radar cross section with cover, is also tabulated. Although the C-band signal suffers less loss when the surface is smooth, consistent with the propagation loss per meter plotted in Figure 2, the lower resolution image shows more loss than X-band at the 1-m and 4-m depths for the rough surface. Ku-band produces brighter images of the trihedrals (because they are smooth, flat objects), but exhibits more loss at all depths than either C-band or X-band. It is not expected that the scattering from the bottom of the snow bridge and the crevasse walls will be

significantly different for each frequency band, so the loss is very important in determining which band would be optimum.

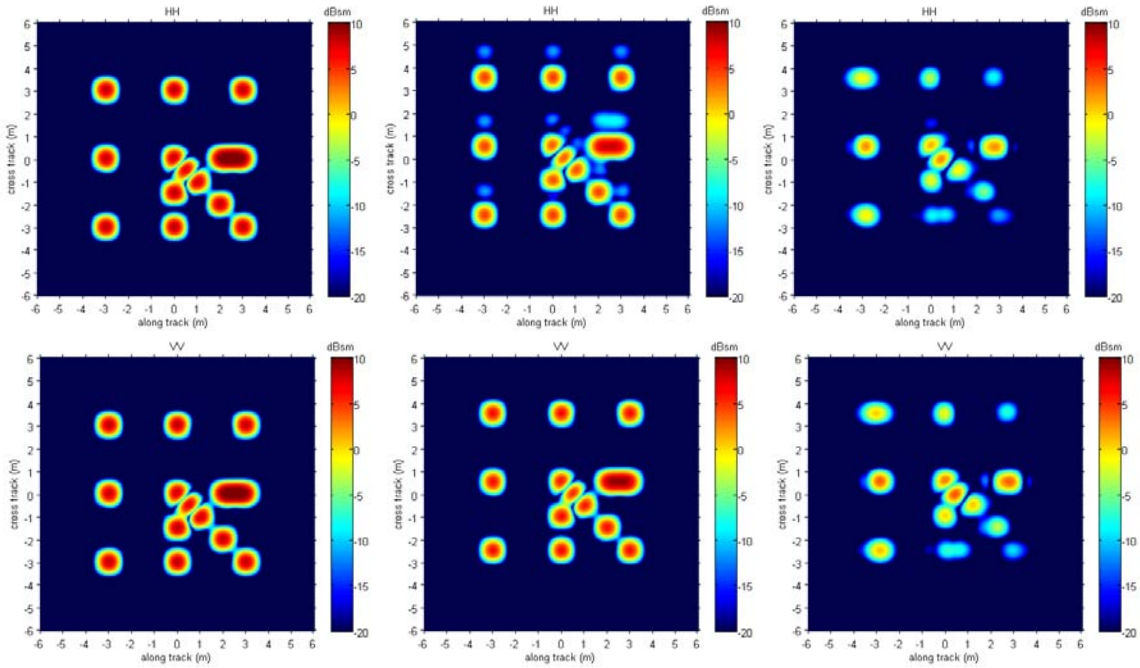

no covering 1-m deep flat layer 1-m deep fractal layer

Figure 26 Comparison of the X-band response of trihedral array uncovered (left), buried under a perfectly flat surface (middle), and buried under a rough, fractal surface (right). The center frequency is 9.5 GHz with 18-inch resolution. The covering is a stack of 50 layers totaling 1 m deep with a density profile corresponding to the Siple Dome composite model.

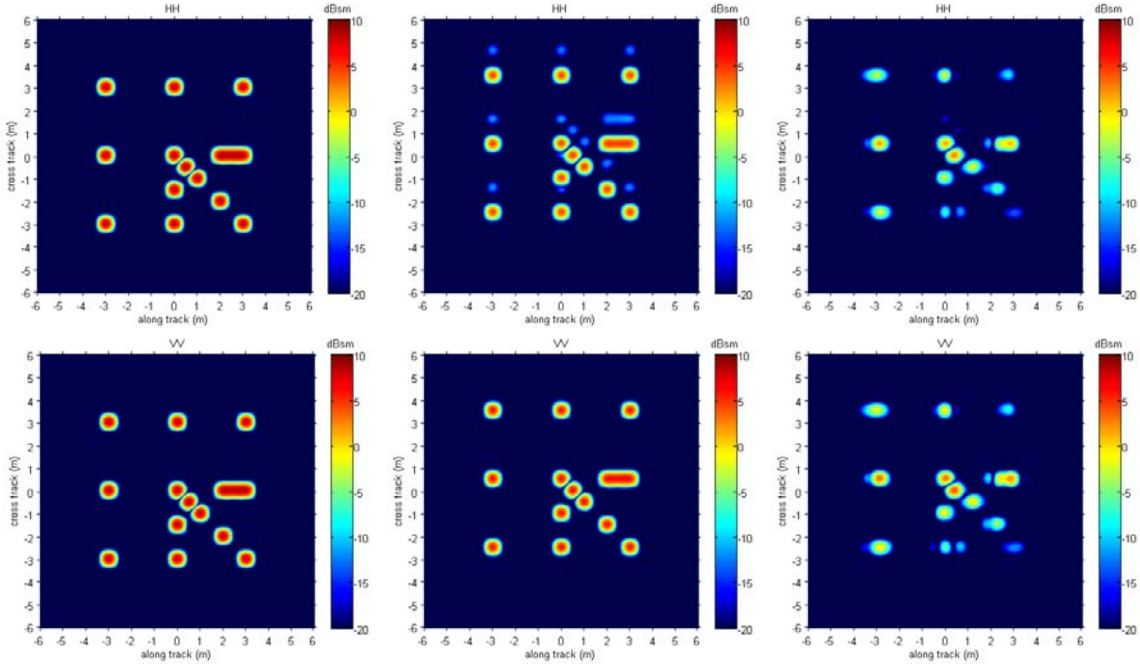

no covering 1-m deep flat layer 1-m deep fractal layer

Figure 27 Comparison of the X-band response of trihedral array uncovered (left), buried under a perfectly flat surface (middle), and buried under a rough, fractal surface. The center frequency is 9.5 GHz with 12-inch resolution. The covering is a stack of 50 layers totaling 1 m deep with a density profile corresponding to the Siple Dome composite model.

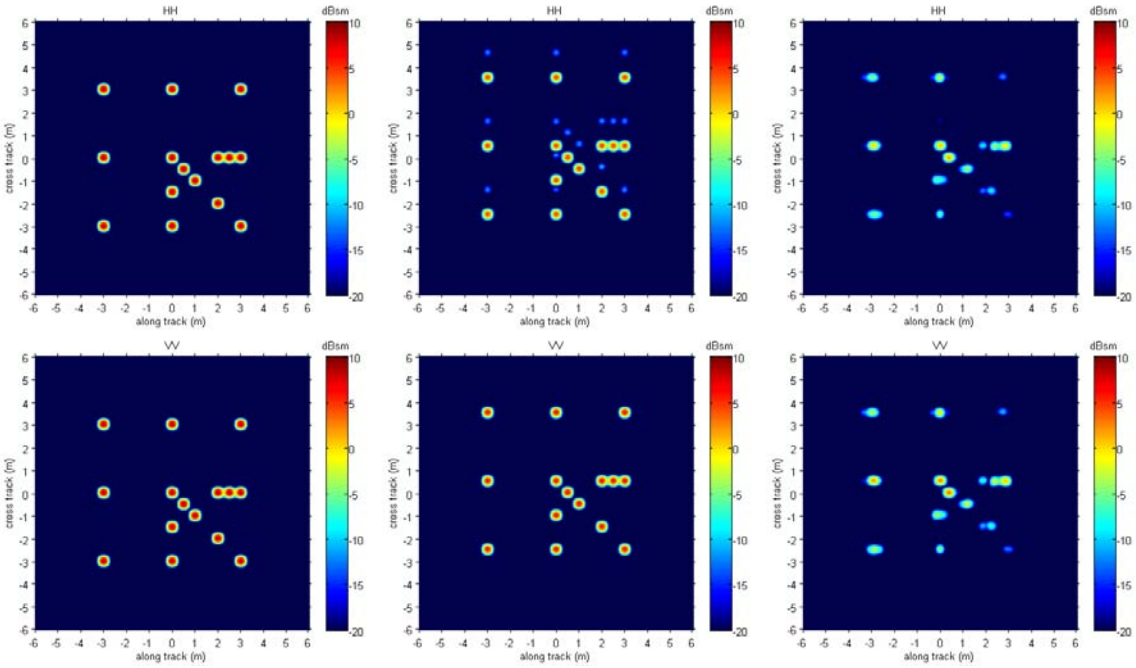

no covering 1-m deep flat layer 1-m deep fractal layer

Figure 28 Comparison of the X-band response of trihedral array uncovered (left), buried under a perfectly flat surface (middle), and buried under a rough, fractal surface. The center frequency is 9.5 GHz with 8-inch resolution. The covering is a stack of 50 layers 1-m deep with a density profile corresponding to the Siple Dome composite model.

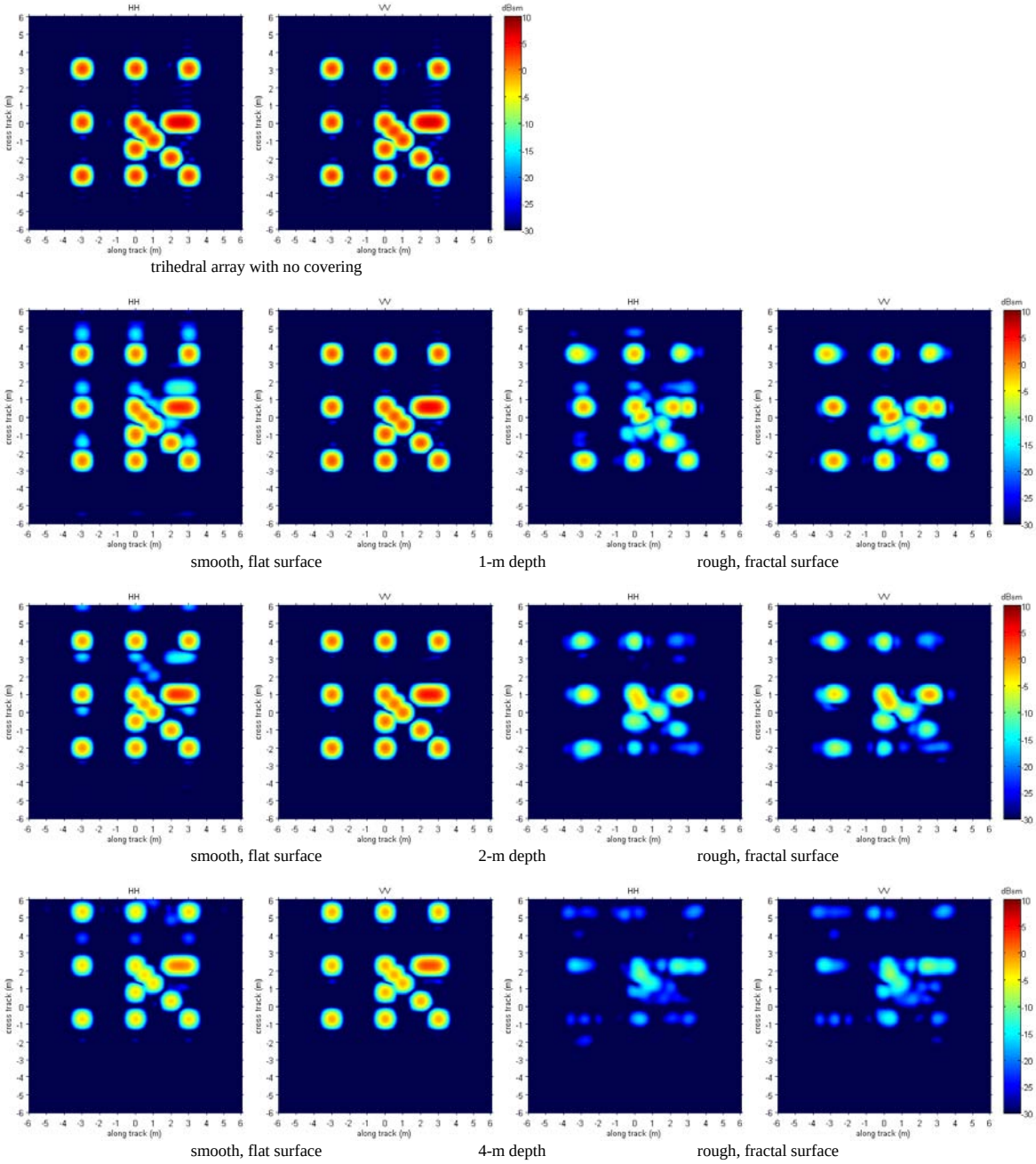

Figure 29 C-band response of the trihedral array buried under a smooth, flat surface (left) and buried under a rough, fractal surface (right), for three depths of snow and glacial ice. The center frequency is 5.45 GHz, and the bandwidth corresponds to 18-inch resolution. The top row is the reference response, with no covering over the array. The covering is a stack of 2-cm thick layers totaling 1 m deep (next to top), 2 m deep (next to bottom), and 4 m deep (bottom). The density profile corresponds to the Siple Dome composite model.

Table 6 Peak radar cross section of the trihedral reflector array with and without the presence of the snow and glacial ice cover, at C-band with 18-inch resolution.

	peak radar cross section (dBsm)			minimum loss (dB)	
depth (m)	no cover	smooth cover	fractal cover	smooth cover	fractal cover
1	6.9	5.7	0.4	1.2	6.5
2	6.9	4.7	–0.6	2.2	7.1
4	6.9	2.4	–8.5	4.5	15.4

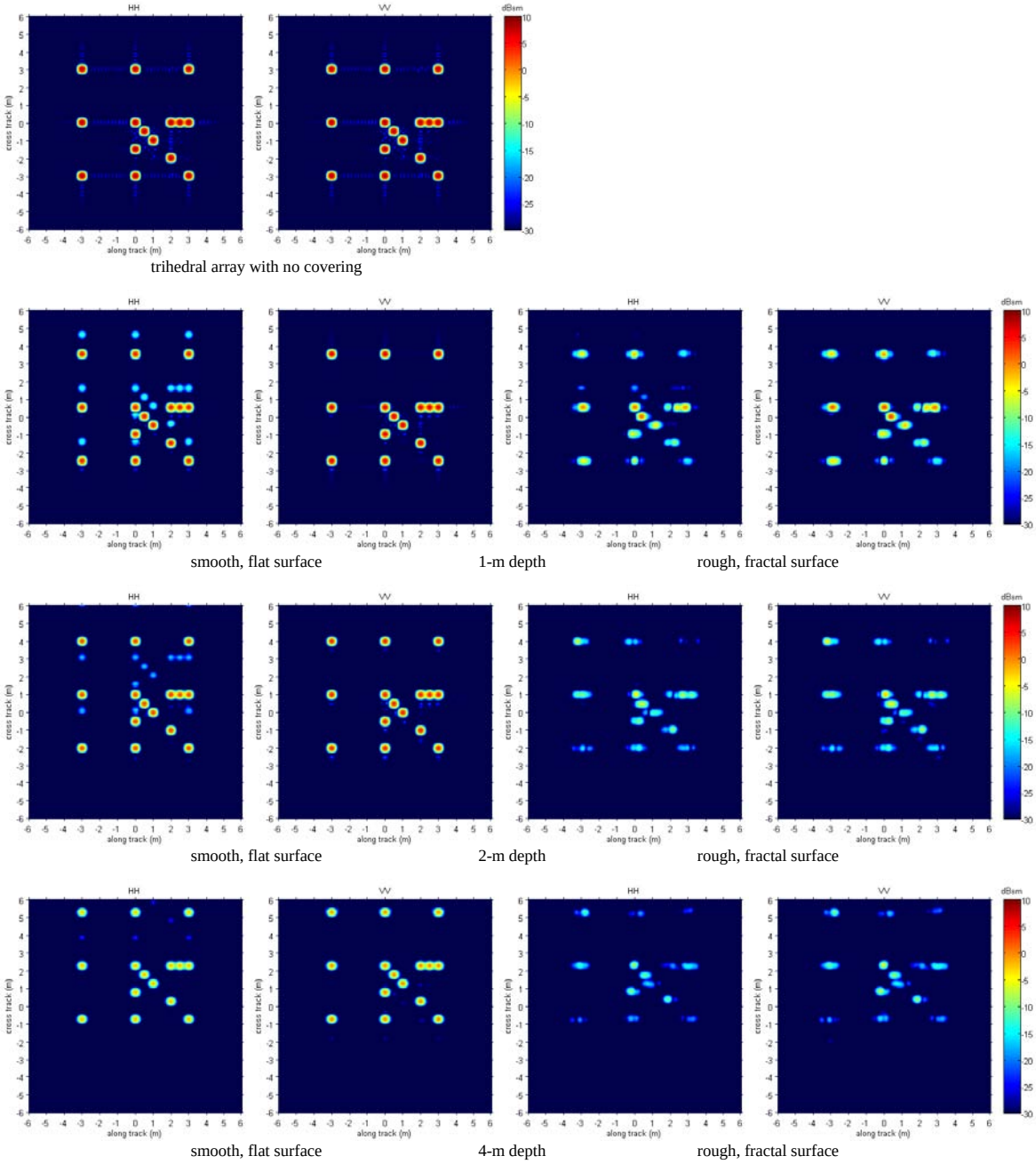

Figure 30 X-band (9.5 GHz) 8-inch resolution response of the trihedral array buried under a smooth, flat surface (left) and a rough, fractal surface (right), for three depths of snow and glacial ice. The top row is the reference response, with no covering over the array. The covering is a stack of 2-cm thick layers totaling 1 m deep (next to top), 2 m deep (next to bottom), and 4 m deep (bottom). The density profile corresponds to the Siple Dome composite model.

Table 7 Peak radar cross section of the trihedral reflector array with and without the presence of the snow and glacial ice cover, at X-band with 8-inch resolution.

	peak radar cross section (dBsm)			minimum loss (dB)	
depth (m)	no cover	smooth cover	fractal cover	smooth cover	fractal cover
1	8.4	6.3	2.8	2.1	5.6
2	8.4	4.3	–2.3	4.1	10.7
4	8.4	0.2	–5.4	8.2	13.8

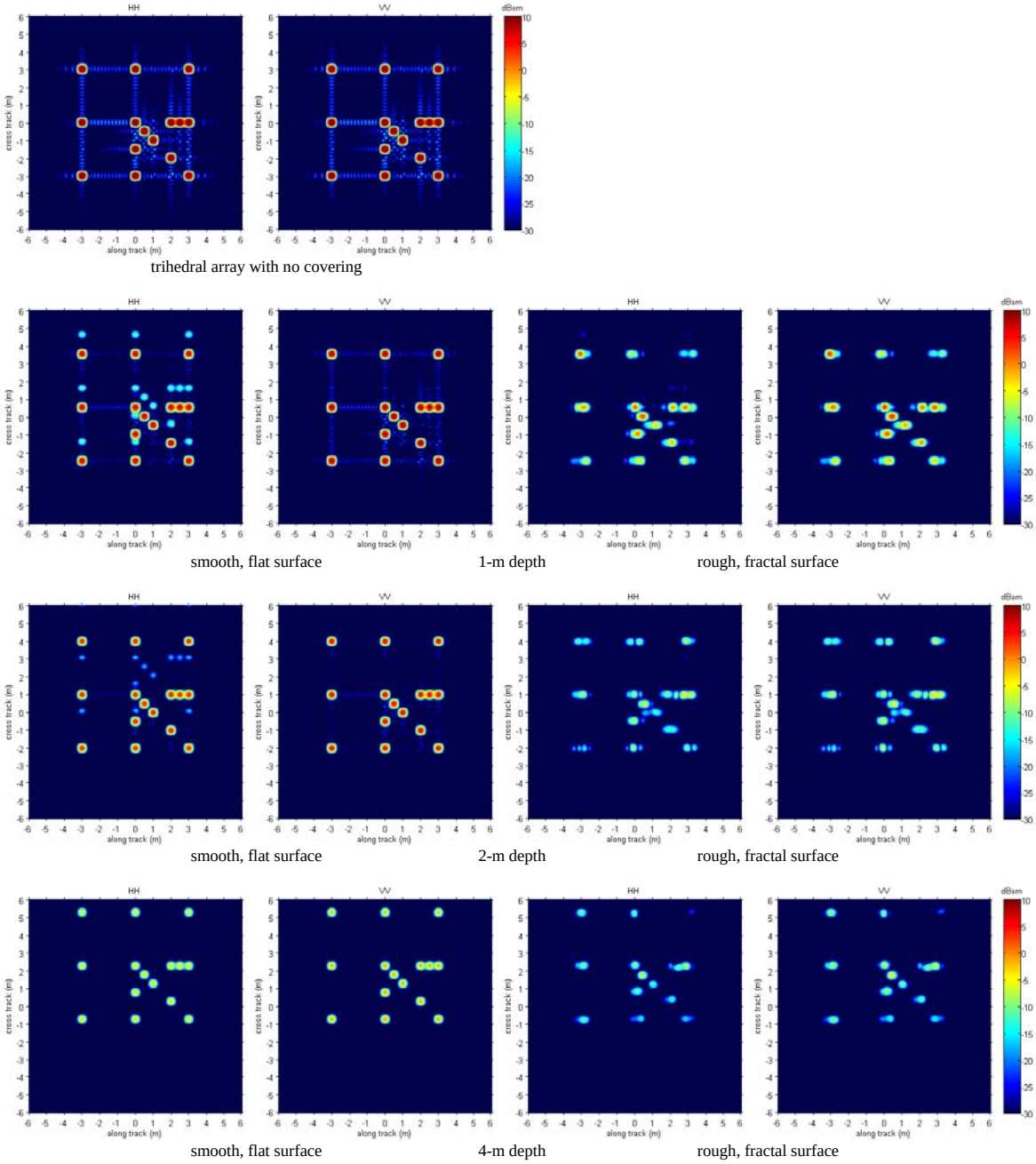

Figure 31 Ku-band (16.8 GHz) 8-inch resolution response of the trihedral array buried under a smooth, flat surface (left) and buried under a rough, fractal surface (right), for three depths of snow and glacial ice. The top row is the reference response, with no covering over the array. The covering is a stack of 2-cm thick layers totaling 1 m deep (next to top), 2 m deep (next to bottom), and 4 m deep (bottom). The density profile corresponds to the Siple Dome composite model.

Table 8 Peak radar cross section of the trihedral reflector array with and without the presence of the snow and glacial ice cover, at Ku-band with 8-inch resolution.

	peak radar cross section (dBsm)			minimum loss (dB)	
depth (m)	no cover	smooth cover	fractal cover	smooth cover	fractal cover
1	13.3	9.8	3.9	3.5	9.4
2	13.3	6.3	–2.1	7.0	15.4
4	13.3	–0.7	–3.7	14.0	17.0

Simulated images of the crevasse and snow bridge

A large collection of simulated images of the crevasse and snow bridge is contained in Appendix V. This collection includes 768 images in 96 sets, representing 128 computer simulations. These images encompass the following set of parameters:

Radar band:	C-band, X-band, and Ku-band
Resolution:	18-inch (all bands) and 8-inch (X-band, Ku-band only)
Geometry model:	Crevasse with snow bridge and snow bridge only (without crevasse)
Snow-bridge depth:	0.5 m, 2.0 m, 4.0 m
Permittivity profile:	Siple Dome composite and Newall Glacier (with dip), both at $T = 0°$ C
Depression angle:	15° and 30°
Azimuth angle:	0°, –30°, –60°, and –90°
Polarization:	HH and VV (transmit and receive horizontal, transmit and receive vertical)

The images from each simulation are displayed in three different formats: monochrome reflection coefficient (σ_0, dB), color reflection coefficient (σ_0, dB), and monochrome 4th-root of power (typical SAR image format). By using permittivity profiles at a temperature of 0° C, a worst-case propagation model for *dry* snow is obtained.

Note: azimuth is measured positive in the direction from the $\hat{\mathbf{x}}$ axis toward the negative $\hat{\mathbf{y}}$ axis. Thus, when the radar is at $0°$ azimuth, it is looking down the $\hat{\mathbf{x}}$ axis. Similarly, when it is at $-90°$ azimuth, it is looking down the $\hat{\mathbf{y}}$ axis, and azimuth of $-30°$ or $-60°$ is looking between the positive $\hat{\mathbf{x}}$ and $\hat{\mathbf{y}}$ axes. See Figure 16 and Figure 20 for the location of these axes.

As stated earlier, the top of the snow-bridge region in this model is slightly rougher than the surrounding material (see Figure 17). For some azimuth angles, this leads to stronger scattering from the top surface of the snow-bridge region than from the surrounding surface. The scattering from a point in the interior region (on the bottom of the snow bridge or on the crevasse wall) is at a greater range than the corresponding point directly above it on the top surface. This additional range causes a time delay, and, when imaged, these interior points appear at a greater range in the image. Scattering components that are delayed sufficiently that they appear beyond the extent of the truncated geometry will be easily discernable in the images. When the delay is not sufficient to extend outside the truncated geometry of the model, the returns from depth will cause the image of the crevasse to be broadened when compared to its extent on the surface. However, care must be taken to not confuse the scattering directly from the top surface of the snow bridge with scattering from the interior. Only those components that are delayed in time, and thus appear at a greater range, are from the interior. Because the model produces a strong return from the surface of the snow bridge, its location in the image can be easily indentified. The image from interior points is then indentified by its increased range in relation to the surface image. This is a potential point of confusion, since the surface image is quite prominent in many of the images, and could be easily confused with the image of the below-surface features of the crevasse. Thus, appropriate care must be taken when interpreting the images.

All three radar bands can support imaging at 18-inch resolution, but only X-band and Ku-band can support 8-inch resolution. However, Figure 2 shows that C-band will have an advantage with less loss and greater penetration depth. To answer whether or not improved penetration depth or finer resolution is most important, examine Figure 32 and Figure 33. These images are formed with a depression angle of 30° and azimuth of 0°. The radar is looking down the length of the crevasse, which seems to be the worst aspect, based on images from the Sandia Antarctic mission in December, 2006 [9]. In this example, the snow bridge is 2 m deep, with dielectric properties based on the Siple Dome composite profile. The images are presented as the 4th root of power, which is a typical presentation for SAR images.

Figure 32 compares the response among the three radar bands when the resolution is 18 inches. Within the square image of the top surface, it is difficult to distinguish the crevasse and snow bridge from the surface clutter on either side. The image of the crevasse should be a vertical strip in the center. However, the delayed response from the interface between the ice and the air at the bottom of the snow bridge is clearly present, especially in the HH-polarized data. This response is not brighter than the surrounding surface, but because the model is limited in extent and surrounded by vacuum, the delayed response shows clearly in the void above the image of the surface. The response is weakest at Ku-band, especially in the VV-polarized image, but any advantage between C- and X-band is less clear at this resolution.

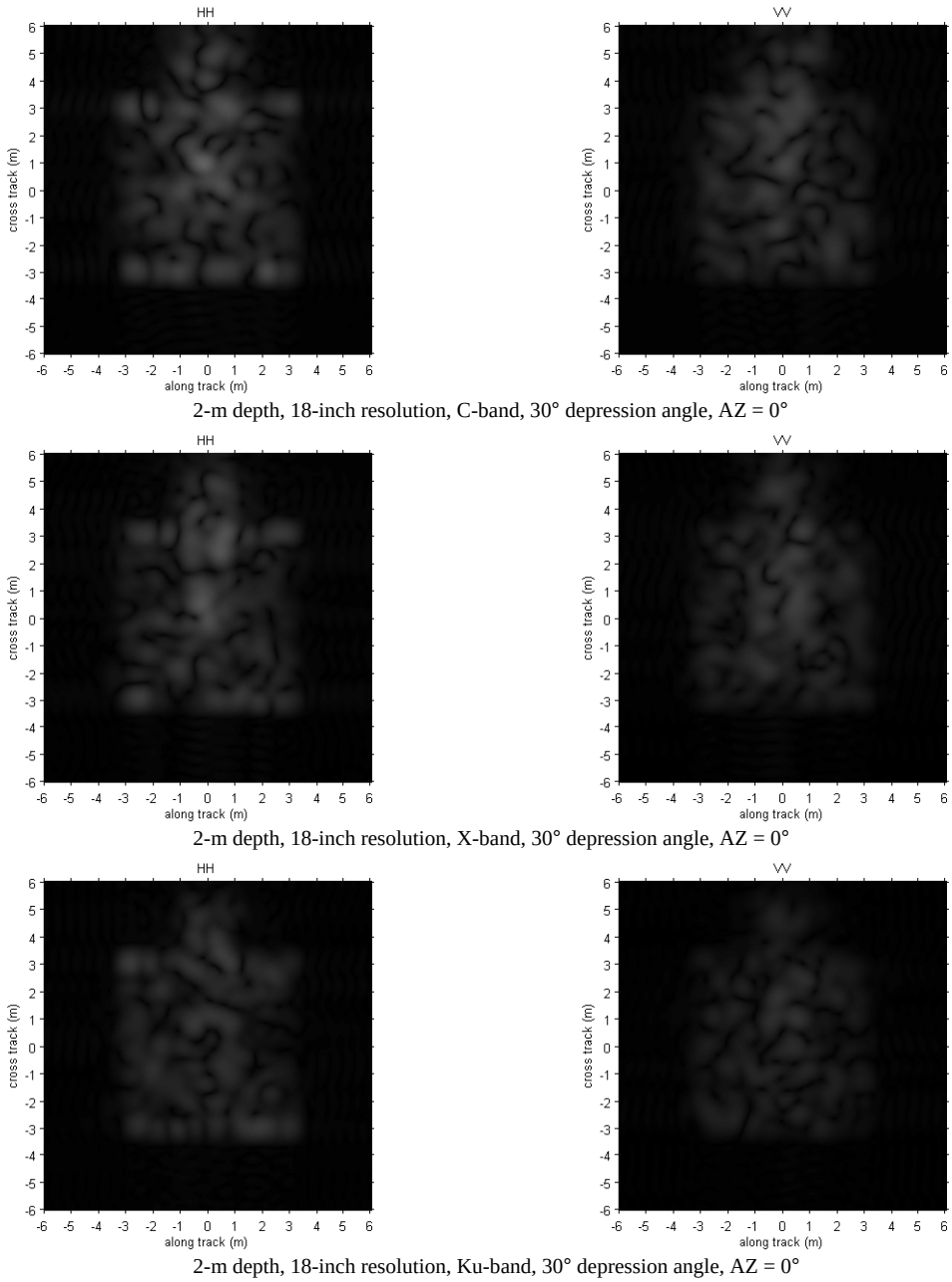

Figure 32 Comparison of response in the three radar bands for 2-m depth Siple Dome model with 18-inch resolution, 30° depression angle, and 0° azimuth. (plotted as 4th root of power)

The 8-inch-resolution image at X-band in Figure 33 clearly demonstrates the advantage of the higher resolution available at X-band, even over the better penetration depth at C-band. The snow-bridge

region is clearly visible in the HH-polarized image, even in the portion of the image where it overlaps the surface response. Figure 33 also shows that the snow bridge is not as clear at Ku-band as it is at X-band, implying that the additional propagation loss at the higher frequency is taking its toll.

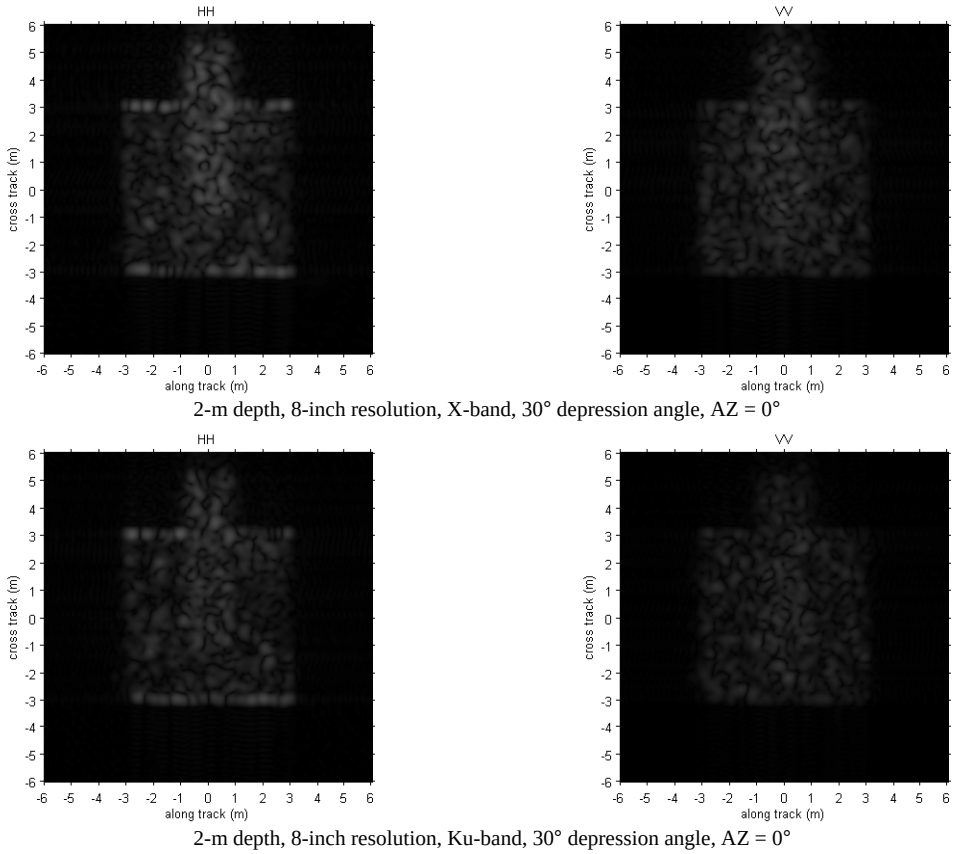

Figure 33 X- and Ku-band responses at 8-inch resolution with snow-bridge depth of 2 m, Siple Dome model, 30° depression angle, and 0° azimuth (plotted as 4th root of power .

When the scattered return comes primarily from the region near the bottom of the snow bridge, a bright response will occur at an offset in range, consistent with the depth. If the top surface scatters weakly, there will be a dark region at the near-range part of the crevasse image. When significant scattering occurs both near the surface of the snow bridge and at the bottom of the snow bridge, then the additional delay can cause the crevasse can appear wider than it really is, as illustrated in Figure 34. With sufficient resolution, the image of the bottom of the snow bridge, if deep enough, can appear to be entirely separated from the image associated with surface scattering, as illustrated in Figure 35, where the depth of the snow bridge is 4 m.

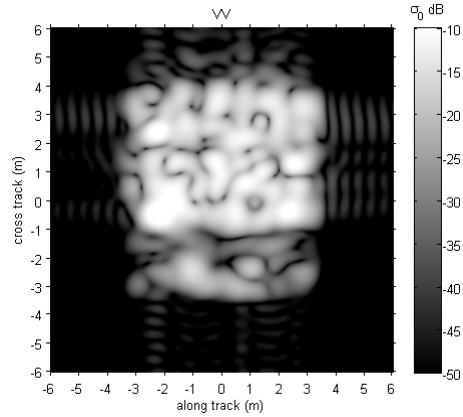

Figure 34 *Crevasse with snow bridge, 2-m depth, 18-inch resolution,* $f_c = 9.5$ GHz *, 90° azimuth, 30° depression angle (from Figure V-34).*

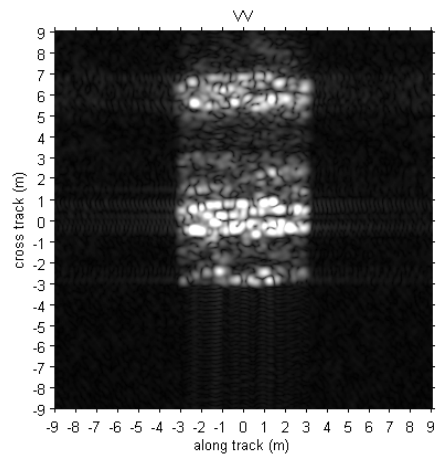

Figure 35 *Snow bridge only, 4-m depth, 8-inch resolution,* $f_c = 9.5$ GHz *, 90° azimuth,30° depression angle, 4th-root of power (from Figure V-78).*

Snow bridge only, without crevasse walls

With this model for the crevasse and snow bridge, the dominant scattering at depth comes from the interface between the bottom of the snow bridge and the air interior to the crevasse. The crevasse walls provide only a minor contribution. The computational burden is quite heavy for the complete model of the crevasse and snow bridge. The model of the top surface with the snow bridge alone is significantly smaller. By terminating the surface layers on either side of the snow bridge with a dielectric half-space, the deeper part of the glacier is included. By terminating the snow bridge with air, the discontinuity leading to the hollow crevasse is included. Since the walls of the crevasse are missing, direct scattering from the walls of the crevasse are not included. Images formed with the complete model (top two rows) and with only the top layers and snow bridge (bottom two rows) are shown in Figure 36. The depth of the top layer is 2 m. The differences in the images computed from the two models are very subtle.

These are X-band images, with 8-inch resolution, and the model measures $6 \times 6 \times 6$ m (6 m = 190 wavelengths at 9.5 GHz). The computations for the complete model require considerably more time than for the snow bridge alone. For example, computing the phase history for the entire model at X-band with 8-inch resolution, at elevation of 30° and azimuth of –60°, required $66^h\ 44^m\ 4.44^s$ on an Intel® Xeon® X5365 CPU core running at 3.00GHz . The same calculation with only the snow bridge required only $27^h\ 30^m\ 26.6^s$. For this reason, the computations at some of the depths were

performed with only the snow bridge, without the crevasse walls. These are indicated in Appendix V, where appropriate.

The conclusion is that, at least for snow bridge depths of about 2 m and larger, the scattering contribution from the crevasse walls is minor compared to the scattering from the discontinuity associated with the hollow crevasse.

Crevasse and snow bridge, 8-inch resolution at X-band, f_c = 9.5 GHz

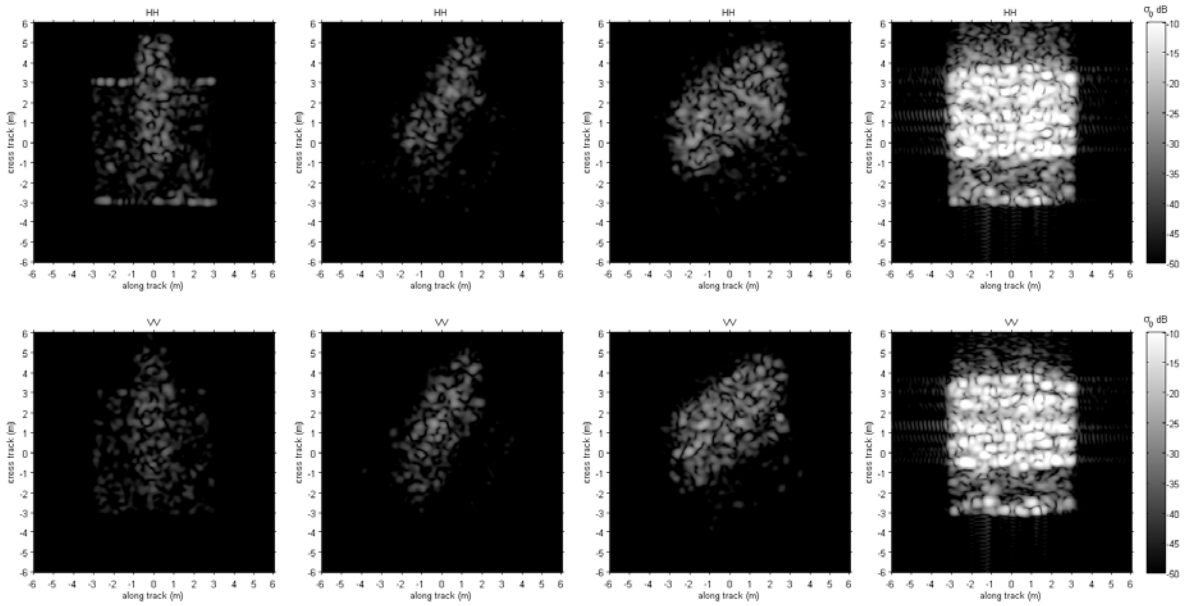

Snow bridge only, 8-inch resolution at Ku-band, f_c = 9.5 GHz

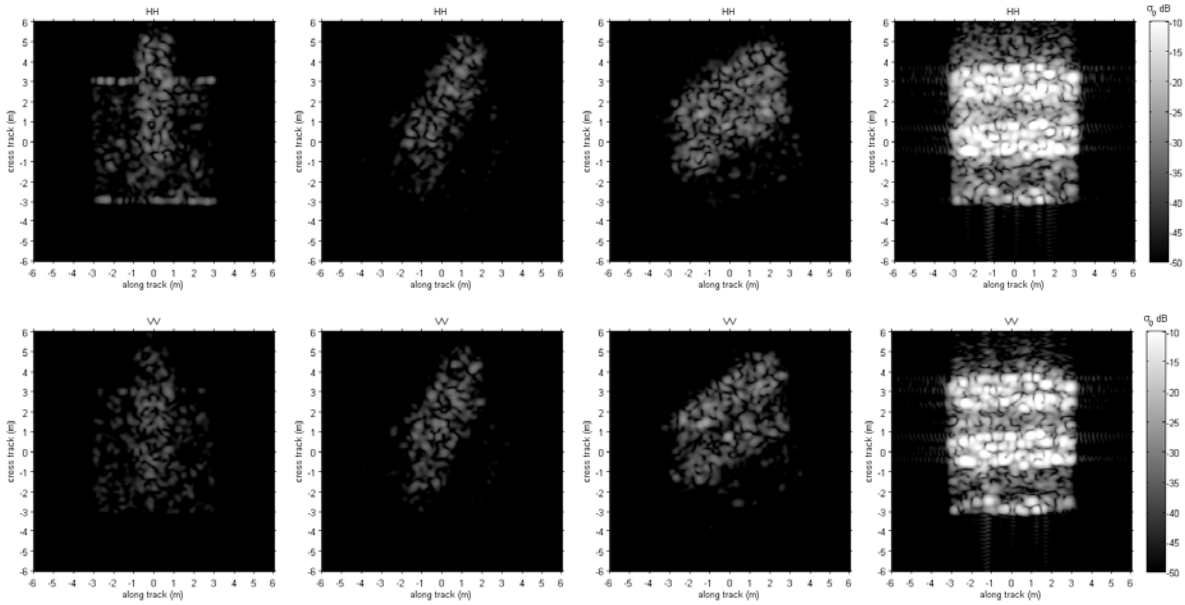

Figure 36 Comparison of responses at X-band for crevasse with snow bridge and snow bridge only , 2.0-m depth, 30° depression angle, magnitude plot (dB).

Optimum radar band for imaging crevasses

Having established that finer resolution is a significant advantage, C-band is no longer attractive, even though it exhibits lower propagation loss in ice. One might expect that X-band would perform better than Ku-band at the same resolution, since propagation losses will be greater at Ku-band. The modeled results are consistent with this expectation, as illustrated in Figure 37. In this case, the

snow-bridge depth is 4 m, and to save time, the computation only included the snow bridge. The dielectric properties are based on the Siple Dome composite profile, and the resolution is 8 inches. The top two rows are X-band images, while the bottom two rows are Ku-band images. The presence of the snow bridge is very apparent in the X-band image. The delay is sufficient so that the image from the surface features and the image from the air-dielectric interface at the bottom of the snow bridge are well separated. In the Ku-band images, the response from depth is considerably weaker than in the X-band images. This provides evidence that X-band is the best choice for this resolution.

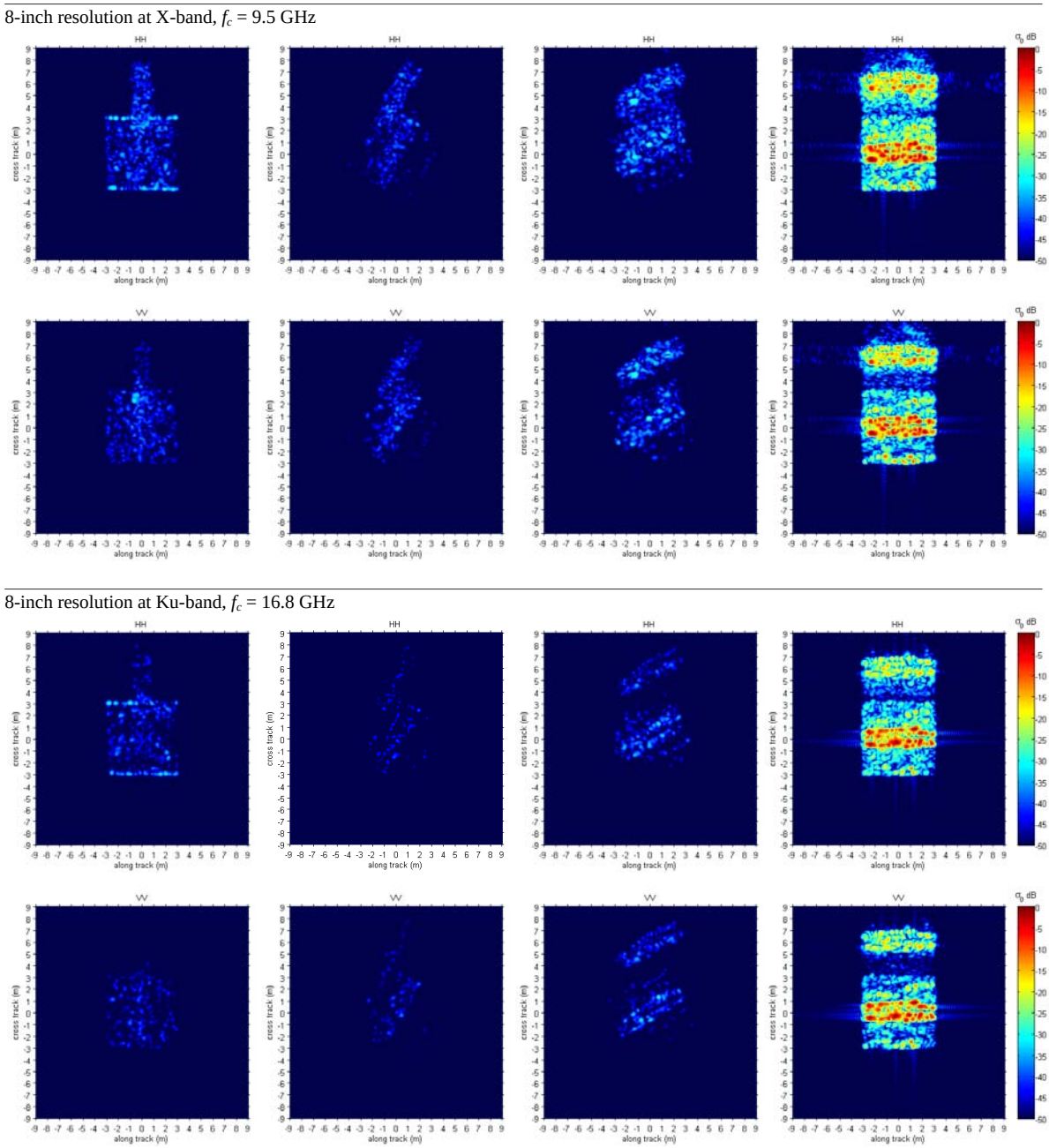

Figure 37 Comparison of responses at X-band and Ku-band for snow bridge,4.0-m depth, 30° depression angle, magnitude (dB).

Effect of depression angle

The choice of depression angle affects how bright the image of the snow bridge appears, as illustrated in Figure 38 and Figure 39. The image of the 2-m-depth Siple Dome snow bridge at azimuth angle –30° becomes brighter as the depression angle increases from 15° to 45°. However,

when the depression angle is about 30°, the direct return from the surface begins to become more apparent. For this surface-roughness model, the top surface of the snow bridge appears brighter than the adjacent surface, making the snow bridge obvious at all of these depression angles. Although an optimum depression angle will likely depend on the details of the surface roughness, there appears to be an optimum depression angle to maximize contrast between the surface returns and the snow-bridge returns. In this case, the contrast is clearly poorer at 15° and 45°, and the contrast begins to deteriorate about 20° and 40°. The best contrast is at a depression angle of about 30°, but there is little change in the vicinity of this angle.

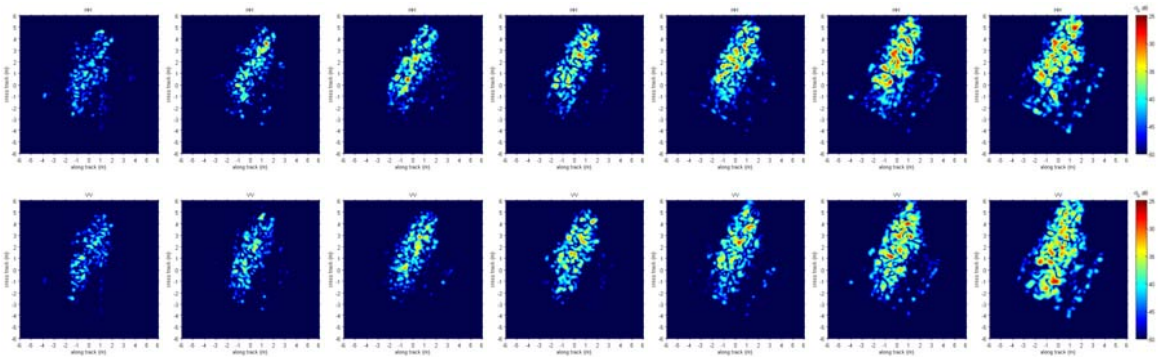

15° *20°* *25°* *30°* *35°* *40°* *45°*

Figure 38 Magnitude plot (dB), snow bridge only, 2-m depth, 8-inch resolution, $f_c = 9.5$ GHz *, AZ = –30° at several depression angles.*

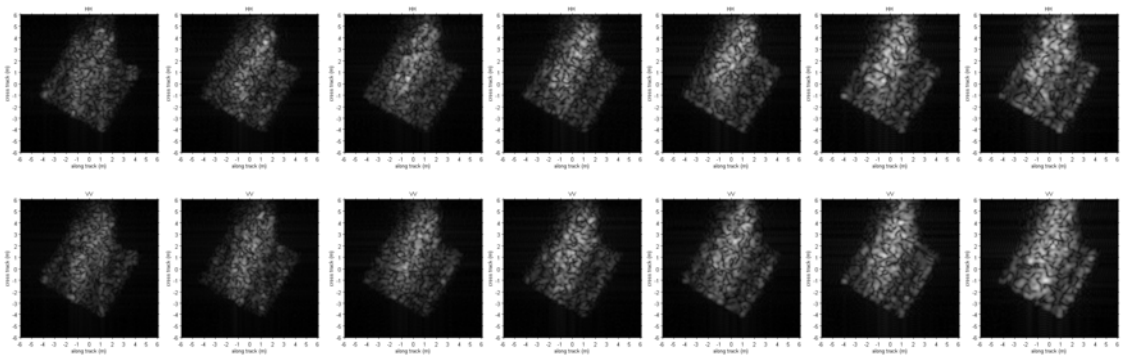

15° *20°* *25°* *30°* *35°* *40°* *45°*

Figure 39 Fourth root of power (typical SAR image format), snow bridge only, 2-m depth, 8-inch resolution, $f_c = 9.5$ GHz *, AZ = –30° at several depression angles.*

Effect of non-monotonic density profile

The smooth, gradual change in permittivity with depth produces little direct reflection. However, with the Newall Glacier data, there is a fairly sharp dip in the density at a depth of about 2.1 m (Figure 8), with a corresponding dip in the permittivity (Figure 14). The low density at this depth is not as abrupt as the change from the snow bridge to the air-filled crevasse, but it might be expected to produce measurable backscatter and be visible in the SAR image. Examination of the HH polarized image at 0° azimuth in Figure 40 illustrates this. In addition to the delayed return from the bottom of the snow bridge, visible at the middle of the top of the image, the entire top edge of the image has been extended. (The top surface stops at the bright edge at cross-track range of 3 m.) In this case, the contribution from the density dip is not quite as bright as the surface clutter, and would probably not be visible if the extent of the model had not been truncated. Nevertheless, this is an indication that information about density variations less severe than the presence of an air-filled crevasse can be present in the SAR phase history. This information might be accessible through the application of interferometric or tomographic techniques. However, current techniques are

dominated by the brightest return at a given position, so if the return from depth is overlaid onto a brighter surface feature, it will be difficult, if not impossible, to detect.

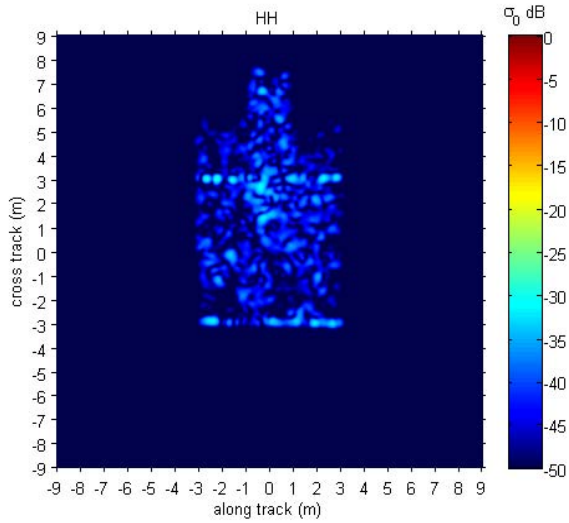

Figure 40 *X-band image of a 4-m deep snow bridge, using the Newall Glacier profile containing the dip in density at a depth of about 2 m, 8-inch resolution,* $f_c = 9.5$ GHz *, 0° azimuth, 30° depression angle.*

For an additional example, the permittivity profile on either side of the snow bridge was set to match the Newall Glacier profile *without* the dip, and the profile of the snow bridge was set to the Newall Glacier profile *with* the dip. Both profiles were terminated with a dielectric half-space, so that the model did *not* include the abrupt discontinuity associated with the void of the crevasse. A portion of the simulated SAR image of this configuration is shown in Figure 41. The resolution is 8 inches at X-band, with 30° depression angle and 0° azimuth. The part of the image extending beyond the top edge of the square image of the surface is caused by reflection from the dip in the permittivity profile. The extension measures slightly more than 2 m beyond the edge, consistent with the position of the minimum in the profile. The total thickness of the model, before the half-space termination, is 4 m. The scattering from the dip in permittivity is fairly weak, however, and is visible because it extends into the dark region outside the extent of the model.

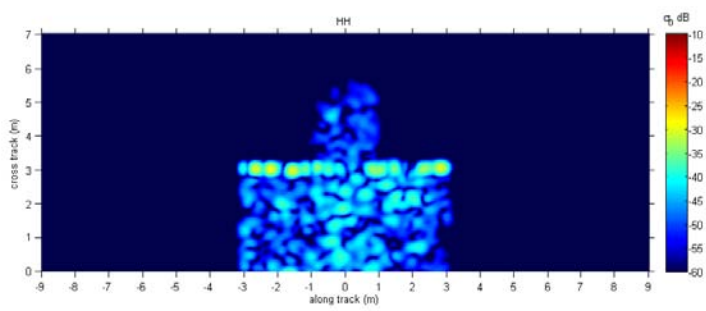

Figure 41 *Simulated SAR image of the snow bridge model with Newall Glacier profile, for 8-inch resolution at X-band, 30° depression angle, and 0° azimuth. The snow-bridge region incorporates the dip, but the adjacent material does not. There is no air-filled crevasse in the model: all permittivity profiles are terminated with a dielectric half-space.*

This Page Intentionally Blank

Conclusions and recommendations

It has been illustrated that the dry snow and glacial ice are sufficiently transparent at X-band that significant radar return can be obtained at depths to at least four meters. It has also been shown that significant reflection occurs from the bottom of the snow bridge, at the interface between the snow and the void of the crevasse. This reflection is delayed in time because of the depth and the slower light speed in the medium, and its contribution will overlay onto the surface clutter at a range beyond the actual location of the snow bridge. The image from the bottom of the snow bridge will be obscured if the surface clutter at that location is of comparable or greater brightness. Additional scattering at depth will occur from the walls of the crevasse. However, it has been demonstrated that the contribution from the walls may be less significant than that from the bottom of the snow bridge, at least with the single example of crevasse geometry examined in this study. This is a surprise, since it has been suggested that scattering from the walls of the crevasse would be the dominant component. Clearly, the walls can be efficient scattering surfaces, but whether a significant portion of the scattered energy is scattered back to the radar depends on the details of the geometry. A better understanding of the geometry of the crevasse and snow bridge is needed to improve the fidelity of the model. Nevertheless, it is important to see that scattering from the dielectric-to-air interface at the bottom of the snow bridge *can* be a dominant contributor.

Because the glacial ice exhibits measureable propagation loss at microwave frequencies, scattering from features at depth need to be fundamentally brighter than the surface clutter onto which they are overlaid, if these features are to be detected in a two-dimensional SAR image. When the structure at the bottom of the snow bridge or on the surface of crevasse walls is rougher than the top surface of the glacier, it is likely that the scattering from depth will be visible against surface clutter. Unfortunately, at this time there is no way to be certain that this will always be the case. However, since it is has been shown that the glacier exhibits good transparency at X-band, it may be possible to reliably identify the image of the bottom of the snow bridge and the crevasse walls by using interferometry or tomography. Standard algorithms may not be adequate, however, so this remains an area for future research. If successful, such an approach might allow a more reliable detection of the presence of a snow bridge over a crevasse, and even provide some measure of the depth of the snow bridge.

This study focused on modeling dry snow and glacial ice, not wet snow. Applying the permittivity models at $T = 0°\ \mathrm{C}$ represents a worst-case model in terms of propagation loss. However, this model assumes there is no liquid present, even at $T = 0°\ \mathrm{C}$. The propagation losses for wet snow can be considerably higher, but the loss is extremely variable for different environments. When even small amounts of liquid are present, the loss is very sensitive to the impurity content (both to the chemical composition and to the concentration), which can be different at different locations, even in the same environment. Because of the extreme variability across environments and locations, it will be necessary to model the complex permittivity of wet snow using a range of values for the loss tangent. Wet snow should be considered in future studies.

This study has demonstrated the viability of using an extended physical-optics method, the shooting and bouncing ray method, to compute phase histories for imaging a crevasse covered by a snow bridge. The particular implementation of the SBR method used in this study was designed with a focus on PEC objects, PEC objects with thin dielectric coatings, dielectric layers bounded by dielectric half-space, and thin dielectric objects surrounded by air [25]. The modeling of a dielectric gradient is accomplished by modeling a solid object with surfaces only, and by applying reflection and transmission coefficients computed for the layered media. When the surface has structure, such as the fractal surface used to simulate the sastrugi on the Antarctic glaciers, there is one noticeable drawback: the surface geometry of the bottom surface matches that of the top surface precisely. In a real snow bridge, it is very likely that the top surface is smoother than the interior bottom surface,

where ice crystals are known to grow into interesting shapes. Unfortunately, the simulation did not support the modeling of this condition, and the top and bottom surfaces of the snow bridge had identical fractal surfaces. The result is that the scattering from the dielectric-to-air interface at the bottom of the snow bridge had to compete with similar scattering from the air-to-dielectric interface at the top surface. Future work should focus on eliminating this shortcoming, and direct the modeling to allow different surface structures on the top and bottom surfaces of the snow bridge.

Long computation times of several days for just one phase history have been encountered with the detailed fractal-surface models. The SBR method should be able to advantageously utilize parallel processing, making use of the large number of stream processors being implemented in modern graphics processors [31]. Future efforts should also consider implementing the SBR method for parallel processing.

When viewing the data in the form of SAR images, the brain's ability to recognize patterns makes recognition of the signature of the crevasse and snow bridge relatively easy. Although this study emphasized computation of simulated SAR images, useful information also can be obtained from simpler models. For example, instead of computing complete SAR phase histories, time-domain response computed with the radar located at a single position can be useful for understanding the scattering mechanisms. Since this computation is considerably faster than computing a complete phase history, more variations in geometry can be examined. This approach could be applied in the future to efficiently identify appropriate geometrical configurations to study in more detail with complete image simulations.

Appendix I – Building a fractal surface

Strictly, a fractal surface is one which exhibits self-similarity (or statistical self-similarity when the surface has a random character) at all scales. However, for the purposes of computer modeling, the number of scales must be limited; it is not practical to decrease the scale without limit. In contrast, a true mathematical fractal can be examined at any scale without limit, and the fractal function maintains its self-similarity. The surface described here might best be designated a fractal-like surface, but the term fractal surface will continue to be used.

The fractal surface utilized here is not based on a self-similar function, but on an algorithm that enforces self-similarity over a limited number of scale sizes. The algorithm begins with a surface divided coarsely into one or a few triangular facets. This beginning state is called level 0. As the algorithm progresses to higher levels, the facets from the previous level are divided by creating new nodes at the midpoint of the edges of the parent triangle. Each parent triangle becomes four triangles. Each new node is then moved a distance δ along the parent triangle's normal vector. The distance δ is a uniform random variable such that

$$-\delta_{level} < \delta < \delta_{level} \tag{I-1}$$

where

$$\delta_{level} = \eta^{level-1}\delta_{max} \tag{I-2}$$

with $0 < \eta < 1$ and δ_{max} is the maximum deviation to be applied at level one. As the algorithm proceeds, the scale decreases, and the peak random deviation that can be applied to the new nodes decreases with the scale. With the bisection of the edges and setting $\eta = 1/2$, the statistical properties at each scale are self-similar.

Consider a single triangle, as illustrated on the left in Figure I-1. For many applications, the equilateral triangle is desirable, but triangles of unequal sides can be used as well. The triangle is divided by placing new nodes at the bisection of each side and connecting all of the nodes to form four triangles, as illustrated in Figure I-1. Defining the initial triangle to be level 0, the first division will be level 1, with each subsequent division labeled accordingly, as illustrated.

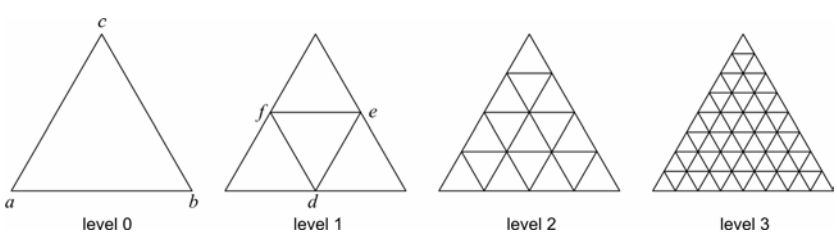

level	facets	nodes	edges
0	1	3	3
1	4	6	9
2	16	15	30
3	64	45	108

Figure I-1 Illustration of a single triangle as it is subdivided at different levels.

Thus, at level 0, nodes {*a*, *b*, *c*} are connected to form three edges, which is the initial triangle. At level 1, nodes {*d*, *e*, *f*} are added at the bisection of the edges. The four triangles are {*a*,*d*,*f*}, {*d*,*b*,*e*}, {*e*,*c*,*f*}, and {*d*,*e*,*f*}. Note that the nodes have been ordered in a right-hand direction. By exchanging the order of any two nodes in a triangle, the order will be in the left-hand direction. The right-hand ordering will be used here.

While the illustration in Figure I-1 is two-dimensional, it could just as easily represent the surface of some smooth three-dimensional object. Consider first triangle, with nodes {*a*, *b*, *c*}. These

points can be considered vectors in some coordinate system. Thus point *a* is located by vector $\vec{\mathbf{a}}$, point *b* by $\vec{\mathbf{b}}$, and so on. The unit normal to the facet is

$$\hat{\mathbf{n}}_{\{a,b,c\}} = \frac{\left(\vec{\mathbf{b}}-\vec{\mathbf{a}}\right)\times\left(\vec{\mathbf{c}}-\vec{\mathbf{b}}\right)}{\left|\left(\vec{\mathbf{b}}-\vec{\mathbf{a}}\right)\times\left(\vec{\mathbf{c}}-\vec{\mathbf{b}}\right)\right|} = \frac{\left(\vec{\mathbf{c}}-\vec{\mathbf{b}}\right)\times\left(\vec{\mathbf{a}}-\vec{\mathbf{c}}\right)}{\left|\left(\vec{\mathbf{c}}-\vec{\mathbf{b}}\right)\times\left(\vec{\mathbf{a}}-\vec{\mathbf{c}}\right)\right|} = \frac{\left(\vec{\mathbf{a}}-\vec{\mathbf{c}}\right)\times\left(\vec{\mathbf{b}}-\vec{\mathbf{a}}\right)}{\left|\left(\vec{\mathbf{a}}-\vec{\mathbf{c}}\right)\times\left(\vec{\mathbf{b}}-\vec{\mathbf{a}}\right)\right|}. \tag{I-3}$$

To reach level 1, the new nodes are

$$\vec{\mathbf{d}} = \frac{\vec{\mathbf{a}}+\vec{\mathbf{b}}}{2} + \delta\hat{\mathbf{n}}_{\{a,b,c\}}, \tag{I-4}$$

$$\vec{\mathbf{e}} = \frac{\vec{\mathbf{b}}+\vec{\mathbf{c}}}{2} + \delta\hat{\mathbf{n}}_{\{a,b,c\}}, \tag{I-5}$$

and

$$\vec{\mathbf{f}} = \frac{\vec{\mathbf{a}}+\vec{\mathbf{c}}}{2} + \delta\hat{\mathbf{n}}_{\{a,b,c\}}, \tag{I-6}$$

where the random deviation, δ, is taken to be an independent draw for each node.

Let *n* be the level of subdivision. Beginning with a single triangle, the number of facets at each level is

$$N_{facet} = 2^{2n}. \tag{I-7}$$

The number of nodes is

$$N_{nodes} = \left(2^n+1\right)\left(2^{n-1}+1\right). \tag{I-8}$$

The number of edges, accounting for the shared edges, is

$$N_{edges} = 3\left(2^n+1\right)2^{n-1}. \tag{I-9}$$

The numbers of facets, nodes, and edges at each level from 0 to 3 are tabulated in Figure I-1.

An example of the evolution of a fractal surface with the application of a 9-level algorithm is illustrated in Figure I-2. The surface at level 0 is entirely flat and smooth. As can be seen, levels 1 and 2 determine the large-scale shape of the surface. As the number of the level increases, the detail becomes finer, and the deviation from the previous surface decreases. However, the character of the surface structure at each level (scale) is statistically similar to that of the adjacent levels. At the scale of this illustration, there is little obvious difference between the results of the last three or four levels. That is not surprising, since the ratio of scales from level 1 to level 9 is 256. The additional detail becomes apparent when a small section near the center is magnified, as in the illustration of levels 8 and 9 in Figure I-3. Although the scale at level 9 is comparable to the resolution of the image, the difference in roughness between levels 8 and 9 is still visible.

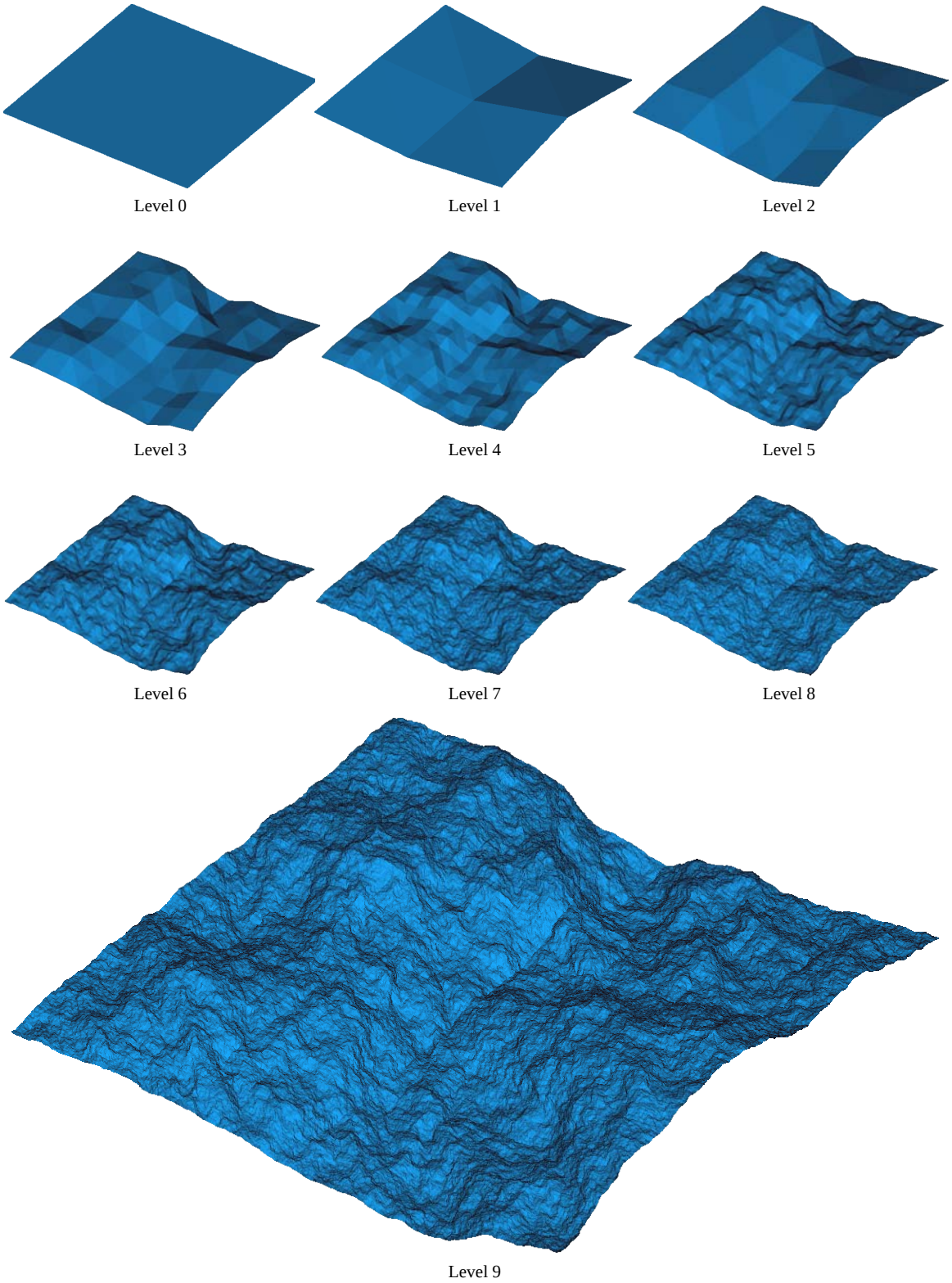

Figure I-2 Evolution of a fractal surface, with 9 levels of iteration.

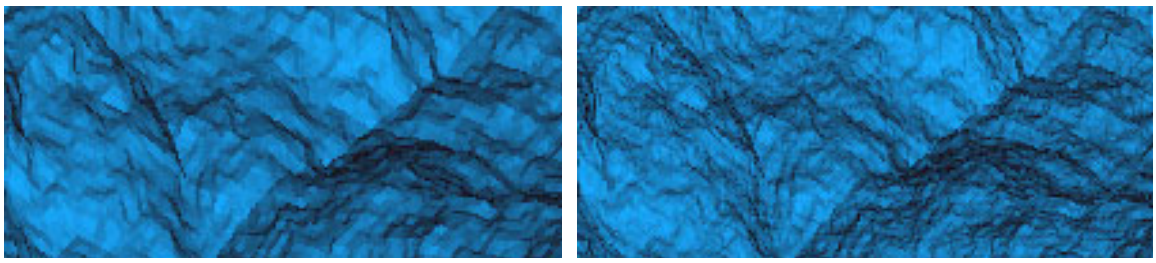

Level 8 Level 9

Figure I-3 Comparison of the detail contained in levels 8 and 9, near the center of the surface.

Appendix II – Shooting and Bouncing Ray (SBR) Method

The solution of Maxwell's equations with rigorous numerical methods generally presents difficulty when structures are large when measured in wavelengths of the electromagnetic field. However, since exact analytic solutions are only available for certain idealized geometries and cannot be obtained for arbitrary structures, computer modeling is still the primary tool to apply. When the objects of interest are small (measured in wavelengths), several rigorous numerical methods can be applied: the method of moments (MoM), the finite-difference-time-domain method (FDTD), the finite-integral-time-domain method (FITD), and finite-element methods (FEM). Several less rigorous methods, each involving physical or mathematical approximations (or both) have been devised to evaluate electromagnetic scattering and propagation in the presence of large structures. Some of these are more rigorous than others, while some (for example geometric optics) provide good visualization and intuition.

The physical-optics (PO) method is often used to obtain scattered fields from large objects. This method is particularly suited to scattering from large perfect-electric-conductor (PEC) surfaces The PO method integrates surface currents against the free-space Green's function to obtain the scattered field. However, rather than rigorously solve for the surface currents as the method of moments (MoM) does, PO assumes the surface currents, based on local geometry and the tangential component of the incident magnetic field. The assumption is fairly accurate on surfaces directly exposed to the source, but it does not accurately account for the behavior of the current at edges, nor does it account for currents that exist in the shadow region. PO can be extended beyond PEC surfaces to include dielectric surfaces by applying the appropriate boundary conditions and using equivalent magnetic currents associated with the tangential electric fields at the dielectric interface. Another extension, called physical theory of diffraction attempts to improve PO by including estimates of the edge currents.

The shooting and bouncing ray (SBR) method is an extension of physical optics, merging geometric optics with physical optics. Usually with physical optics, the incident field is taken to be a plane wave propagating from some specified direction. In the SBR method, the incident field is defined using geometric optics (ray tracing), while the scattered field is computed with physical optics. If only the direct incident rays are used, SBR reduces to physical optics. The advantage of SBR lies in the inclusion of multiple reflections of the incident rays. SBR can be used efficiently to compute the electromagnetic fields, radar cross-section, and coupling between antennas for geometries that are very large with respect to a wavelength. As does PO, the SBR method computes the scattered field from an object by integrating surface currents (both electric and magnetic) against the free-space Green's function to propagate the associated fields to the field point.

Apparently, the SBR method was initially used to analyze scattering from cavities [1], where the multiple reflections of the incident rays produced significant contributions to the currents used to compute the scattered field. The SBR method has been successfully applied to scattering from rough surfaces, with results that agree well with a method-of-moments calculation [2]. Like the method of moments, it is often implemented in the frequency domain. It has, however, also been used to generate inverse-synthetic-aperture-radar images directly in the time domain [3]. The time-domain implementation of SBR, while faster, is not quite as accurate as computing phase histories in the frequency domain [25]. Phase histories will be computed in the frequency domain in this study.

As noted above, unlike simple physical optics, SBR can include the effect of multiple reflections. It does so by tracing rays (representing plane waves) from the source of the incident field, allowing the rays to reflect and refract from and through the various surfaces and materials. The reflected and refracted rays contribute additional components to the PO currents beyond the currents due simply to the direct incident field used in the traditional physical-optics method. Thus, the SBR method can account for multipath propagation. However, it should be noted that the effects of multipath propagation are modeled only by the multiple reflection / refraction of rays originating from the source. Specifically, radiation from secondary sources (surface currents) is not considered in generation of rays in directions other than the specular directions associated with the reflected and refracted rays. The coupling between the currents on various surfaces is modeled only by the specular reflection and refraction of the rays. While this is a significant improvement to the PO method, incorporating those components of the multipath interaction that are usually dominant, situations can be contrived where the more exact coupling modeled with the method of moments is needed to produce accurate and meaningful results. Nevertheless, the SBR method is very useful in situations where the multipath coupling is dominated by specular reflections from the source, such as a source antenna radiating into a region containing many large objects, and other situations that are not tractable with the method of moments or other rigorous methods.

Relationship between MoM and SBR

The level of rigor contained in the shooting-and-bouncing-ray method can be assessed by comparing it with the rigorous method of moments. Both the method of moments and the shooting-and-bouncing-ray method are based on the volume-equivalence and surface-equivalence principles of electromagnetics [26].

In the equivalence principles, the incident field is defined to be the field produced by some source in free space, without the presence of the scattering objects. The scattered field is an additional field component required to satisfy the boundary conditions on the objects. In the equivalence-principle view, currents are induced by the incident field, which become the sources for the scattered field. The scattered field is computed by integrating the equivalent electric currents on the PEC surfaces and the equivalent magnetic and/or electric currents on the boundaries of the permeable objects against the free-space Green's function. The computation is performed in free space, without any objects present, with only the equivalent currents present. The total field at any point is the coherent sum of the incident and scattered field. Since the incident and scattered fields are defined without any objects present, there are no shadowing or blockage issues. In the shadow regions, the incident and scattered fields cancel each other to a lesser or greater degree. Where the field cancellation is imperfect, the total field is described as a diffracted field.

The only difference between MoM and SBR is the way in which the equivalent currents are computed. However, this is a very significant difference: MoM rigorously solves for the currents, where SBR approximates the currents in the same way as the physical-optics approximation. Once the currents are determined, both methods compute the scattered field by integrating the currents against the free-space Green's function.

In the method of moments, interactions between various parts of the object are contained in the solution of an integral equation. The integral equation embodies all of the physics of the problem, including Maxwell's equations and the boundary conditions specific to the problem, with no approximations. However, in order to solve for the unknown currents, the integral equation is discretized by expanding the unknown with an appropriate set of basis functions. If the set spans the space, and is complete, then the solution is still exact. In reality, though, the set must be infinite in order to be complete, but in order to solve the problem numerically, the set

must be truncated. The accuracy and precision of the solution is determined by how the set of basis functions is truncated. In principle, arbitrary precision can be achieved by simply adjusting the truncation to include more basis functions. In practice, the computing resources limit the number of basis functions that can be used. Problems that include objects that are large (measured in wavelengths) require a larger number of basis functions for an accurate solution than do problems containing only smaller objects. Thus, there exists a practical limit to the size of problem that can be handled with MoM.

Rather than solve for the unknown currents directly, the shooting-and-bouncing-ray method simply estimates the currents. As already noted, SBR is an extension of the physical-optics (PO) method, which approximates the currents by relating them to the tangential components of the incident field (defined according to the equivalence principles). SBR simply extends physical optics by adding contributions from reflected rays. Geometric-optics methods are used to trace rays from the incident-field source, allowing for reflection and refraction. The equivalent currents are then approximated as the physical-optics current from the incident field plus contributions from the tangential fields of the reflected and refracted rays. In this way, interactions between various parts of the objects are handled through multiple reflections of the incident rays. Since rays are not generated for the scattered field computed from the equivalent currents, in regions that are not reached directly by incident rays or the reflected rays, no equivalent currents are generated, even if the scattered field is nonzero in these regions. For many applications, this is acceptable, but it does raise questions about using SBR for computing fields inside closed structures with only small openings and some other geometries.

It is well known that the physical-optics current does not include the integrable singularity at edges of PEC objects, nor does it (or SBR) include currents in the shadow region (for example on the back of a PEC sphere). Similarly, PO does not incorporate the interaction between currents. The improvement offered by SBR over PO is the inclusion of an approximate interaction between currents on different objects, through the inclusion of additional physical-optics-like currents caused by reflected and refracted rays. Thus in this sense, the SBR method is a higher-order version of the physical-optics method. While SBR does approximate the physics, it has the advantage of requiring considerably fewer computing resources for a given size problem than the more rigorous methods. Thus, it can handle much larger problems than the method of moments and other rigorous solvers. Fortunately, the computed fields are accurate enough for many purposes. In fact, physical-optics (and the SBR method) can and does predict fields inside shadow regions that are not reached by the incident (or multiple reflected rays). This field is called the physical-optics diffraction field, and is often approximated with Fresnel or Fraunhofer diffraction, where additional mathematical approximations are applied to the “exact” physical optics formula.

The Xpatch® implementation of the SBR method

The Xpatch® software [25, 27] uses the shooting and bouncing ray (SBR) method to compute scattered electromagnetic fields and coupling between antennas for geometries that are very large with respect to a wavelength. A good summary of its capabilities is contained in [28]. As noted above, the SBR method is an extension of the physical-optics (PO) method, which computes the scattered field from an object by integrating surface currents against the free-space Green’s function to propagate the associated fields to the field point.

In PO, the surface currents are assumed to be determined locally by the object’s geometry, composition, and the incident field. For example, the surface electric current density on a perfect electrical conductor (PEC) is related to the tangential magnetic field at the surface, and is assumed to be

$$\vec{\mathbf{J}}_{surface} = 2\hat{\mathbf{n}} \times \vec{\mathbf{H}}_{inc}\,, \qquad \text{(II-1)}$$

where $\vec{\mathbf{J}}_{surface}$ is the surface current, $\hat{\mathbf{n}}$ is the unit normal at the local point on the surface, and $\vec{\mathbf{H}}_{inc}$ is the incident magnetic field. Similarly, for non-PEC materials, the surface current (electric and/or magnetic) can be obtained from the local boundary conditions.

Nevertheless, while the PO surface currents amount to an approximation of the true physics, for large objects the approximation is usually very good. However, if the currents were computed rigorously, for example with the method of moments (MoM), one would discover that the current on a PEC surface rises to a peak at edges, and that there is some current flow around edges toward the back side of the object, so that currents exist in the shadowed region of the object. The SBR method ignores those contributions. While the edge and shadow-region currents do contribute to diffraction, they are not the sole contribution to the diffracted field. The diffracted field is still approximated by PO, although not perfectly.

To understand how PO computes a diffracted field, consider that the physical-optics method depends on the volume equivalence and surface equivalence principles [26]. These principles state that the total field in a region containing an incident field and scattering objects is identical to the coherent sum of the incident field *in free space* plus the field due to the equivalent volumetric and surface currents, also radiating *into free space*. The objects have been replaced by their associated equivalent currents, so the field calculation is now a free-space problem. Thus, the total field anywhere is obtained by the adding the contributions from the currents to the free-space incident field, without any need to consider geometric blockage by the objects. In the shadow region of an object, the incident field and the scattered field radiated by the equivalent currents associated with the object tend to cancel, but usually not entirely. The residual field is the physical-optics diffracted field. The physical-optics diffracted field does not include contributions from the edge currents or the currents that actually flow on the object in the region shadowed from the incident field. However, when the objects are large, the physical-optics diffracted field is a good approximation.

As noted, the SBR method extends PO by including equivalent currents due to multiple reflections in addition to the traditional PO currents caused by the direct incident field alone. With the SBR method, the equivalent currents are obtained by launching (shooting) geometric rays and following the reflected (bouncing) rays. At each point where a ray intersects an object, the equivalent currents are computed, taking into account the reflection coefficients and divergence along the ray path. When a permeable material is encountered, a transmitted ray is also created with an intensity determined by the local transmission coefficient. The transmitted and reflected rays are followed until they escape the environment, or until a “bounce limit” is reached. In the special case that no rays other than those associated with the incident field are included, the SBR method reduces to the PO method.

Xpatch® has been demonstrated to produce results which appear to be accurate and faithful to physical optics and the SBR method. The results of some validation tests are given in Appendix III.

Appendix III – Some validation tests for Xpatch®

A limited set of field-strength and radar-cross-section values computed with Xpatch® will be compared to values computed with the physical optics method, the finite-integral time-domain solver in CST Microwave Studio [29], and the SAIC Full-wave solver (SAF) [30], as appropriate.

Perfectly conducting circular disk

First, the scattered field of a perfect-electrical-conductor (PEC) circular disk will be considered. This test will examine the field on a plane behind the disk, and in particular, in the shadow of the disk. Consider a perfectly conducting disk with diameter of 3 m, as illustrated in Figure III-1. The field will be computed on the observation plane indicated in the illustration, which will be located at 2.5 cm and 1 m behind the PEC disk. The incident field is a plane wave, propagating in the $-\hat{\mathbf{z}}$ direction as shown. The field will be evaluated at the position given by $\vec{\mathbf{r}}$, and $\vec{\mathbf{r}}'$ locates a point on the surface of the PEC disk. The field is polarized so the electric-field vector is in the $\hat{\mathbf{y}}$ direction. The field computed with Xpatch® in the observation plane will be compared with that computed by the exact physical-optics method, the 1st-order physical-optics method, the Fresnel approximation, the Fraunhofer approximation, and the rigorous finite-integral time-domain solver.

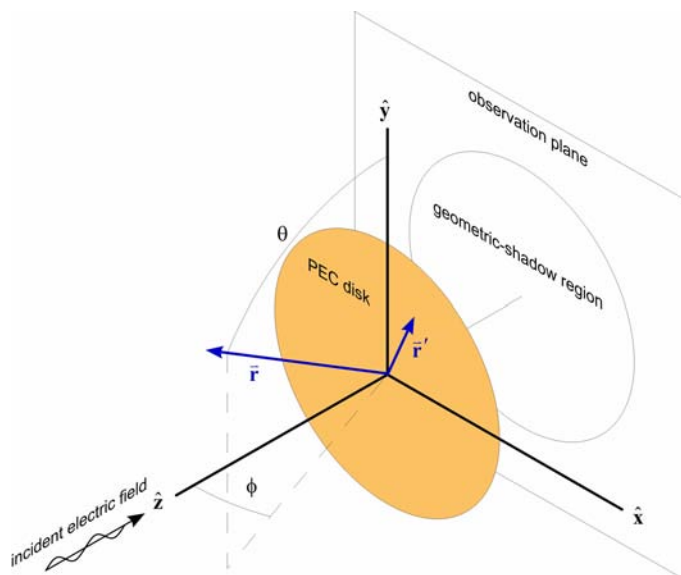

Figure III-1 Illustration of the geometry for scattering from a PEC circular disk.

When the incident field is a plane wave, propagating in the $-\hat{\mathbf{z}}$ direction, with the electric field in the $\hat{\mathbf{y}}$ direction, the exact physical-optics field can be shown to be

$$\vec{\mathbf{E}}_{total}\left(\vec{\mathbf{r}}\right)=E_0\left(\begin{array}{l}\hat{\mathbf{y}}e^{jk_0z}-\dfrac{jk_0}{2\pi}\displaystyle\int_0^{2\pi}\int_0^{a}\left(1-\dfrac{j}{k_0\left|\vec{\mathbf{r}}-\vec{\mathbf{r}}'\right|}-\dfrac{1}{k_0^2\left|\vec{\mathbf{r}}-\vec{\mathbf{r}}'\right|^2}\right)\dfrac{e^{-jk_0\left|\vec{\mathbf{r}}-\vec{\mathbf{r}}'\right|}}{\left|\vec{\mathbf{r}}-\vec{\mathbf{r}}'\right|}\hat{\mathbf{y}}\rho d\rho d\phi\\ +\dfrac{jk_0}{2\pi}\displaystyle\int_0^{2\pi}\int_0^{a}\left(1-\dfrac{3j}{k_0\left|\vec{\mathbf{r}}-\vec{\mathbf{r}}'\right|}-\dfrac{3}{k_0^2\left|\vec{\mathbf{r}}-\vec{\mathbf{r}}'\right|^2}\right)\dfrac{e^{-jk_0\left|\vec{\mathbf{r}}-\vec{\mathbf{r}}'\right|}}{\left|\vec{\mathbf{r}}-\vec{\mathbf{r}}'\right|}\dfrac{\hat{\mathbf{y}}\cdot\left(\vec{\mathbf{r}}-\vec{\mathbf{r}}'\right)}{\left|\vec{\mathbf{r}}-\vec{\mathbf{r}}'\right|^2}\left(\vec{\mathbf{r}}-\vec{\mathbf{r}}'\right)\rho d\rho d\phi\end{array}\right), \qquad \text{(III-1)}$$

where E_0 is the amplitude of the incident plane-wave electric field, $k_0=2\pi/\lambda$, λ is the free-space wavelength, the radius of the disk is a, and $\vec{\mathbf{r}}'=\rho\left(\hat{\mathbf{x}}\cos\varphi+\hat{\mathbf{y}}\sin\varphi\right)$. By neglecting terms proportional to $\left|\vec{\mathbf{r}}-\vec{\mathbf{r}}'\right|^{-n}$, where $n>1$, the 1st-order physical-optics field is obtained,

$$\vec{\mathbf{E}}_{total}^{1^{st}\text{-}order}\left(\vec{\mathbf{r}}\right)=E_0\left(\hat{\mathbf{y}}e^{jk_0z}-\frac{jk_0}{2\pi}\int_0^{2\pi}\int_0^a\left(\hat{\mathbf{y}}-\hat{\mathbf{y}}\cdot\frac{\left(\vec{\mathbf{r}}-\vec{\mathbf{r}}'\right)}{\left|\vec{\mathbf{r}}-\vec{\mathbf{r}}'\right|}\frac{\left(\vec{\mathbf{r}}-\vec{\mathbf{r}}'\right)}{\left|\vec{\mathbf{r}}-\vec{\mathbf{r}}'\right|}\right)\frac{e^{-jk_0\left|\vec{\mathbf{r}}-\vec{\mathbf{r}}'\right|}}{\left|\vec{\mathbf{r}}-\vec{\mathbf{r}}'\right|}\rho d\rho d\varphi\right). \tag{III-2}$$

By applying an approximation for square root in $\left|\vec{\mathbf{r}}-\vec{\mathbf{r}}'\right|$, the Fresnel and Fraunhofer approximations are obtained,

$$\vec{\mathbf{E}}_{total}^{Fresnel}\left(\vec{\mathbf{r}}\right)=E_0\left(\hat{\mathbf{y}}e^{-jk_0z}-\frac{jk_0}{2\pi}\frac{e^{-jk_0r}}{r}\hat{\mathbf{y}}\cdot\left(\bar{\bar{\mathbf{I}}}-\hat{\mathbf{r}}\hat{\mathbf{r}}\right)\int_0^{2\pi}\int_0^a e^{jk_0\left(r'\hat{\mathbf{r}}\cdot\hat{\mathbf{r}}'-\frac{r'^2}{2r}\left(1-\left(\hat{\mathbf{r}}\cdot\hat{\mathbf{r}}'\right)^2\right)\right)}\rho d\rho d\varphi\right), \tag{III-3}$$

and

$$\vec{\mathbf{E}}_{total}^{Fraunhofer}\left(\vec{\mathbf{r}}\right)=E_0\left[\hat{\mathbf{y}}e^{-jk_0z}-a\frac{e^{-jk_0r}}{r}\hat{\mathbf{y}}\cdot\left(\bar{\bar{\mathbf{I}}}-\hat{\mathbf{r}}\hat{\mathbf{r}}\right)\frac{J_1\left(k_0a\sin\theta\right)}{\sin\theta}\right], \tag{III-4}$$

where the unit vectors are $\hat{\mathbf{r}}=\vec{\mathbf{r}}/\left|\vec{\mathbf{r}}\right|$ and $\hat{\mathbf{r}}'=\vec{\mathbf{r}}'/\left|\vec{\mathbf{r}}'\right|$, $r=\left|\vec{\mathbf{r}}\right|$, and $J_1\left(x\right)$ is the cylindrical Bessel's function of the first kind and order 1.

In Figure III-2, total field is plotted on the observation plane located 2.5 cm behind the 3-m diameter PEC disk. The frequency is 1 GHz, and the incident field strength of the plane wave is $E_0=-29.1\text{ dB}\left(\text{V/m}\right)$, The field computed by the SBR method as implemented in Xpatch® is essentially the same as computed by 1st-order physical optics, (III-2). Diffraction rings are clearly visible in both the shadow and directly illuminated regions. However, exact physical optics, (III-1), produces a darker shadow, but the there is essentially no difference between the fields computed in the illuminated region by the three methods. When compared to the rigorous finite-integral time-domain solution, plotted Figure III-3, we see that the true shadow is darker still. For a narrow ring just inside the edge of the shadow, the field computed by the exact physical optics method is very similar to that computed by the finite-integral time-domain method, which in turn is very similar to that compute by SBR. However, SBR clearly over-predicts the field strength deeper in the shadow.

When the observation plane is moved to a distance of 1 m behind the 3-m diameter PEC disk, the SBR method agrees very well with both exact physical optics and the finite-integral time-domain method, as illustrated in Figure III-4. The scale is identical for each of the plots in Figure III-4, and the dynamic range from blue to red is 22 dB. Note that neither the Fresnel, (III-3), nor Fraunhofer, (III-4), approximation gives a good result for the shadow at this distance. For these approximations to be useful, the distance, *R*, from the disk to the field point should satisfy

$$R>>\sqrt[3]{\frac{\pi a^4}{4\lambda}}$$

for the Fresnel approximation, and

$$R>>\frac{2\pi a^2}{\lambda}$$

for the Fraunhofer approximation. Compare these with the traditional far-field boundary for antenna pattern measurements,

$$R>\frac{2D^2}{\lambda}=\frac{8a^2}{\lambda}.$$

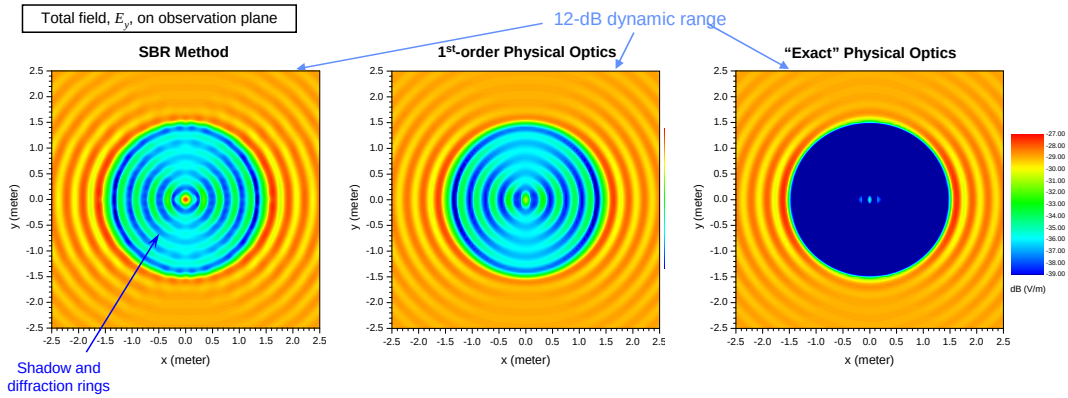

Figure III-2 Computed total field when the observation plane is 2.5 cm behind a PEC disk with diameter of 3 m.

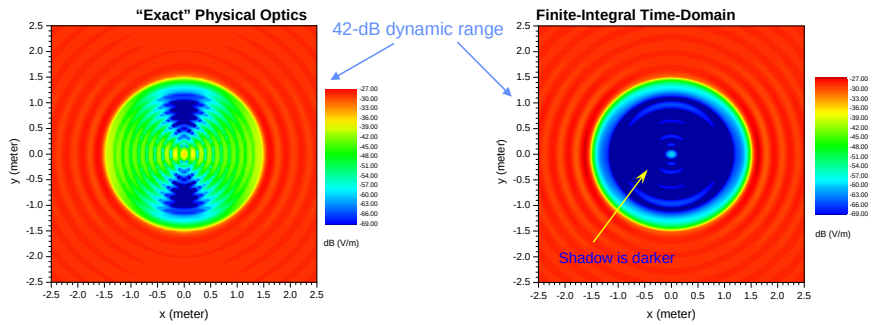

Figure III-3 Comparison of total field computed with exact physical-optics and the finite-integral time-domain methods, when the observation plane is 2.5 cm behind a PEC disk with diameter of 3 m.

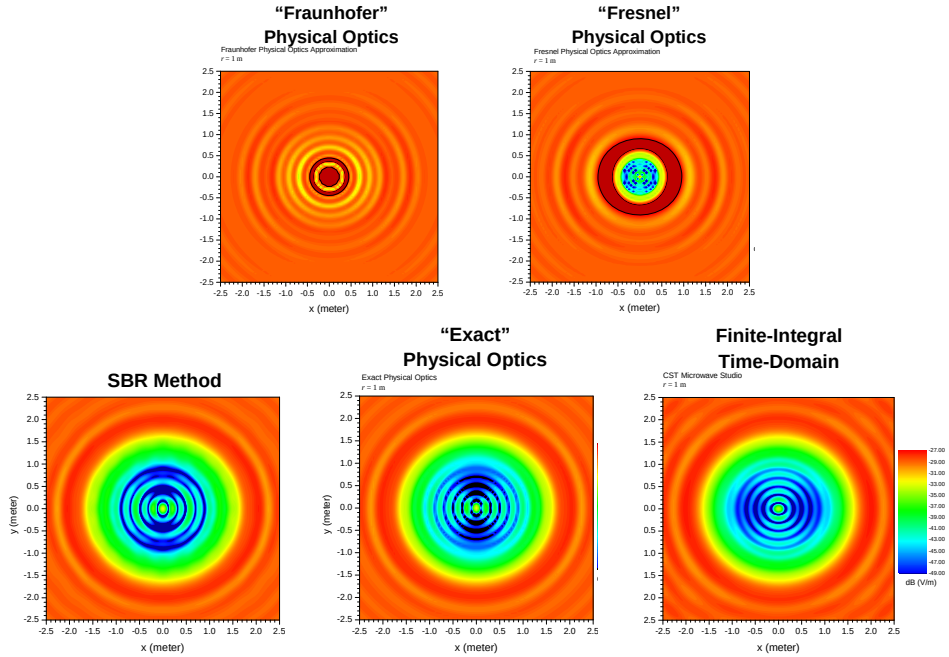

Figure III-4 Comparison of the total field computed with the Fraunhofer approximation, the Fresnel approximation, SBR method, the exact physical-optics method, and the finite-integral time-domain method, when the observation plane is 1 m behind a PEC disk with diameter of 3 m.

The radar cross section of a PEC trihedral corner reflector is computed with Xpatch® and compared with the results from the SAIC Full-wave solver (SAF), using the Multi-level Fast Multiple Algorithm (MLFMA) [30]. The trihedral, illustrated in Figure III-5, has corner-edge length of 100 mm and mesh size of 1.5 mm. The radar cross section is plotted in Figure III-6 as a function of frequency, when the radar is at azimuth 45° and elevation 35.26°, so that the incident vector has the same angular distance to each of the coordinate axes. Figure III-7 shows the radar cross section at 16.8 GHz, when azimuth varies while the elevation of the radar remains at 35.26°. In general, the agreement is quite good between the approximate solver (Xpatch®) and the rigorous solver (SAF).

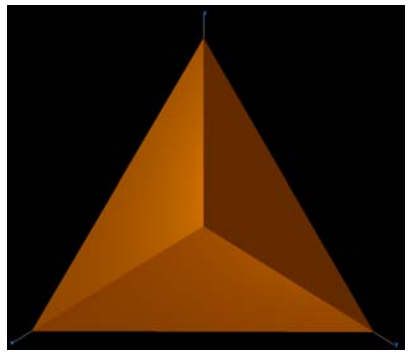

Figure III-5 Illustration of trihedral-corner-reflector model, with corner-edge length of 100 mm.

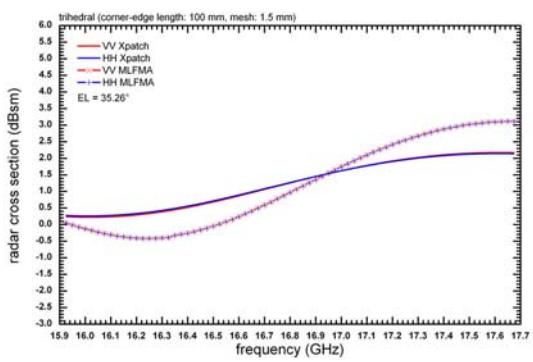

Figure III-6 Radar cross section of the trihedral corner reflector at Ku-band, with the radar at azimuth 45° and elevation 35.26°.

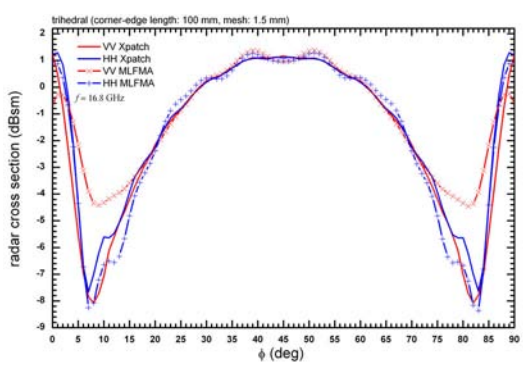

Figure III-7 Radar cross section of the trihedral corner reflector at 16.8 GHz, with the radar at elevation 35.26°.

Rectangular dielectric slab

The radar cross section of a simple rectangular dielectric slab (Figure III-8) will be modeled with the following parameters

$a = b = 100$ mm

$t_1 = 10$ mm

$\varepsilon_1 = 1.3 + j0.0$

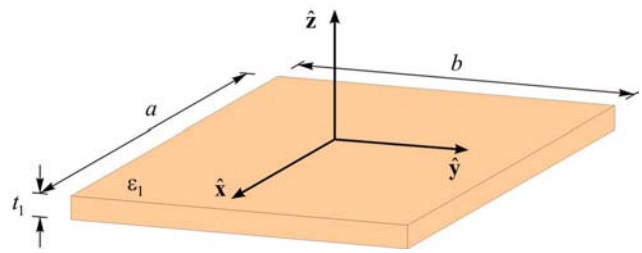

Figure III-8 Rectangular dielectric slab with dimensions.

The Xpatch® solver requires a triangular surface mesh, as illustrated in Figure III-9. However, only the front surface is used in the simulation, since the thickness is taken into account in the definition of the dielectric. Although there is an option to use a closed surface with a bulk material definition, it appears that the best results are obtained with the single open-surface model. A comparison of the monostatic radar cross section at normal incidence ($\theta = 0°$) and oblique incidence for the open- and close-surface models is shown in Figure III-10 through Figure III-13. There is considerable difference between the two models. However, a comparison with the results from an integral-equation solver (SAIC Fast Solver [30]) shows that the open-surface model agrees best, especially at or near normal incidence. At oblique incidence ($\theta = 30°, 60°$), the character of the solutions agree (peaks and valleys agree), but Xpatch® under-predicts the RCS. It is believed that the results from the SAIC Fast Solver are the most accurate.

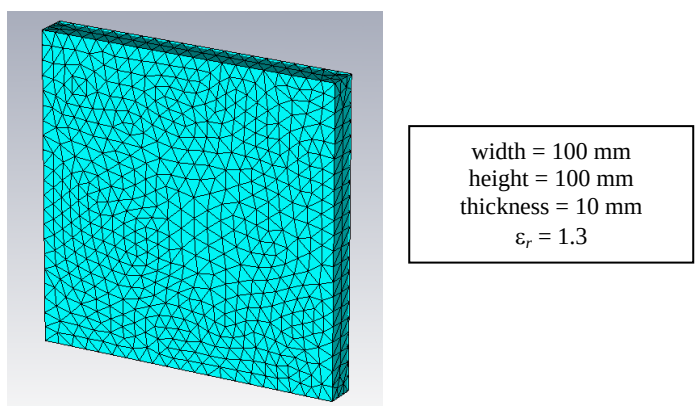

Figure III-9 Dielectric slab with triangular surface mesh.

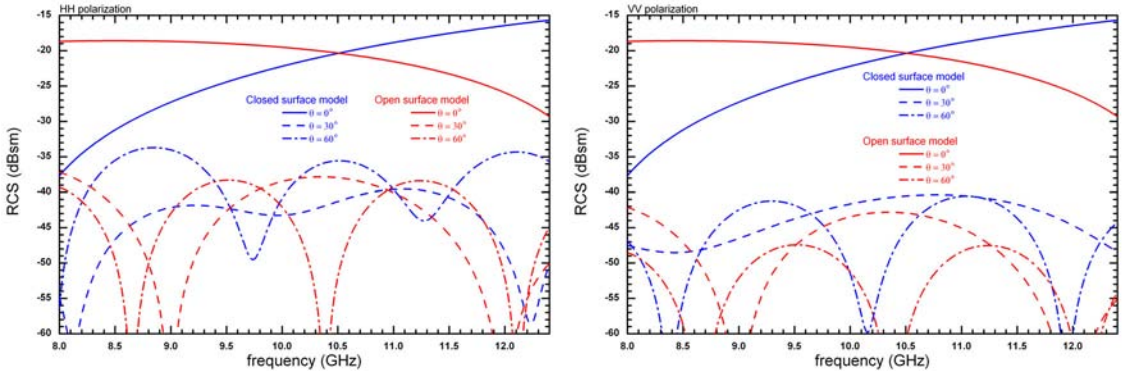

Figure III-10 Comparison of the monostatic radar cross section computed by Xpatch® with the single open-surface model (red), and the closed-surface model (blue).

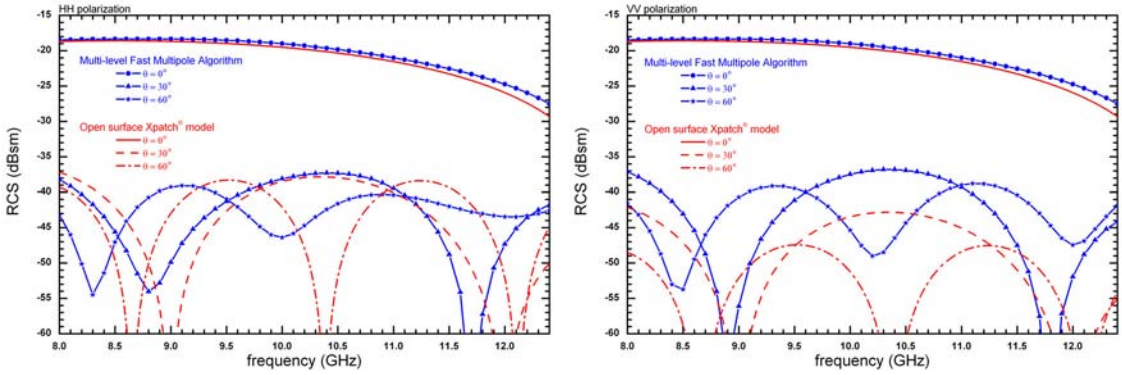

Figure III-11 Comparison of the monostatic radar cross section computed by Xpatch® with the single open-surface model (red) and the SAIC Fast Solver (multi-level fast multipole algorithm) (blue).

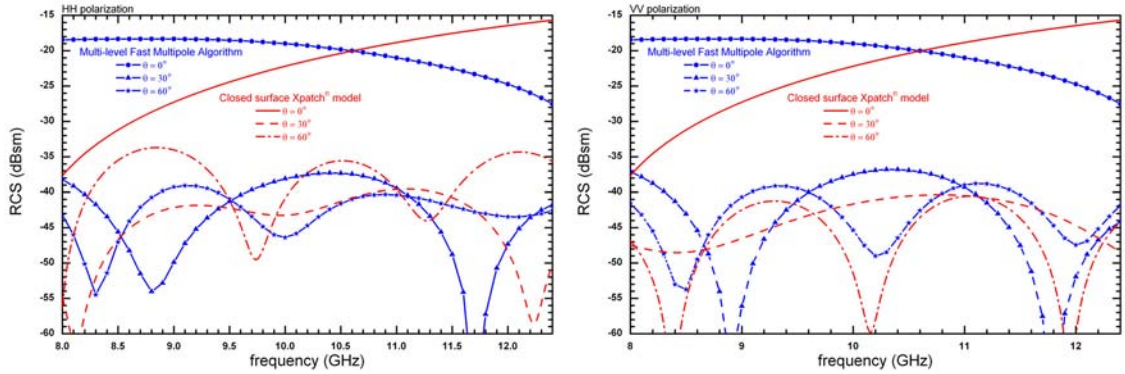

Figure III-12 Comparison of the monostatic radar cross section computed by Xpatch® with the closed-surface model without blockage checking (red) and the SAIC Fast Solver (multi-level fast multipole algorithm) (blue).

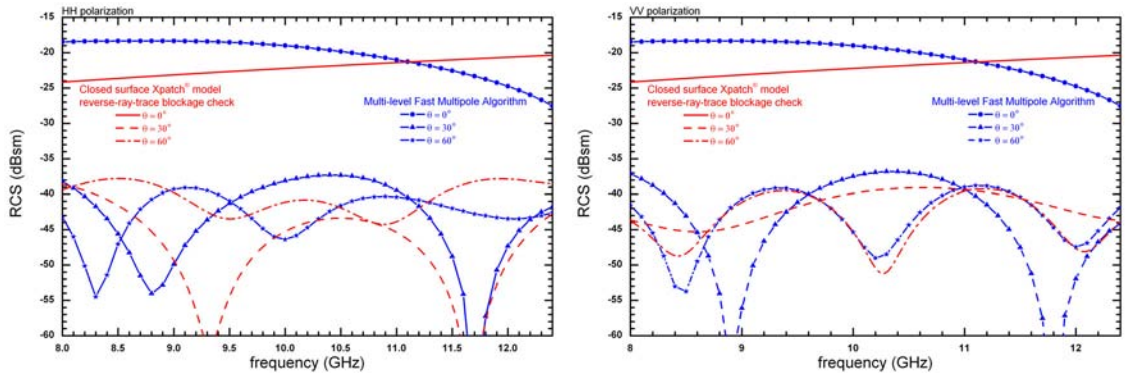

Figure III-13 Comparison of the monostatic radar cross section computed by Xpatch® with the closed-surface model with reverse ray trace (red) and the SAIC Fast Solver (multi-level fast multipole algorithm) (blue).

Finite-integral time-domain model – normal incidence

The slab in Figure III-8 is modeled with the transient solver, using open boundaries. The dielectric properties of the slab are $\varepsilon_r = 1.3 - j0.0$ and $\mu_r = 1.0 - j0.0$. For two different runs, the boundaries are placed at 20 mm and 30 from the surface of the slab. The maximum mesh step is less than 1.6 mm. The field-decay criterion is –40 dB.

The radar cross section as a function of frequency is plotted in Figure III-14. The considerable disagreement between the solutions is troublesome. The implication is that the absorbing boundary used by the CST solver is not adequate for this problem.

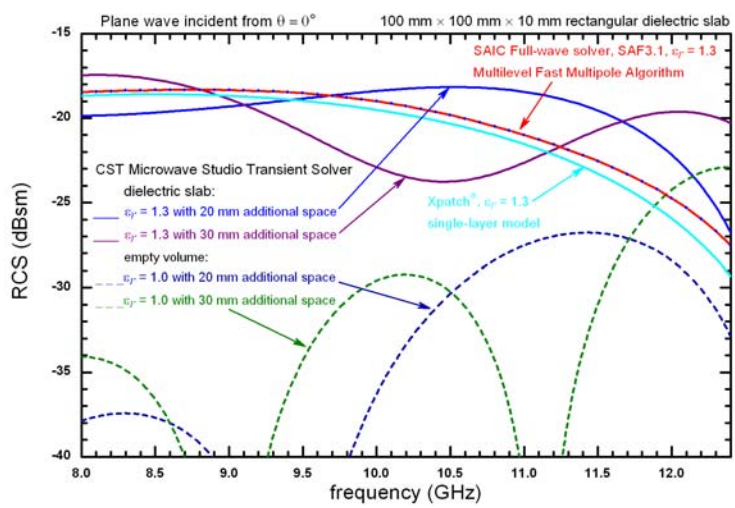

Figure III-14 Radar cross section of dielectric slab for normal incidence and emptyspace, computed with transient solver (VV polarization).

The discrepancies between the two CST transient solver solutions require examination. Since the volume of the solution space, and consequently the distance to the absorbing boundaries, it is reasonable to expect that the disagreement is related to the absorbing boundary. Although designated a Perfectly Matched Layer [29], the boundary is not a perfect absorber. Because the dielectric constant of the slab is low, the scattering from it will also be much lower than from a perfect electrical conductor (PEC). Thus, it is reasonable to suspect that an interaction between the scattering from the slab and the residual scattering from the boundary is present. An accurate

scattering model is needed that does not depend on the performance of an absorbing boundary is needed.

Method of Moments and Multilevel Fast Multipole Algorithm

The radar cross section the rectangular dielectric slab (Figure III-8) will be modeled with the SAIC Full-wave solver (SAF) [30]. SAF is an electromagnetic scattering computation program based on the Method of Moments (MoM) solution of the hybrid volume-surface integral equation. The solver incorporates the Multilevel Fast Multipole Algorithm (MLFMA), and provides efficiency in computation speed and memory requirements. Since MoM incorporates the radiation condition into the formulation, no absorbing boundary is necessary. Figure III-15 compares the computed normal-incidence radar cross section of the dielectric slab using MLFMA (blue), Xpatch® (red), CST integeral-equation iterative MLFMA solver (green), and the CST integral-equation direct MoM solver (purple). The agreement among all of the codes is within less than 1 dB at 8 GHz to about 2 dB at 12.4 GHz. The Xpatch® model uses the single-surface model for the slab.

The radar cross section at 10 GHz as a function of the angle θ, measured from the surface normal, is plotted in *Figure* III-*16*. The multilevel fast multipole method agrees very well with the method of moments using the iterative solver. The agreement with Xpatch® is very good for both VV and HH polarizations from normal incidence to about $\theta = 17°$. The VV results from Xpatch® begin to deviate for larger angles, with substantial disagreement $40° < \theta < 60°$. However, the agreement for HH is much better, and is quite good from normal incidence to around $\theta = 60°$.

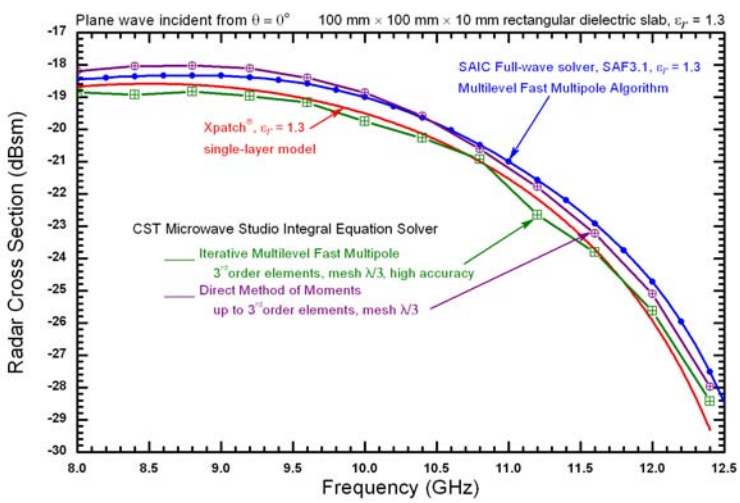

Figure III-15 Radar cross section for normal incidence, computed with various solvers (linear polarization).

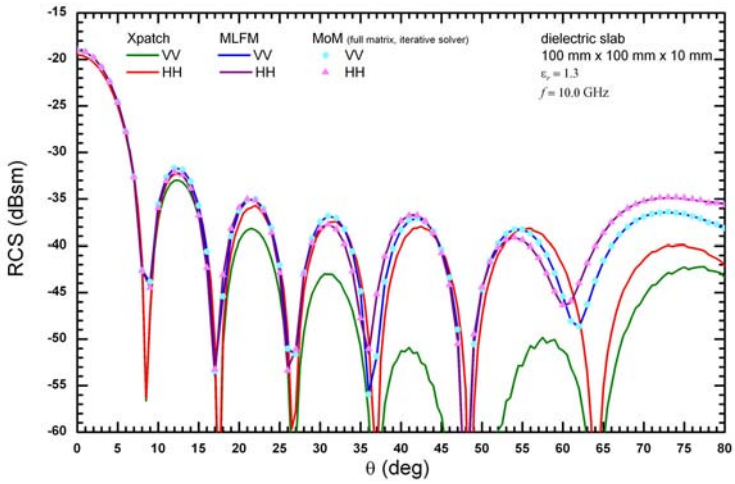

Figure III-16 Radar cross section of a dielectric slab, with $\varepsilon_r = 1.3 - j0$ *, as a function of angle from normal as computed by Xpatch®, the MLFM method, and full-matrix MoM.*

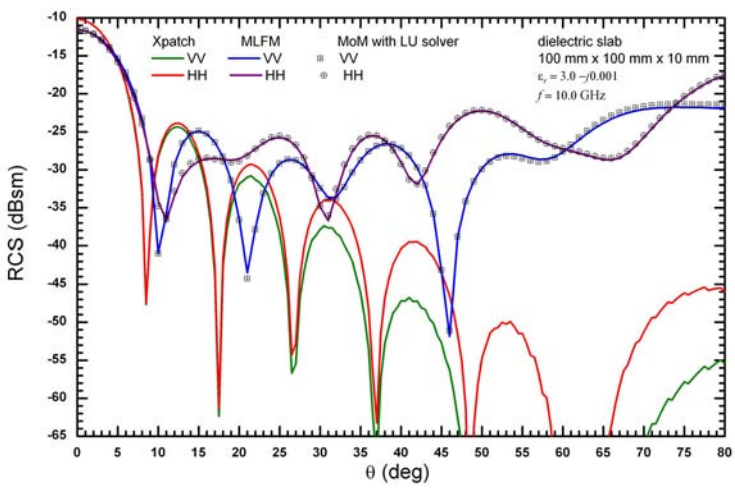

Figure III-17 Radar cross section of a dielectric slab with $\varepsilon_r = 3.0 - j0.001$*, as a function of angle from normal as computed by Xpatch®, the MLFM method, and full-matrix MoM.*

Dielectric slab covering a PEC corner reflector

Another test example is illustrated in Figure III-18, where a dielectric slab is placed in front of a PEC triangular trihedral corner reflector. The trihedral dimension along the corner edges is 100 mm. The slab is 150 mm along each side, and is 10 mm thick. The slab is located 2.5 cm along the normal vector from the face of the trihedral.

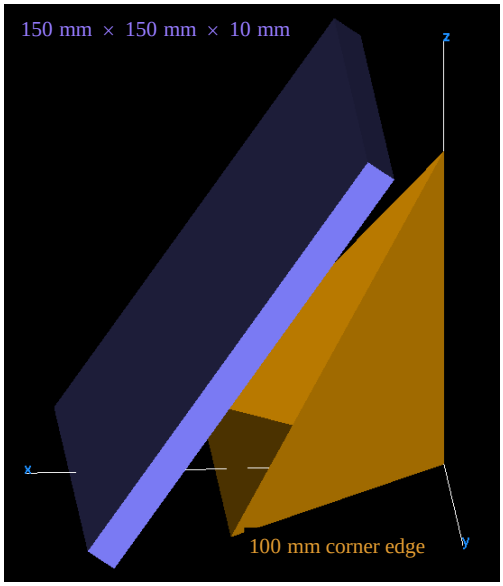

Figure III-18 Test example with dielectric slab in front of a triangular trihedral corner reflector.

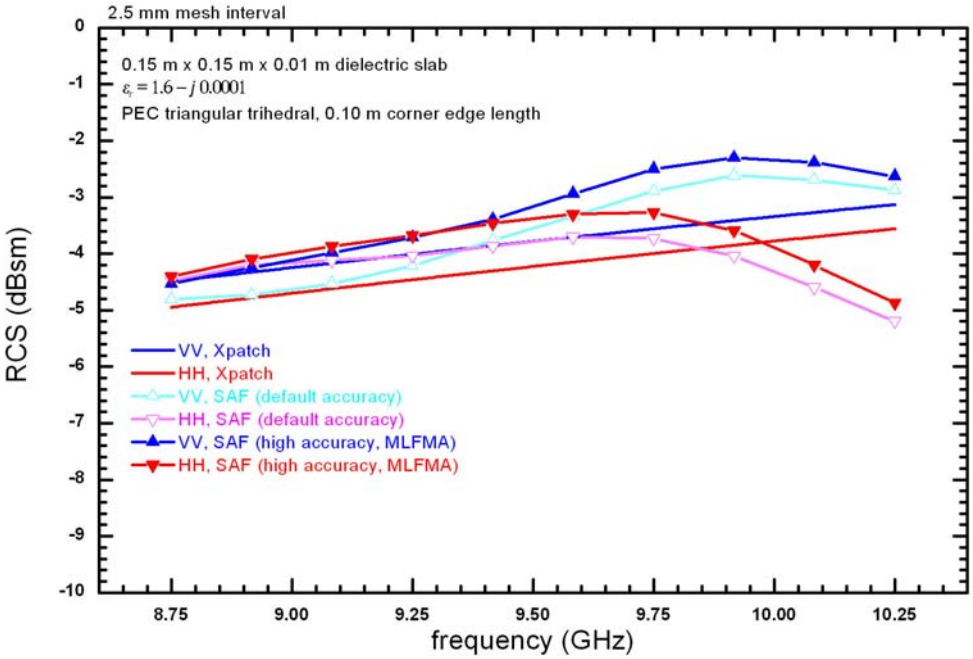

Figure III-19 Comparison of Xpatch and SAF (MLFMA) solutions for the radar cross section of the trihedral and slab configuration in Figure III-18 at elevation 30°.

Appendix IV – Considerations for computing SAR phase histories with Xpatch®

The Xpatch® code has features which allow the computation of synthetic-aperture-radar phase histories. However, since the code is an approximation of the true physics, artifacts can be introduced into the computed phase history. Two important code settings, the maximum number of bounces and the multi-look field compensation, will be examined.

Maximum-bounce limit

The Xpatch® software allows the choice of the maximum number of bounces considered when determining the physical-optics currents. The importance of this setting is not limited only to simulation of SAR images, but impacts the accuracy of all computations. The number of bounces really refers to the number of ray segments, beginning with the initial incident ray. Apparently, the choice of the single-bounce model would be equivalent to the simple physical-optics model with plane-wave illumination, since only the first ray hit contributes to the physical-optics current. In this case, there will be no contributions from reflections. When the maximum-bounce choice is set to two, the incident ray will reflect from the location of the first hit to a second possible hit, in the case of non-penetrable materials. In the case of penetrable materials, there would be both a reflected ray and a transmitted ray. In this case, the ray path would not extend beyond two segments in either the reflected or transmitted path, including the incident segments. The rays are tracked up to the maximum number of bounces (segments), or until they pass outside the volume containing the model. Rays are also terminated at bulk media or perfect absorbers. The maximum number of bounces must be chosen to provide a trade off between fast execution and accuracy.

To see the effect of limiting the number of bounces, consider a single trihedral corner reflector. Simulated SAR images will be computed for several values for the limit. The corner reflector measures 0.221 m on the corner edge. The parameters for the simulation are:

Xpatch® settings:

- First-bounce algorithm: z-buffer
- Use all bounce contributions (total field)
- Center frequency: 9.5 GHz
- Bandwidth: 1.775 GHz
- Number frequencies: 512
- Synthetic-aperture width: 10.7°
- Azimuth: 0°
- Elevation: 30°

FFT settings:

- Taylor weight, $\bar{n} = 4$, $SLL = -35$
- Zero-padding factor = 4
- Resolution: 0.1 m

The simulated SAR images are shown in Figure IV-1 for 1, 2, 3, and 5 maximum bounces. As expected, it is clear that 1 or 2 bounces are insufficient to properly model the trihedral; the image of the trihedral is distorted by spreading in the along-track direction. (The reason the error is manifested as spreading in the along-track direction is discussed in the next section.) With the maximum-bounce limit set to 3, the response of the trihedral looks like the ideal point-spread function that is expected with these parameters. Increasing the limit to 5 bounces has no additional effect, since the rays leave the volume after the third reflection. Thus, a maximum of three reflections is all that is needed to properly define the complete physical-optics current on

the trihedral surface. More complex objects may require a larger maximum in order to create a high-fidelity image.

In a complex scene, the maximum number of reflections allowed should be chosen to ensure that all the important contributions to the physical-optics current are included, without unduly increasing the computer run time. Setting the limit higher than necessary can greatly increase the run time.

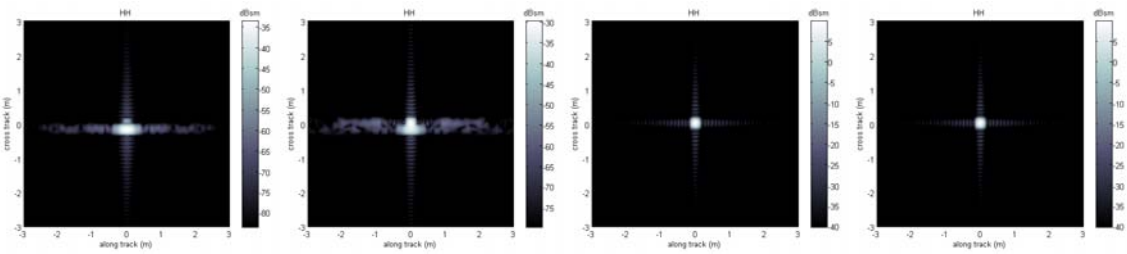

1 bounce 2 bounces 3 bounces 5 bounces

Figure IV-1 Simulated SAR image of a trihedral corner reflector with the maximum number of bounces limited as indicated.

Multi-look field compensation

Because the physical-optics current is obtained by ray tracing the incident field, non-physical discontinuities can occur in the phase history. The effect of a discontinuity in the phase history is to spread energy over the range of the Fourier transform when an image is created. The discontinuity occurs as a result of geometric shadowing of various features in the scene as the source moves across the angular aperture. Since the discontinuities are a function of the azimuth angle (position of the radar in the synthetic aperture), the energy is spread in the along-track direction and not in the cross-track direction. Fortunately, Xpatch® includes a computational feature, called Multi-look Field Compensation to mitigate this problem.

The Multi-look Field Compensation option has two parameters, a window size measured in azimuth bins, and an angle-skip size, also measured in azimuth bins [25]. The window is centered at the current azimuth angle, and contributions from other angles within the window, sampled according to the angle-skip size, are weighted and included with the primary contribution from the current azimuth angle. This method smoothes the discontinuity caused to geometric shadowing of the incident field, but avoids severe degradation of the along-track resolution in the resulting image. Two examples will illustrate the problem, and the effectiveness of the Multi-look Field Compensation option.

First, consider a single trihedral corner reflector located at the origin. A perfectly absorbing strip is placed in front of the trihedral so that it is completely shadowed over 1° of the synthetic aperture. The relevant geometry is illustrated in plan view in Figure IV-2

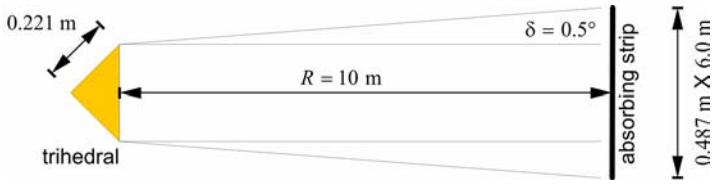

Figure IV-2 Plan view of the geometry used in the Multi-look Field Compensation example.

The trihedral is imaged with and without the absorbing strip, using the following parameters:

Xpatch® settings:

- First-bounce algorithm: z-buffer
- Use all bounce contributions (total field)
- Maximum bounce: 5
- Center frequency: 9.5 GHz
- Bandwidth: 1.775 GHz
- Number frequencies: 512
- Synthetic-aperture width: 10.7°
- Azimuth: 0°
- Elevation: 30°

FFT settings:

- Taylor weight, $\bar{n} = 4$, $SLL = -35$
- Zero-padding factor = 4
- Resolution: 0.1 m

The magnitude of the computed phase history is illustrated in Figure IV-3. The phase history at far left is for the trihedral without any blockage. The amplitude is fairly uniform, but increases slightly in the frequency (k_y) direction. At center left is the phase-history amplitude with the absorber strip in place, but without multi-look field compensation. The strong discontinuity is very apparent. Applying multi-look field compensation with 10 samples within a window 100 bins wide softens the discontinuity a small amount (center right), but increasing the window to 500 bins (with 10 samples) produces a smooth transition (far right). The SAR images associated with these phase histories are shown in Figure IV-4. The shadowing causes significant smearing of the trihedral image in the along-track direction (center left). Applying the multi-look field compensation significantly improves the image (far right).

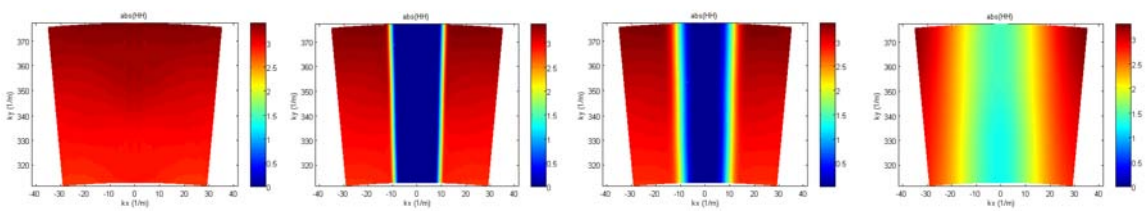

trihedral, no blockage | no multi-look | multi-look (100, 10) | multi-look (500, 50)

Figure IV-3 Magnitude of the phase history computed with no blockage (left), with the blockage illustrated in Figure IV-2 (center left), and with multi-look field compensation,(center right and right). The multi-look windows contain 100 and 500 bins, respectively, with spacing of 10 and 50 bins.

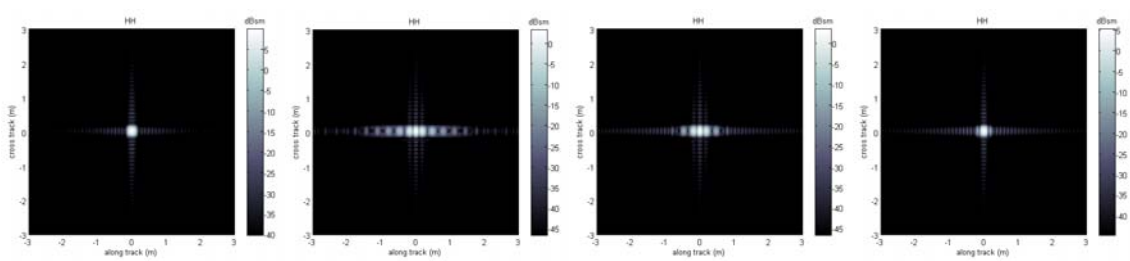

trihedral, no blockage | no multi-look | multi-look (100, 10) | multi-look (500, 50)

Figure IV-4 SAR image of trihderal with no blockage (left), with the blockage illustrated in Figure IV-2 (center left), and with multi-look field compensation,(center right and right). The multi-look windows contain 100 and 500 bins, respectively, with spacing of 10 and 50 bins.

The second example images a rough PEC fractal surface, illustrated in Figure IV-5. The following parameters were applied:

Xpatch® settings:

- First-bounce algorithm: z-buffer
- Use all bounce contributions (total field)
- Maximum bounce: 5
- Center frequency: 9.5 GHz
- Bandwidth: 0.3550 GHz
- Number frequencies: 256
- Synthetic-aperture width: 2.14°
- Azimuth: 0°
- Elevation: 15°

FFT settings:

- Taylor weight, $\bar{n} = 4$, $SLL = -35$
- Zero-padding factor = 4
- Resolution: 0.5 m

The simulated SAR images, with several choices for the multi-look field compensation parameters are illustrated in Figure IV-6. The severe smearing in the along-track direction without the multi-look field compensation (far left) is completely unacceptable. However, the smearing is essentially eliminated when the window width is 100 bins, sampled every 10 bins (far right).

These two examples demonstrate that the multi-look field compensation option in Xpatch® is effective in mitigating the smearing caused by the geometric shadowing of the illumination. The optimum choice of the window width and sampling interval appears to be somewhat dependent on the specific situation.

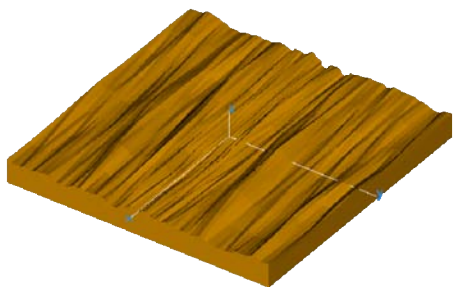

Figure IV-5 Rough-surface model, using a three-level fractal model, used to illustrate the multi-look field compensation option.

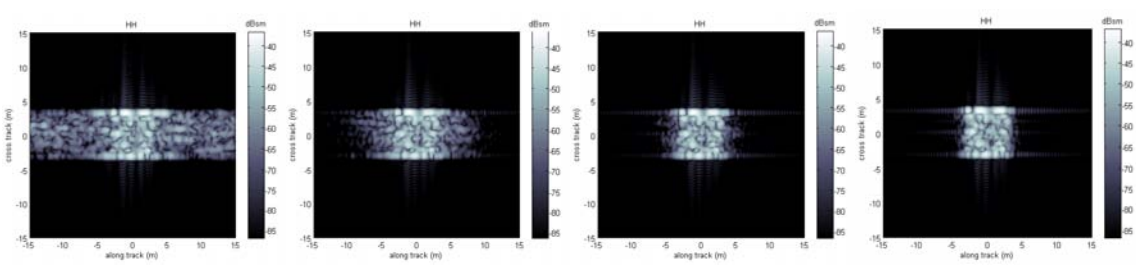

no multi-look | multi-look (25, 5) | multi-look (50, 5) | multi-look (100,10)

Figure IV-6 Simulated SAR image of the rough-surface model, with several parameters for the multi-look field compensation.

Sampling the reflection / transmission coefficient table

When the surface to be modeled is a dielectric, Xpatch® will build a reflection coefficient table with frequency and incident angle as parameters into the table. Apparently, the number of angles is fixed at 90 [25]. However, the number of frequencies can be equal to or smaller than the number of frequencies used in the simulation. For multilayer dielectrics, the frequency dependence can be strong, and it is necessary to build the table for each frequency rather than use coarse sampling. When the reflection coefficient is not sampled sufficiently with frequency, aliasing occurs, as illustrated in Figure IV-7. Here, the radar cross section is plotted for a rectangular dielectric slab, one meter on each side and one-half meter thick, for normal incidence and linear polarization. The parameters for the computation are:

Xpatch® settings:

- First-bounce algorithm: z-buffer
- Use all bounce contributions (total field)
- Maximum bounce: 5
- Center frequency: 9.5 GHz
- Bandwidth: 1.7471 GHz
- Number frequencies: 512
- Azimuth: 0°
- Elevation: 90°

FFT settings:

- Zero-padding factor = 4
- Kaiser weighting
- Sidelobe level: –60 dB
- Resolution: 0.07 m

The dielectric has 25 layers, each 2 cm thick. The dielectric permittivity profile is from the Siple C model. For the plot on the left, the reflection coefficient was computed for every tenth frequency and the values were extracted from the table using the "nearest neighbor" method. For the plot on the right, the reflection coefficient was computed at each of the 512 frequencies used on the computations. While the true scattering profile is essentially unchanged by the inadequate sampling, the aliased components are strong, only about 17 dB below the correct profile.

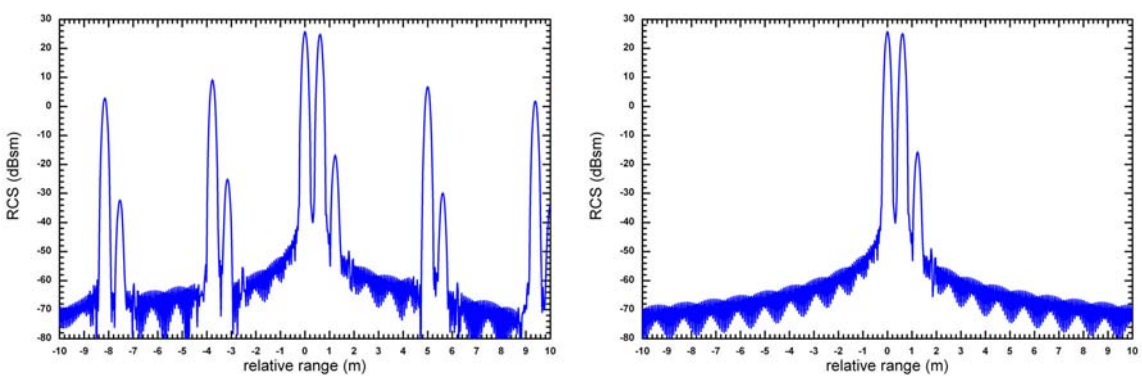

compute reflection coefficient for every 10th frequency *compute reflection coefficient for every frequency*

Figure IV-7 Example of range aliasing that is caused by inadequate sampling of the reflection coefficient with frequency.

This page intentionally blank

Appendix V – SAR images of the crevasse and snow bridge

This appendix contains simulated SAR images created from the geometry described in the main text. All images are based on the same top surface structure, although the thickness and number of layers beneath the top surface and in the snow bridge vary. Images were formed with and without the crevasse walls present. Most of the images are based on the density profile for the composite Siple Dome data, although a small set uses the Newall Glacier profile, which includes the dip in density. A key to the parameters associated with each figure are listed in Table V-1.

Table V-1 Key for the parameters of the simulated SAR images.

	Crevasse Walls Included	Snow-bridge Depth (m)			Radar Band			Resolution (inch)		Density Profile		Image Format			Depression Angle	
		0.5	2.0	4.0	C	X	Ku	18	8	Siple Dome	Newall Glacier	Monochrome (dB)	4^{th}root of power	Color (dB)	15°	30°
Figure V-1	•	•			•			•		•		•			•	
Figure V-2	•	•			•			•		•		•				•
Figure V-3	•	•				•		•		•		•			•	
Figure V-4	•	•				•		•		•		•				•
Figure V-5	•	•					•	•		•		•			•	
Figure V-6	•	•					•	•		•		•				•
Figure V-7	•	•				•			•	•		•			•	
Figure V-8	•	•				•			•	•		•				•
Figure V-9	•	•					•		•	•		•			•	
Figure V-10	•	•					•		•	•		•				•
Figure V-11	•	•			•			•		•			•		•	
Figure V-14	•	•			•			•		•			•			•
Figure V-12	•	•				•		•		•			•		•	
Figure V-13	•	•				•		•		•			•			•
Figure V-15	•	•					•	•		•			•		•	
Figure V-16	•	•					•	•		•			•			•
Figure V-17	•	•				•			•	•			•		•	
Figure V-18	•	•				•			•	•			•			•
Figure V-19	•	•					•		•	•			•		•	
Figure V-20	•	•					•		•	•			•			•
Figure V-21	•	•			•			•		•				•	•	
Figure V-22	•	•			•			•		•				•		•
Figure V-23	•	•				•		•		•				•	•	
Figure V-24	•	•				•		•		•				•		•
Figure V-25	•	•					•	•		•				•	•	
Figure V-26	•	•					•	•		•				•		•

	Crevasse Walls Included	Snow-bridge Depth (m)			Radar Band			Resolution (inch)		Density Profile		Image Format			Depression Angle	
		0.5	2.0	4.0	C	X	Ku	18	8	Siple Dome	Newall Glacier	Monochrome (dB)	4^{th}root of power	Color (dB)	15°	30°
Figure V-27	•	•				•			•	•				•	•	
Figure V-28	•	•				•			•	•				•		•
Figure V-29	•	•					•		•	•				•	•	
Figure V-30	•	•					•		•	•				•		•
Figure V-31	•		•		•			•		•		•			•	
Figure V-32	•		•		•			•		•		•				•
Figure V-33	•		•			•		•		•		•			•	
Figure V-34	•		•			•		•		•		•				•
Figure V-35	•		•				•	•		•		•			•	
Figure V-36	•		•				•	•		•		•				•
Figure V-37	•		•			•			•	•		•			•	
Figure V-38	•		•			•			•	•		•				•
Figure V-39	•		•				•		•	•		•			•	
Figure V-40	•		•				•		•	•		•				•
Figure V-41	•		•		•			•		•			•		•	
Figure V-42	•		•		•			•		•			•			•
Figure V-43	•		•			•		•		•			•		•	
Figure V-44	•		•			•		•		•			•			•
Figure V-45	•		•				•	•		•			•		•	
Figure V-46	•		•				•	•		•			•			•
Figure V-47	•		•			•			•	•			•		•	
Figure V-48	•		•			•			•	•			•			•
Figure V-49	•		•				•		•	•			•		•	
Figure V-50	•		•				•		•	•			•			•
Figure V-51	•		•		•			•		•				•	•	
Figure V-52	•		•		•			•		•				•		•
Figure V-53	•		•			•		•		•				•	•	
Figure V-54	•		•			•		•		•				•		•
Figure V-55	•		•				•	•		•				•	•	
Figure V-56	•		•				•	•		•				•		•
Figure V-57	•		•			•			•	•				•	•	
Figure V-58	•		•			•			•	•				•		•
Figure V-59	•		•				•		•	•				•	•	
Figure V-60	•		•				•		•	•				•		•
Figure V-61			•			•			•	•		•			•	

	Crevasse Walls Included	Snow-bridge Depth (m)			Radar Band			Resolution (inch)		Density Profile		Image Format			Depression Angle	
		0.5	2.0	4.0	C	X	Ku	18	8	Siple Dome	Newall Glacier	Monochrome (dB)	4^{th}root of power	Color (dB)	15°	30°
Figure V-62			•			•			•	•		•				•
Figure V-63			•				•		•	•		•			•	
Figure V-64			•				•		•	•		•				•
Figure V-65			•			•			•	•			•		•	
Figure V-66			•			•			•	•			•			•
Figure V-67			•				•		•	•			•		•	
Figure V-68			•				•		•	•			•			•
Figure V-69			•			•			•	•				•	•	
Figure V-70			•			•			•	•				•		•
Figure V-71			•				•		•	•				•	•	
Figure V-72			•				•		•	•				•		•
Figure V-73				•		•			•	•		•			•	
Figure V-74				•		•			•	•		•				•
Figure V-75				•			•		•	•		•			•	
Figure V-76				•			•		•	•		•				•
Figure V-77				•		•			•	•			•		•	
Figure V-78				•		•			•	•			•			•
Figure V-79				•			•		•	•			•		•	
Figure V-80				•			•		•	•			•			•
Figure V-81				•		•			•	•				•	•	
Figure V-82				•		•			•	•				•		•
Figure V-83				•			•		•	•				•	•	
Figure V-84				•			•		•	•				•		•
Figure V-85				•		•			•		•	•			•	
Figure V-86				•		•			•		•	•				•
Figure V-87				•			•		•		•	•			•	
Figure V-88				•			•		•		•	•				•
Figure V-89				•		•			•		•		•		•	
Figure V-90				•		•			•		•		•			•
Figure V-91				•			•		•		•		•		•	
Figure V-92				•			•		•		•		•			•
Figure V-93				•		•			•		•			•	•	
Figure V-94				•		•			•		•			•		•
Figure V-95				•			•		•		•			•	•	
Figure V-96				•			•		•		•			•		•

Crevasse with snow bridge, Siple Dome model, 0.5-m depth

Monochrome, snow-bridge depth is 0.5 m

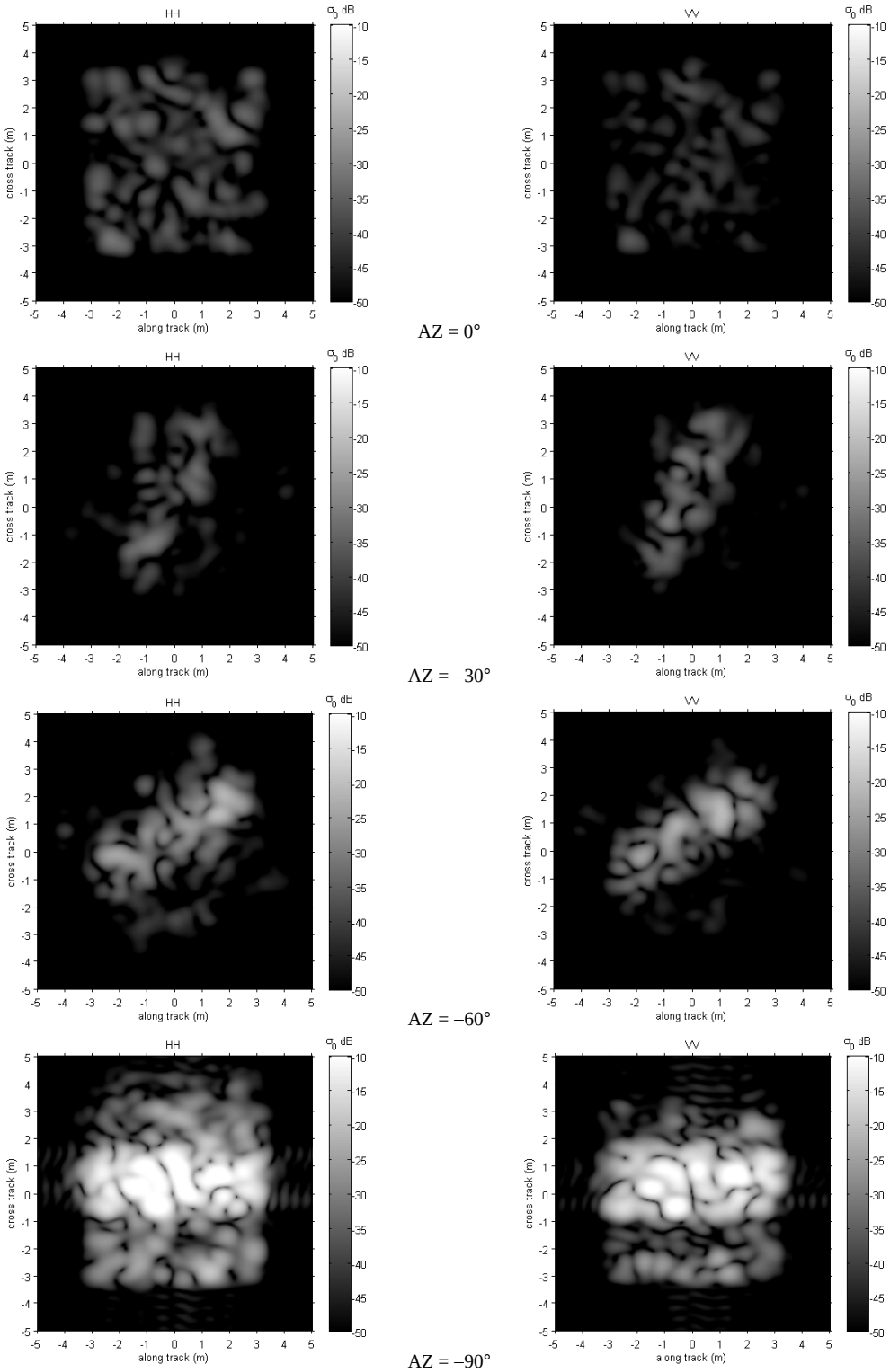

Figure V-1 *Crevasse with snow bridge, 0.5-m depth, 18-inch resolution,* $f_c = 5.45$ GHz *, 15° depression angle.*

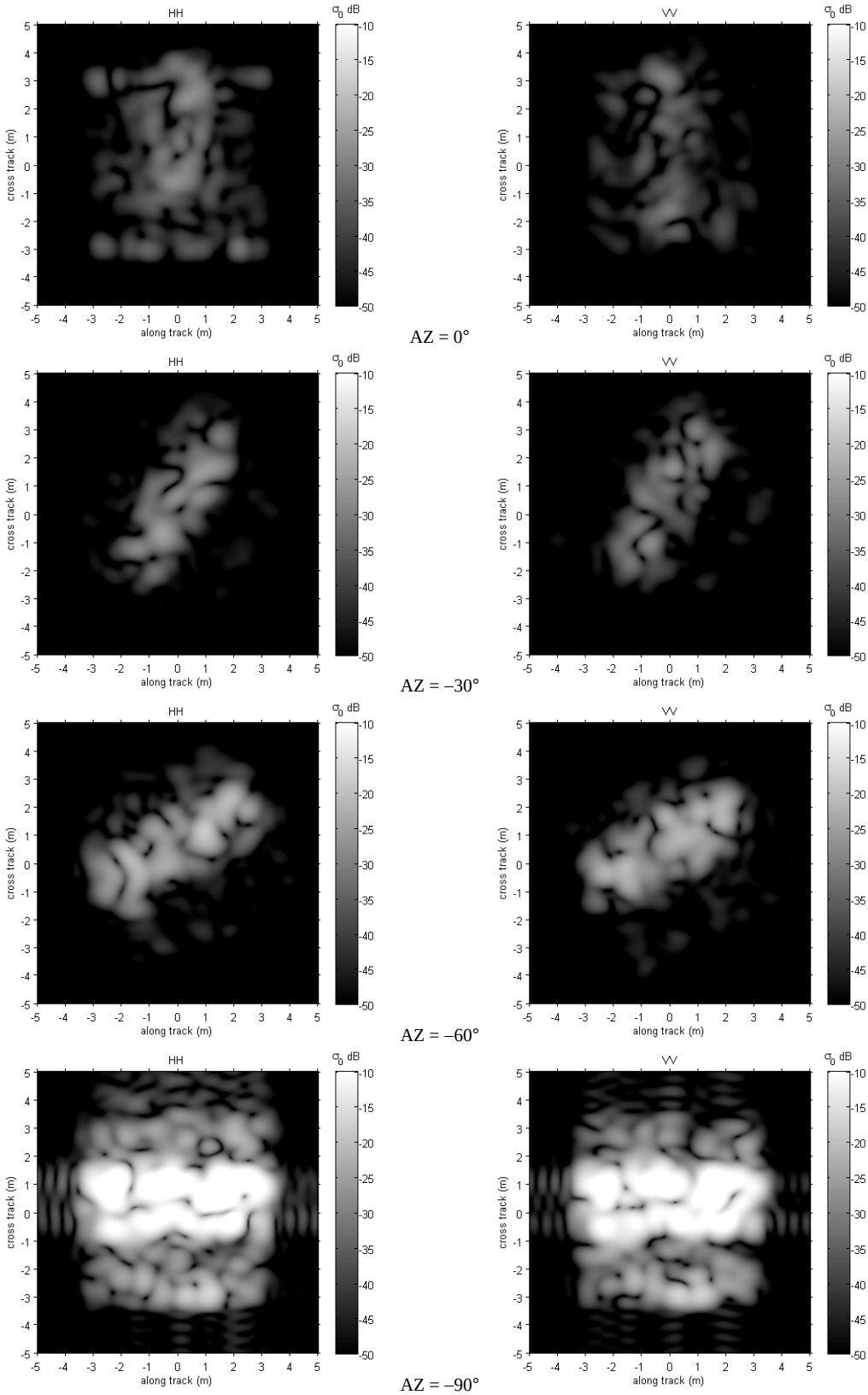

Figure V-2 Crevasse with snow bridge, 0.5-m depth, 18-inch resolution, $f_c = 5.45$ GHz *, 30° depression angle.*

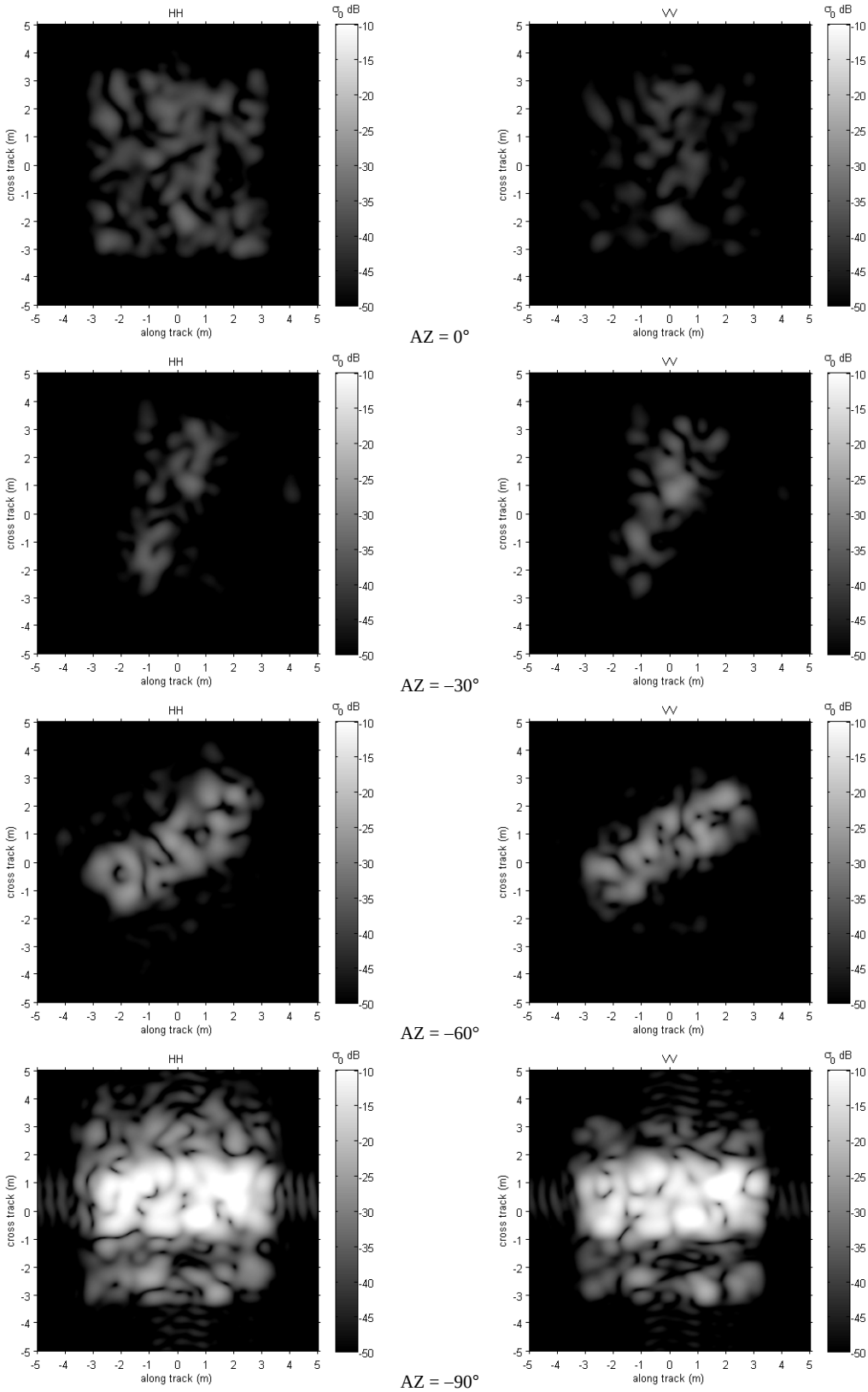

Figure V-3 Crevasse with snow bridge, 0.5-m depth, 18-inch resolution, $f_c = 9.5$ GHz, 15° depression angle.

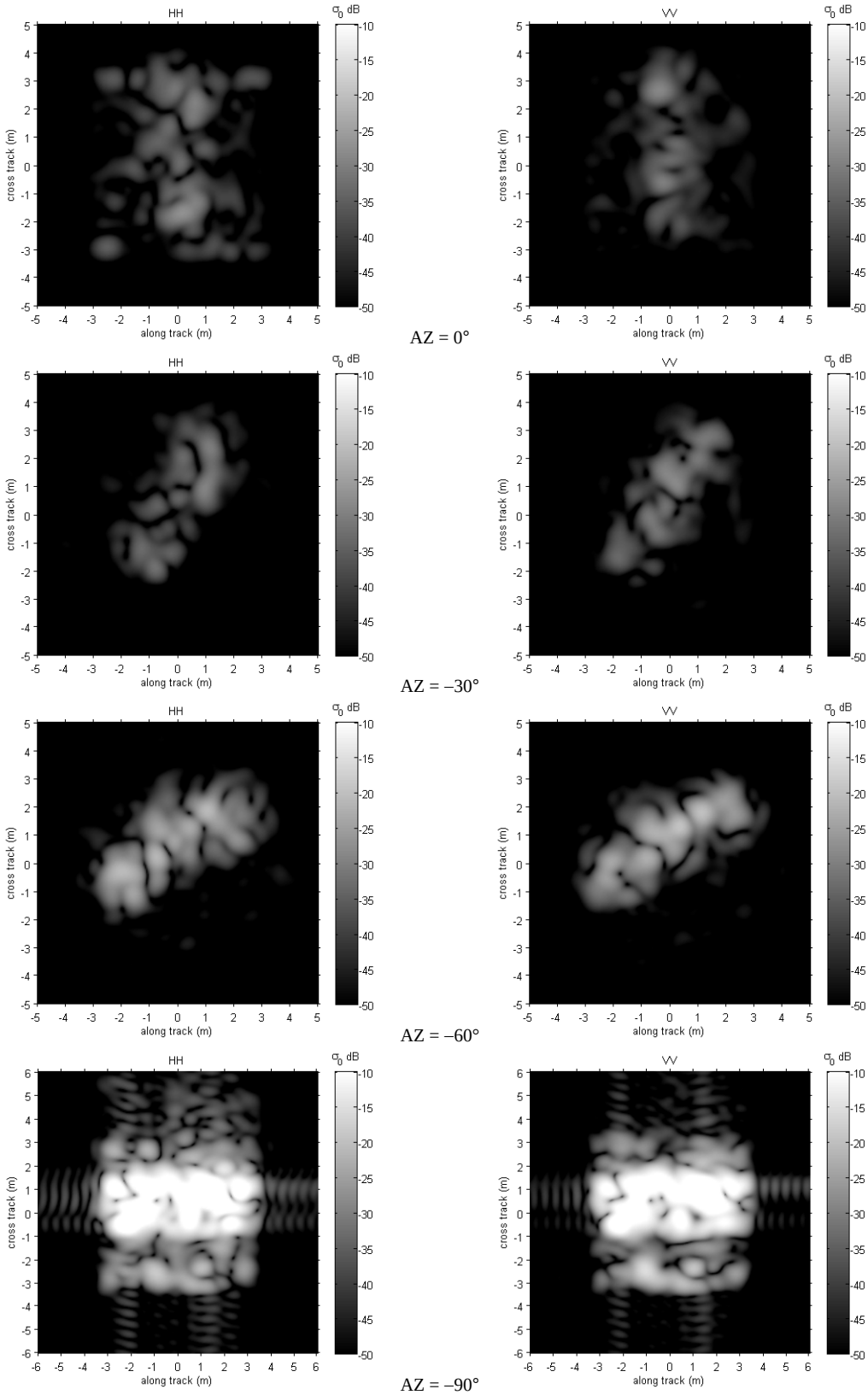

Figure V-4 Crevasse with snow bridge, 0.5-m depth, 18-inch resolution, $f_c = 9.5$ GHz *, 30° depression angle.*

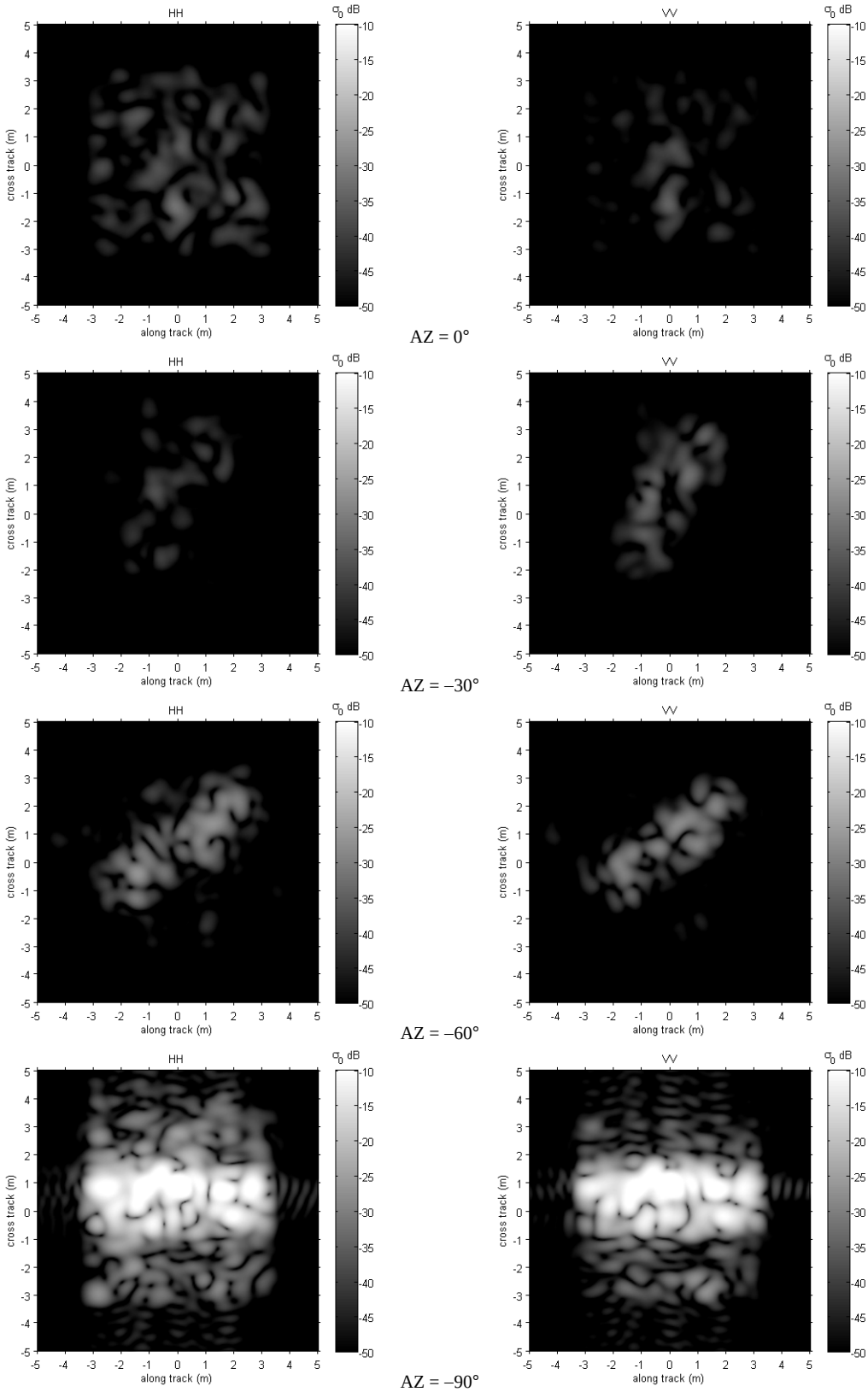

Figure V-5 Crevasse with snow bridge, 0.5-m depth, 18-inch resolution, $f_c = 16.8$ GHz *, 15° depression angle.*

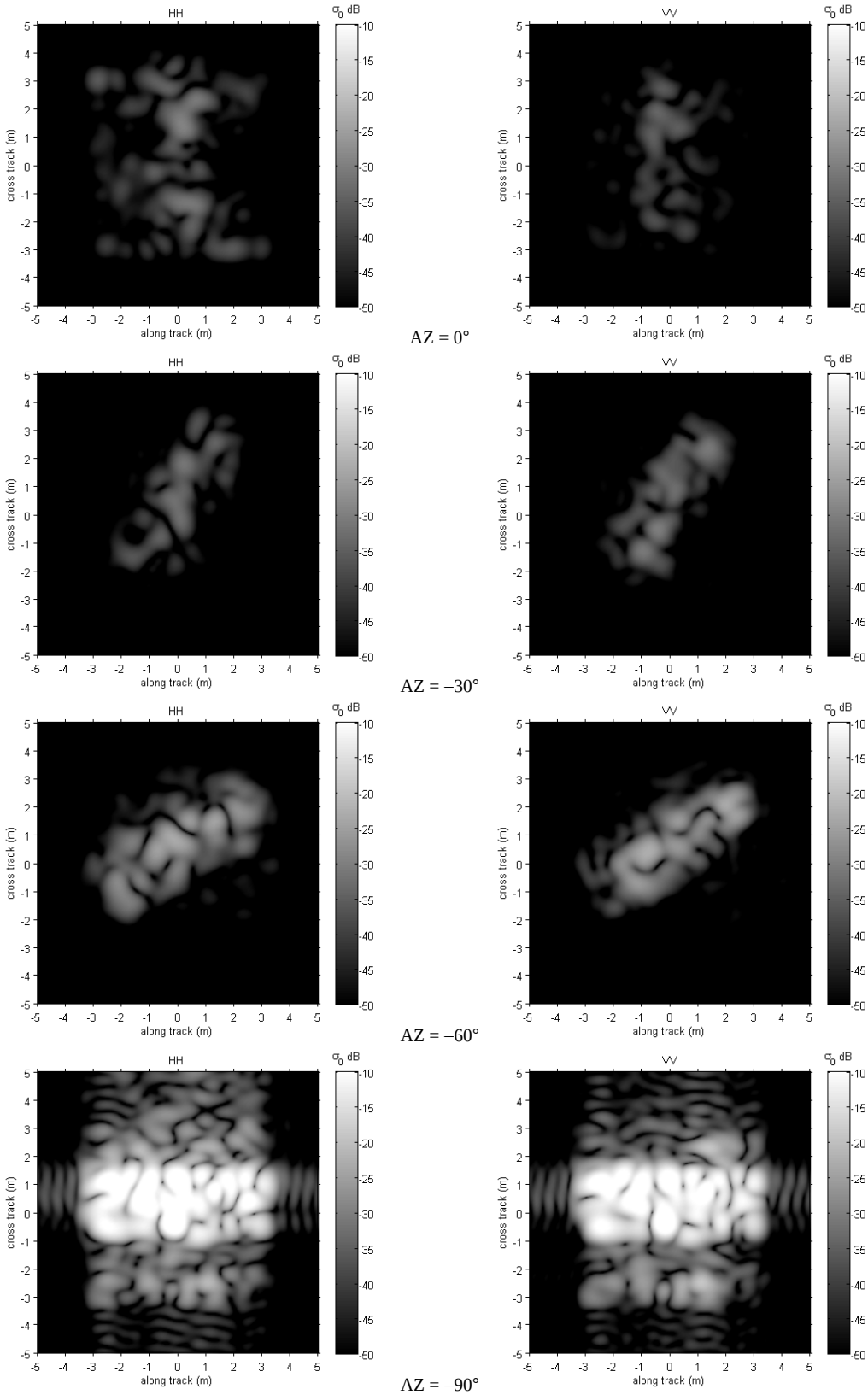

Figure V-6 Crevasse with snow bridge, 0.5-m depth, 18-inch resolution, $f_c = 16.8$ GHz *, 30° depression angle.*

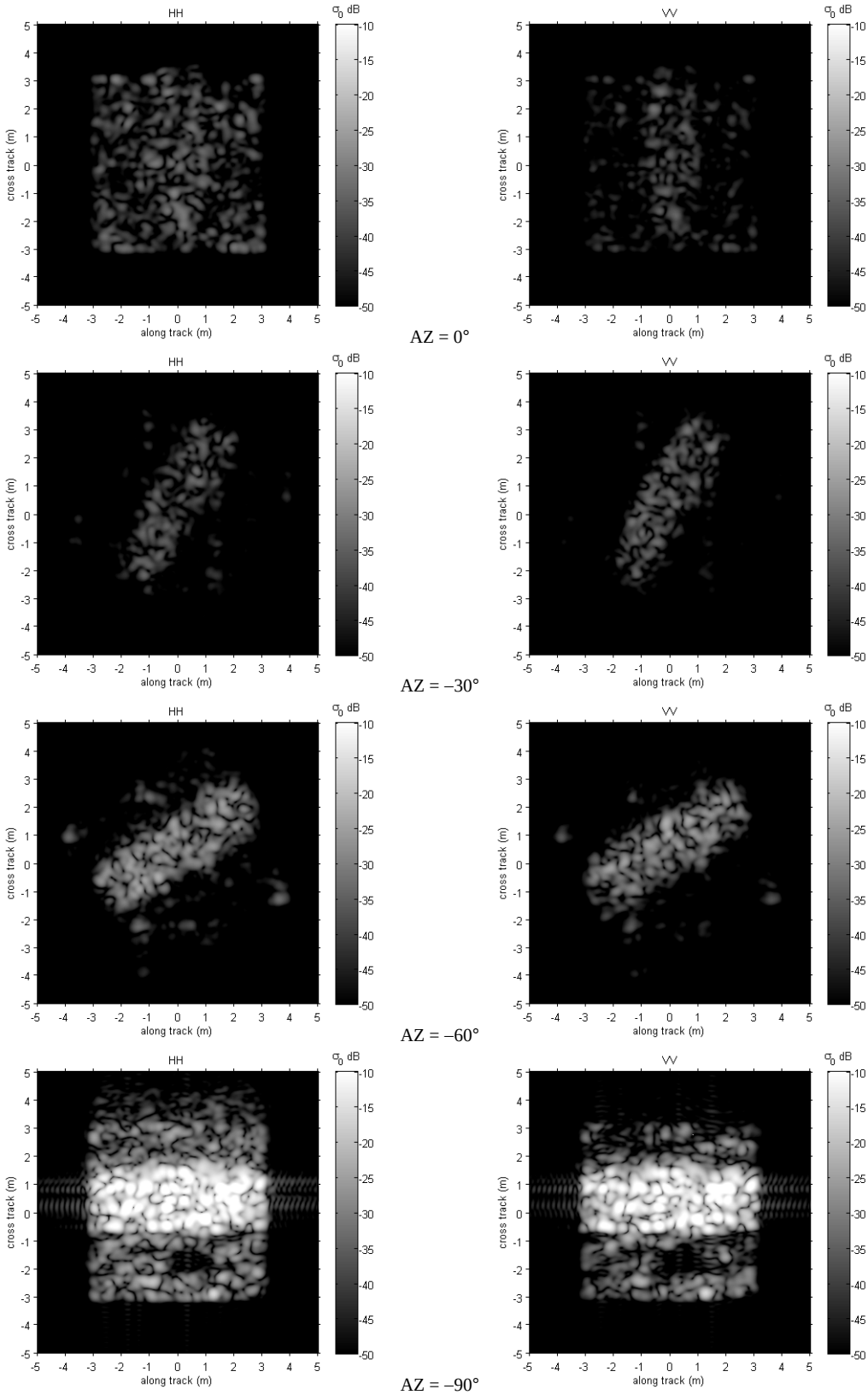

Figure V-7 Crevasse with snow bridge, 0.5-m depth, 8-inch resolution, $f_c = 9.5$ GHz *, 15° depression angle.*

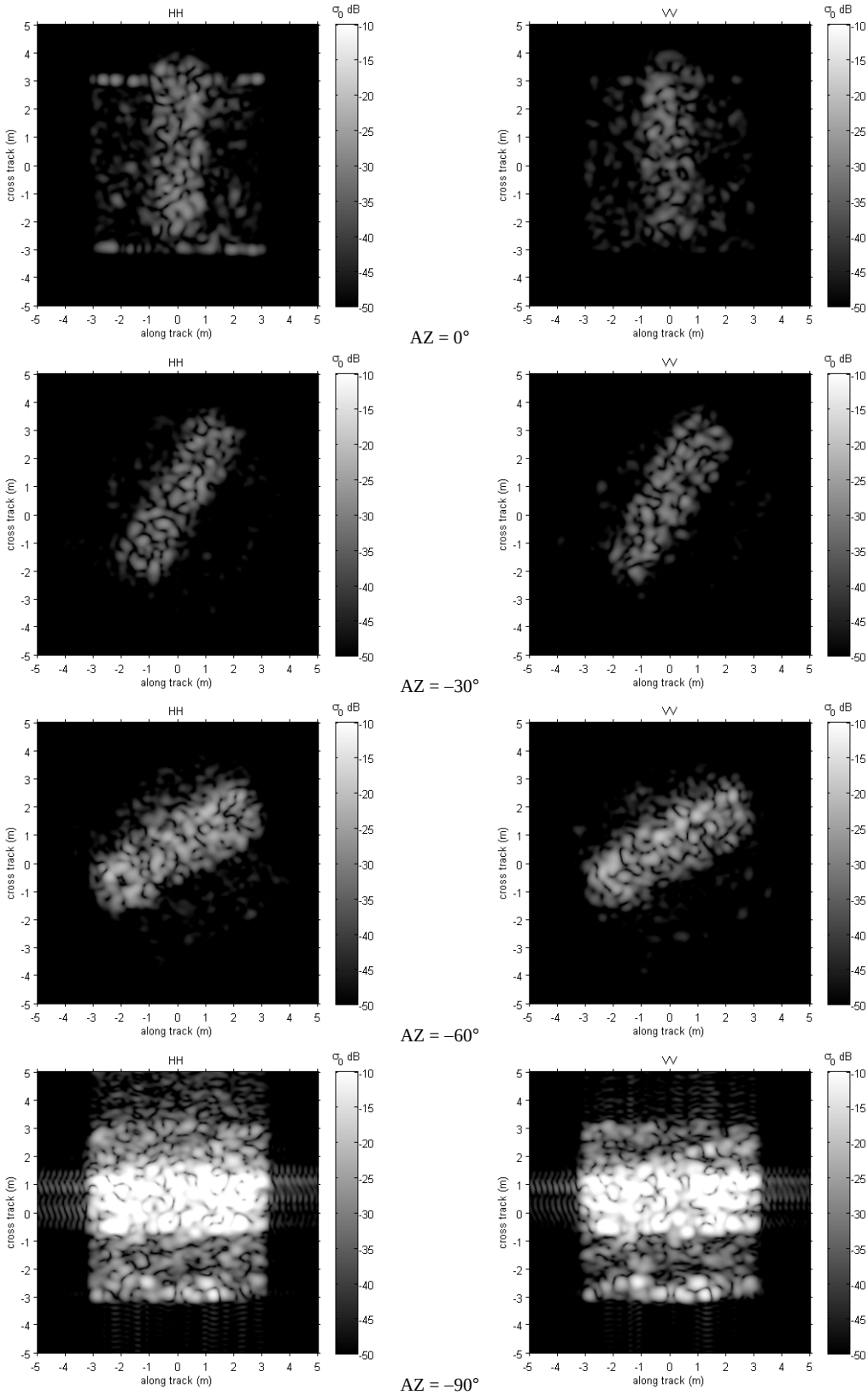

Figure V-8 Crevasse with snow bridge, 0.5-m depth, 8-inch resolution, $f_c = 9.5$ GHz *, 30° depression angle.*

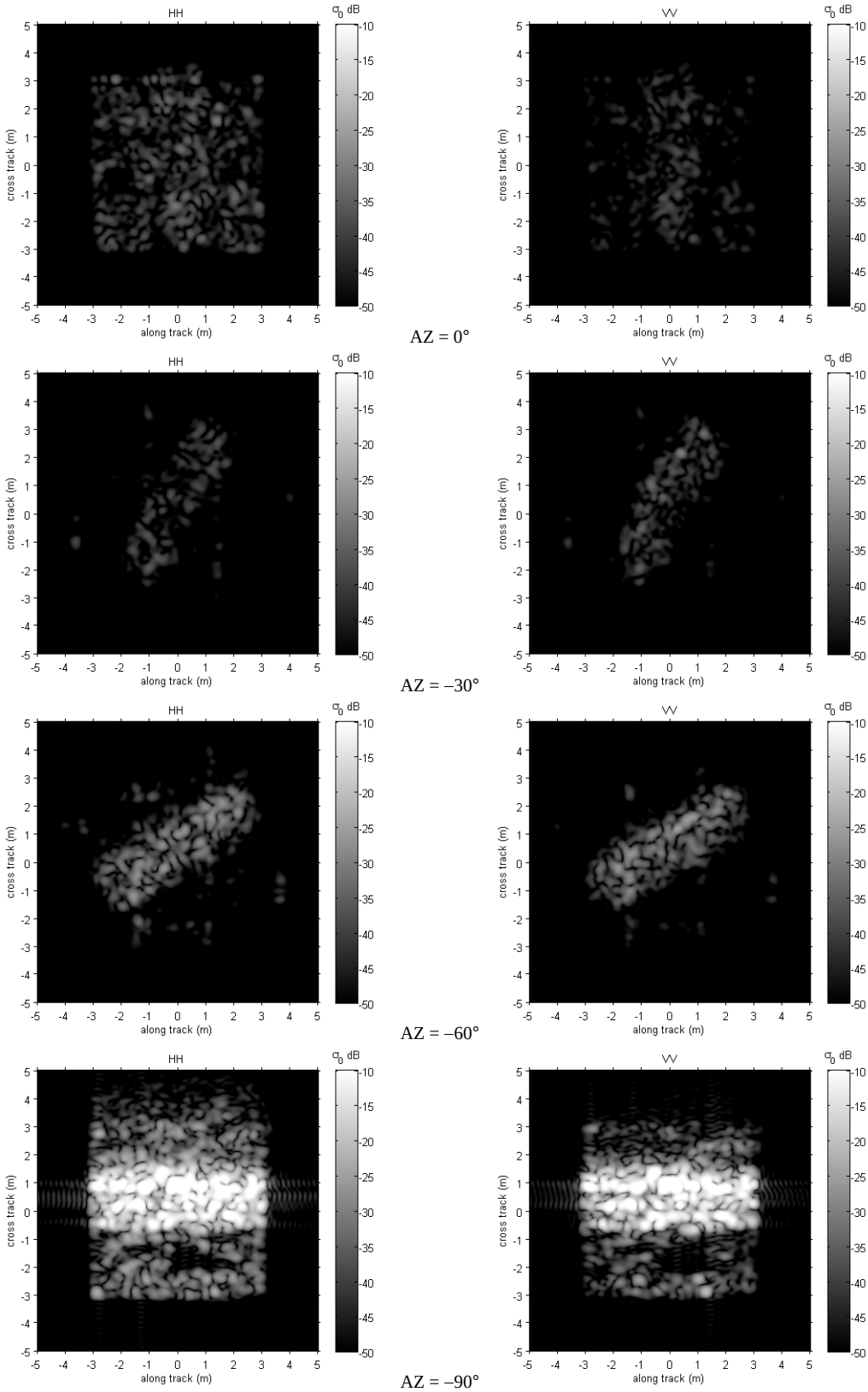

Figure V-9 Crevasse with snow bridge, 0.5-m depth, 8-inch resolution, $f_c = 16.8$ GHz *, 15° depression angle.*

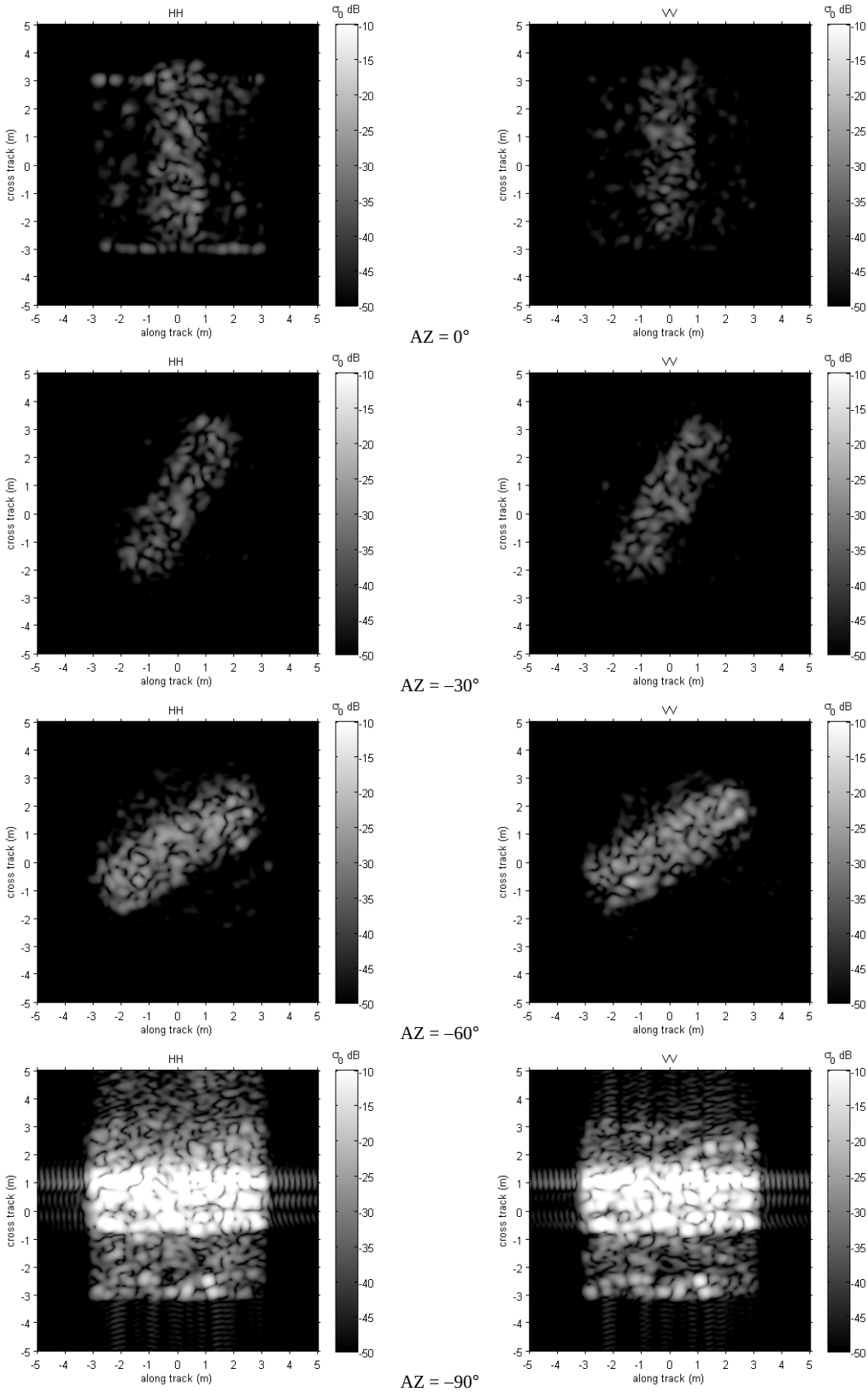

Figure V-10 Crevasse with snow bridge, 0.5-m depth, 8-inch resolution, $f_c = 16.8$ GHz *, 30° depression angle.*

Square root of magnitude (4th root of power), crevasse with snow bridge, 0.5-m depth

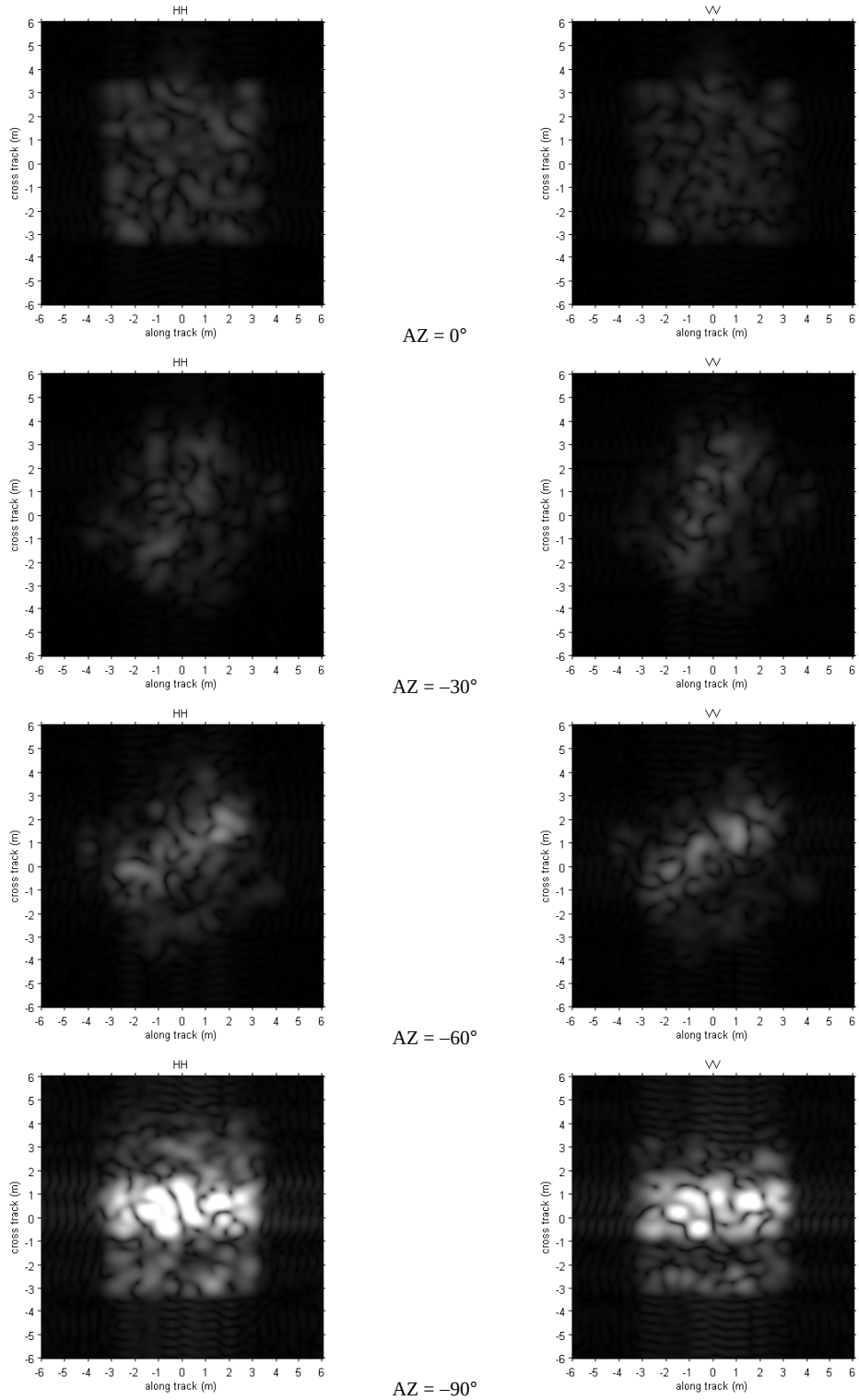

Figure V-11 Crevasse with snow bridge, 0.5-m depth, 18-inch resolution, $f_c = 5.45$ GHz *, 15° depression angle.*

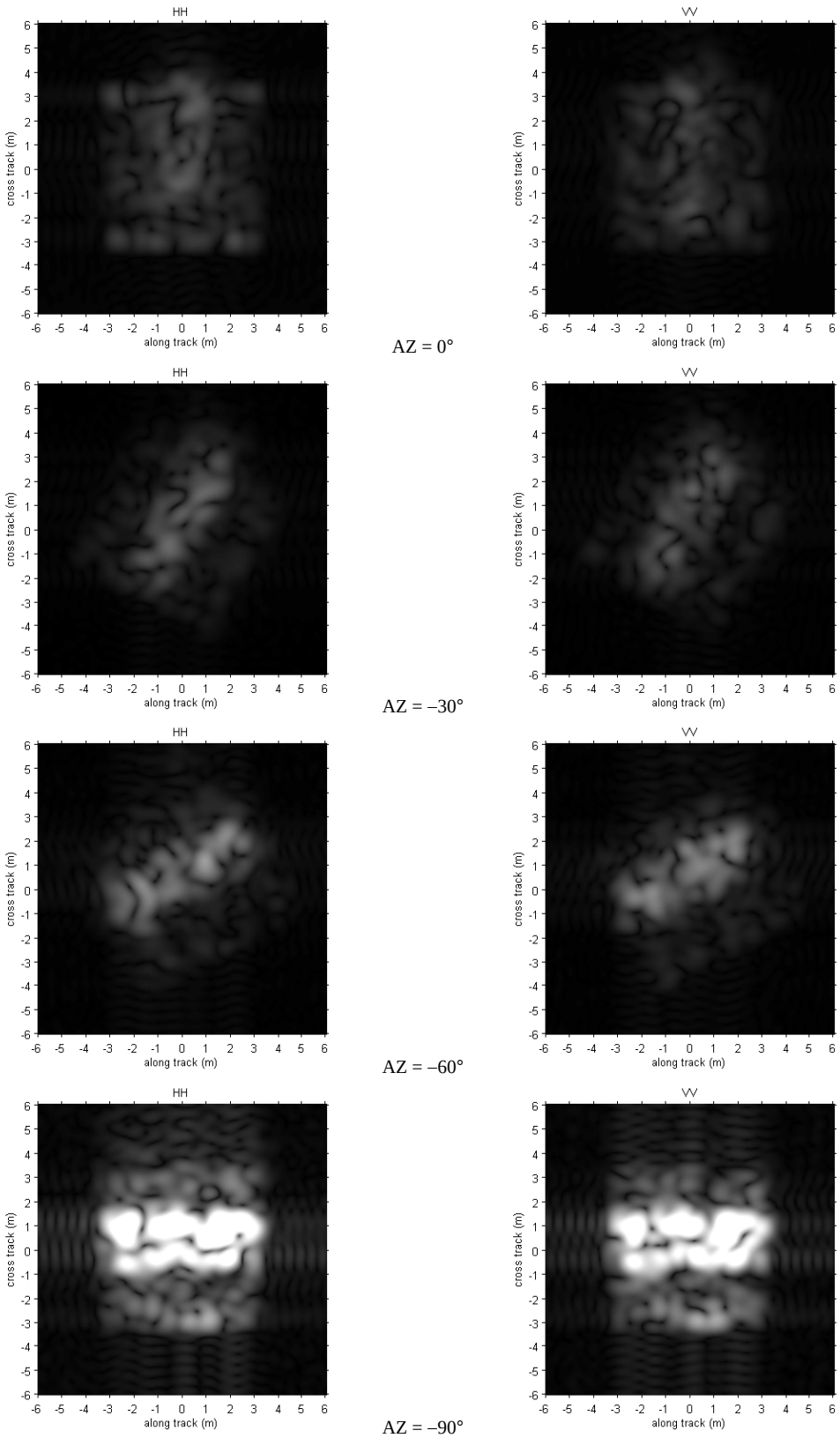

Figure V-12 Crevasse with snow bridge, 0.5-m depth, 18-inch resolution, $f_c = 5.45$ GHz *, 30° depression angle.*

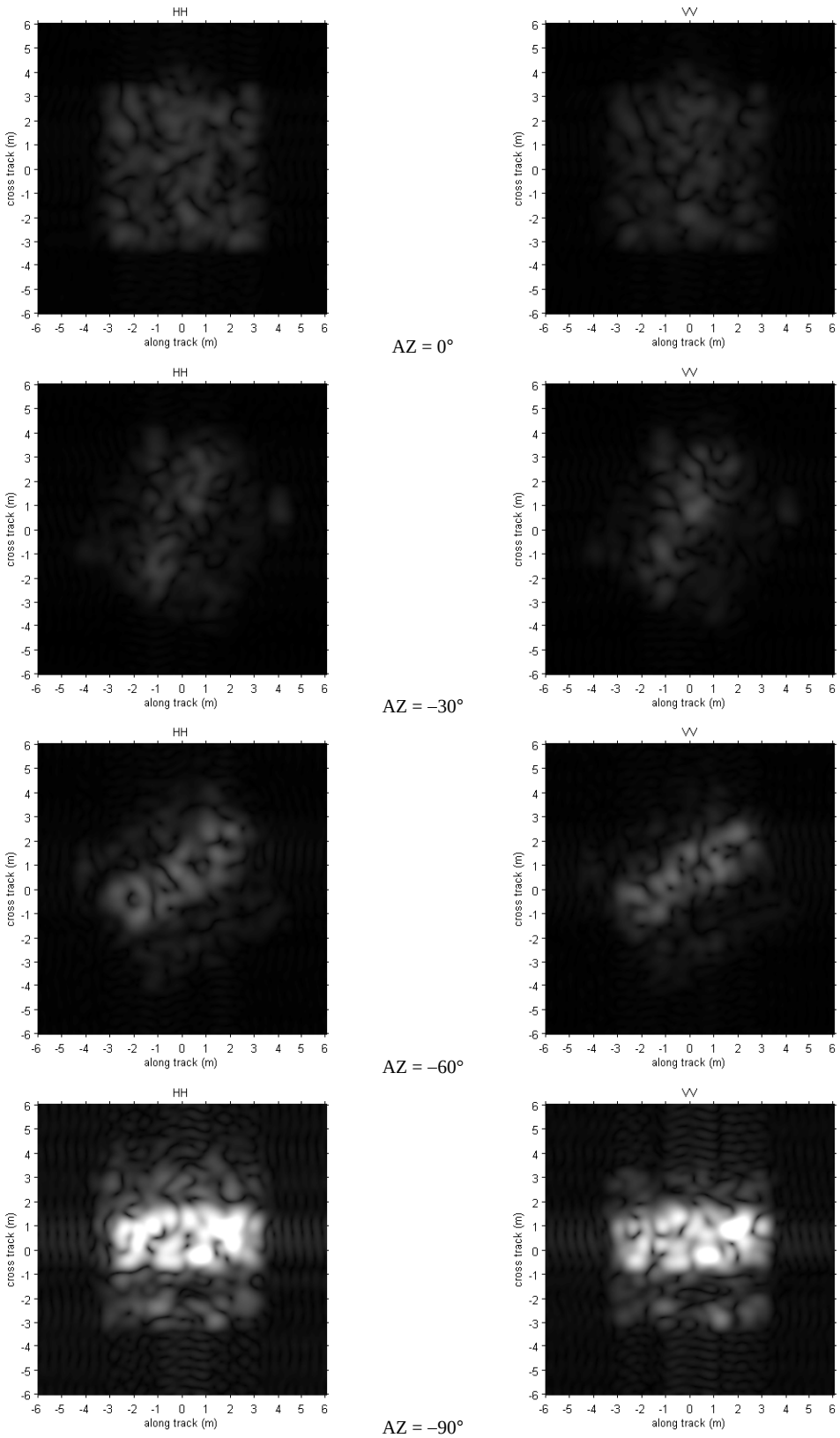

Figure V-13 Crevasse with snow bridge, 0.5-m depth, 18-inch resolution, $f_c = 9.5$ GHz *, 15° depression angle.*

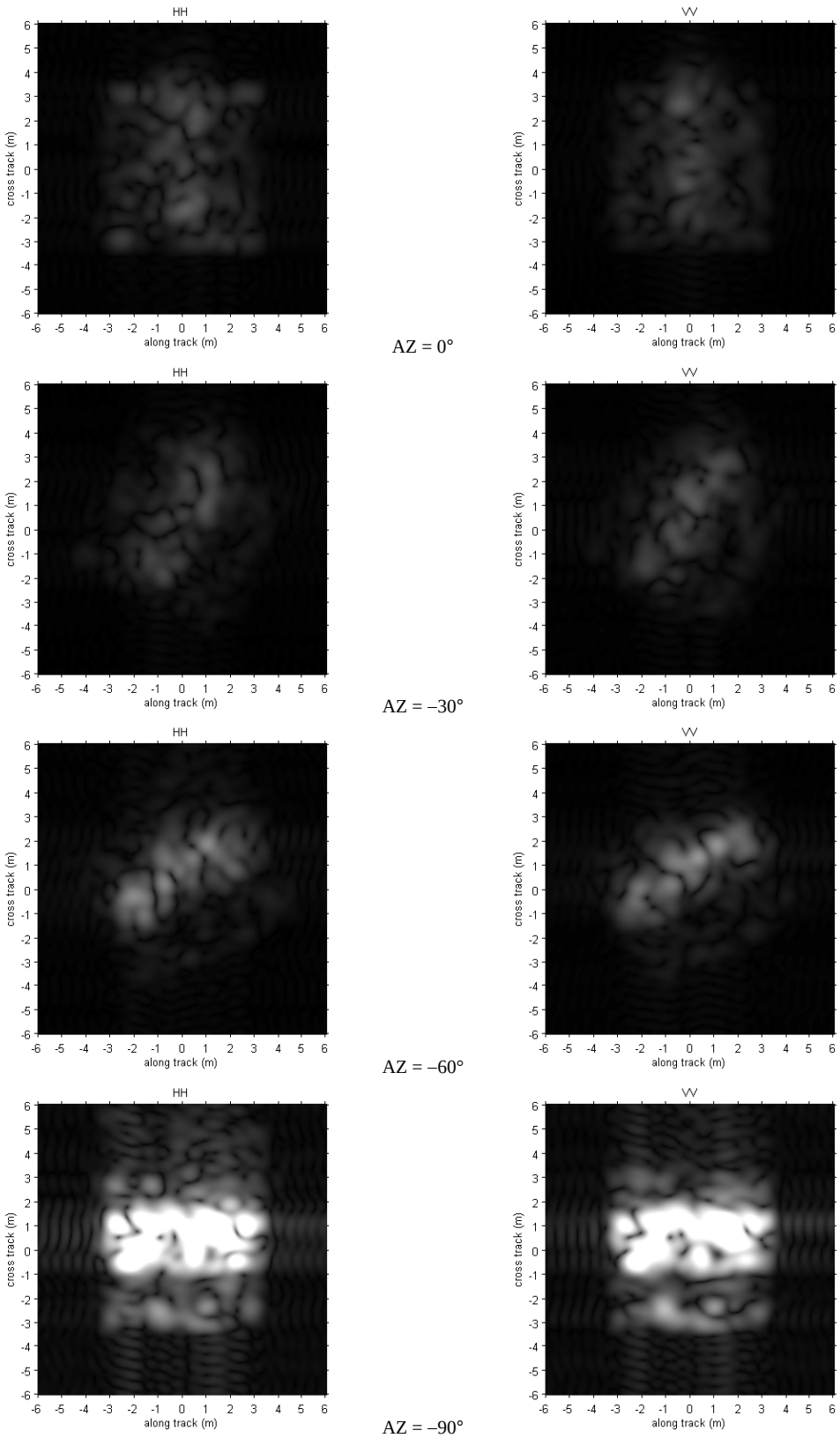

Figure V-14 Crevasse with snow bridge, 0.5-m depth, 18-inch resolution, $f_c = 9.5$ GHz *, 30° depression angle.*

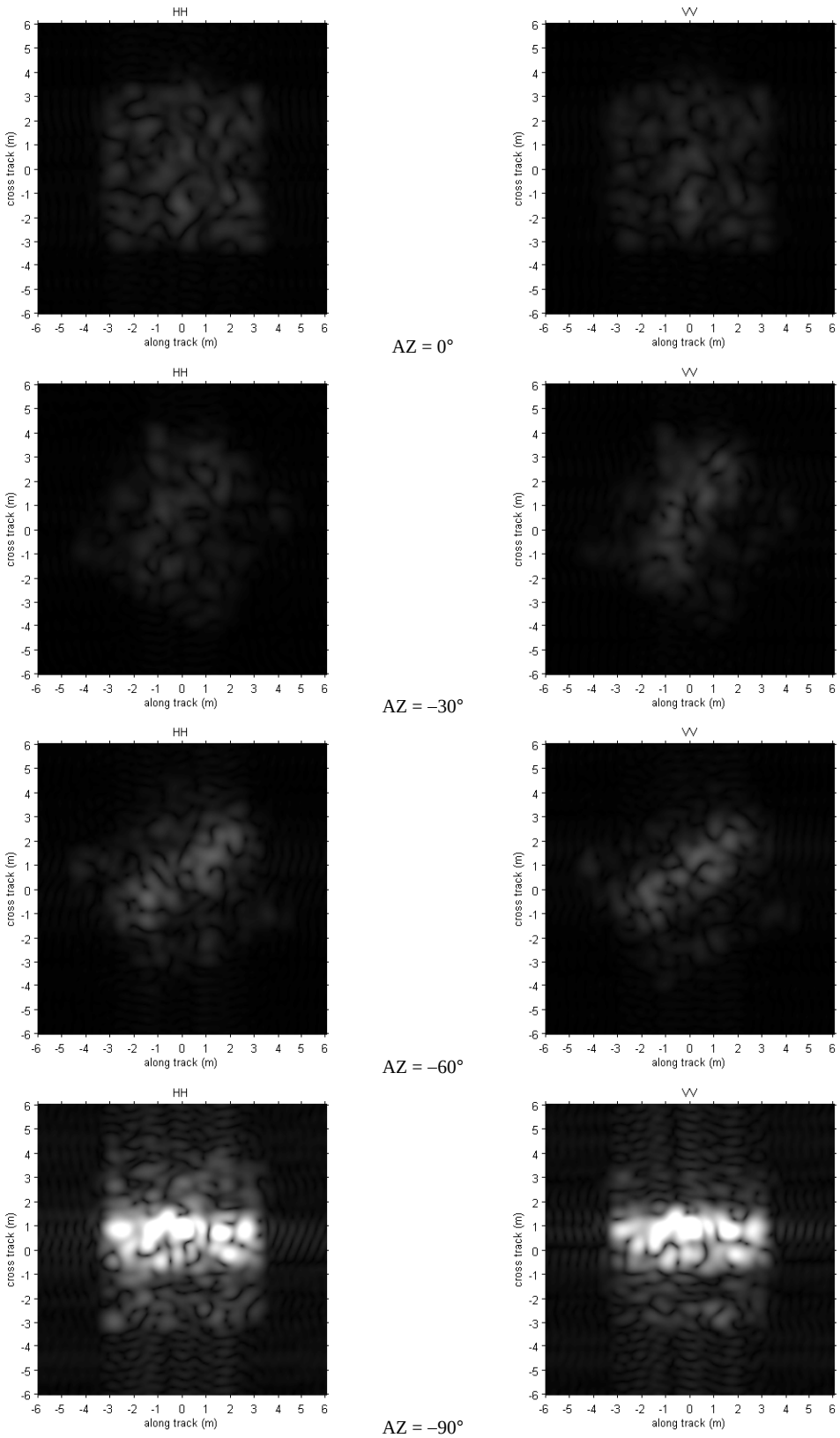

Figure V-15 Crevasse with snow bridge, 0.5-m depth, 18-inch resolution, $f_c = 16.8$ GHz *, 15° depression angle.*

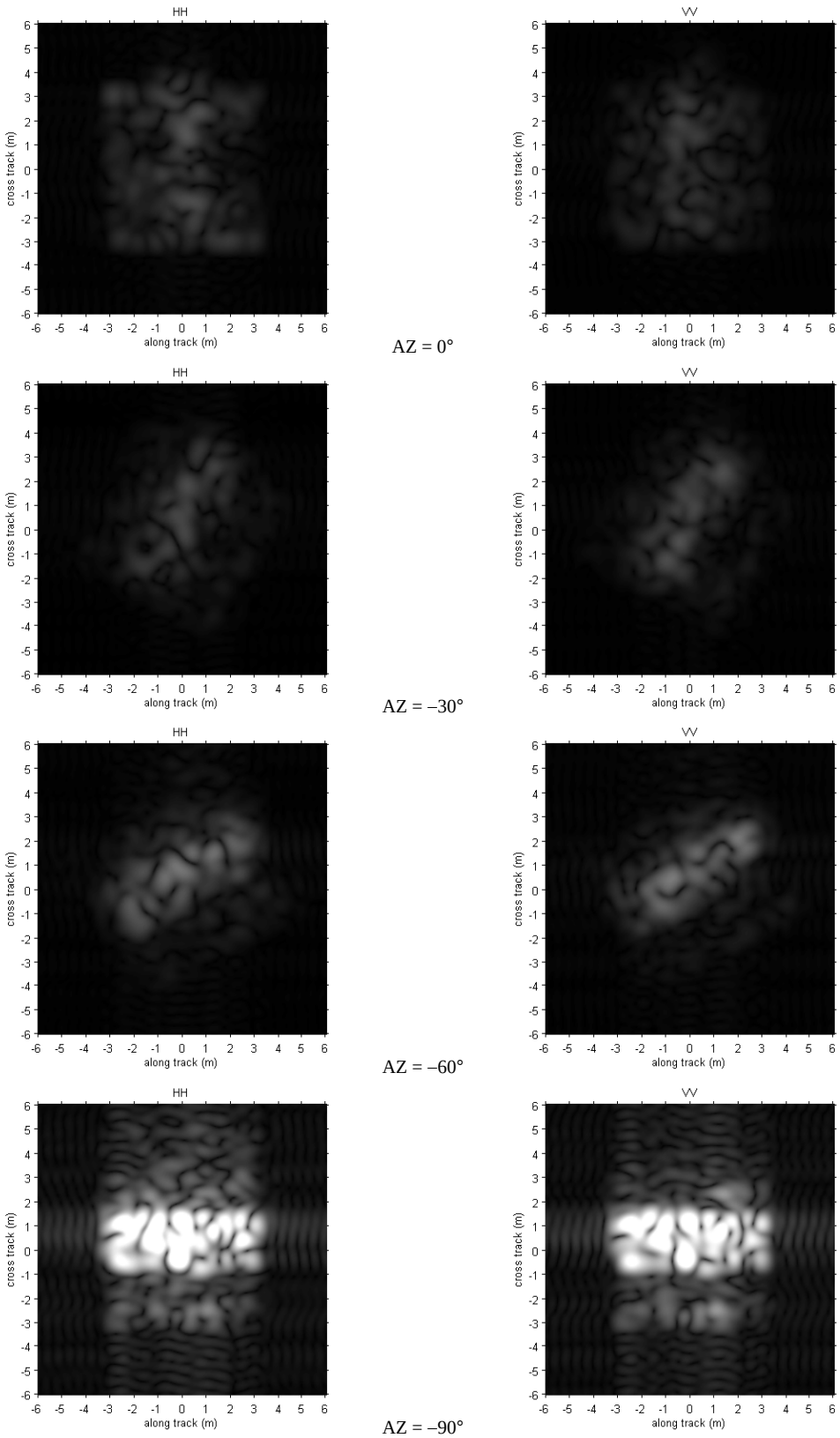

Figure V-16 Crevasse with snow bridge, 0.5-m depth, 18-inch resolution, $f_c = 16.8$ GHz *, 30° depression angle.*

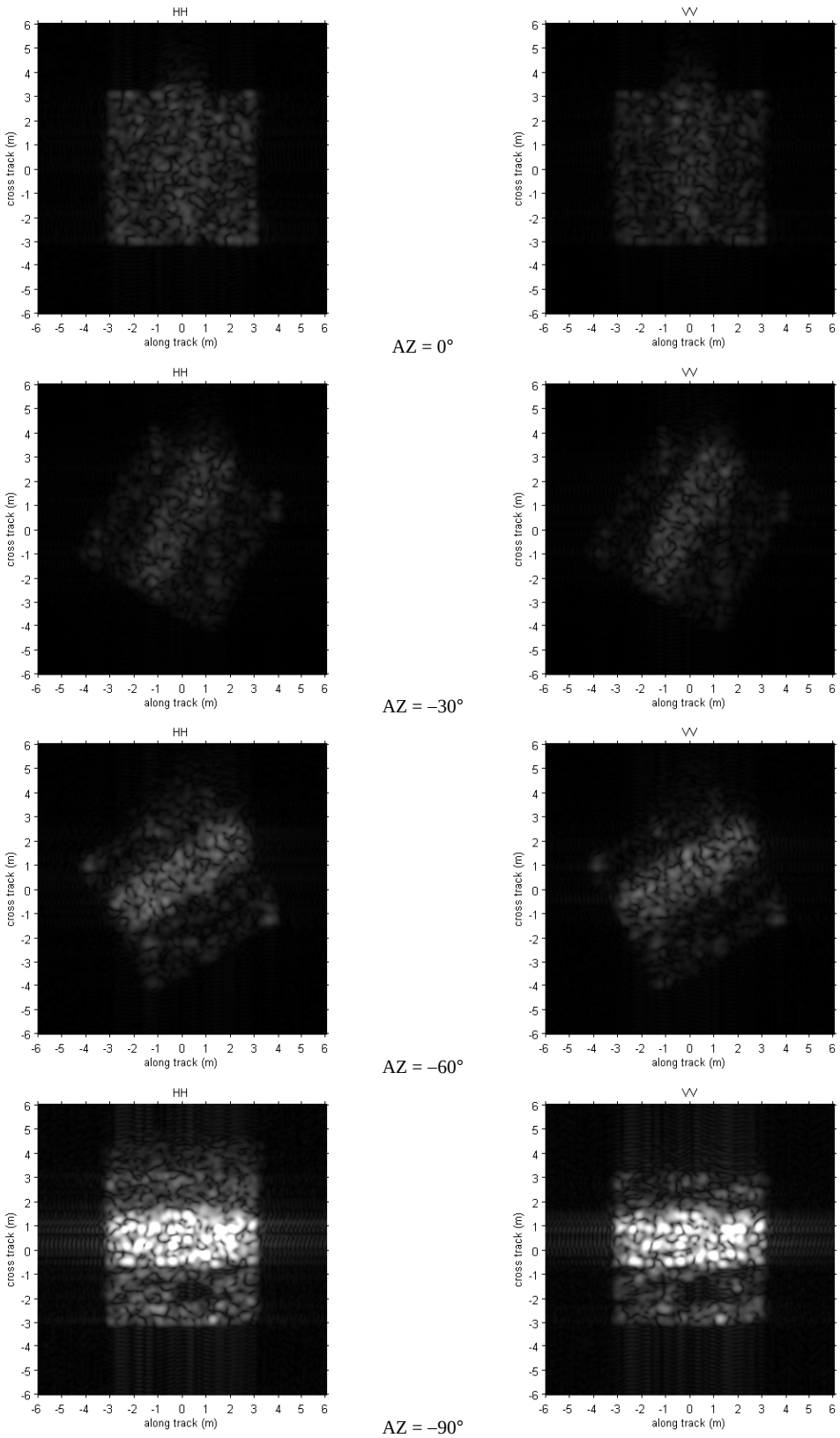

Figure V-17 Crevasse with snow bridge, 0.5-m depth, 8-inch resolution, $f_c = 9.5$ GHz *, 15° depression angle.*

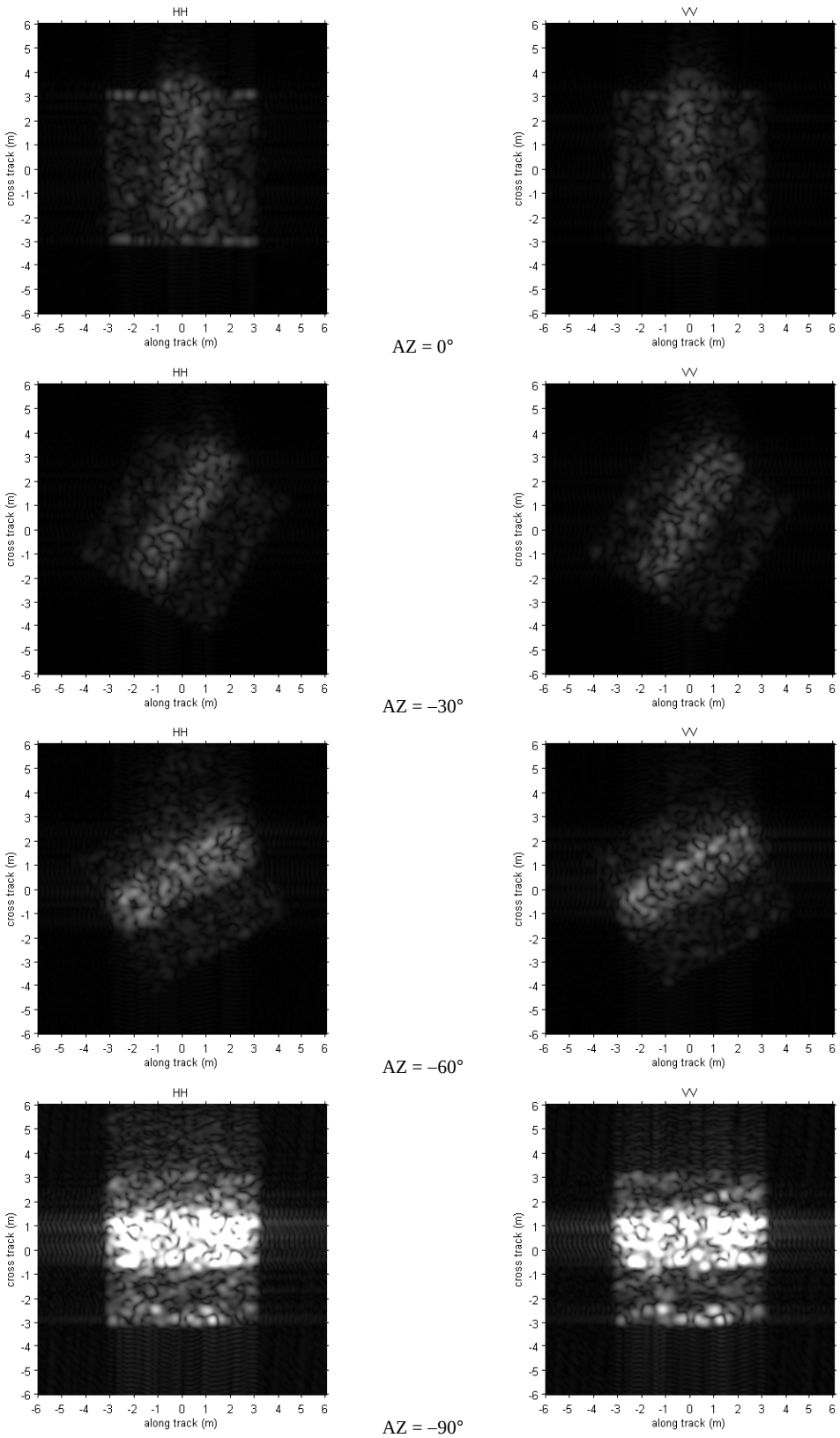

Figure V-18 Crevasse with snow bridge, 0.5-m depth, 8-inch resolution, $f_c = 9.5$ GHz *, 30° depression angle.*

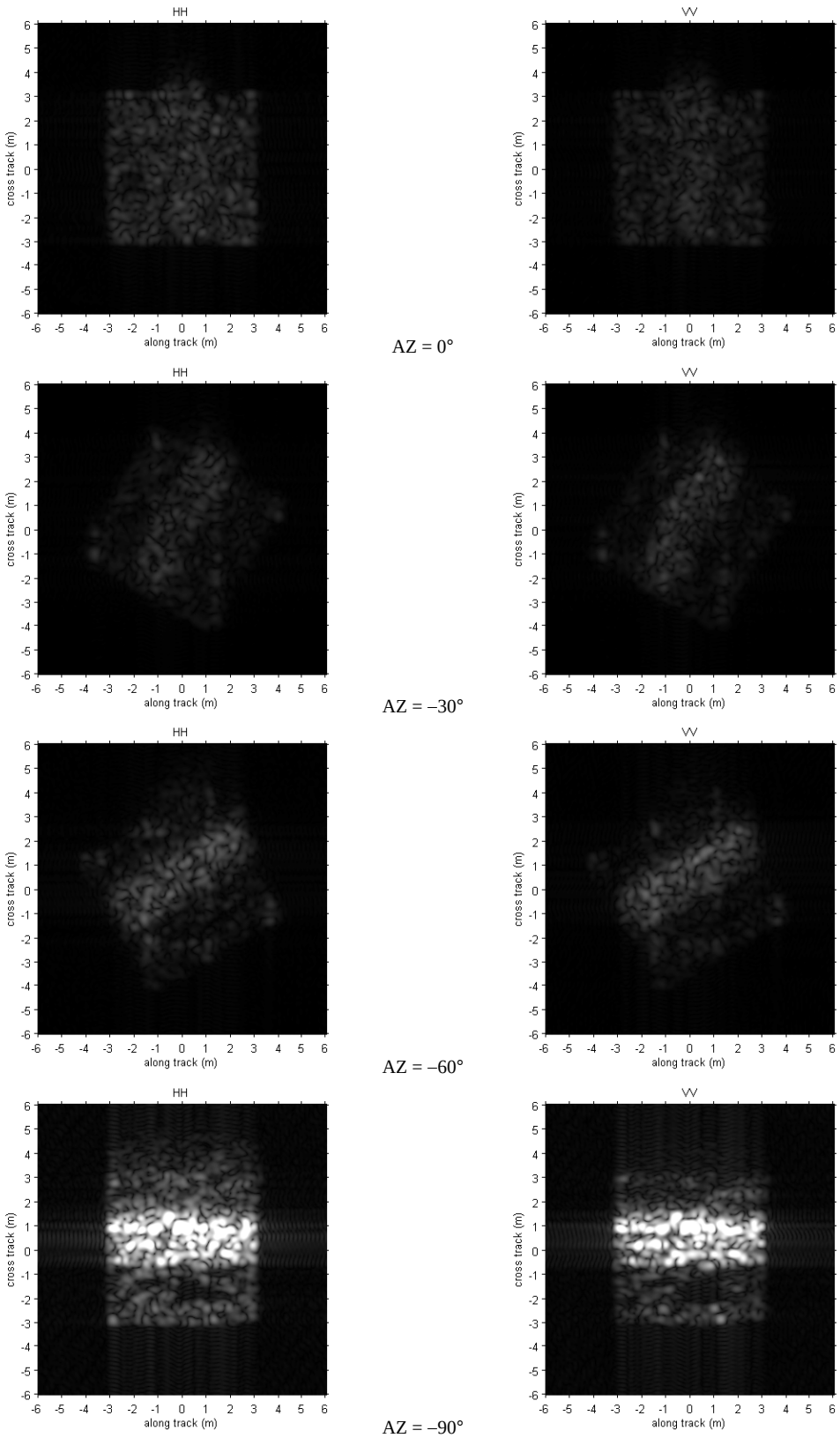

Figure V-19 Crevasse with snow bridge, 0.5-m depth, 8-inch resolution, $f_c = 16.8$ GHz *, 15° depression angle.*

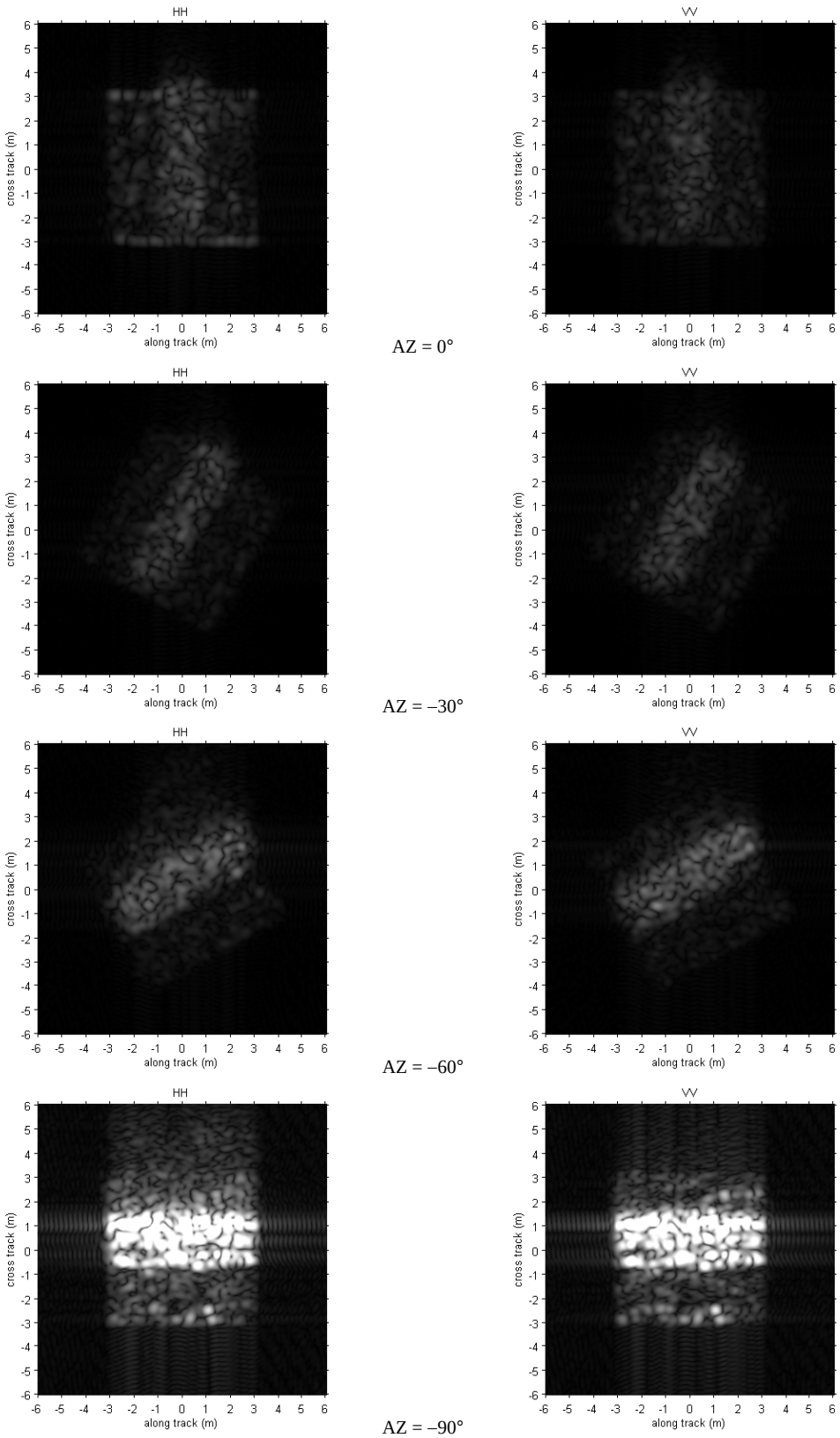

Figure V-20 Crevasse with snow bridge, 0.5-m depth, 8-inch resolution, $f_c = 16.8$ GHz *, 30° depression angle.*

Color, snow-bridge depth is 0.5 m

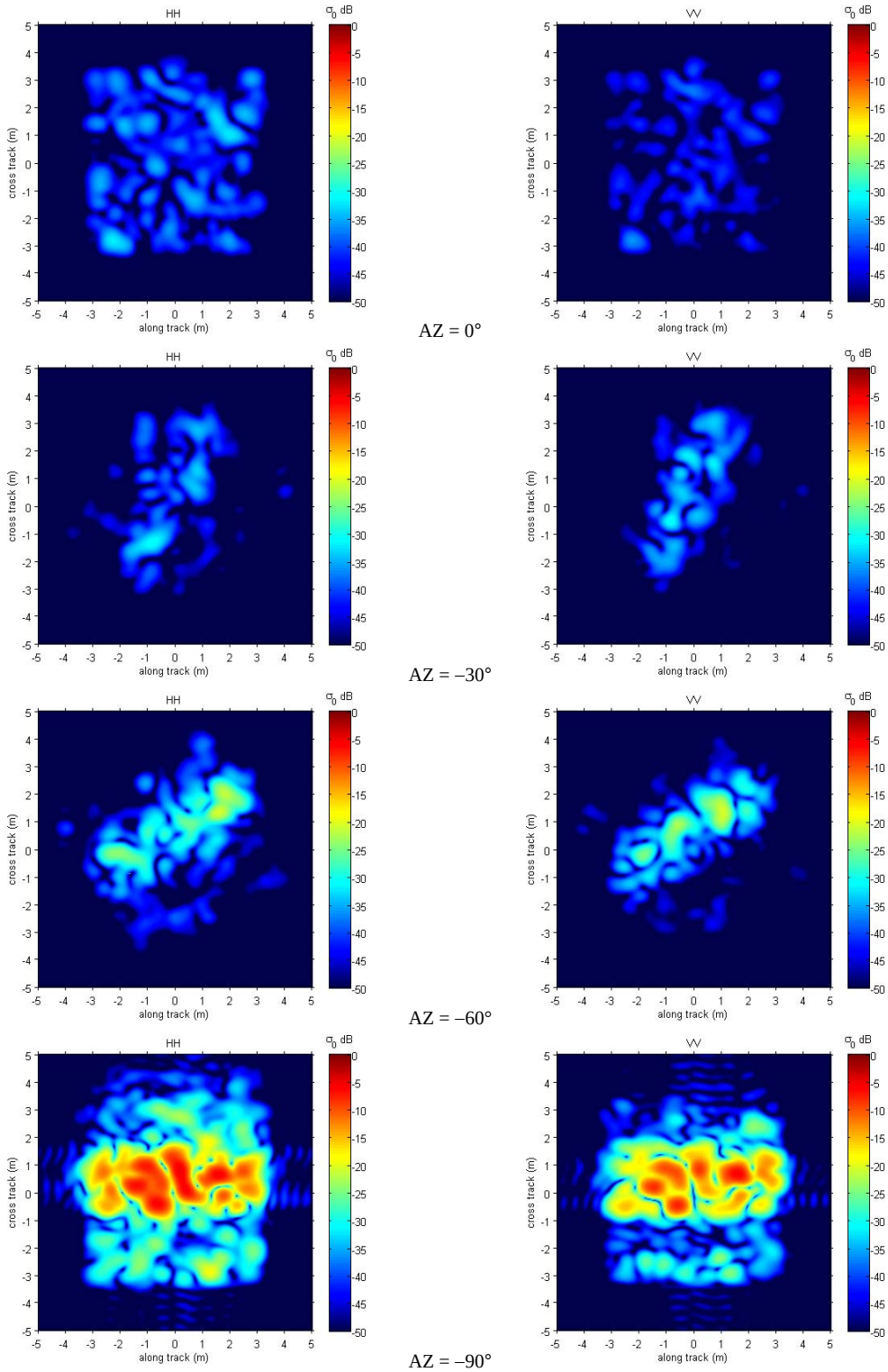

Figure V-21 Crevasse with snow bridge, 0.5-m depth, 18-inch resolution, $f_c = 5.45$ GHz *, 15° depression angle.*

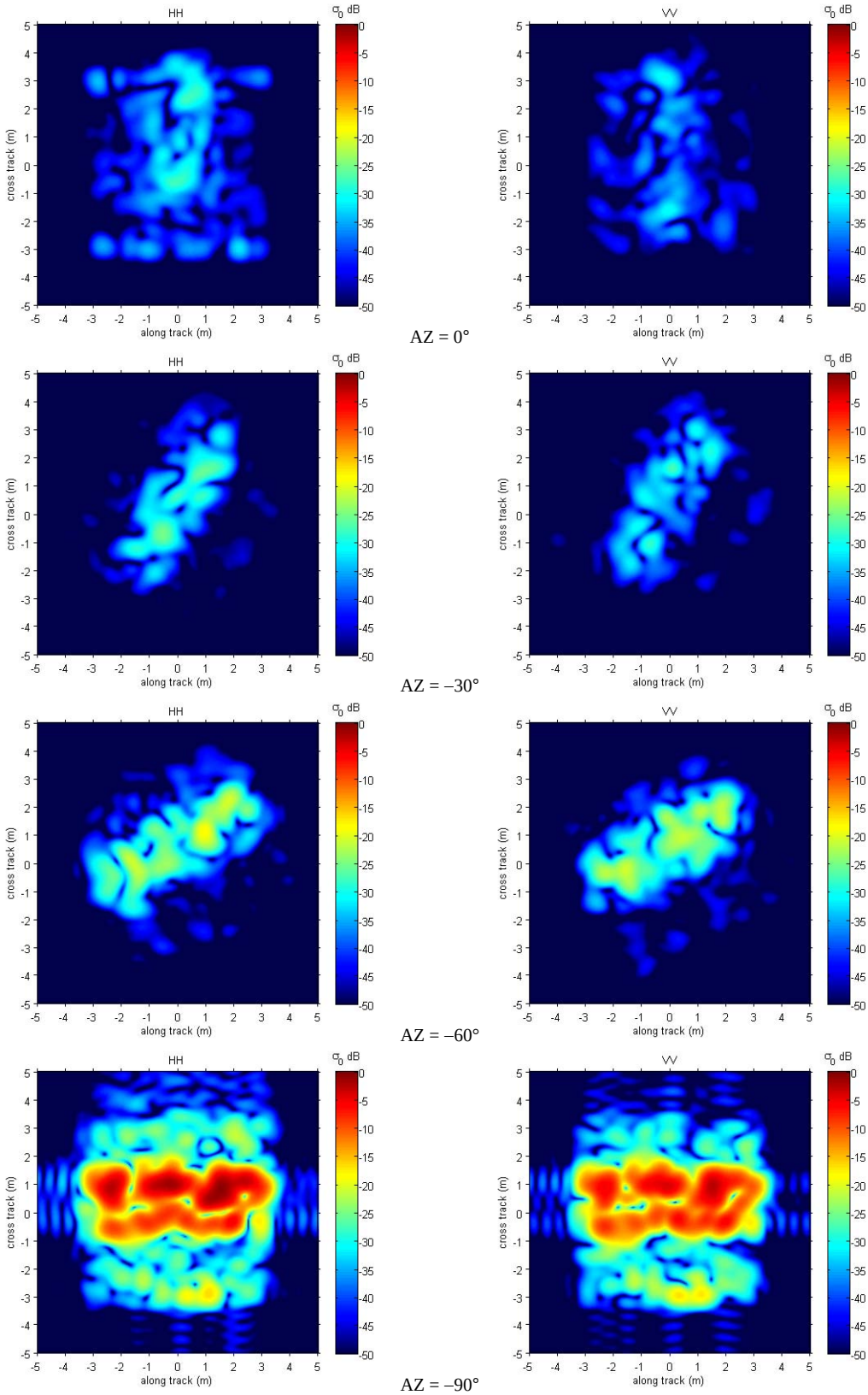

Figure V-22 Crevasse with snow bridge, 0.5-m depth, 18-inch resolution, $f_c = 5.45$ GHz *, 30° depression angle.*

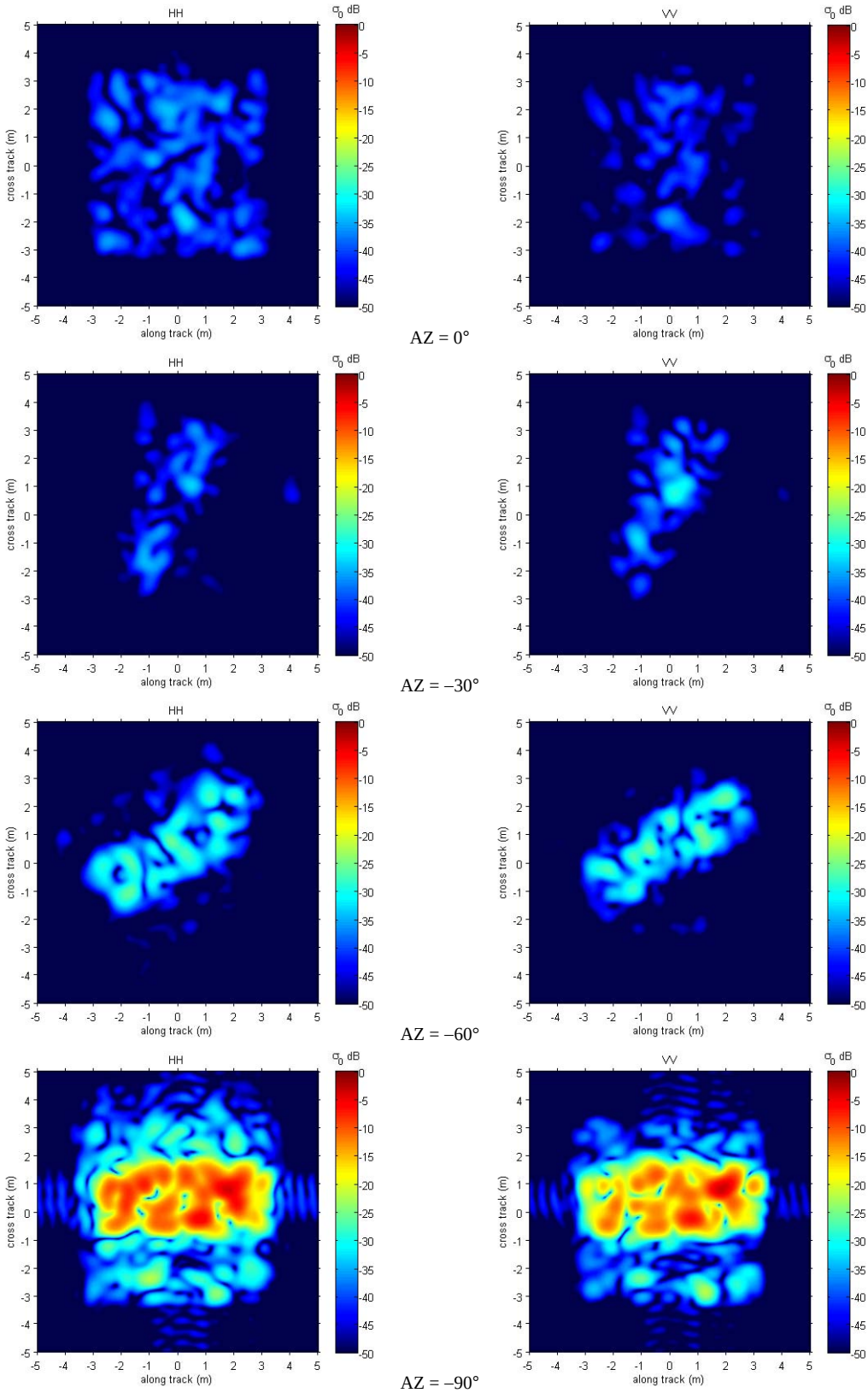

Figure V-23 Crevasse with snow bridge, 0.5-m depth, 18-inch resolution, $f_c = 9.5$ GHz *, 15° depression angle.*

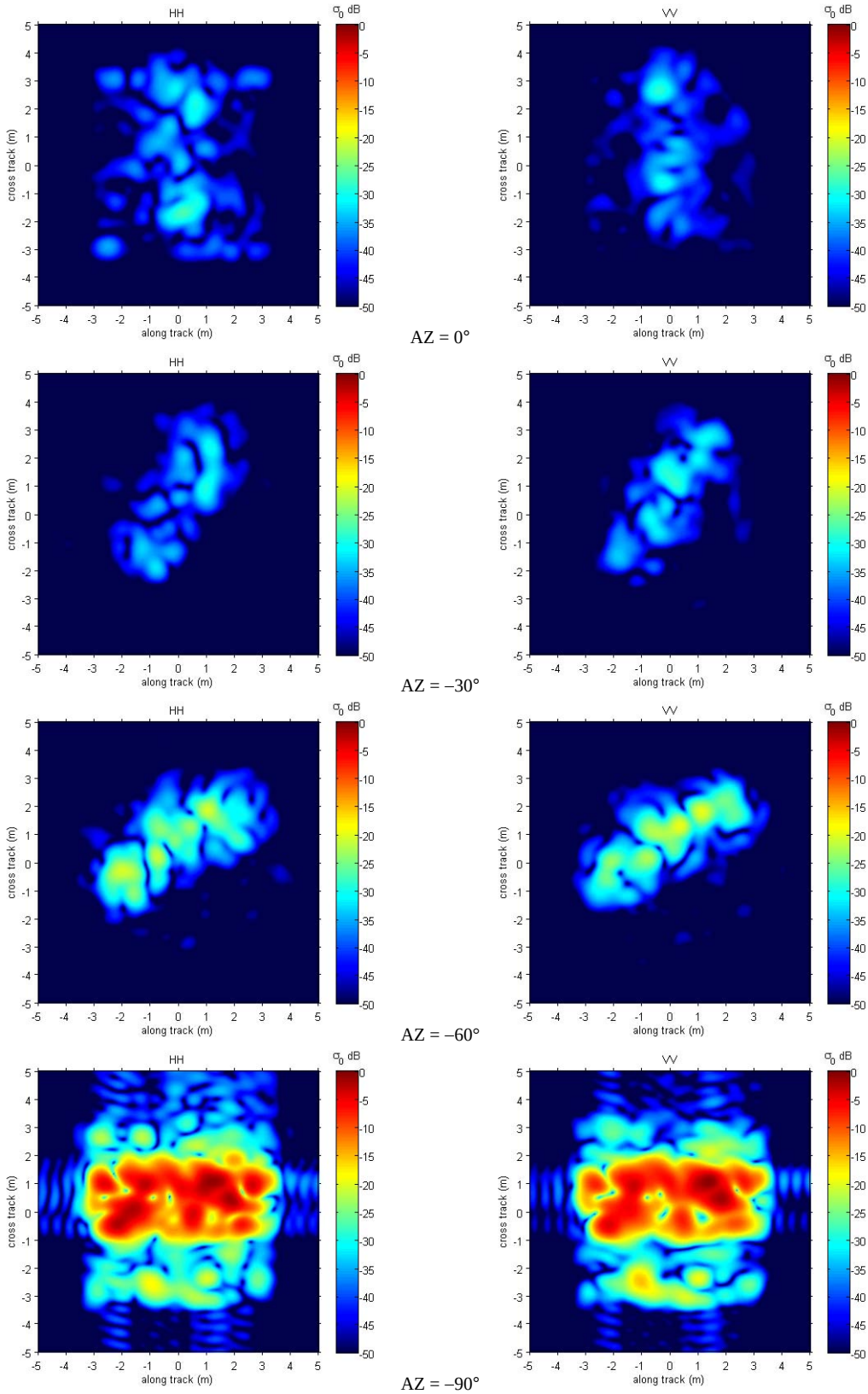

Figure V-24 Crevasse with snow bridge, 0.5-m depth, 18-inch resolution, $f_c = 9.5$ GHz *, 30° depression angle.*

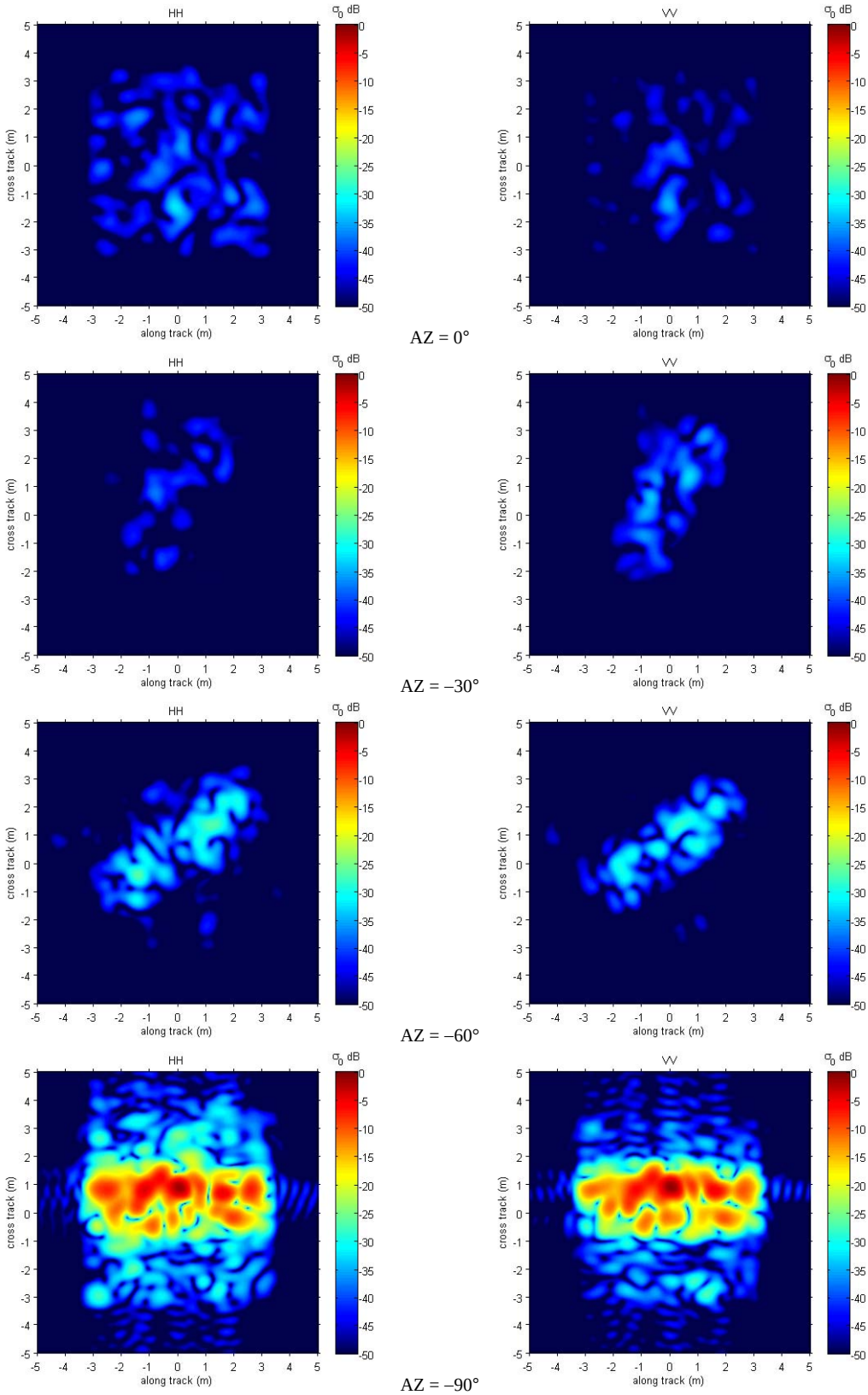

Figure V-25 Crevasse with snow bridge, 0.5-m depth, 18-inch resolution, $f_c = 16.8$ GHz *, 15° depression angle.*

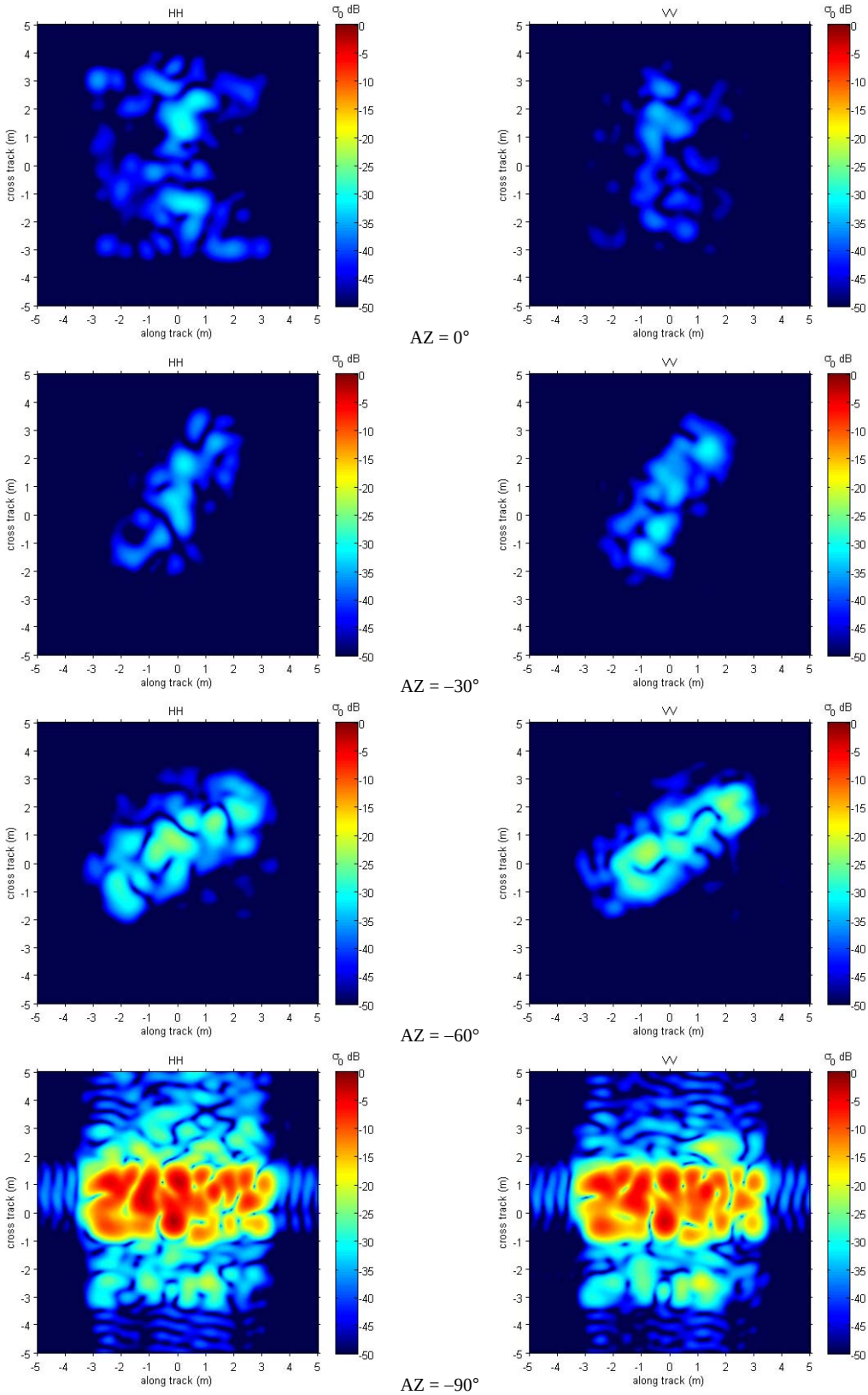

Figure V-26 Crevasse with snow bridge, 0.5-m depth, 18-inch resolution, $f_c = 16.8$ GHz *, 30° depression angle.*

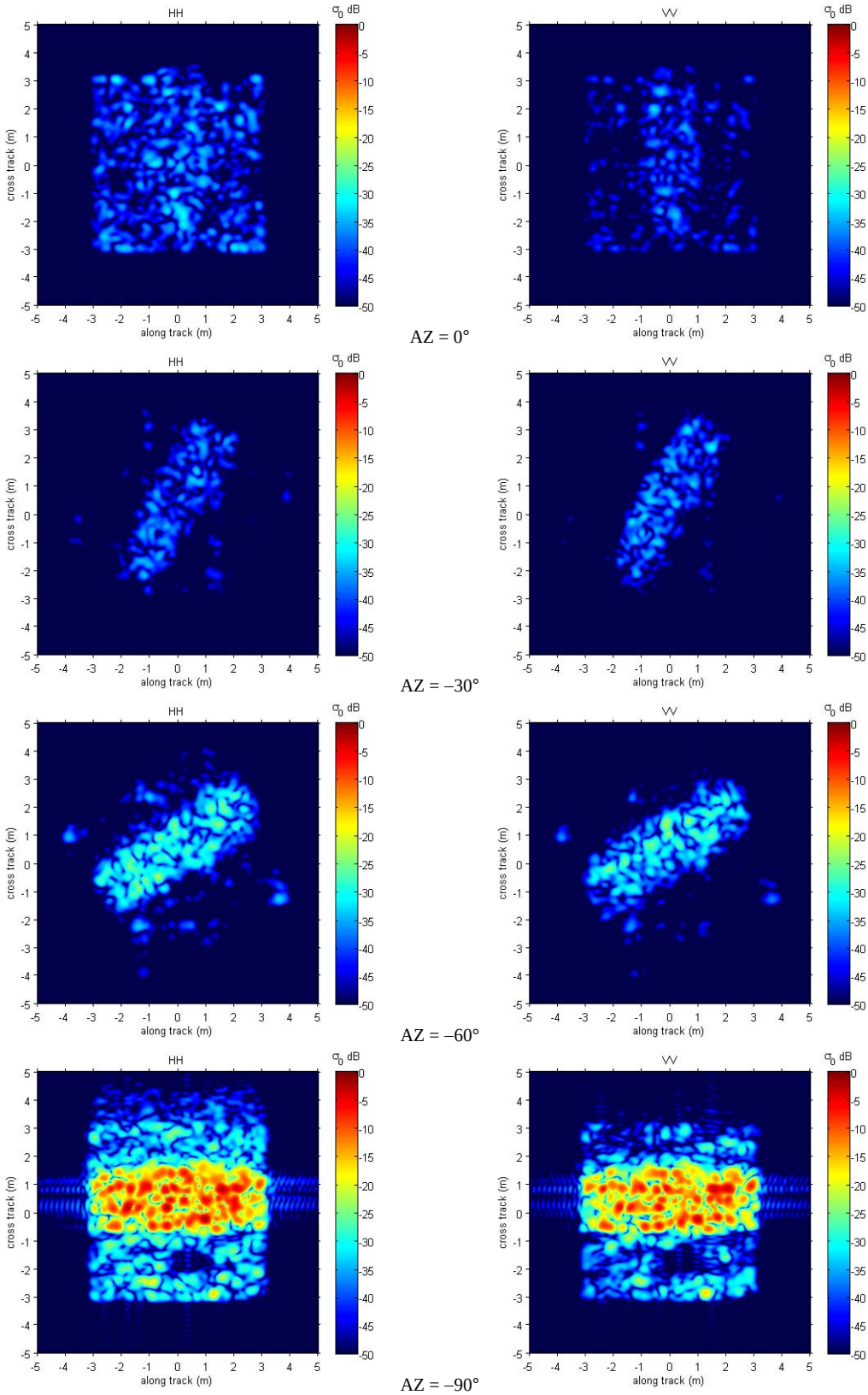

Figure V-27 Crevasse with snow bridge, 0.5-m depth, 8-inch resolution, $f_c = 9.5$ GHz *, 15° depression angle.*

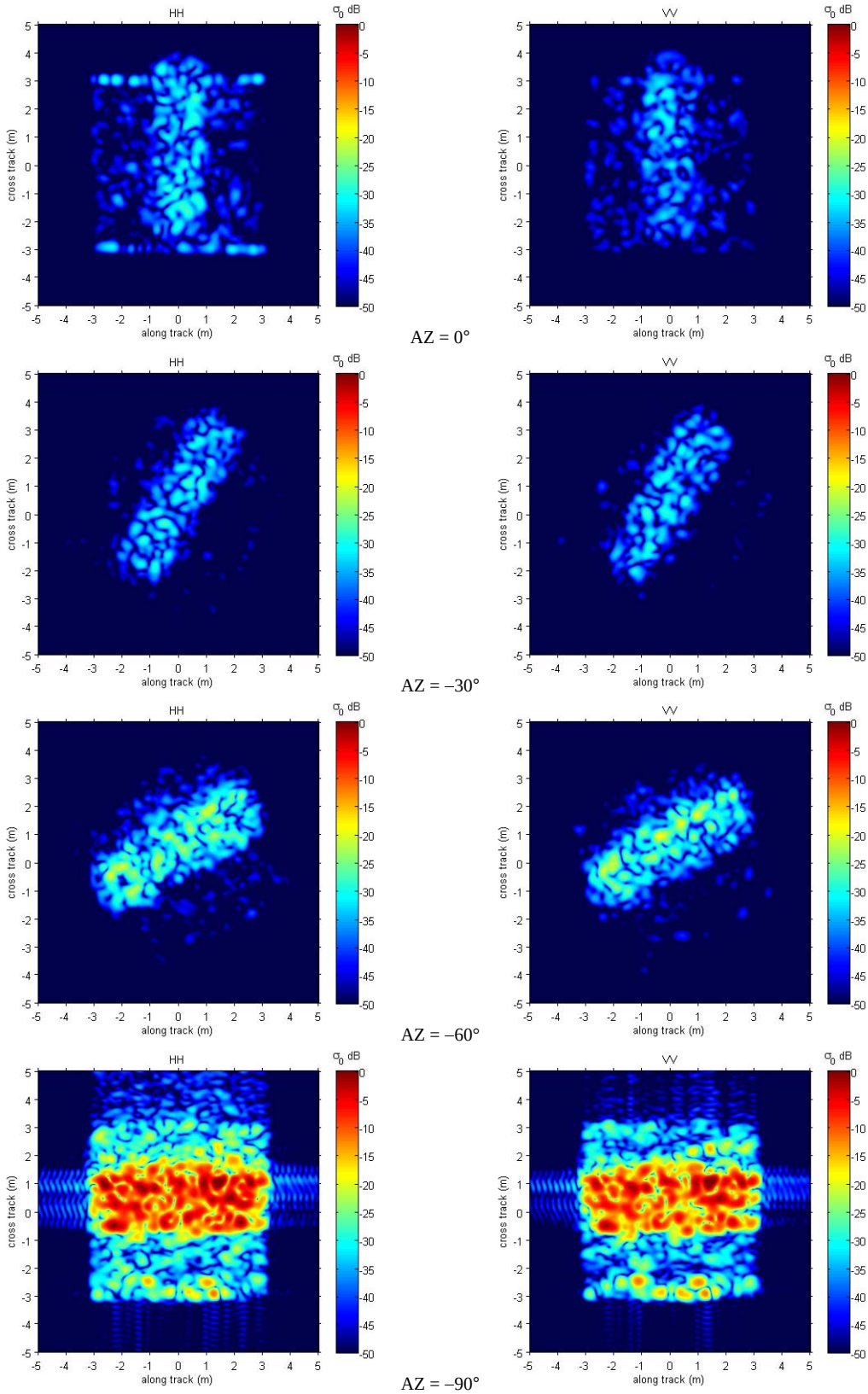

Figure V-28 Crevasse with snow bridge, 0.5-m depth, 8-inch resolution, $f_c = 9.5$ GHz *, 30° depression angle.*

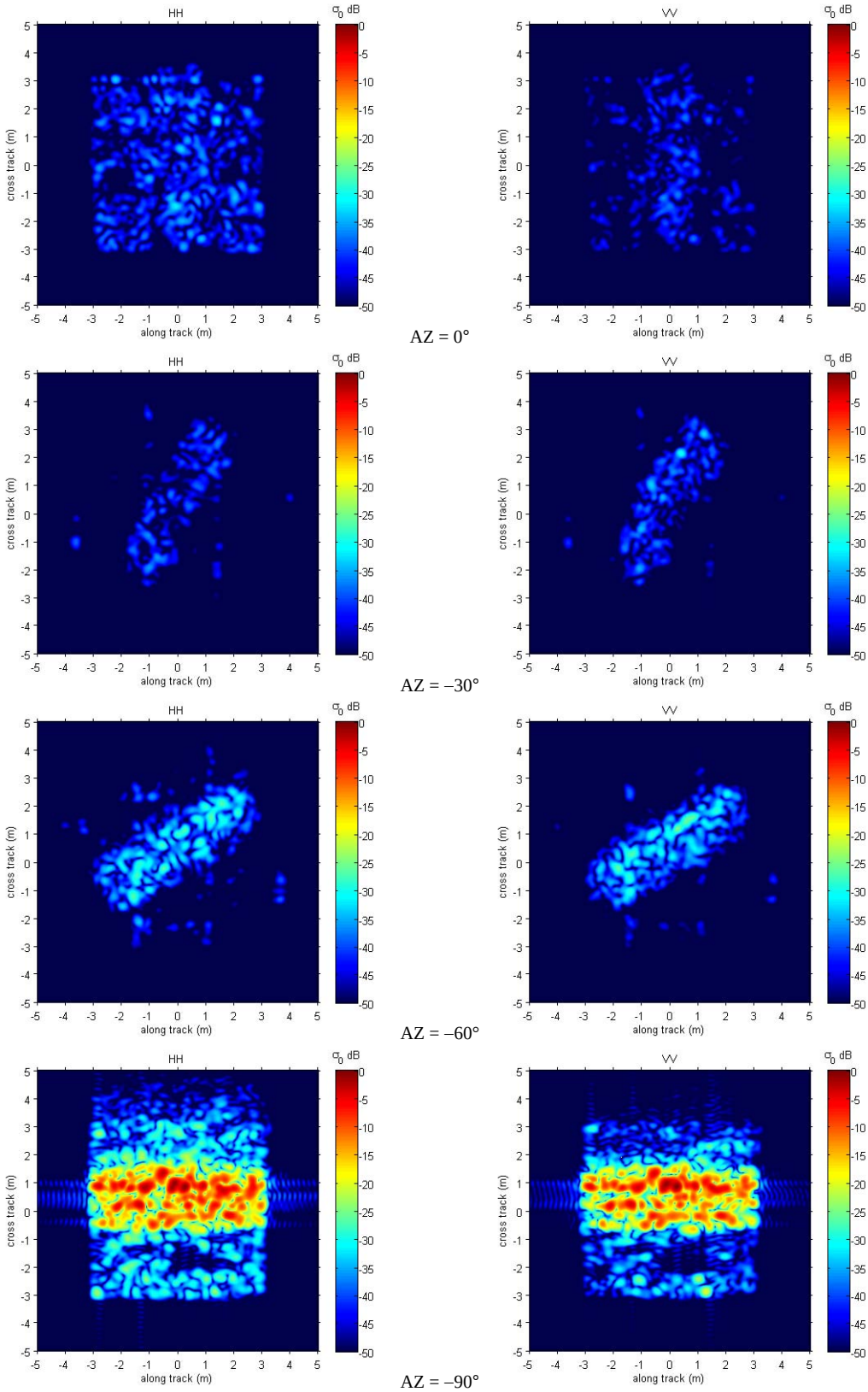

Figure V-29 Crevasse with snow bridge, 0.5-m depth, 8-inch resolution, $f_c = 16.8$ GHz *, 15° depression angle.*

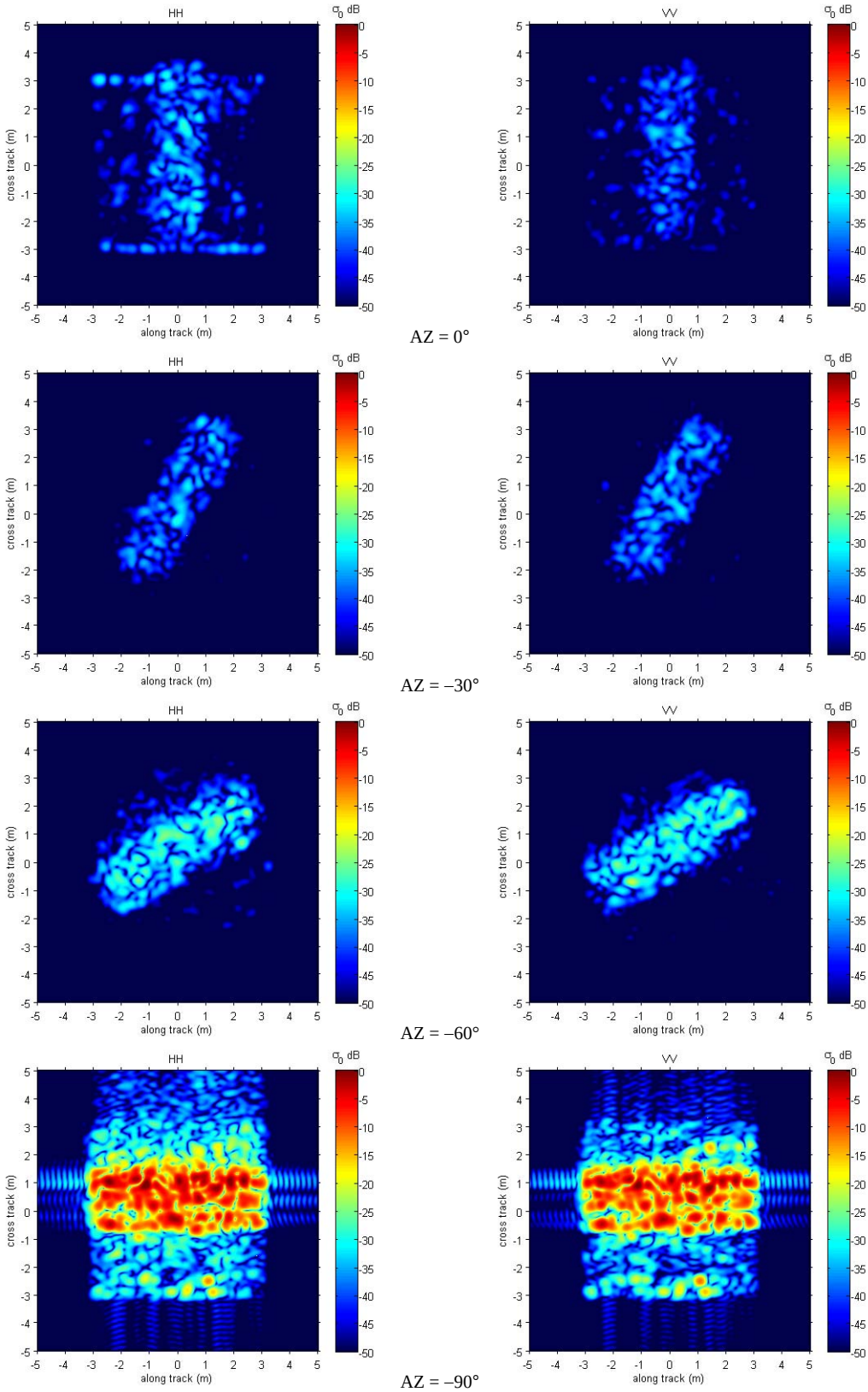

Figure V-30 Crevasse with snow bridge, 0.5-m depth, 8-inch resolution, $f_c = 16.8$ GHz *, 30° depression angle.*

Crevasse with snow bridge, Siple Dome model, 2-m depth

Monochrome, snow-bridge depth is 2.0 m

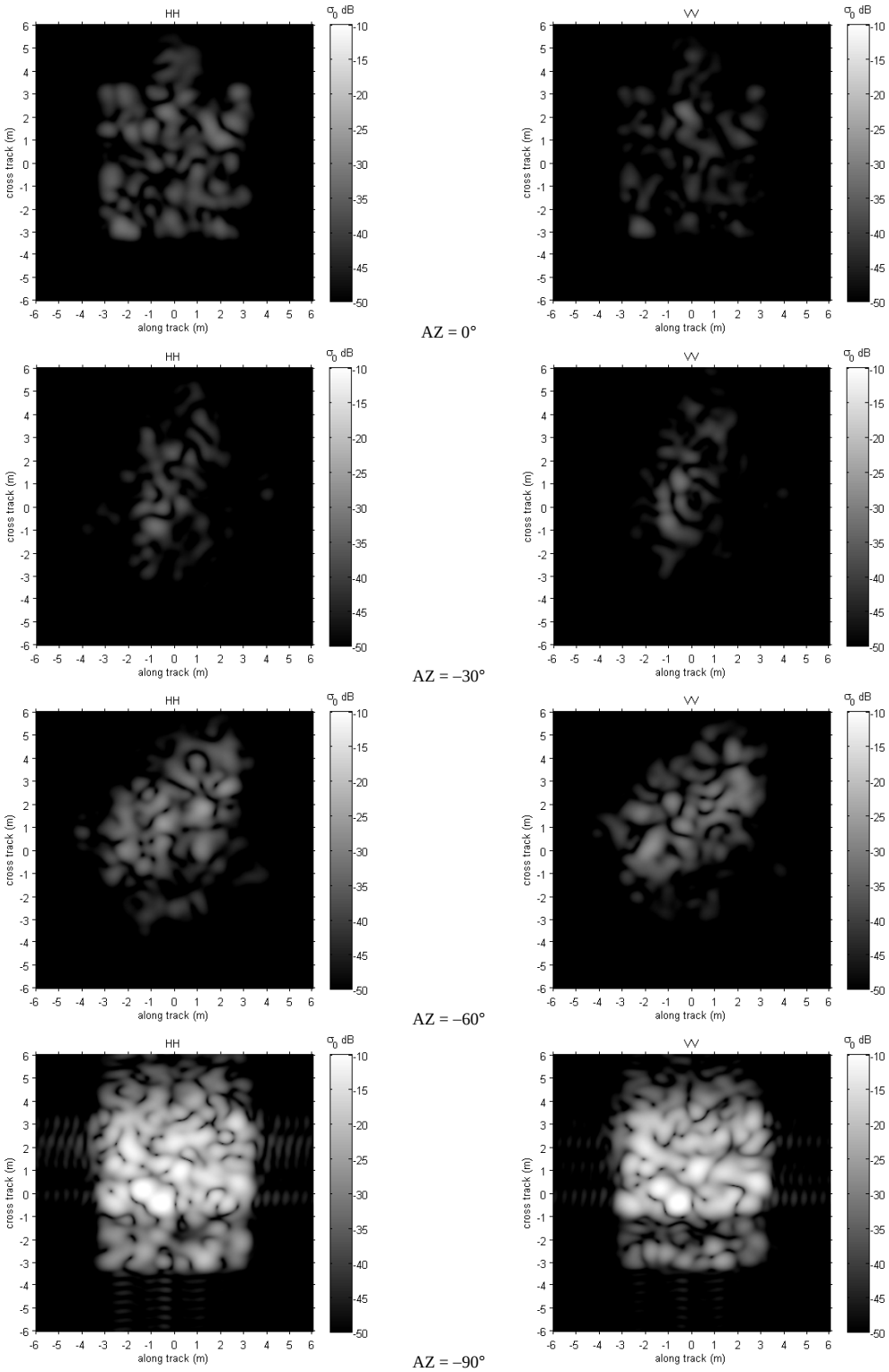

Figure V-31 Crevasse with snow bridge, 2-m depth, 18-inch resolution, $f_c = 5.45$ GHz *, 15° depression angle.*

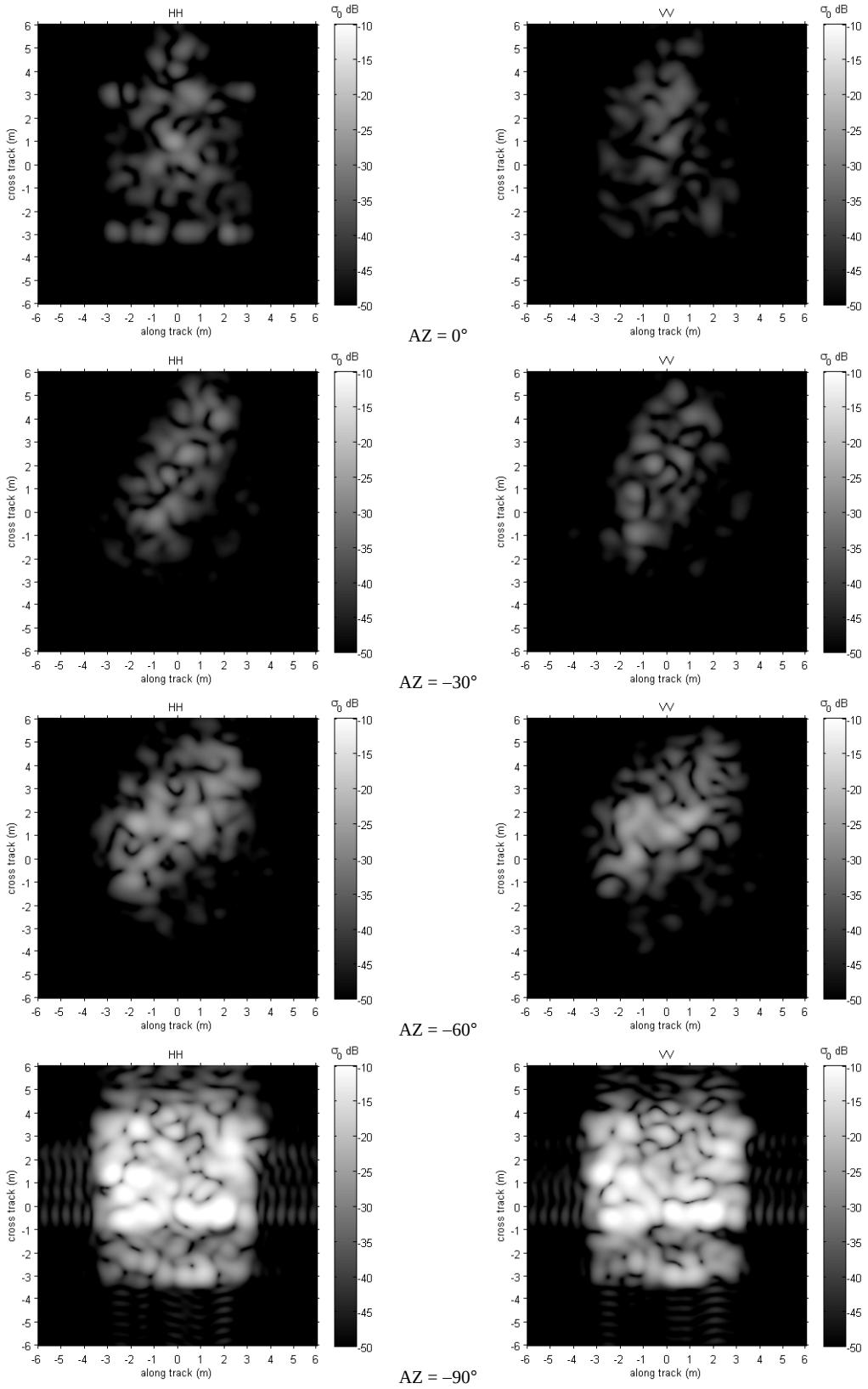

Figure V-32 Crevasse with snow bridge, 2-m depth, 18-inch resolution, $f_c = 5.45$ GHz *, 30° depression angle.*

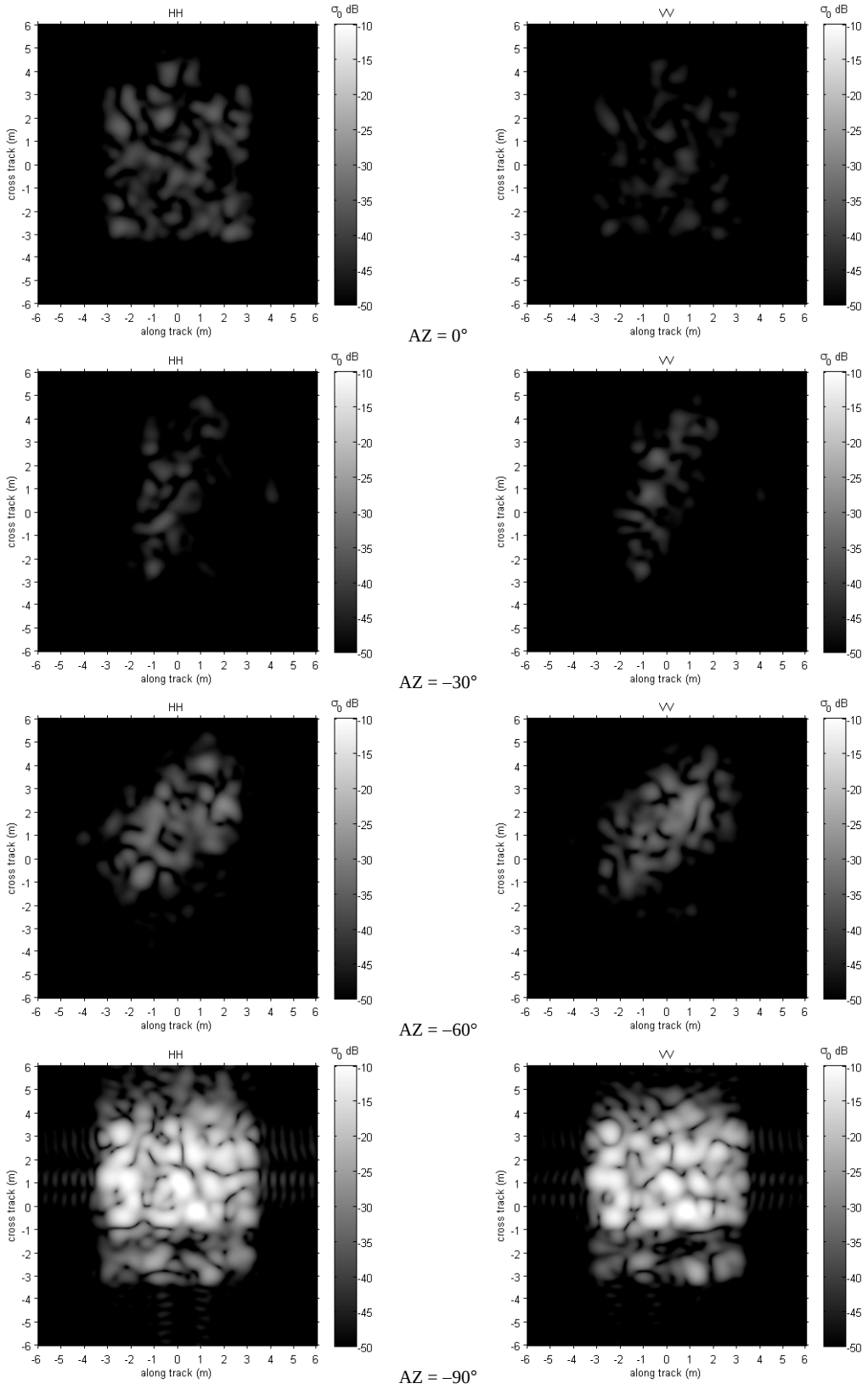

Figure V-33 Crevasse with snow bridge, 2-m depth, 18-inch resolution, $f_c = 9.5$ GHz *, 15° depression angle.*

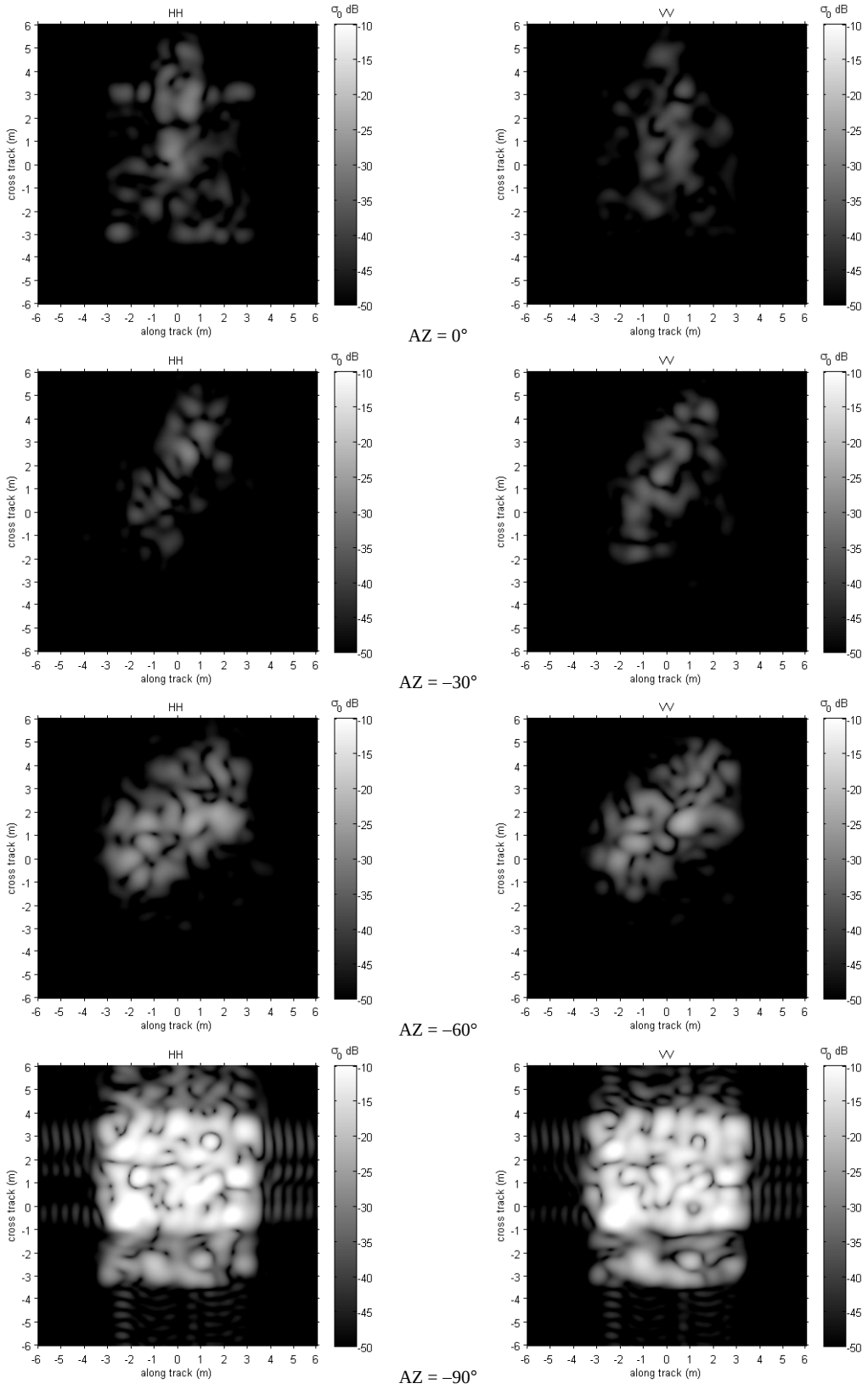

Figure V-34 Crevasse with snow bridge, 2-m depth, 18-inch resolution, $f_c = 9.5$ GHz *, 30° depression angle.*

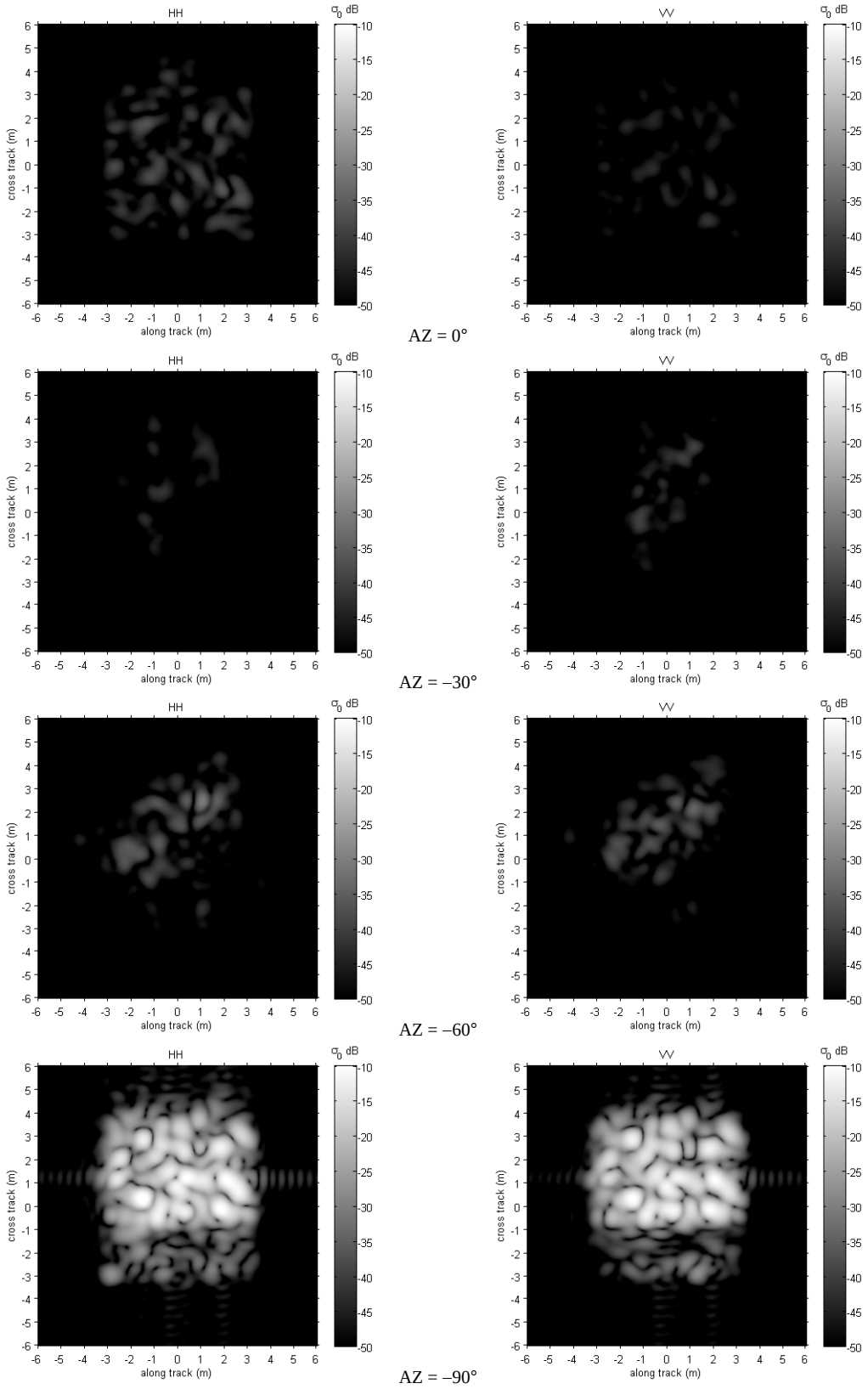

Figure V-35 Crevasse with snow bridge, 2-m depth, 18-inch resolution, $f_c = 16.8$ GHz *, 15° depression angle.*

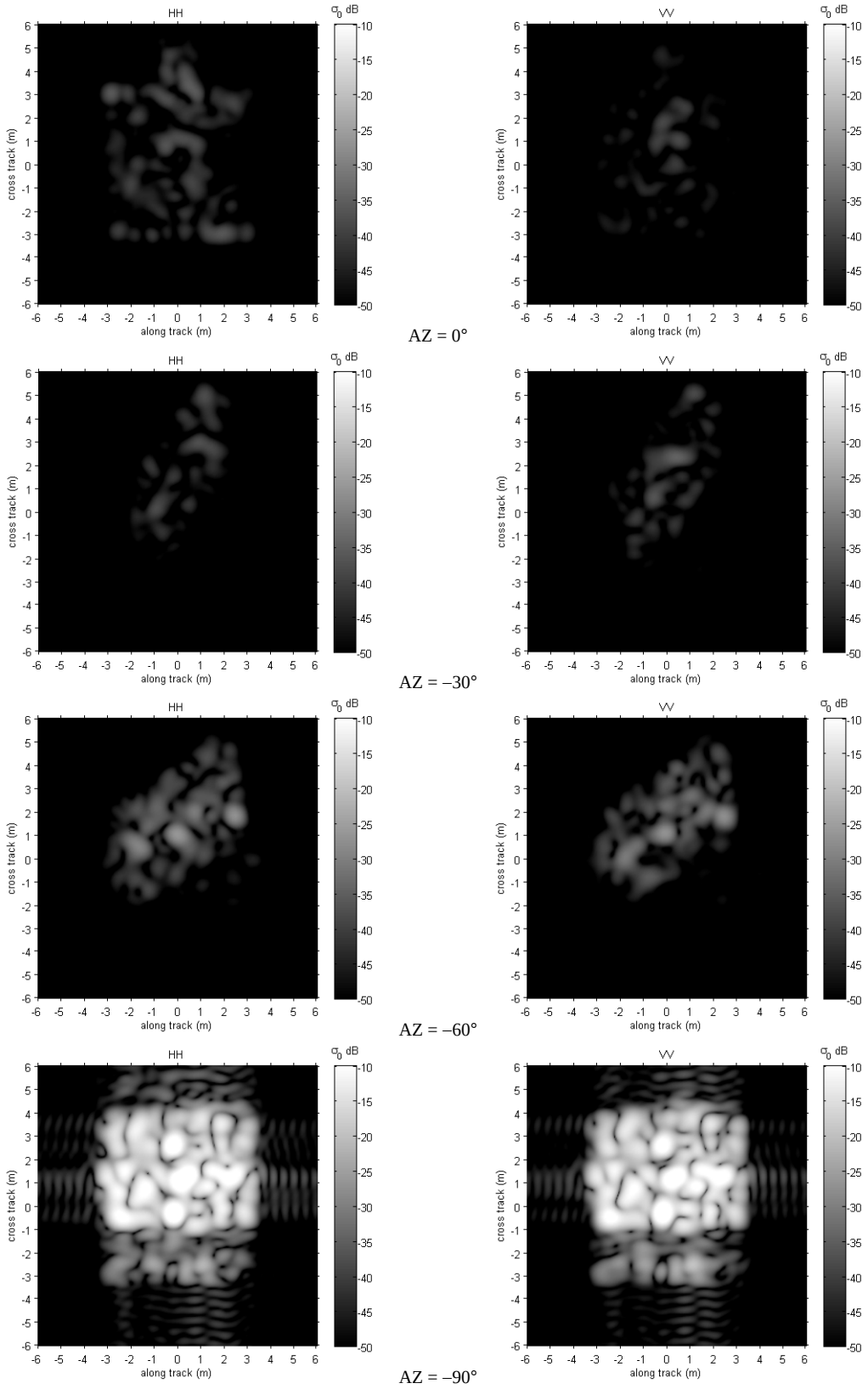

Figure V-36 Crevasse with snow bridge, 2-m depth, 18-inch resolution, $f_c = 16.8$ GHz *, 30° depression angle.*

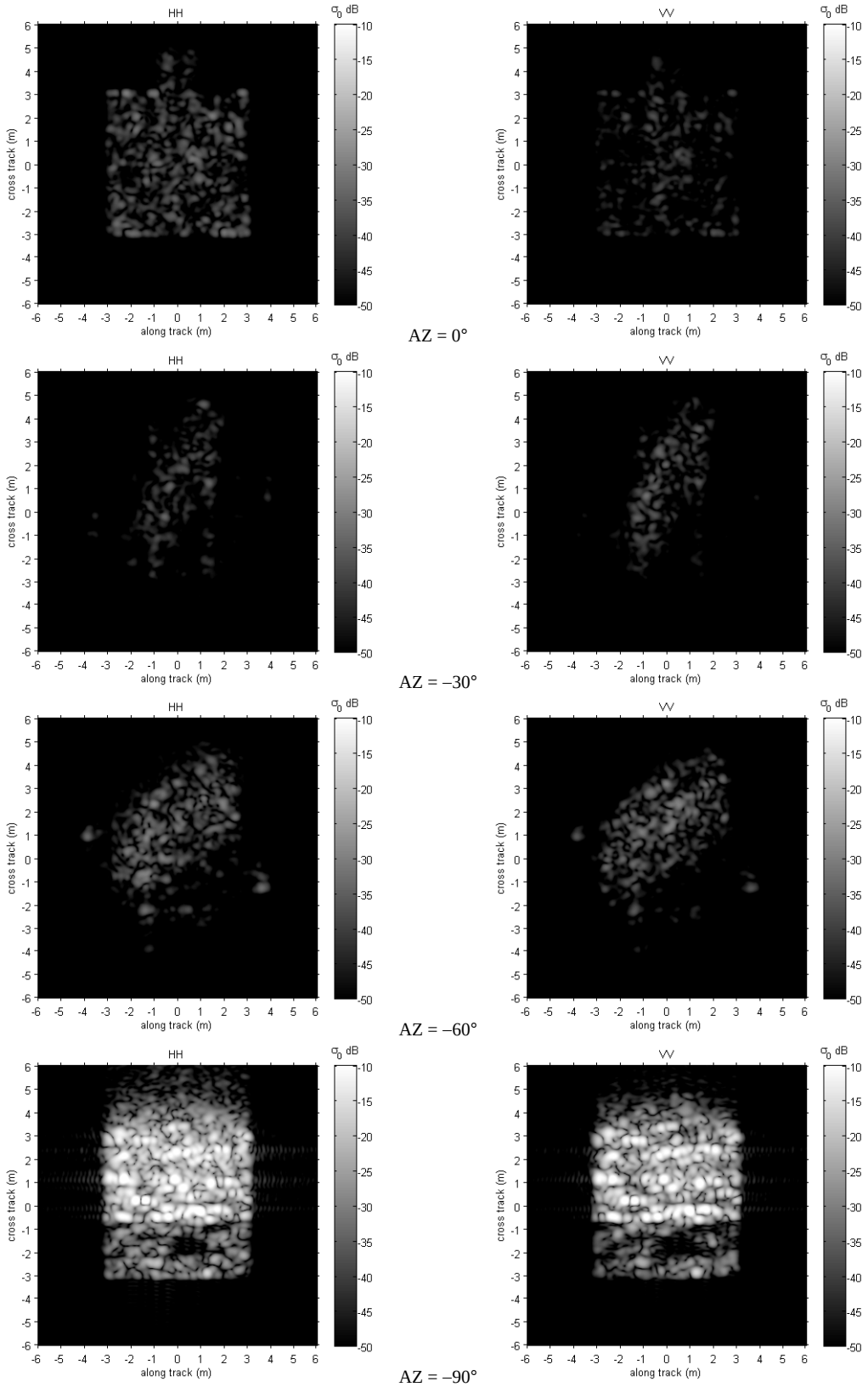

Figure V-37 Crevasse with snow bridge, 2-m depth, 8-inch resolution, $f_c = 9.5$ GHz *, 15° depression angle.*

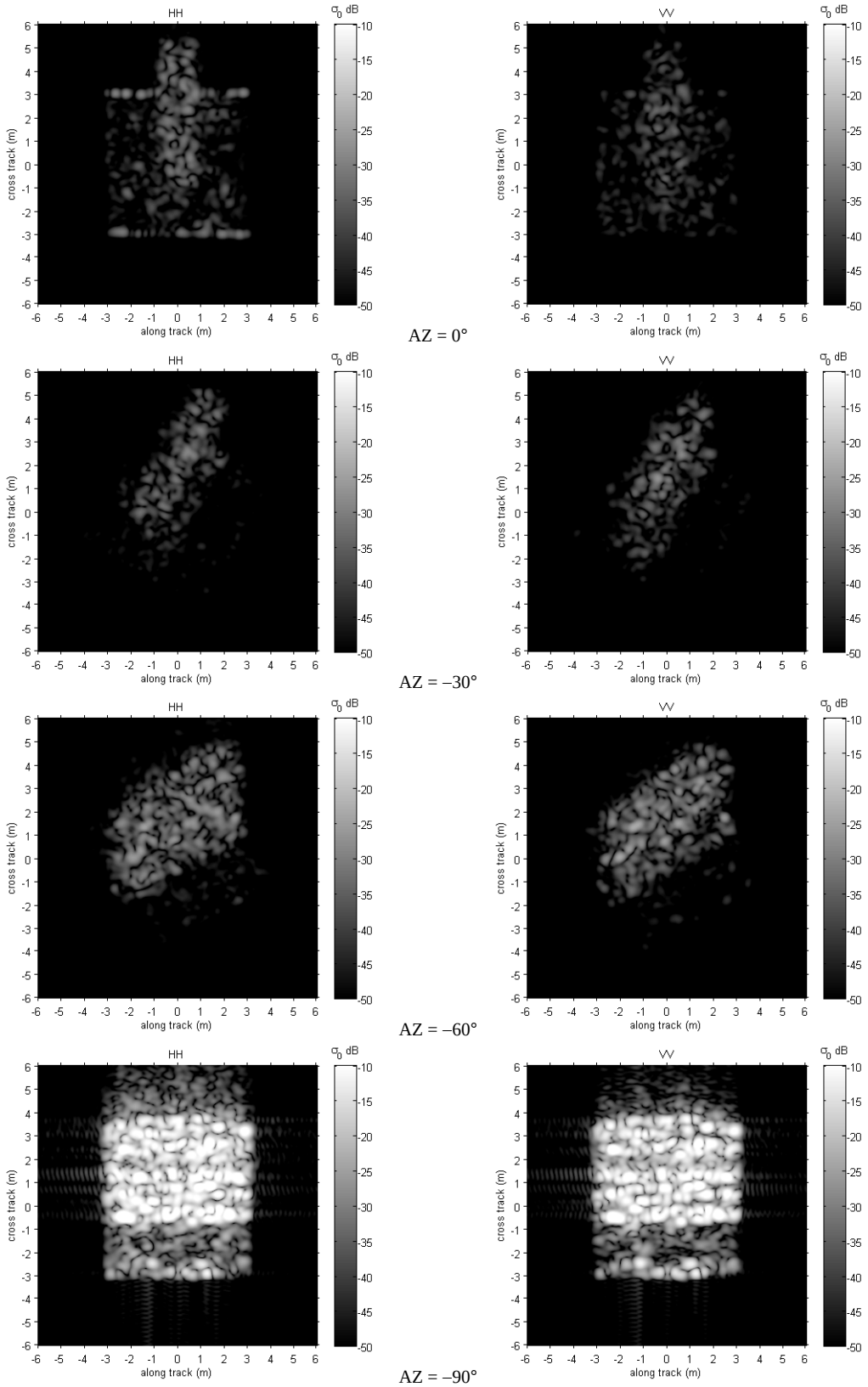

Figure V-38 Crevasse with snow bridge, 2-m depth, 8-inch resolution, $f_c = 9.5$ GHz *, 30° depression angle.*

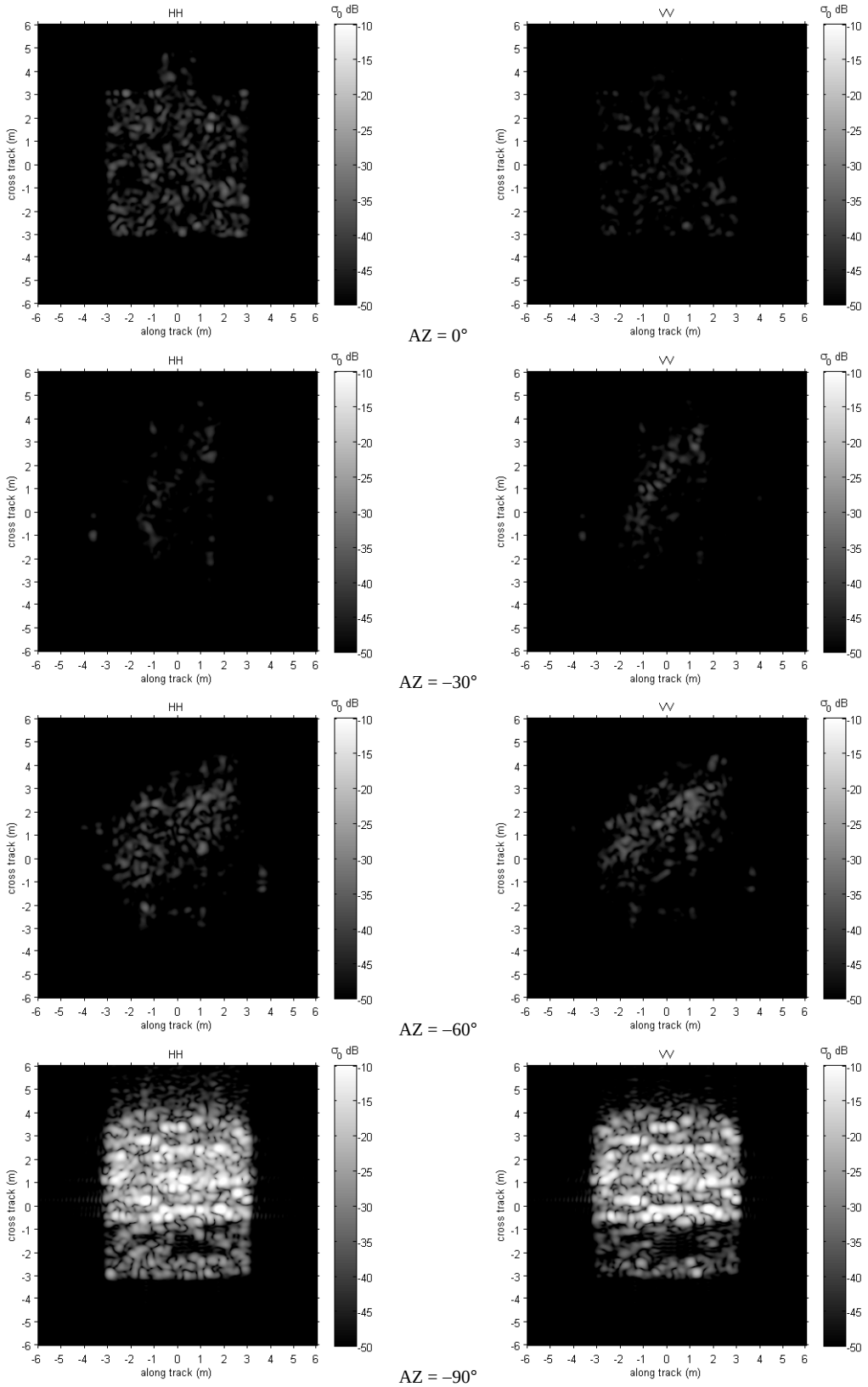

Figure V-39 Crevasse with snow bridge, 2-m depth, 8-inch resolution, $f_c = 16.8$ GHz *, 15° depression angle.*

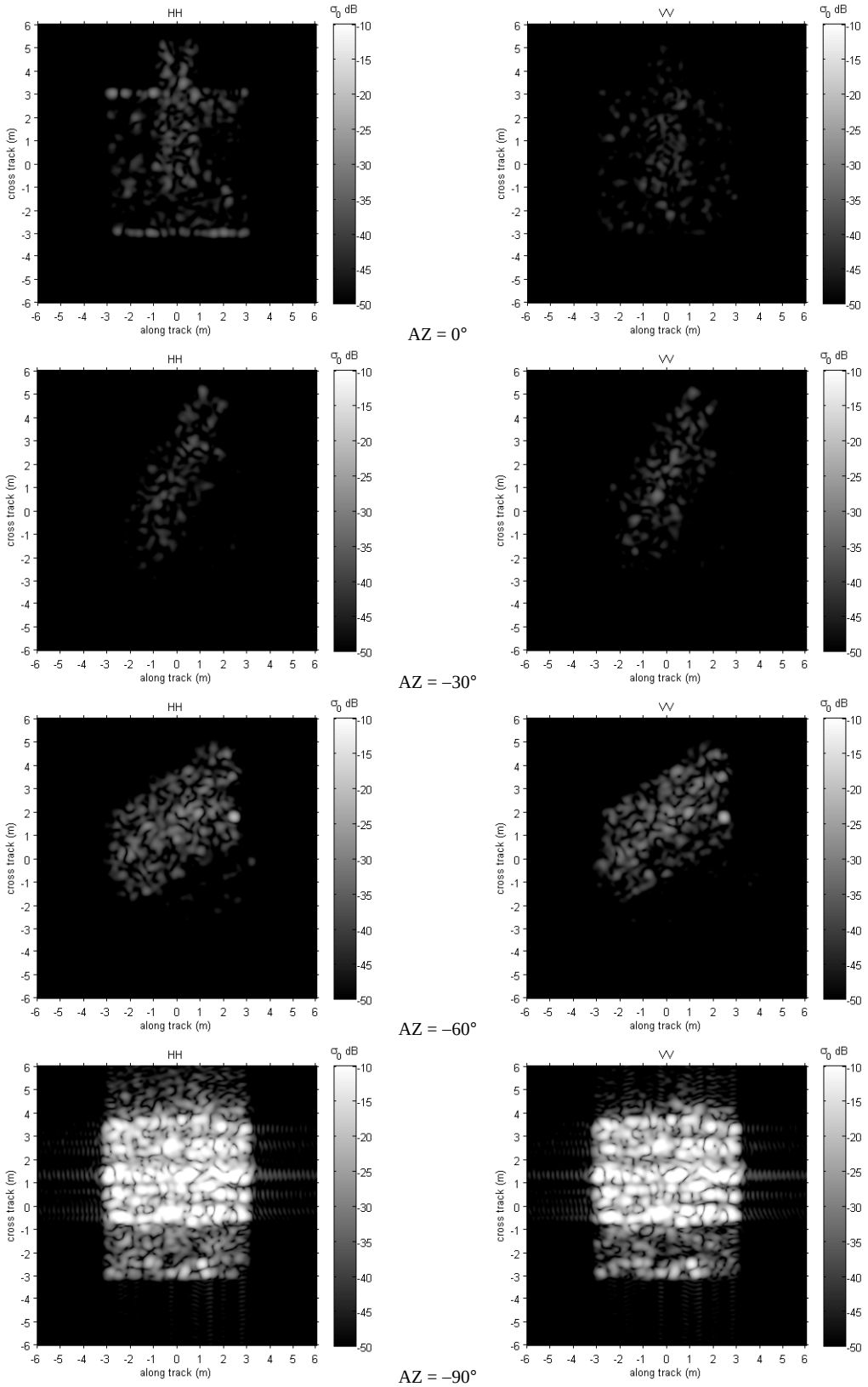

Figure V-40 Crevasse with snow bridge, 2-m depth, 8-inch resolution, $f_c = 16.8$ GHz *, 30° depression angle.*

Square root of magnitude (4th root of power), crevasse with snow bridge, 2-m depth

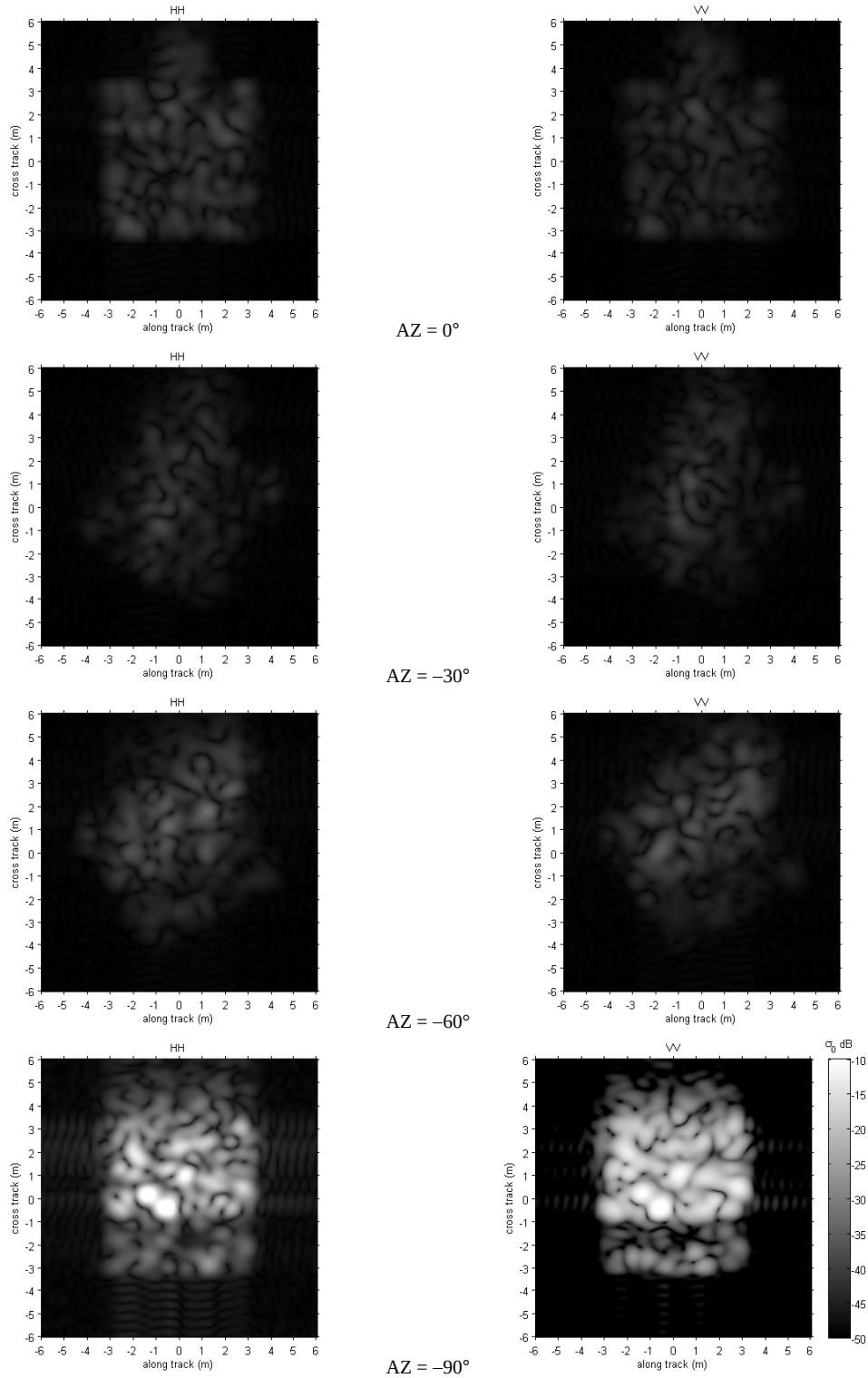

Figure V-41 Crevasse with snow bridge, 2-m depth, 18-inch resolution, $f_c = 5.45$ GHz *, 15° depression angle.*

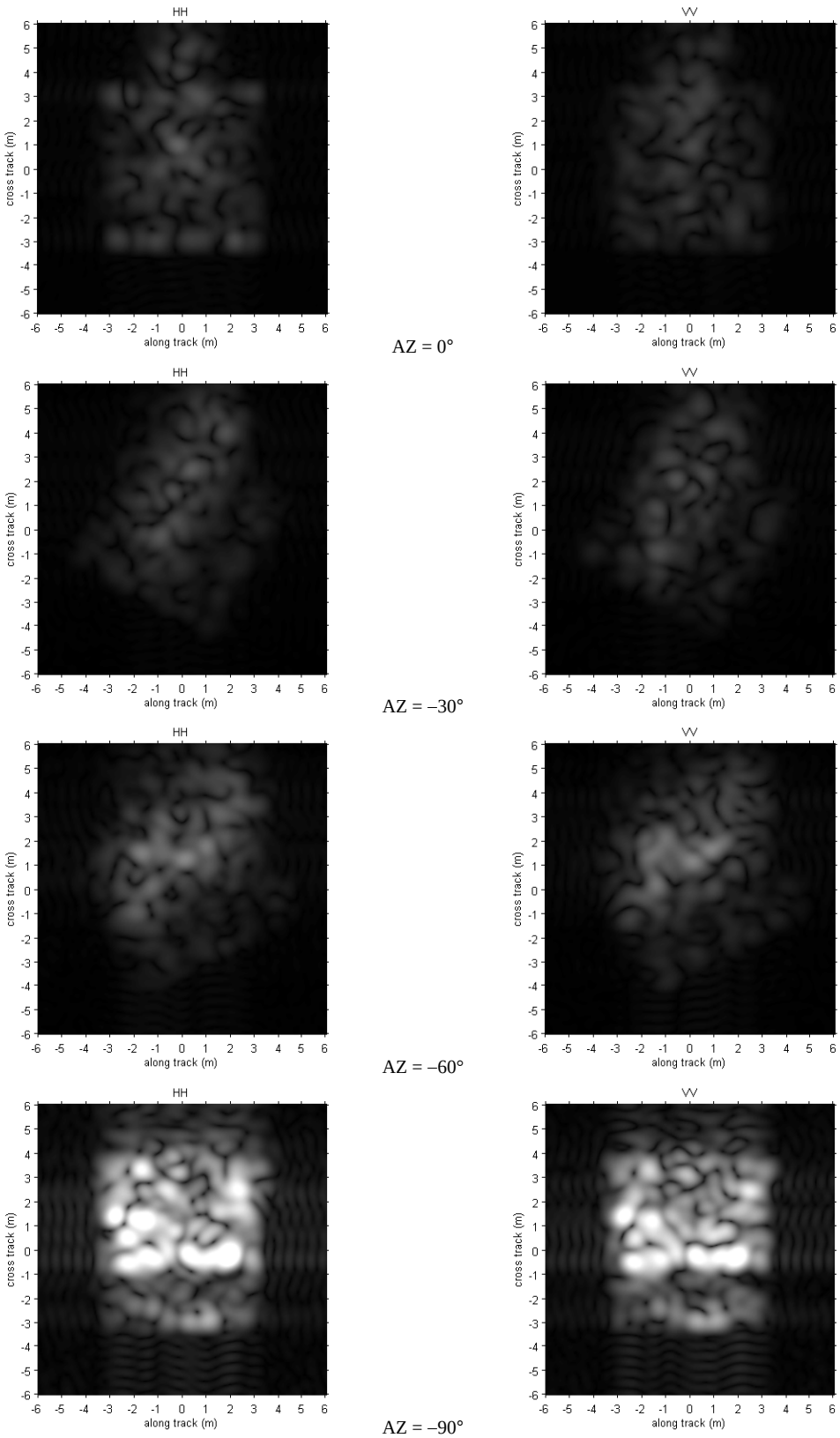

Figure V-42 Crevasse with snow bridge, 2-m depth, 18-inch resolution, $f_c = 5.45$ GHz *, 30° depression angle.*

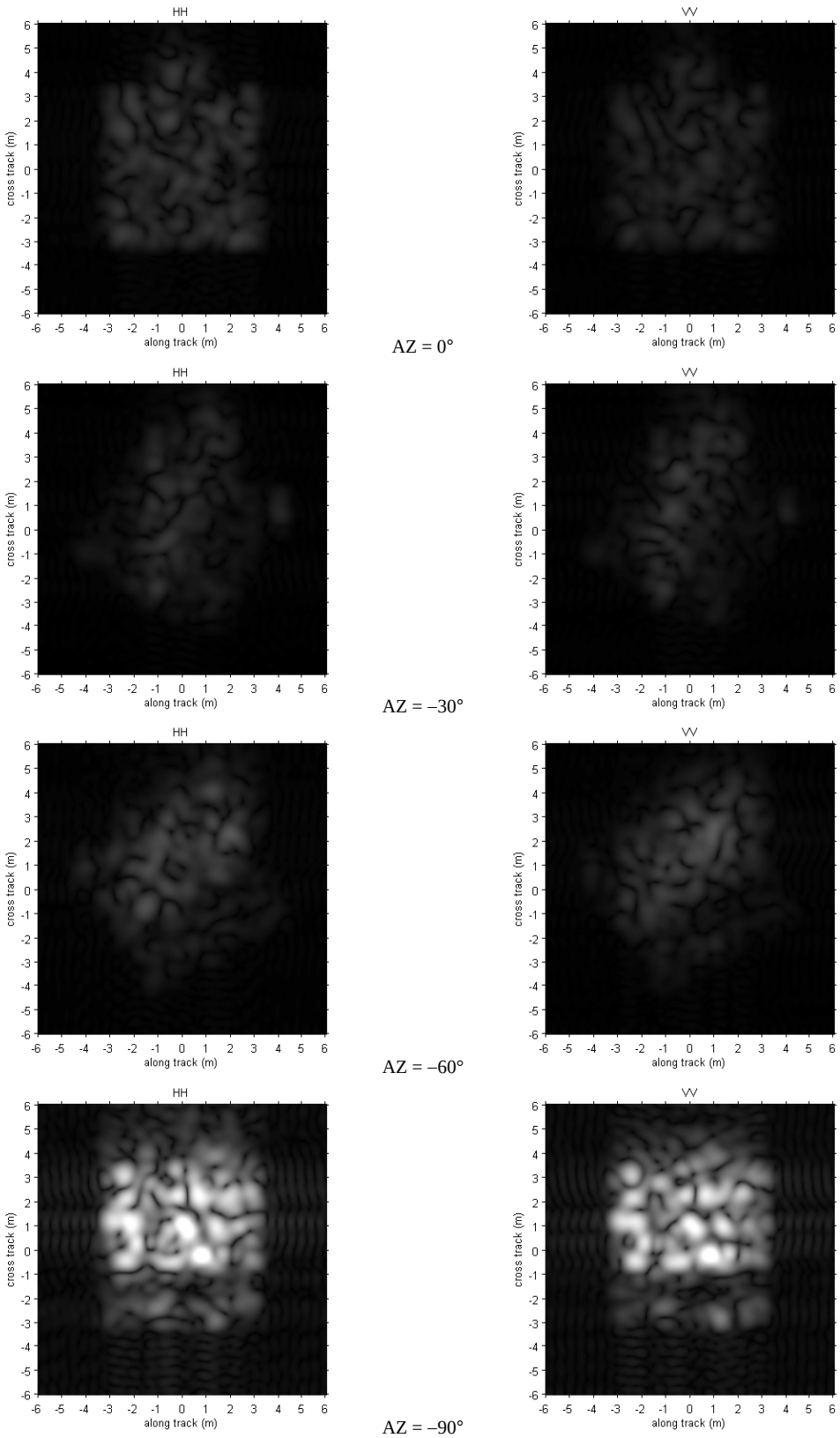

Figure V-43 Crevasse with snow bridge, 2-m depth, 18-inch resolution, $f_c = 9.5$ GHz *, 15° depression angle.*

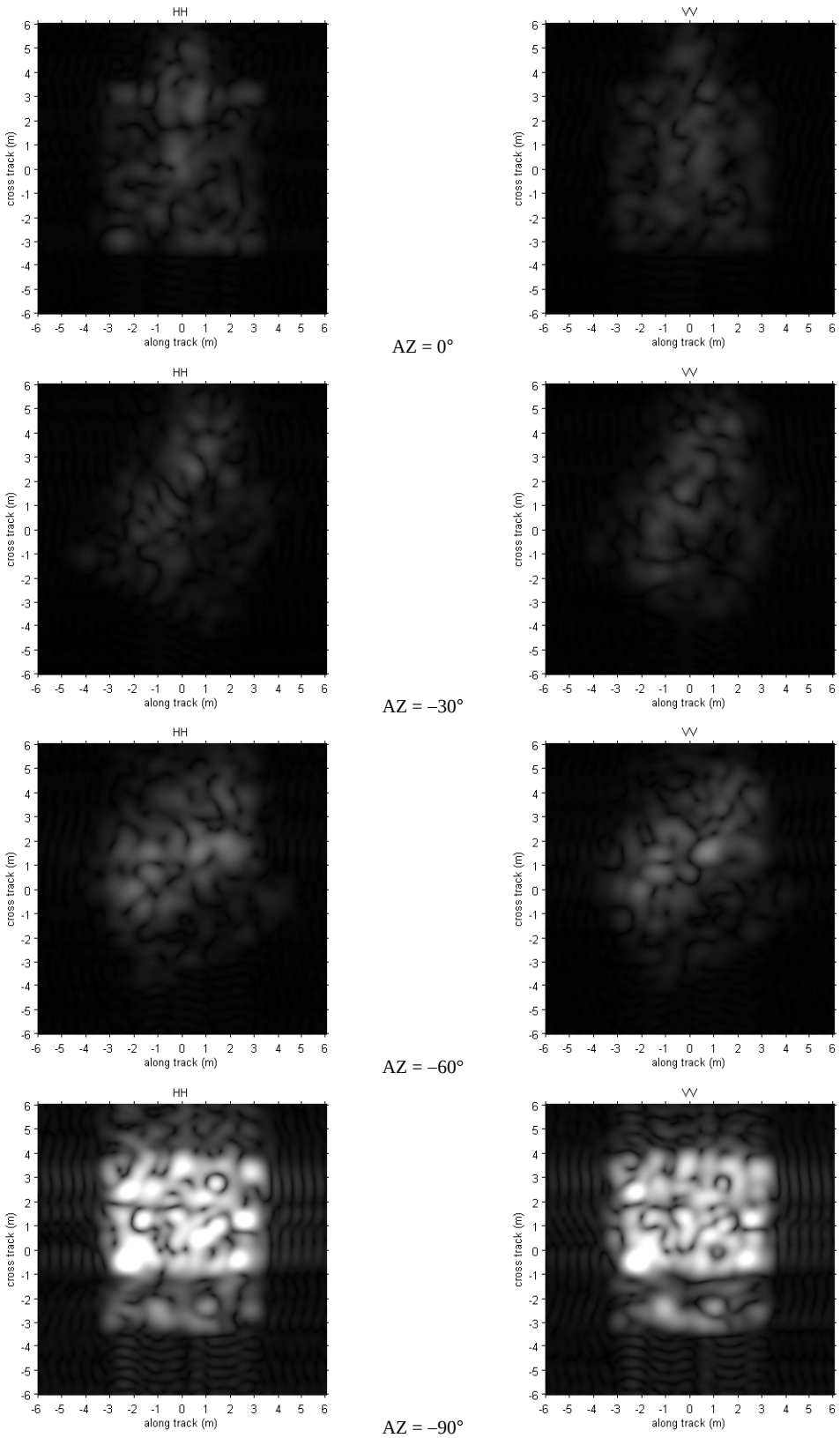

Figure V-44 Crevasse with snow bridge, 2-m depth, 18-inch resolution, $f_c = 9.5$ GHz *, 30° depression angle.*

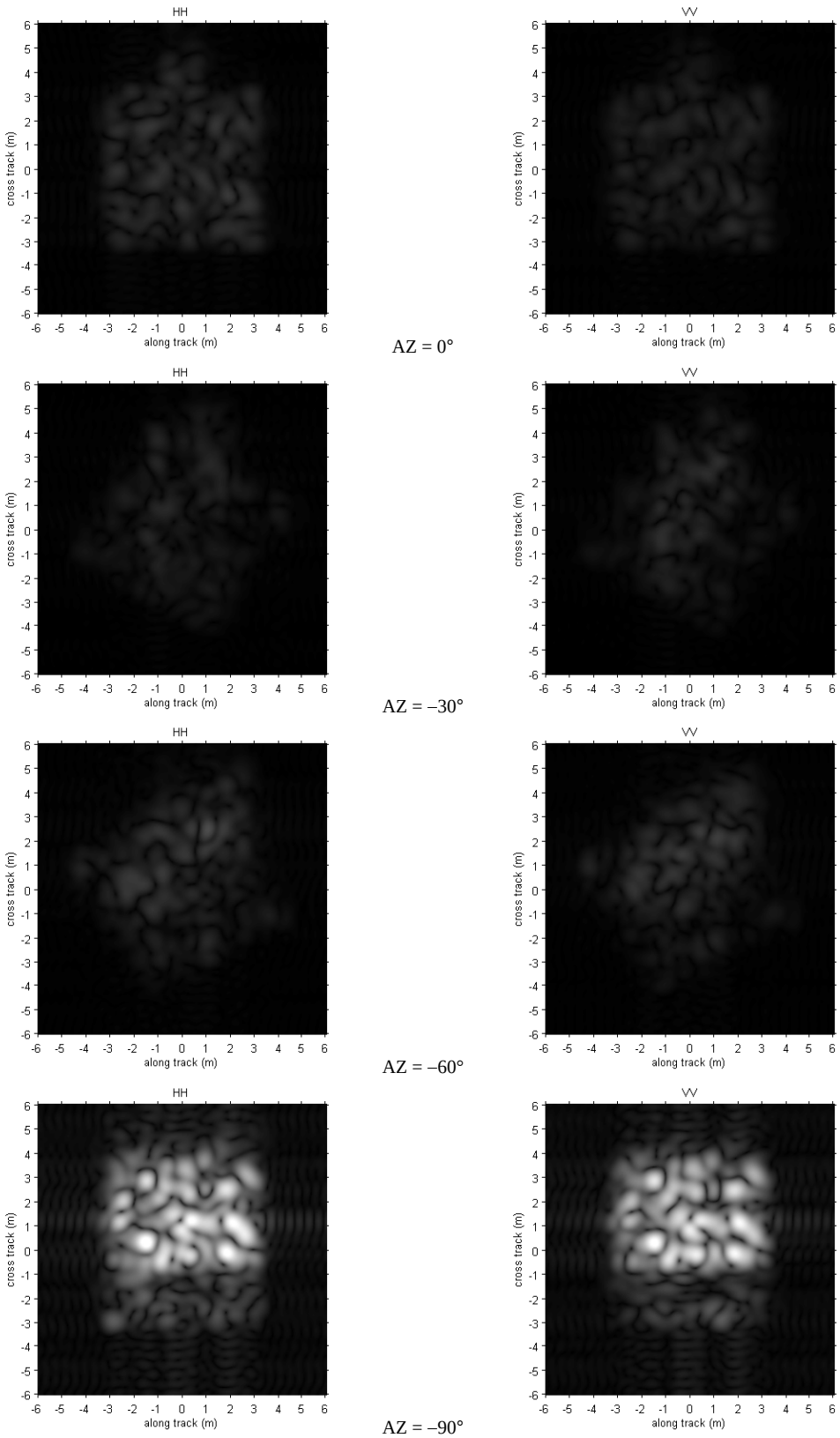

Figure V-45 Crevasse with snow bridge, 2-m depth, 18-inch resolution, $f_c = 16.8$ GHz *, 15° depression angle.*

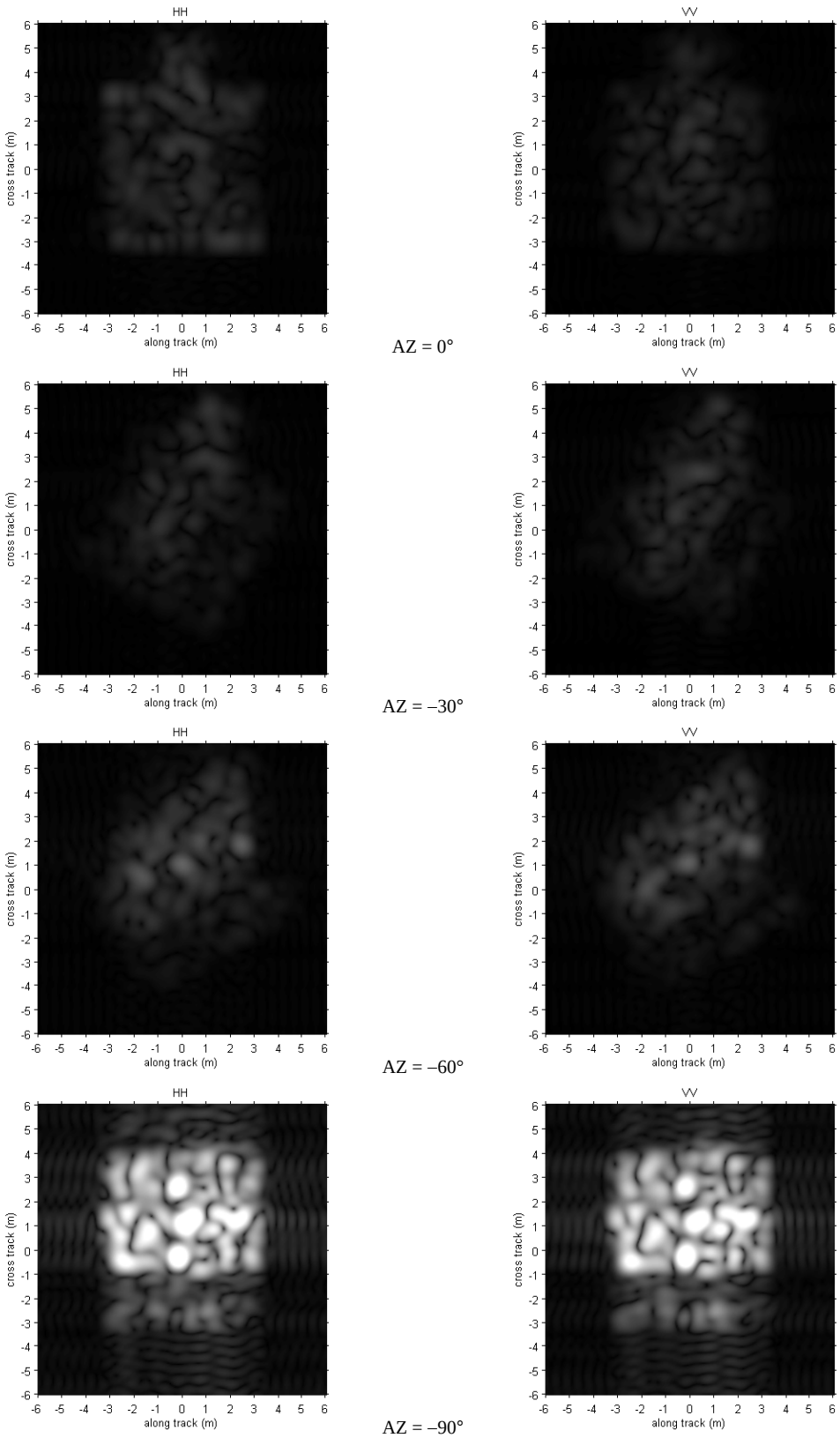

Figure V-46 Crevasse with snow bridge, 2-m depth, 18-inch resolution, $f_c = 16.8$ GHz *, 30° depression angle.*

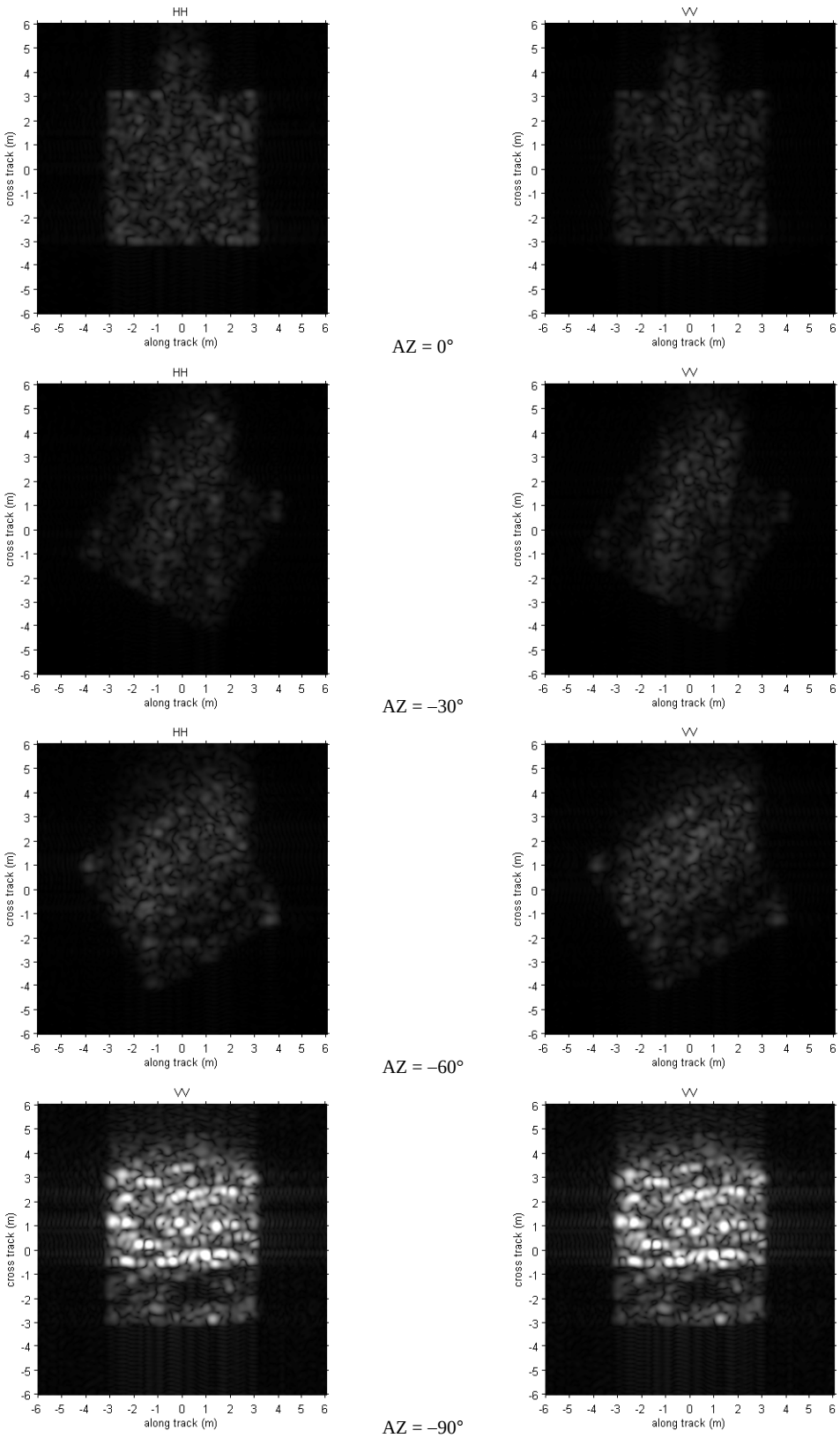

Figure V-47 Crevasse with snow bridge, 2-m depth, 8-inch resolution, $f_c = 9.5$ GHz *, 15° depression angle.*

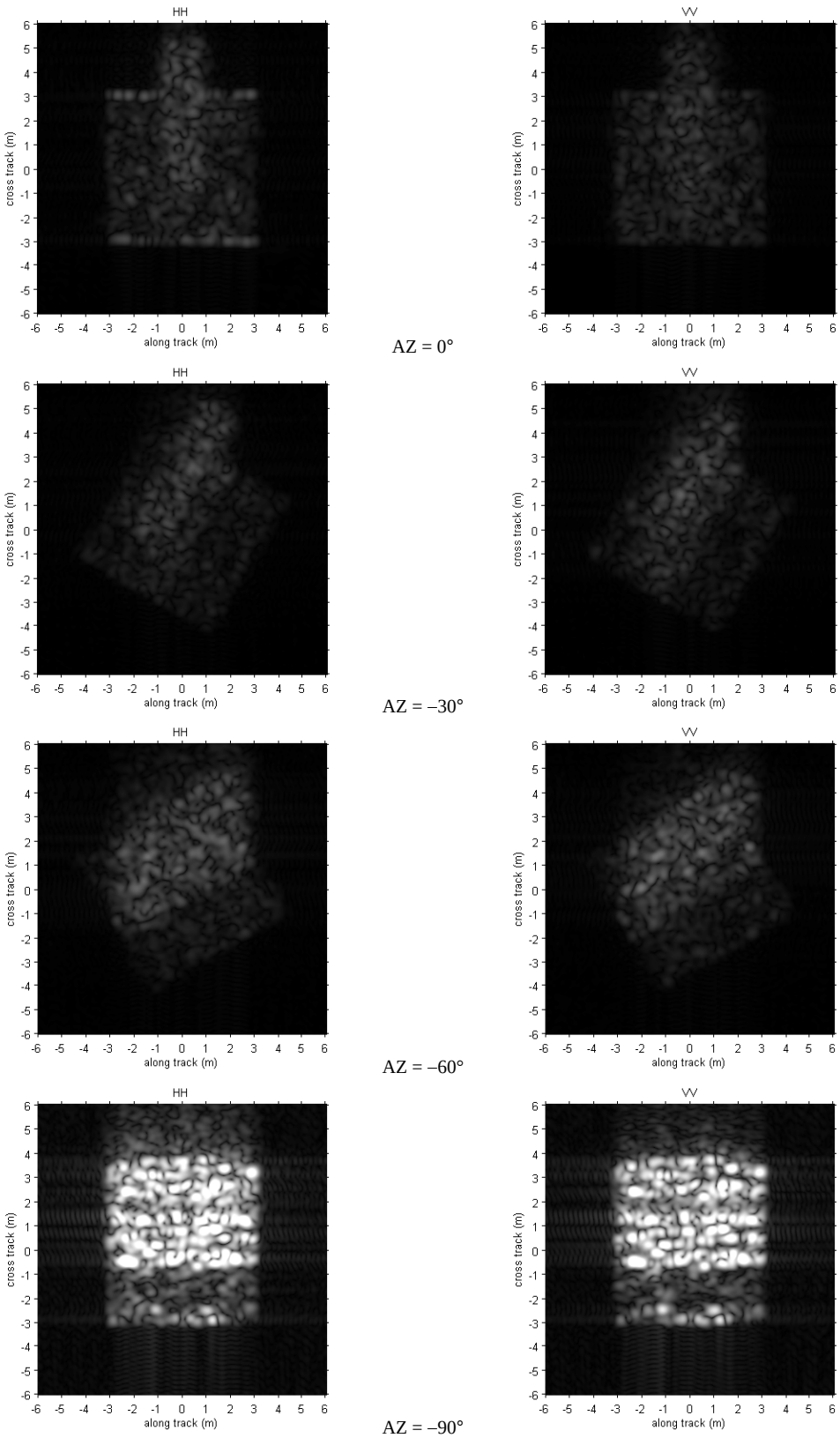

Figure V-48 Crevasse with snow bridge, 2-m depth, 8-inch resolution, $f_c = 9.5$ GHz *, 30° depression angle.*

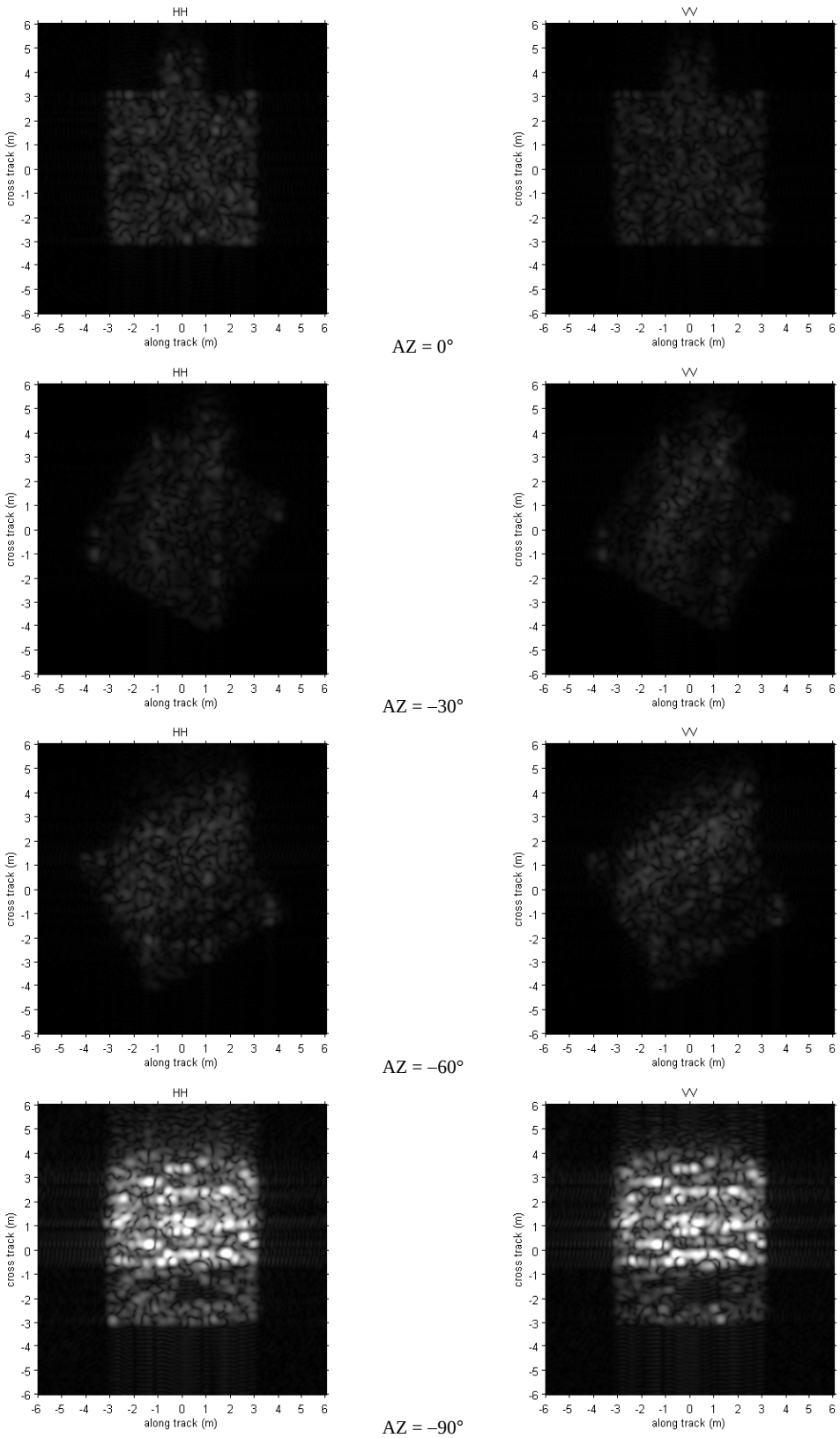

Figure V-49 Crevasse with snow bridge, 2-m depth, 8-inch resolution, $f_c = 16.8$ GHz *, 15° depression angle.*

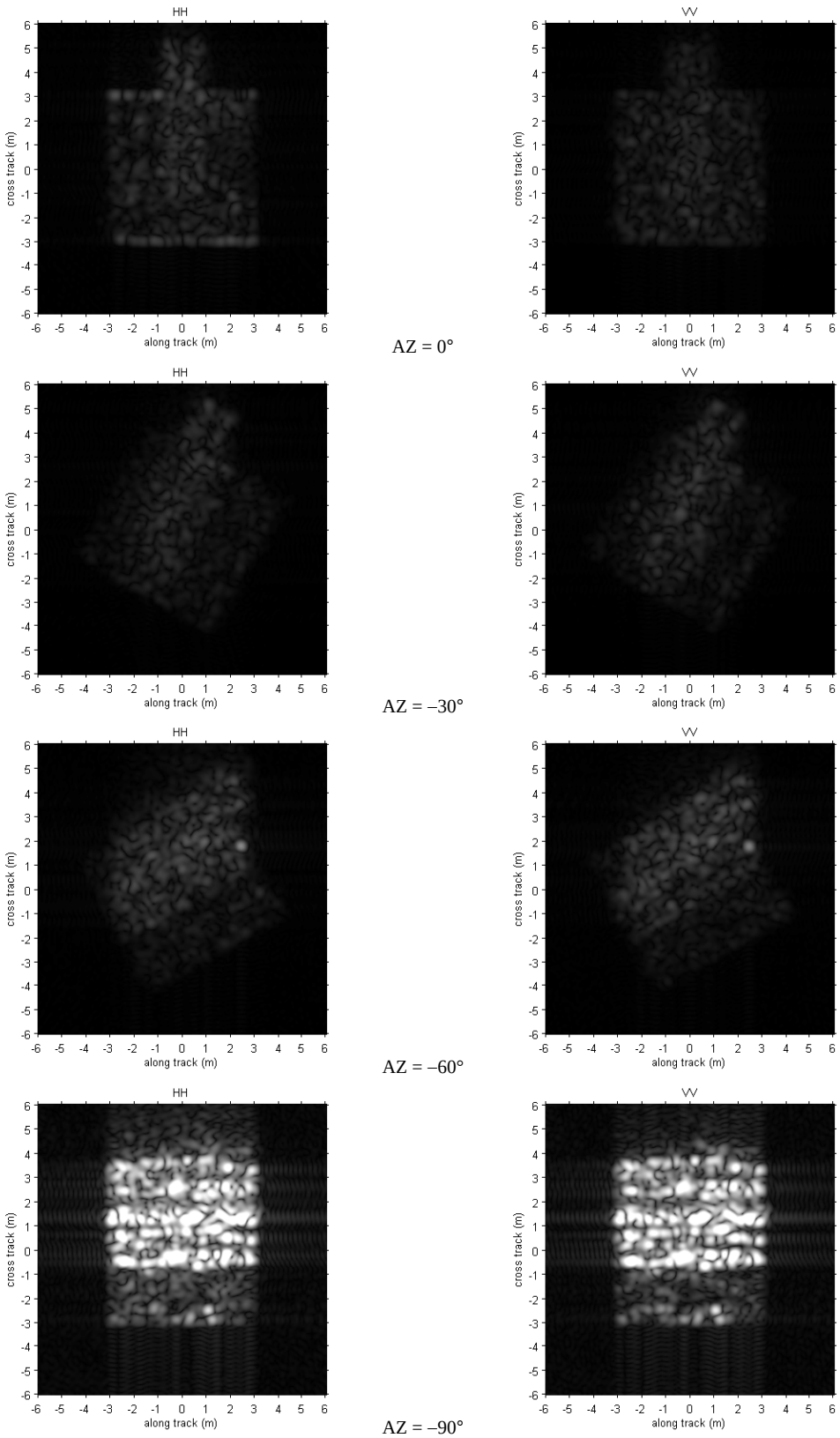

Figure V-50 Crevasse with snow bridge, 2-m depth, 8-inch resolution, $f_c = 16.8$ GHz *, 30° depression angle.*

Color, snow-bridge depth is 2.0 m

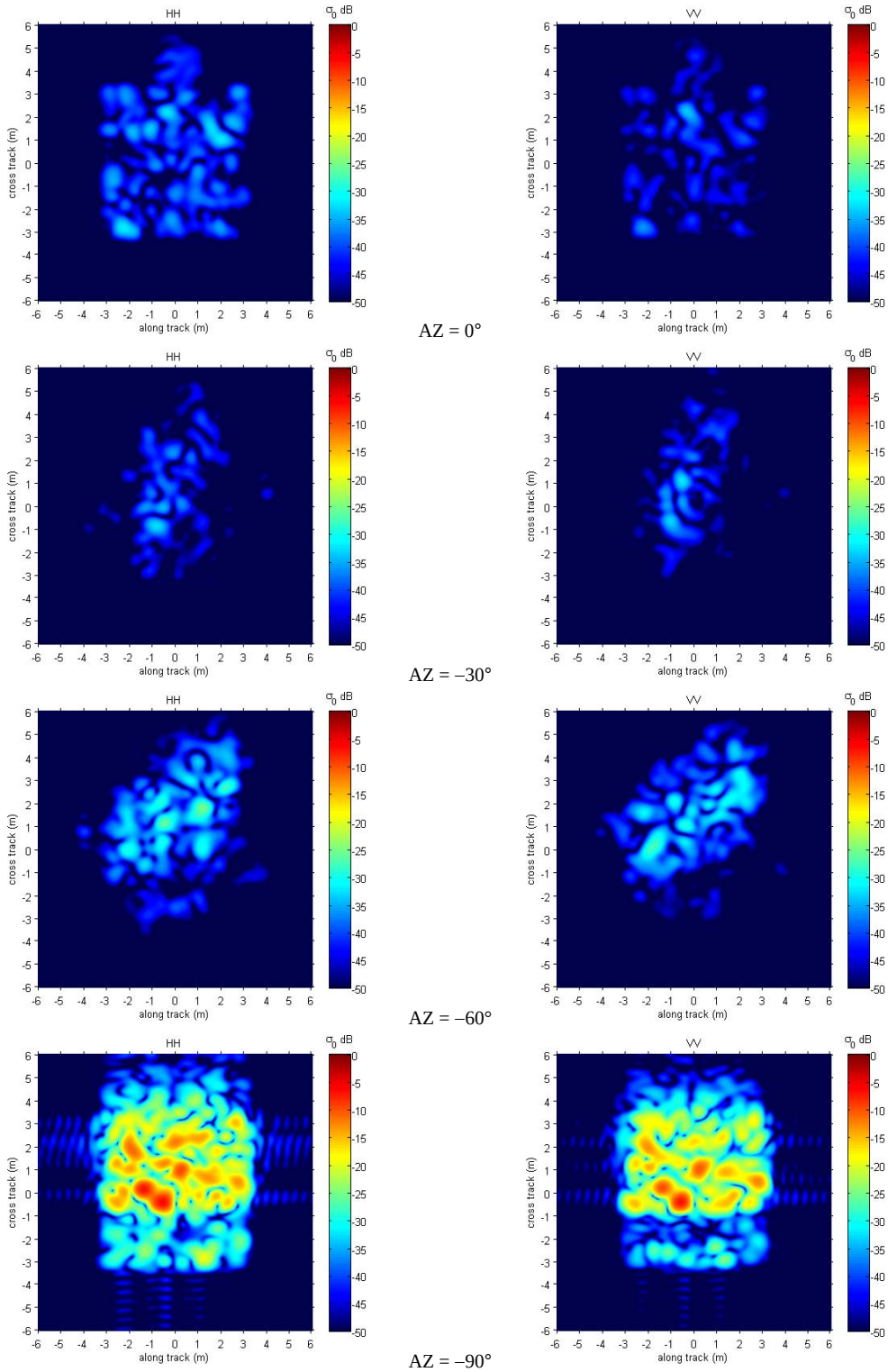

Figure V-51 Crevasse with snow bridge, 2-m depth, 18-inch resolution, $f_c = 5.45$ GHz *, 15° depression angle.*

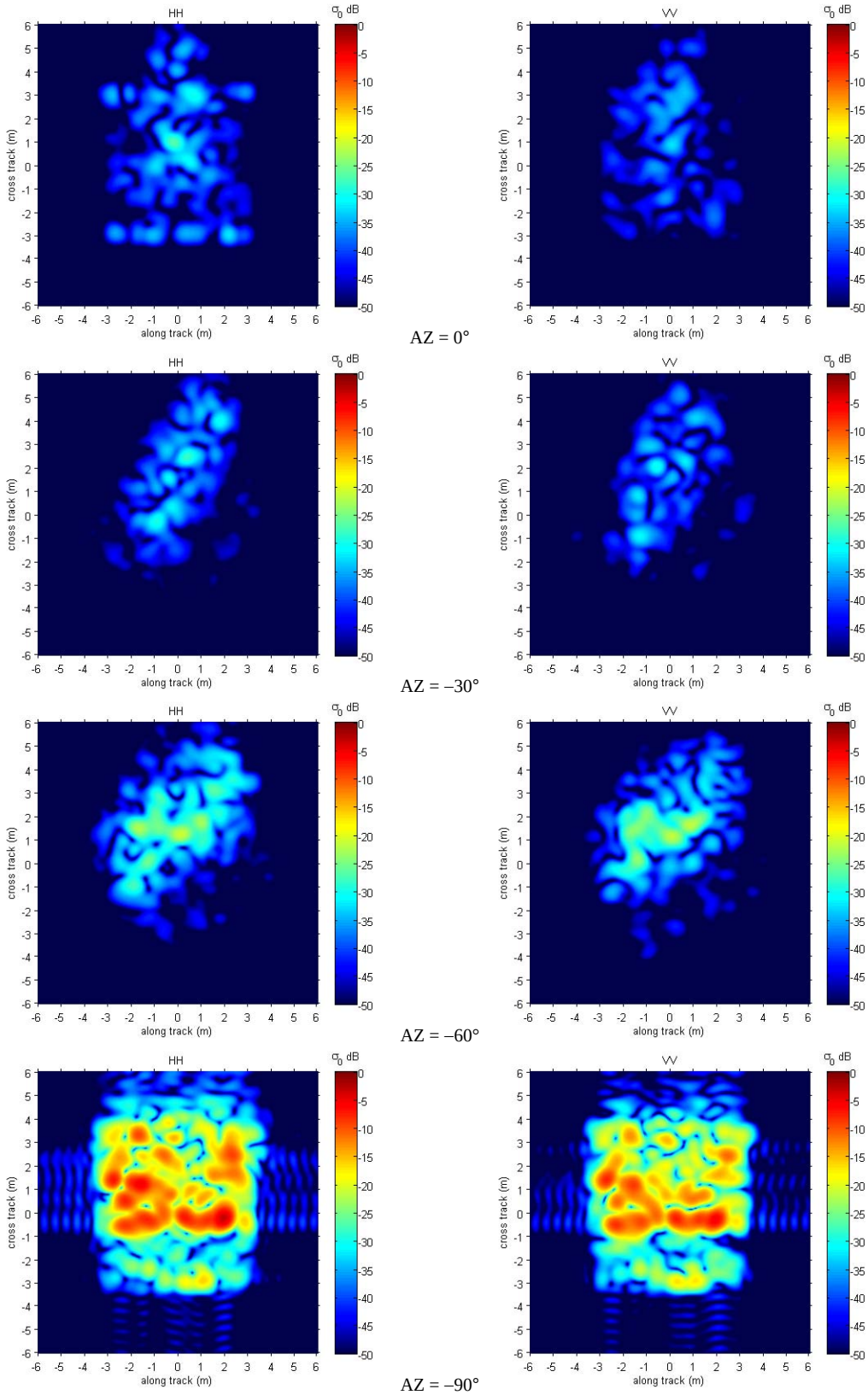

Figure V-52 Crevasse with snow bridge, 2-m depth, 18-inch resolution, $f_c = 5.45$ GHz *, 30° depression angle.*

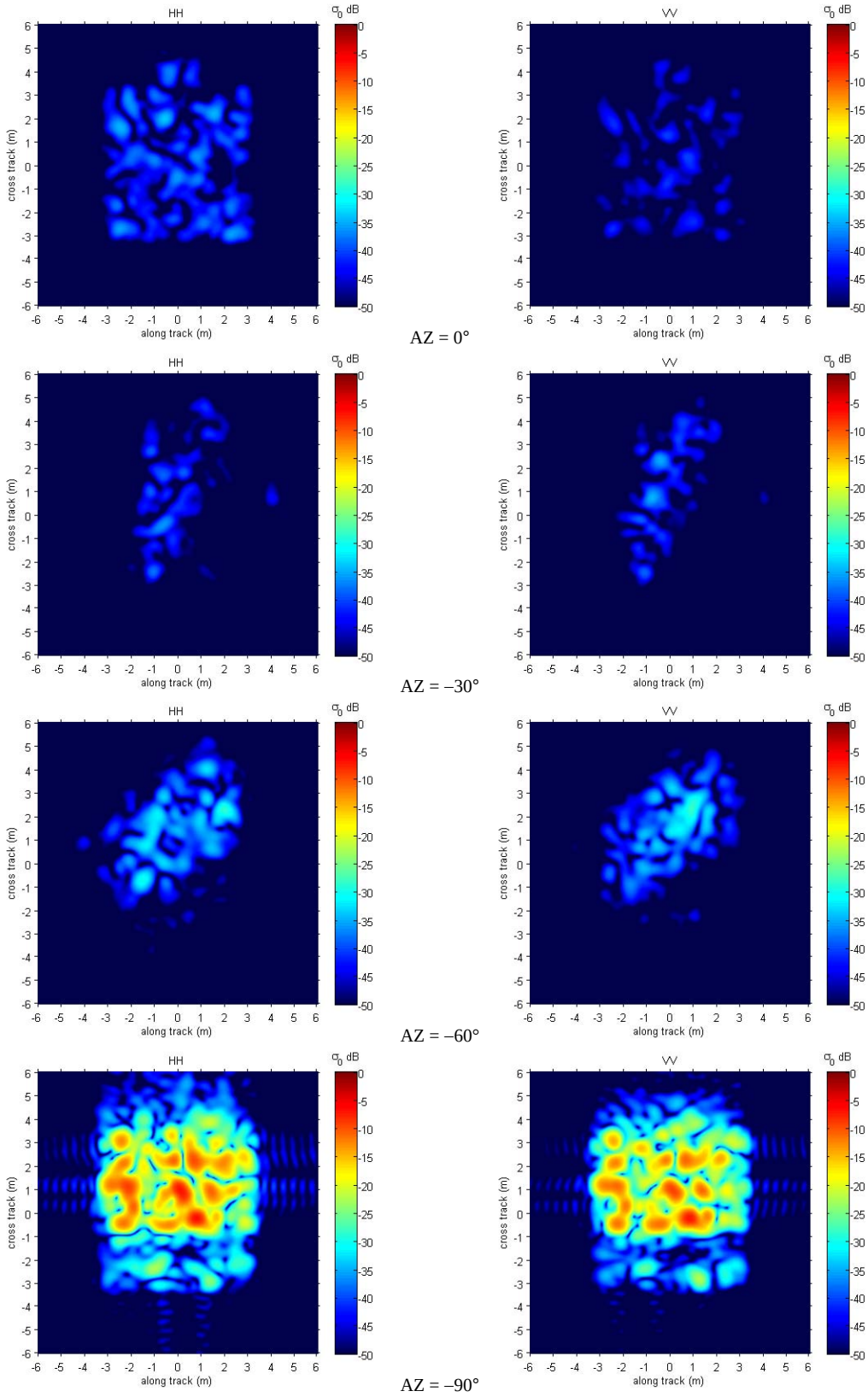

Figure V-53 Crevasse with snow bridge, 2-m depth, 18-inch resolution, $f_c = 9.5$ GHz *, 15° depression angle.*

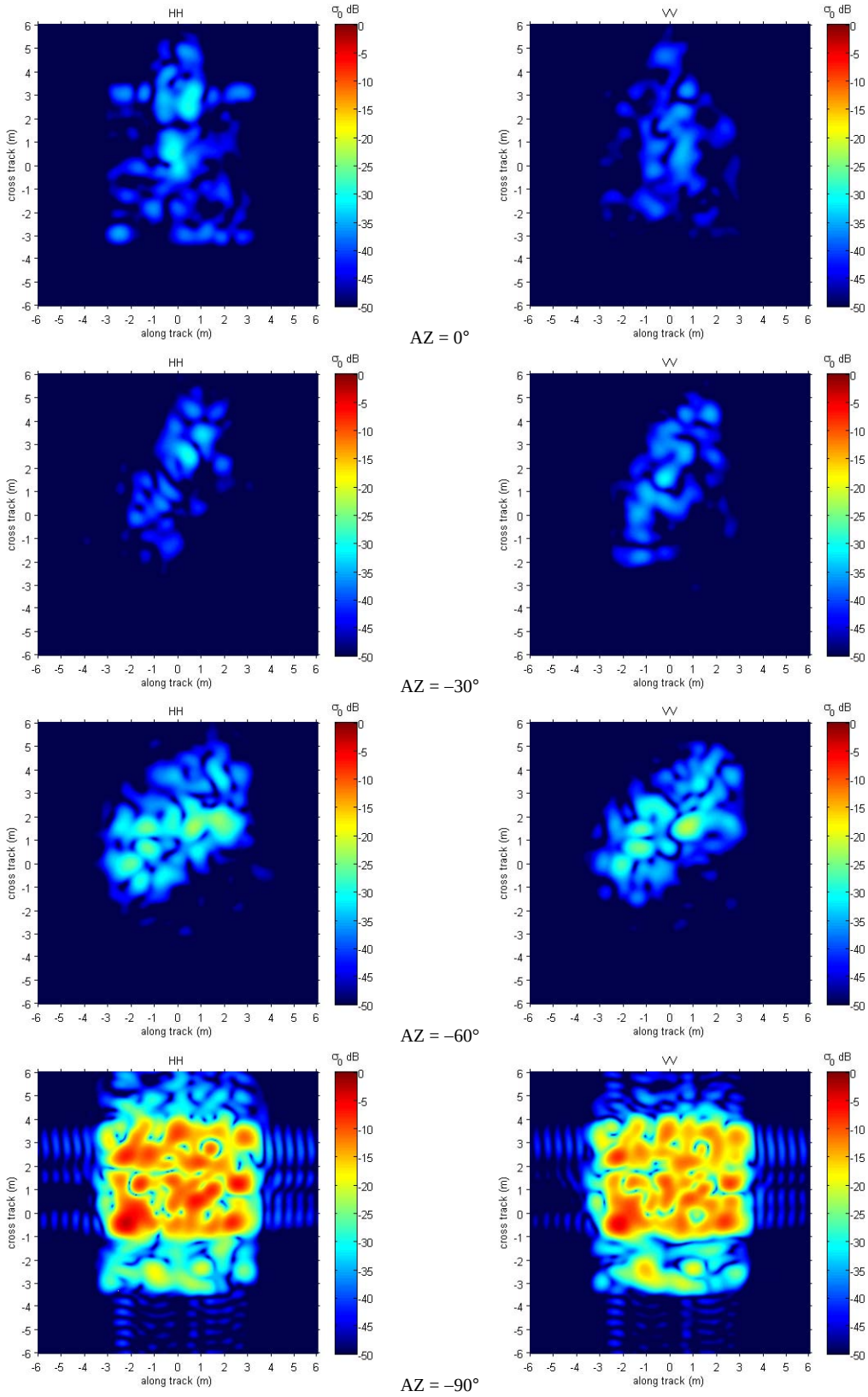

Figure V-54 Crevasse with snow bridge, 2-m depth, 18-inch resolution, $f_c = 9.5$ GHz *, 30° depression angle.*

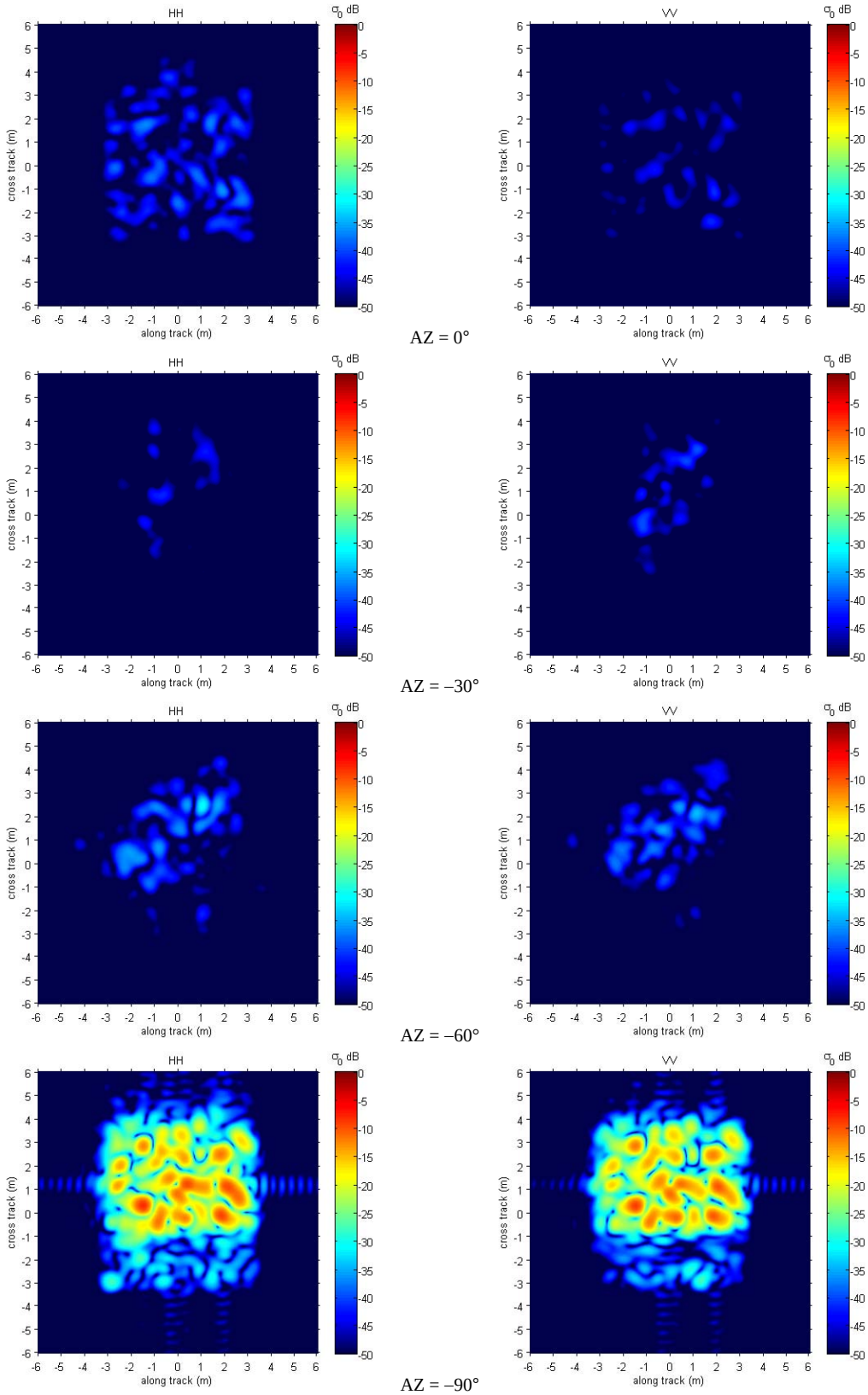

Figure V-55 Crevasse with snow bridge, 2-m depth, 18-inch resolution, $f_c = 16.8$ GHz *, 15° depression angle.*

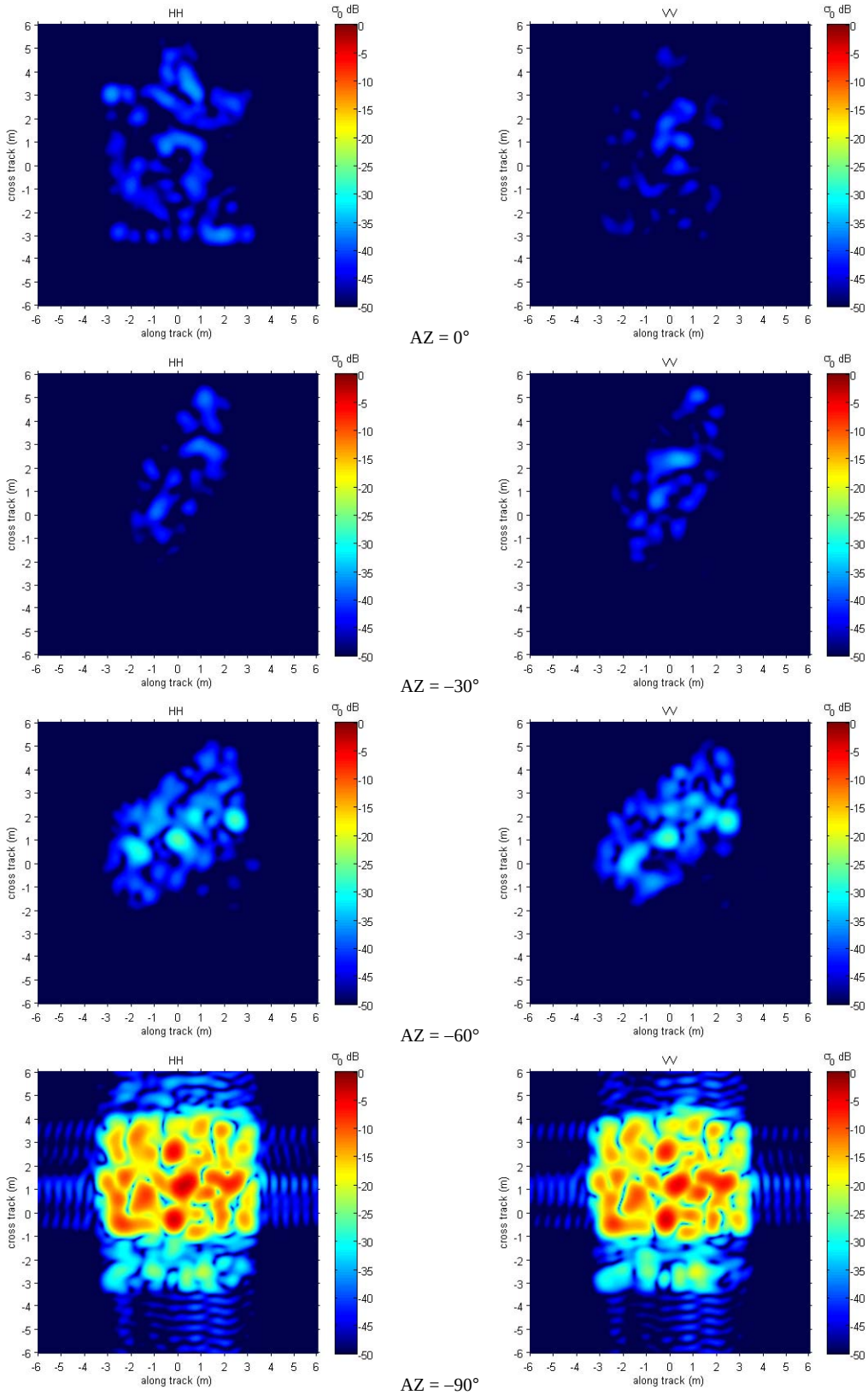

Figure V-56 Crevasse with snow bridge, 2-m depth, 18-inch resolution, $f_c = 16.8$ GHz *, 30° depression angle.*

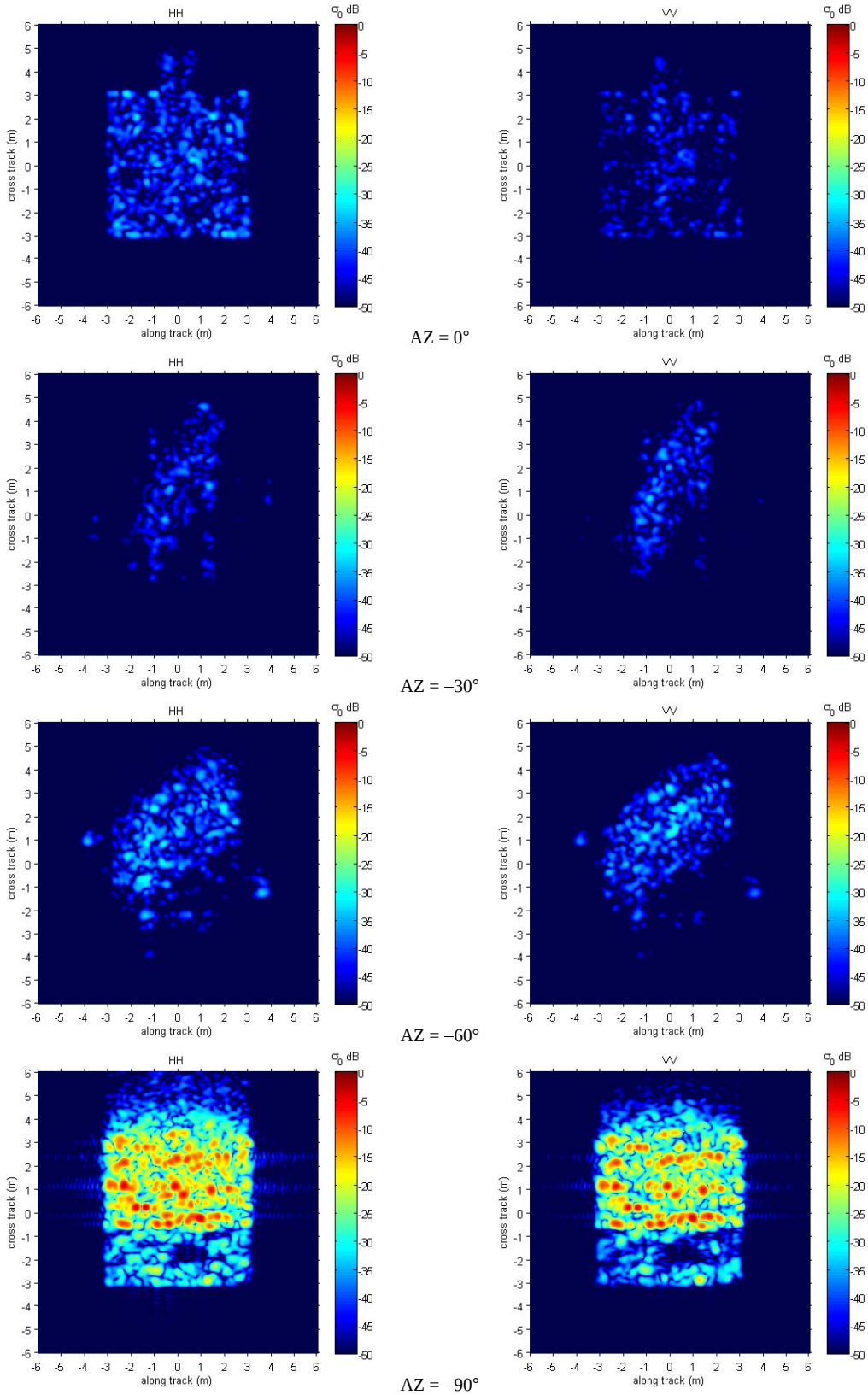

Figure V-57 Crevasse with snow bridge, 2-m depth, 8-inch resolution, $f_c = 9.5$ GHz *, 15° depression angle.*

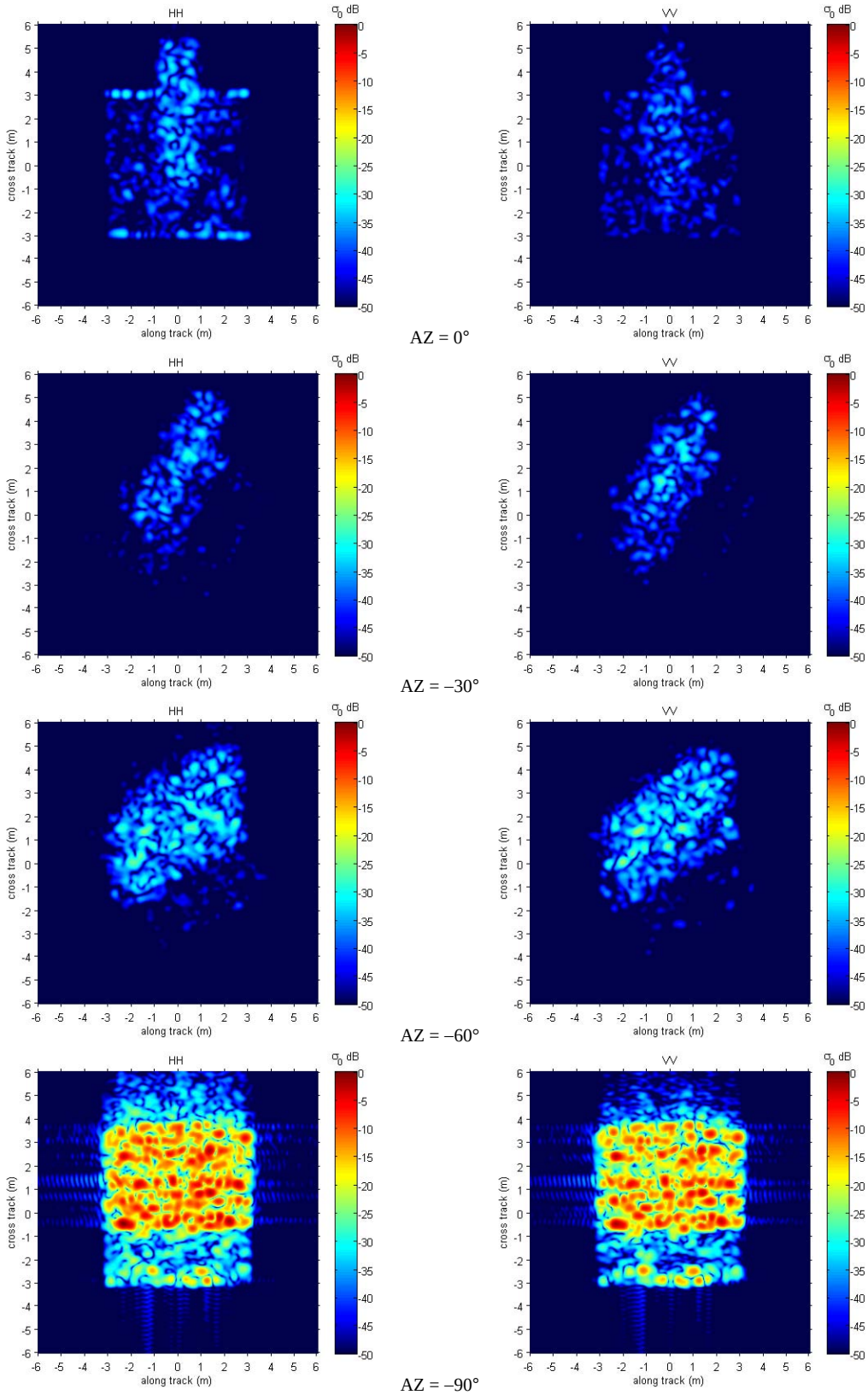

Figure V-58 Crevasse with snow bridge, 2-m depth, 8-inch resolution, $f_c = 9.5$ GHz *, 30° depression angle.*

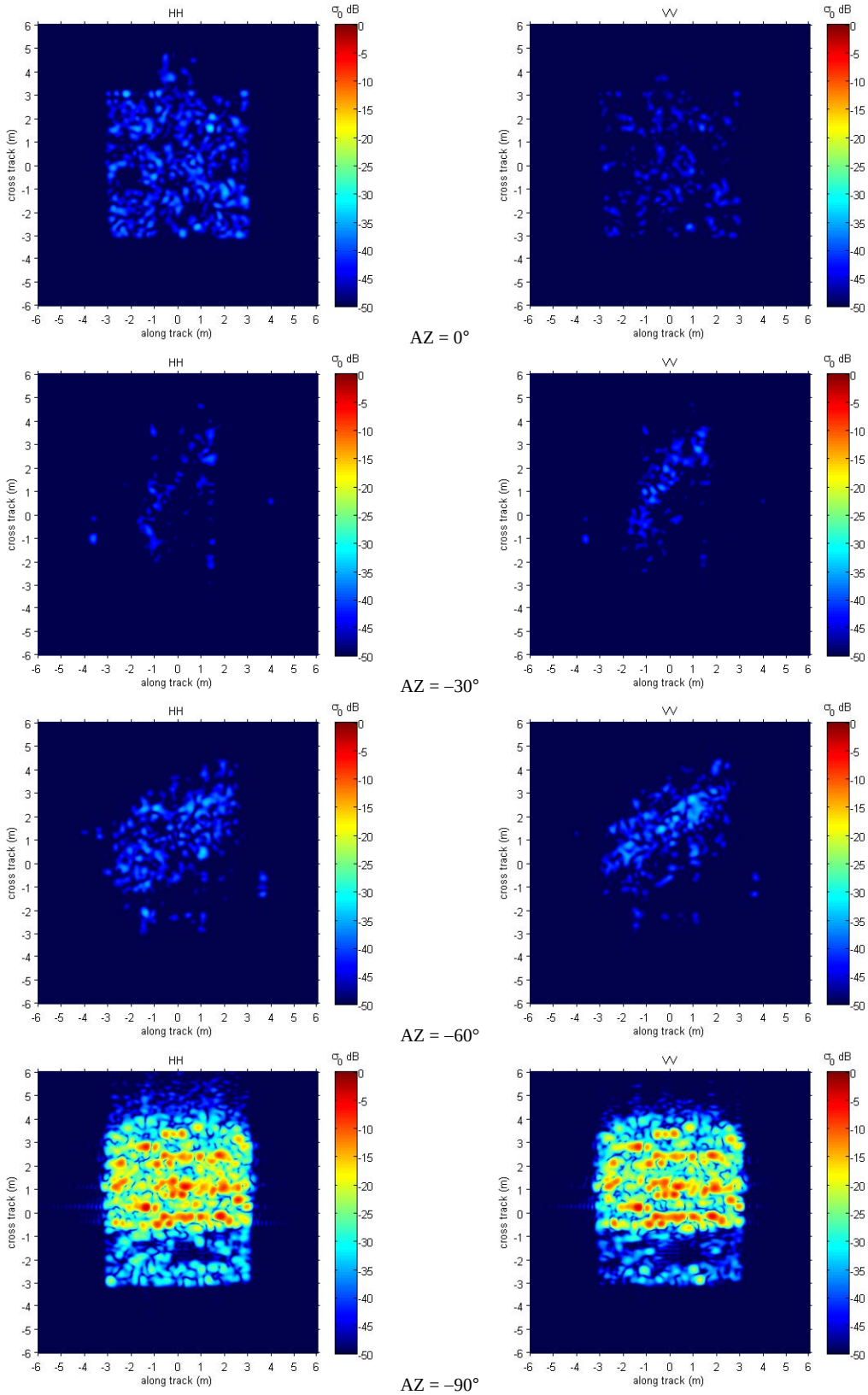

Figure V-59 Crevasse with snow bridge, 2-m depth, 8-inch resolution, $f_c = 16.8$ GHz *, 15° depression angle.*

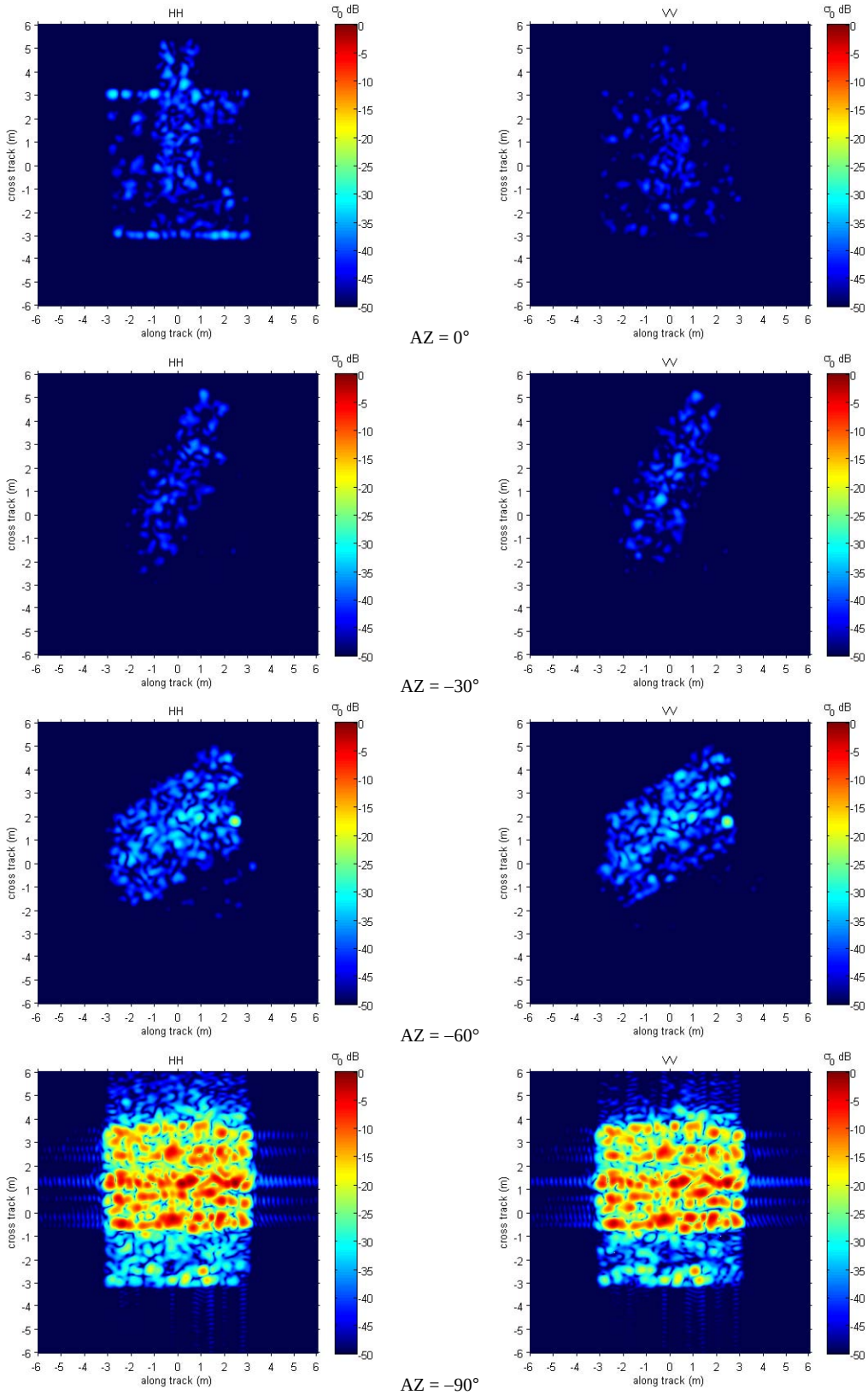

Figure V-60 Crevasse with snow bridge, 2-m depth, 8-inch resolution, $f_c = 16.8$ GHz *, 30° depression angle.*

Snow bridge only, Siple Dome model, 2-m depth

Monochrome, snow-bridge depth is 2.0 m

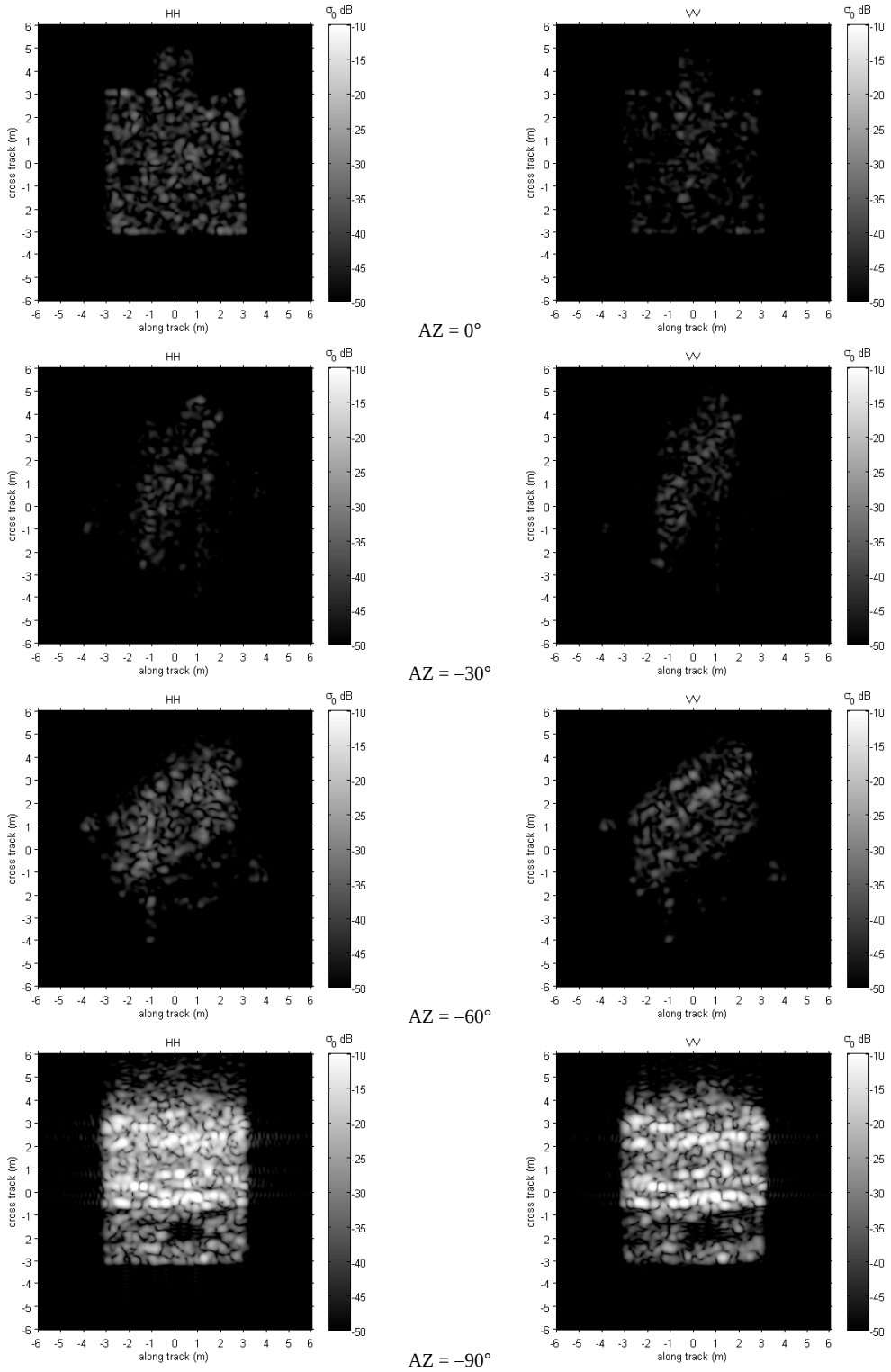

Figure V-61 Snow bridge only, 2-m depth, 8-inch resolution, $f_c = 9.5$ GHz *, 15° depression angle.*

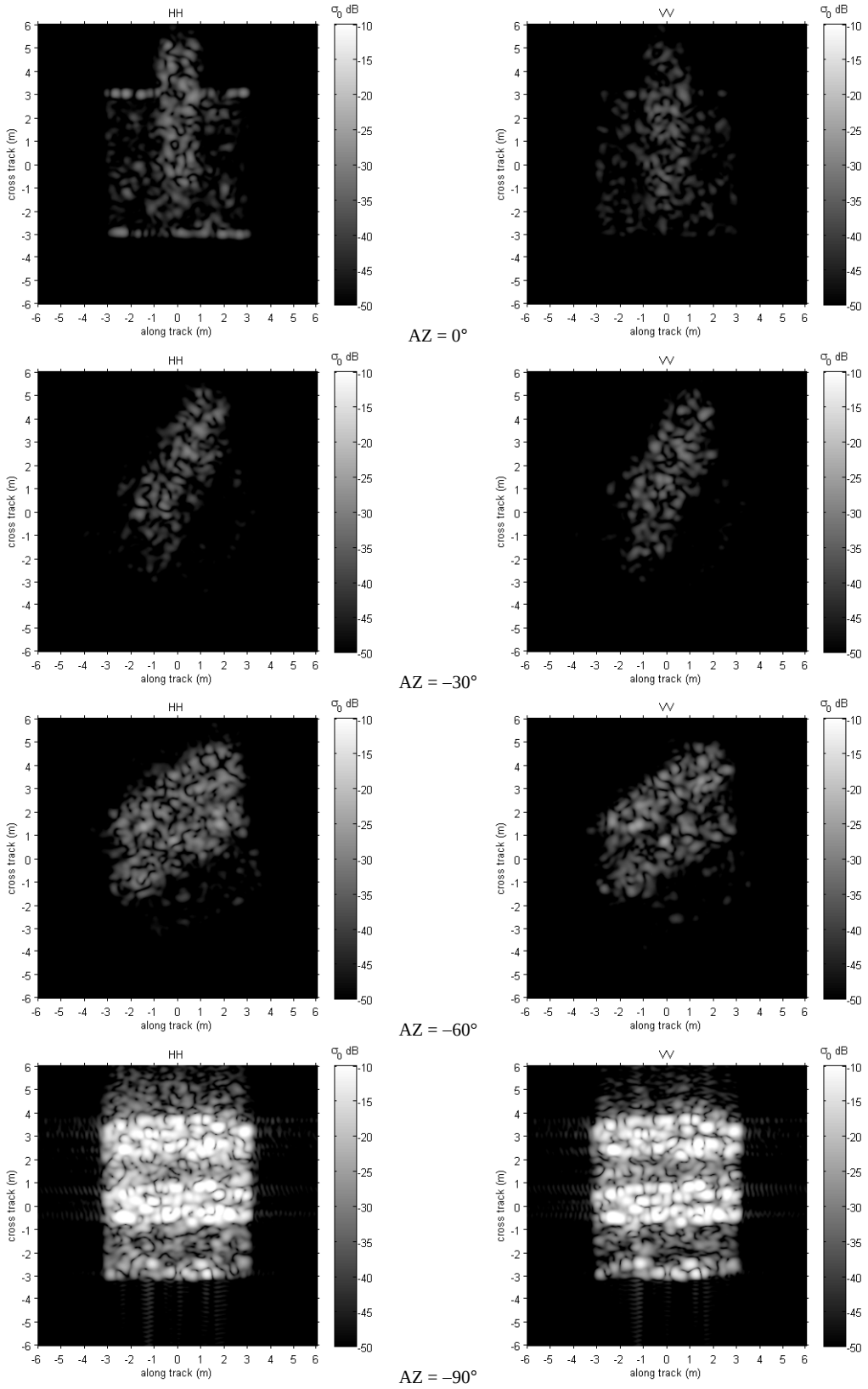

Figure V-62 Snow bridge only, 2-m depth, 8-inch resolution, $f_c = 9.5$ GHz *, 30° depression angle.*

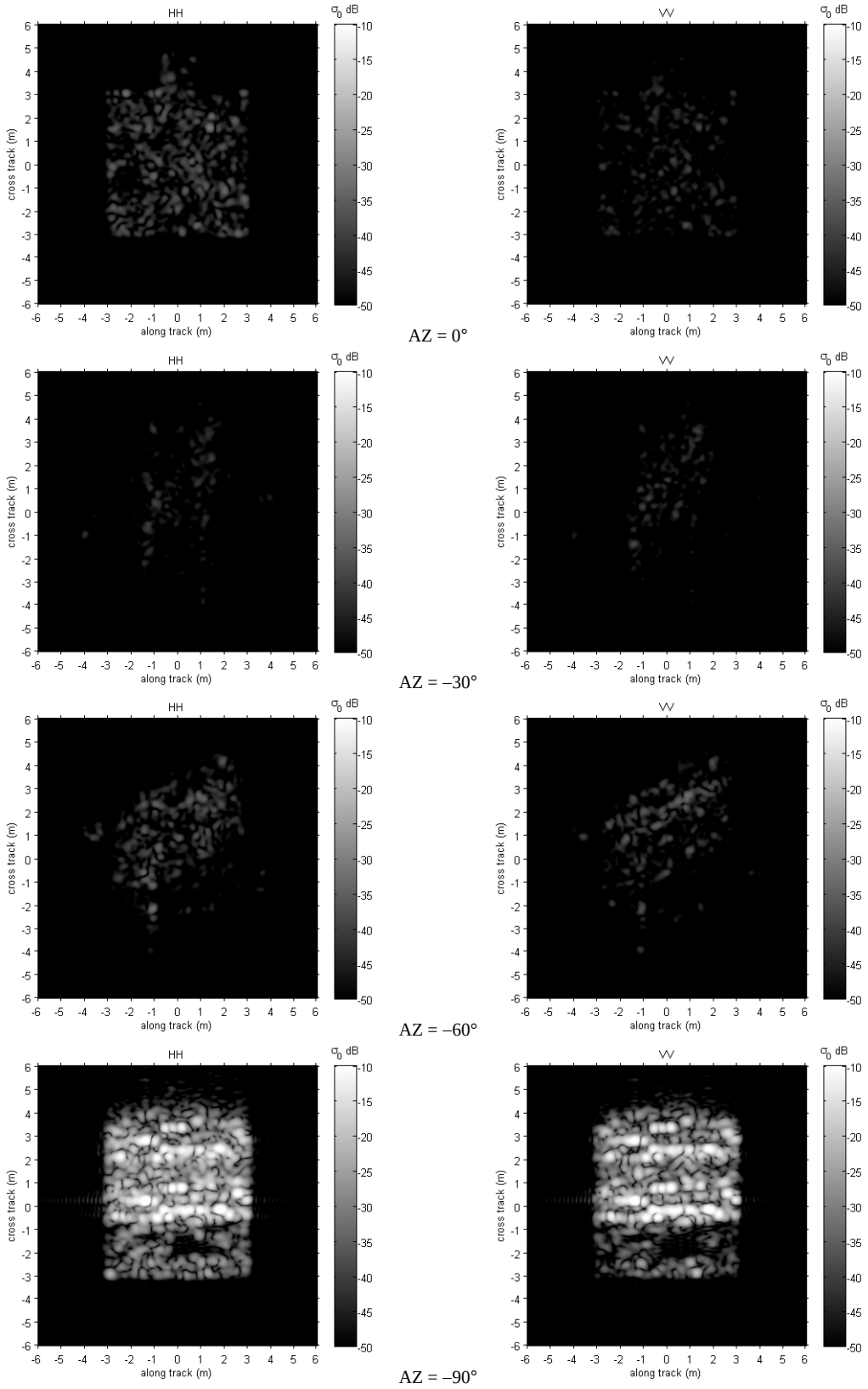

Figure V-63 Snow bridge only, 2-m depth, 8-inch resolution, $f_c = 16.8$ GHz *, 15° depression angle.*

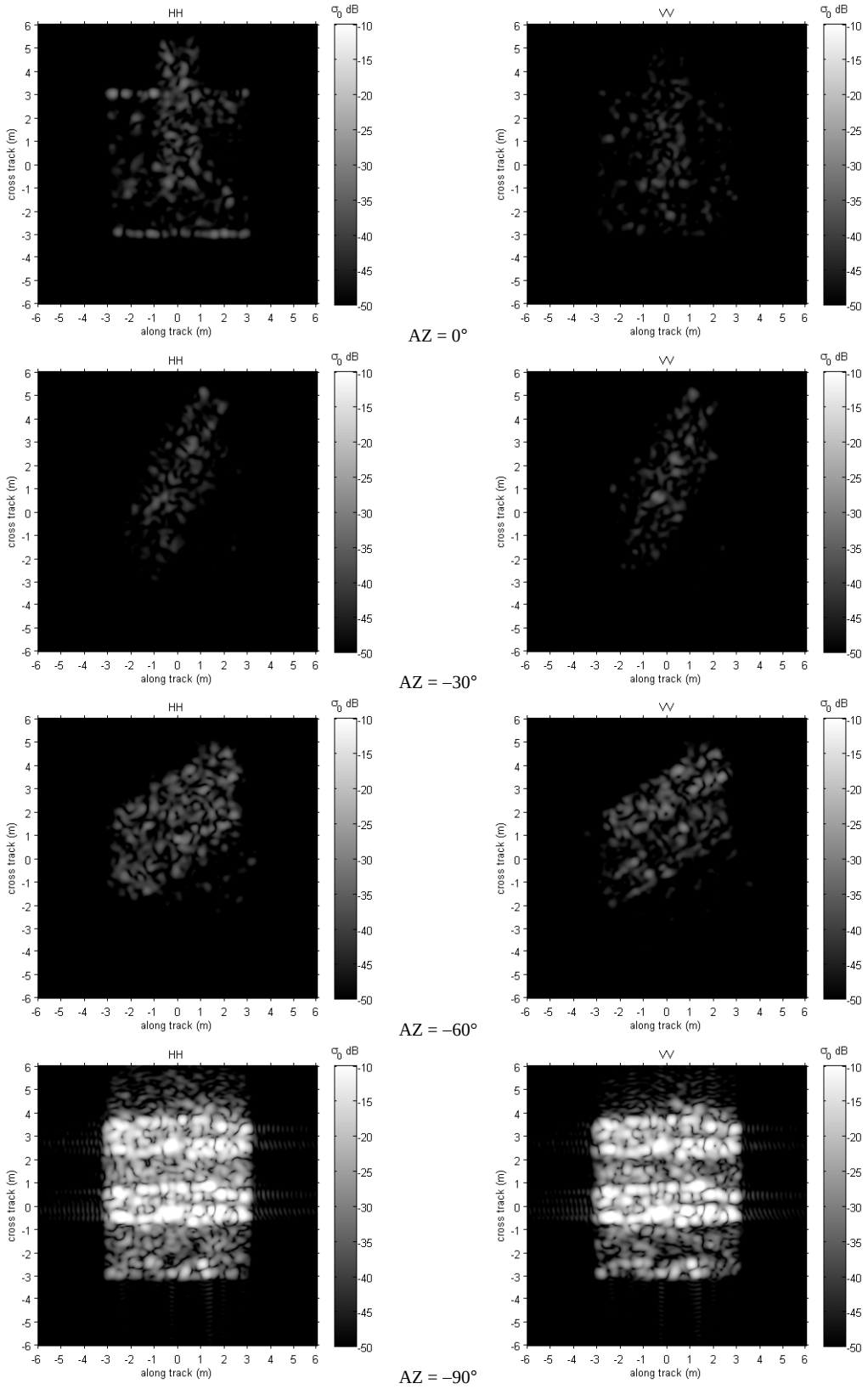

Figure V-64 Snow bridge only, 2-m depth, 8-inch resolution, $f_c = 16.8$ GHz *, 30° depression angle.*

Square root of magnitude (4th root of power), snow bridge only, 2-m depth

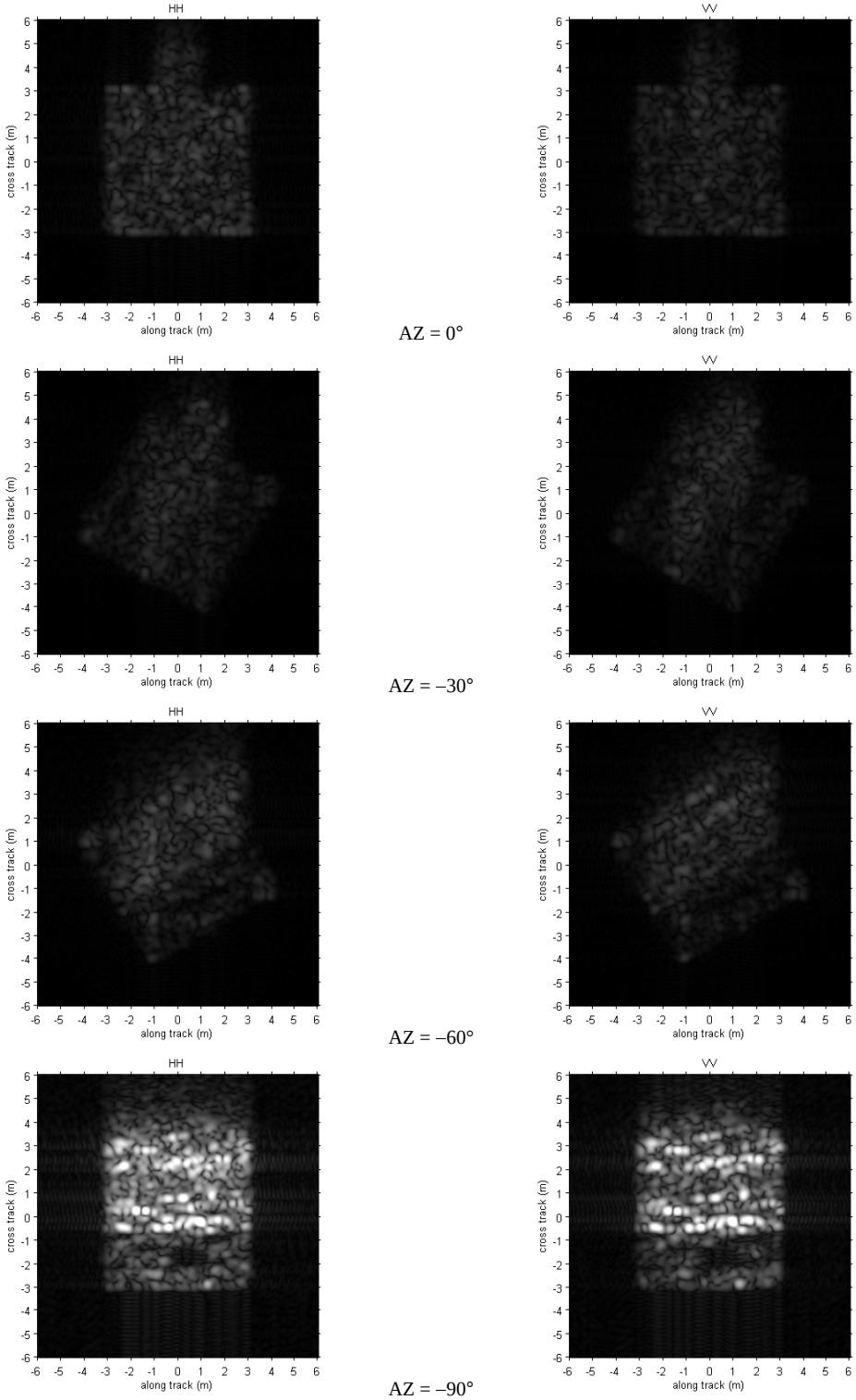

Figure V-65 Snow bridge only, 2-m depth, 8-inch resolution, $f_c = 9.5$ GHz *, 15° depression angle.*

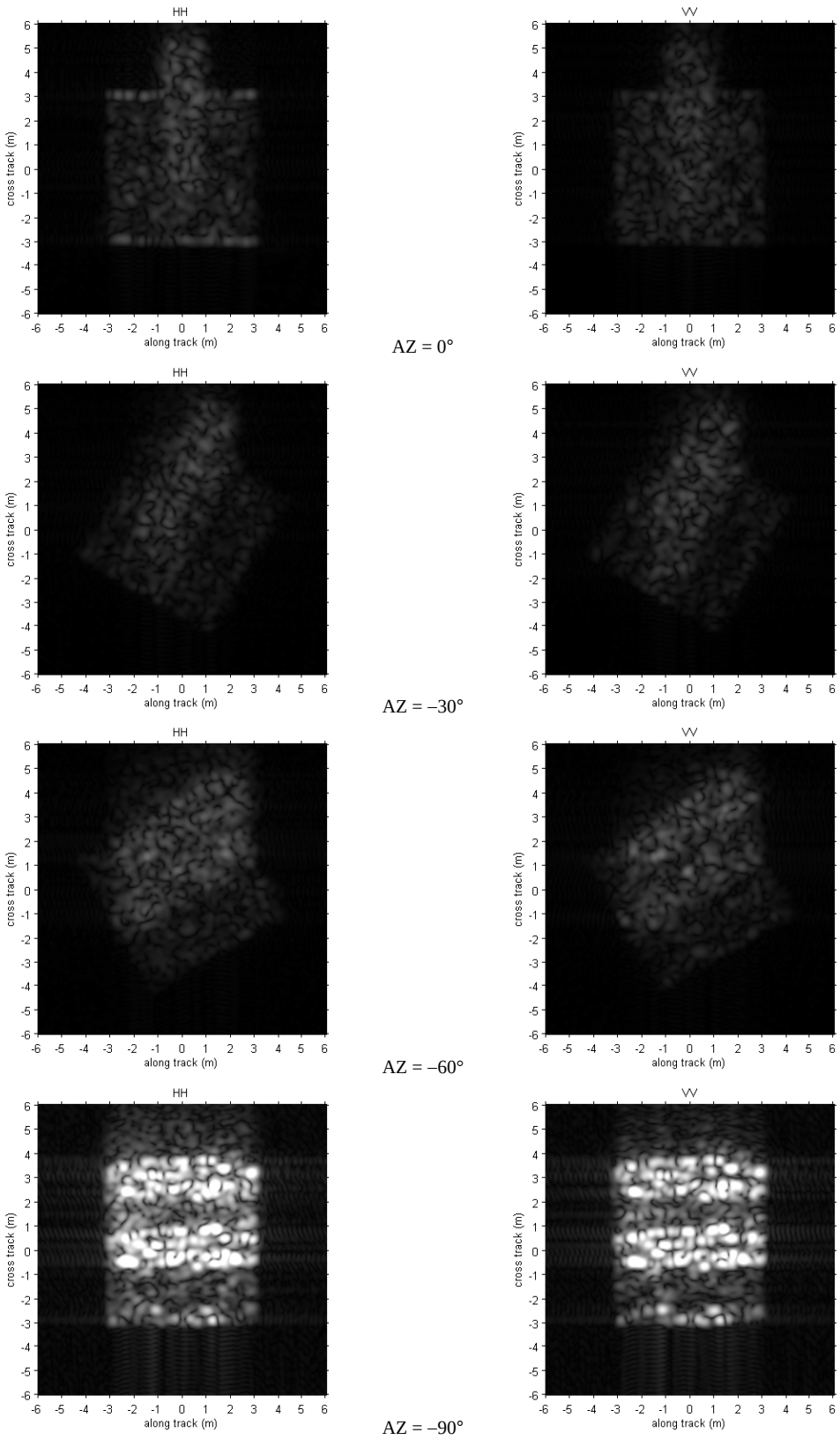

Figure V-66 Snow bridge only, 2-m depth, 8-inch resolution, $f_c = 9.5$ GHz *, 30° depression angle.*

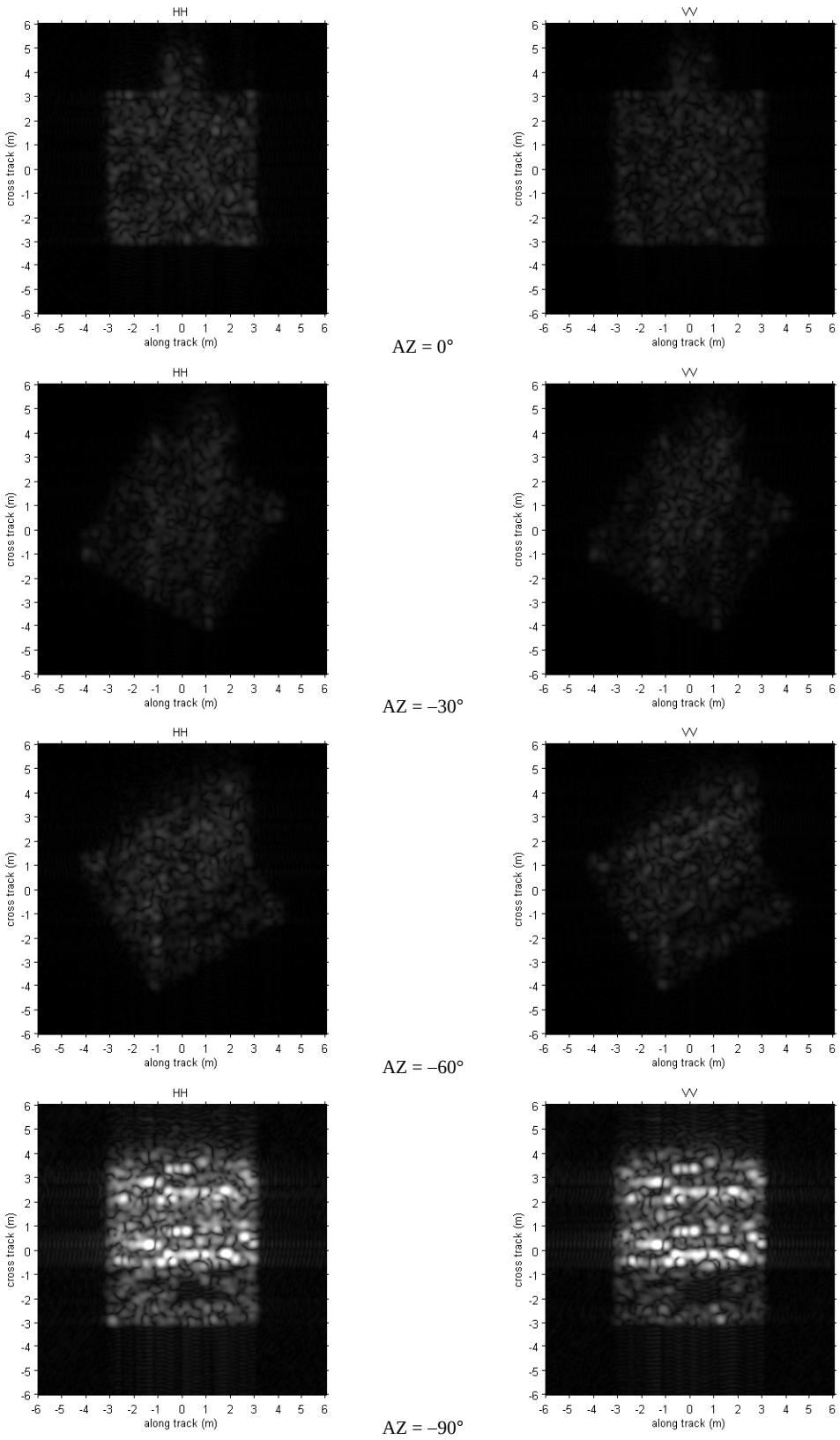

Figure V-67 Snow bridge only, 2-m depth, 8-inch resolution, $f_c = 16.8$ GHz *, 15° depression angle.*

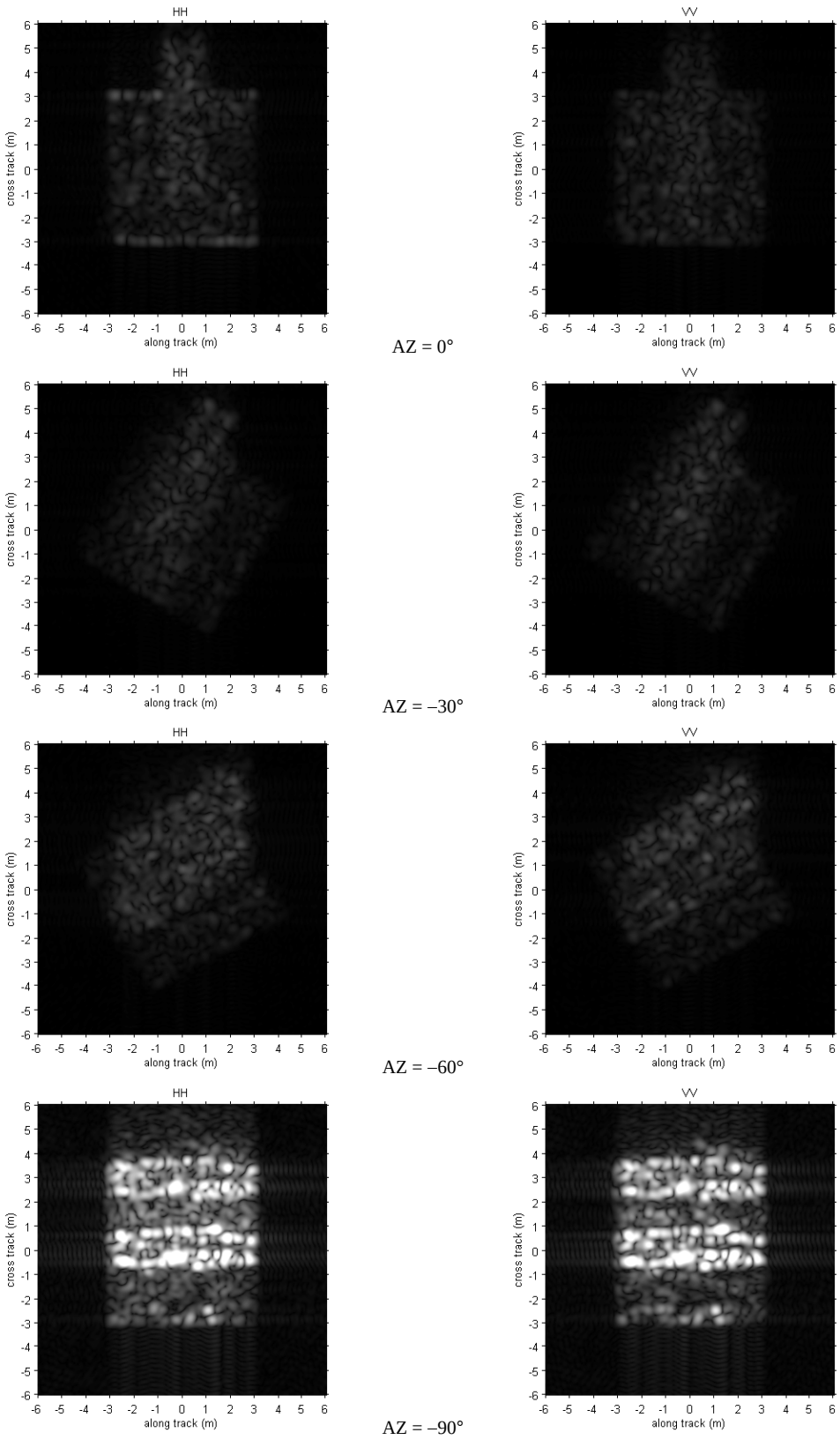

Figure V-68 Snow bridge only, 2-m depth, 8-inch resolution, $f_c = 16.8$ GHz *, 30° depression angle.*

Color, snow bridge only, 2-m depth

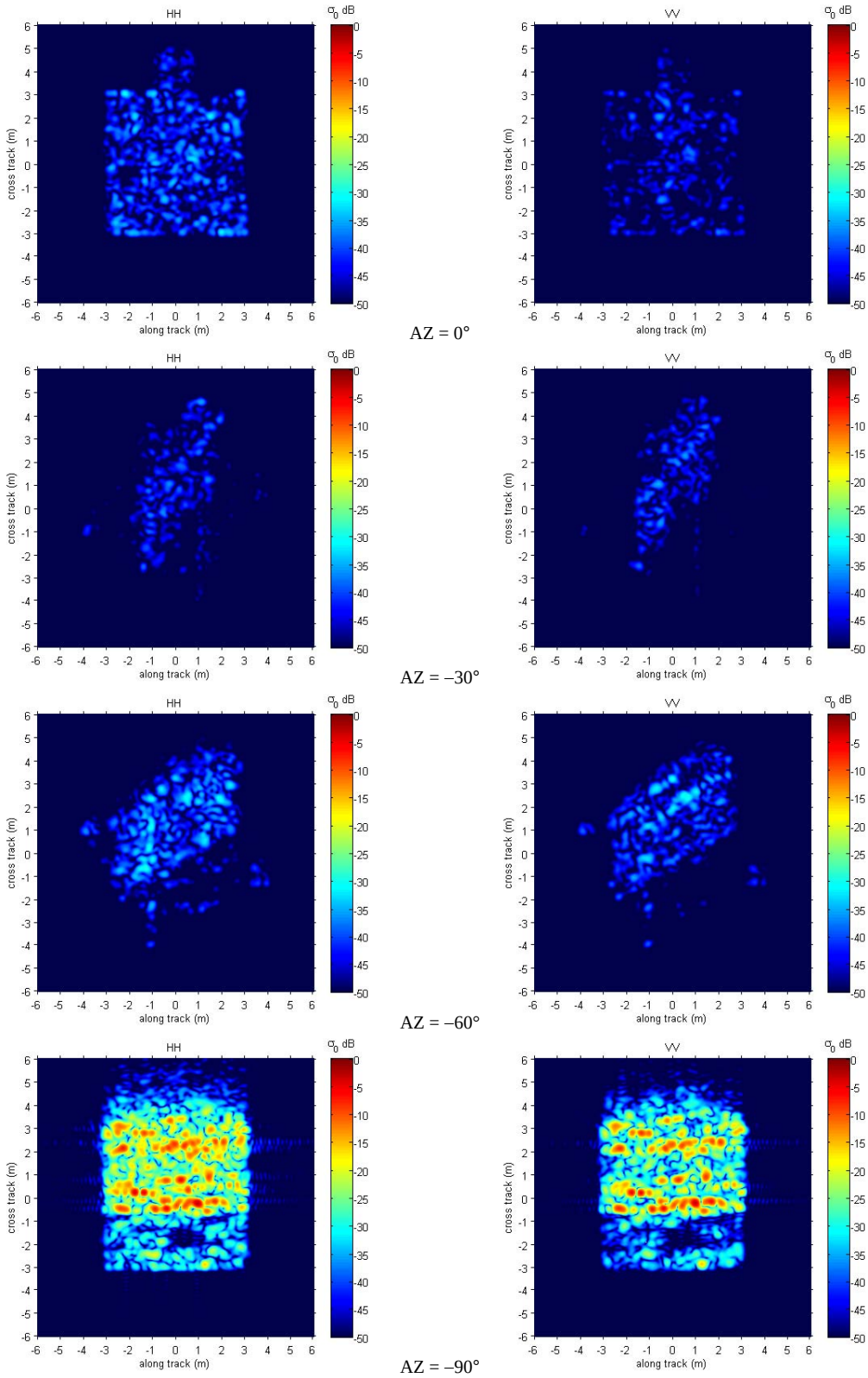

Figure V-69 Snow bridge only, 2-m depth, 8-inch resolution, $f_c = 9.5$ GHz *, 15° depression angle.*

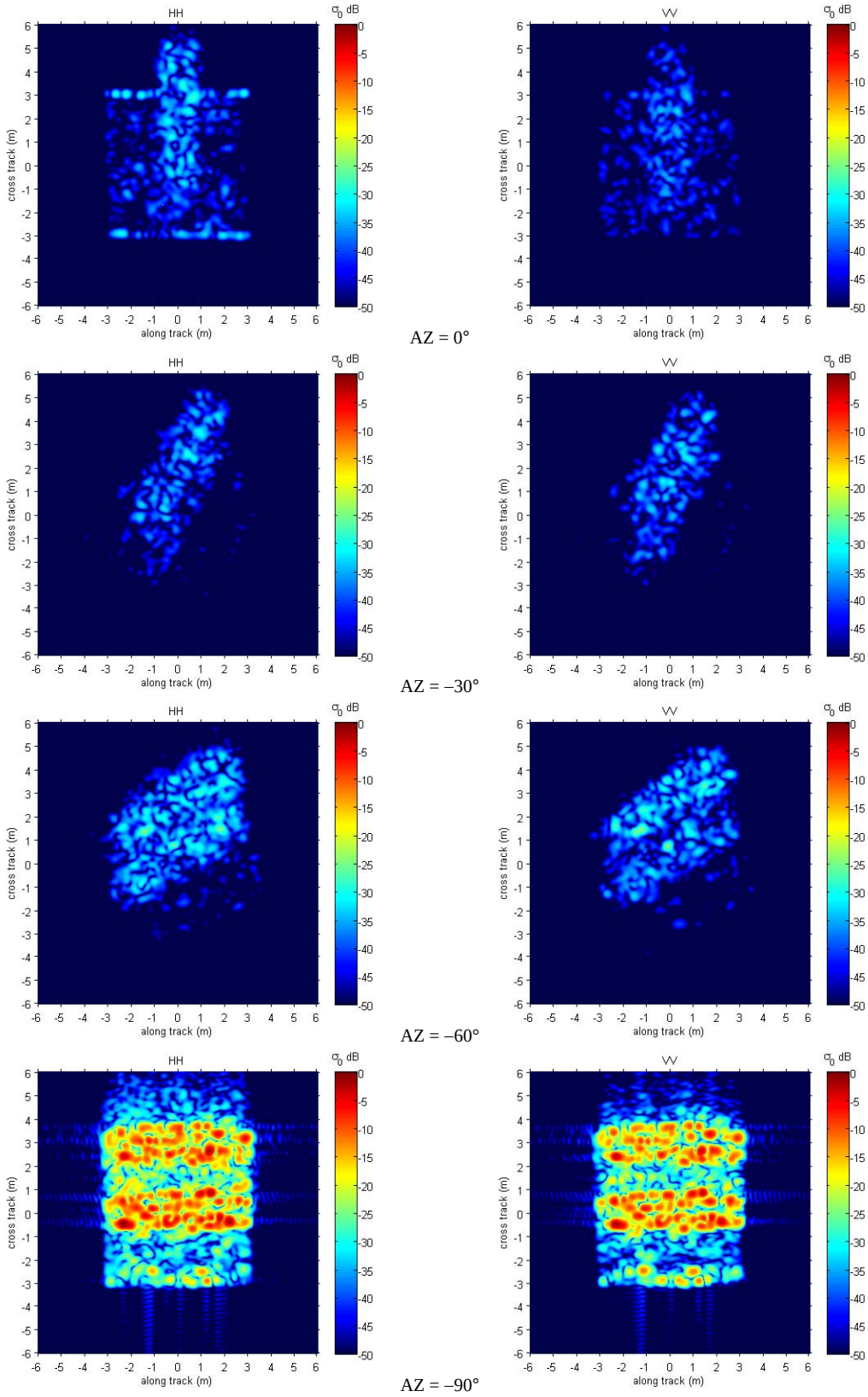

Figure V-70 Snow bridge only, 2-m depth, 8-inch resolution, $f_c = 9.5$ GHz *, 30° depression angle.*

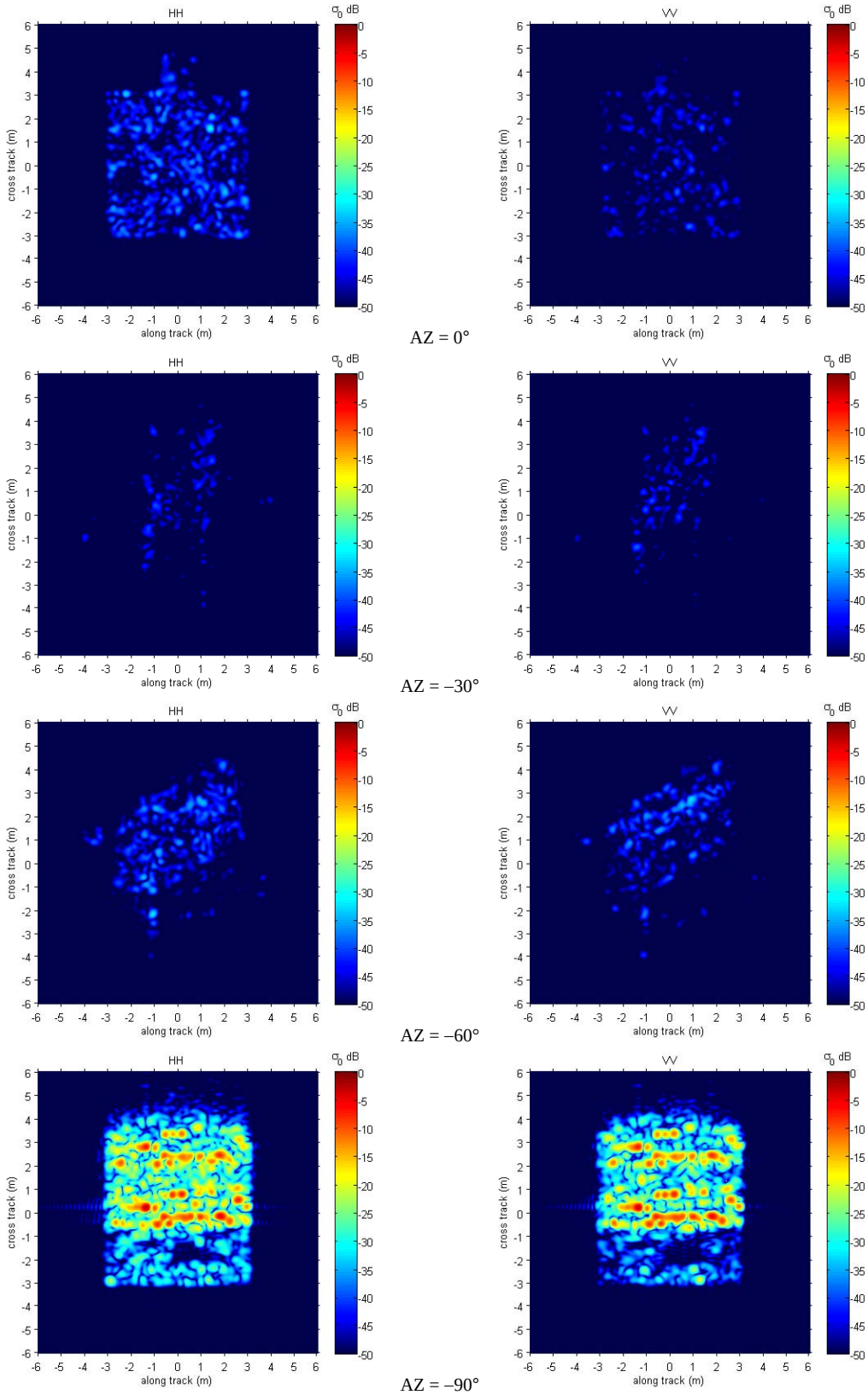

Figure V-71 Snow bridge only, 2-m depth, 8-inch resolution, $f_c = 16.8$ GHz *, 15° depression angle.*

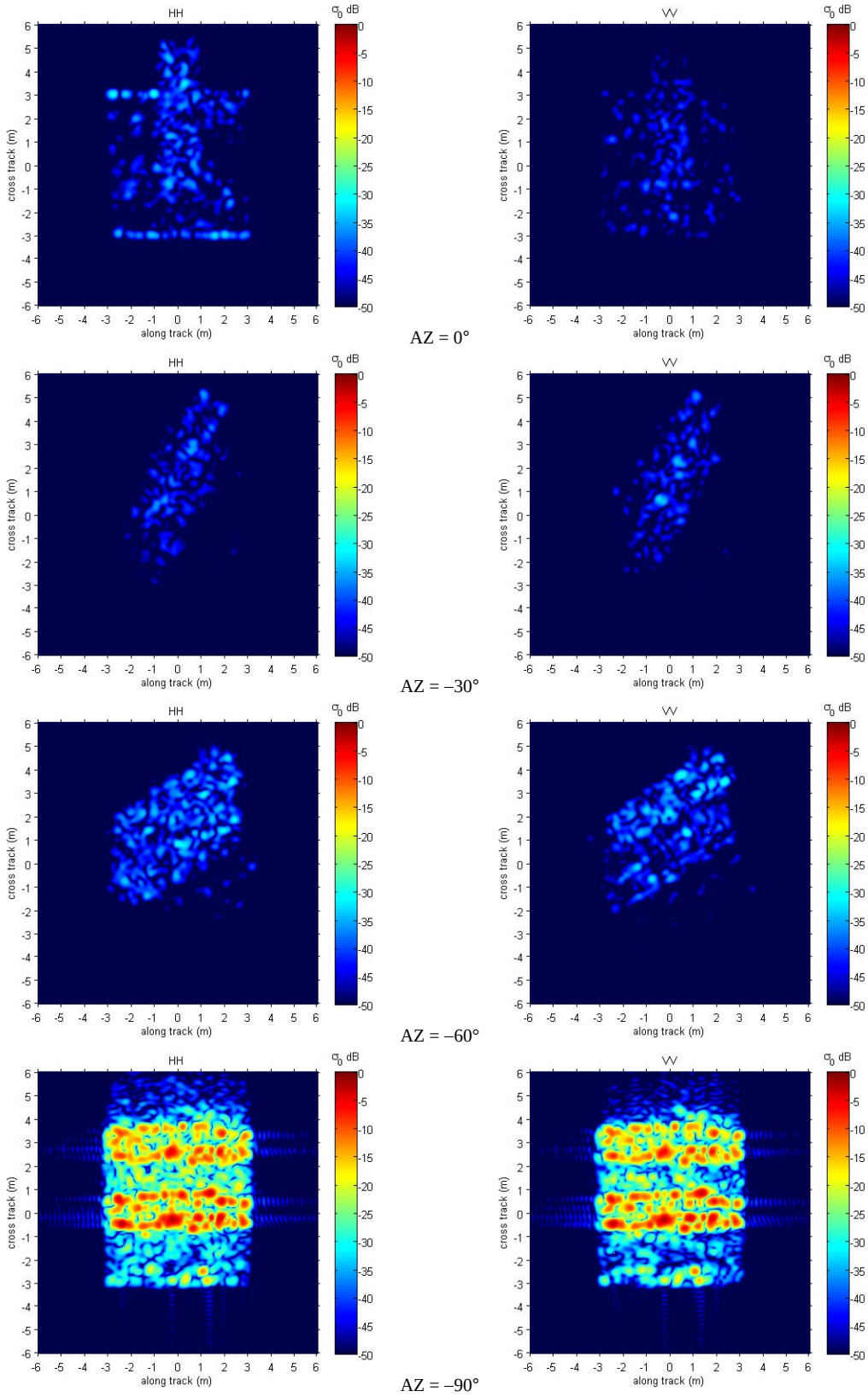

Figure V-72 Snow bridge only, 2-m depth, 8-inch resolution, $f_c = 16.8$ GHz , 30° depression angle.

Snow bridge only, Siple Dome model, 4-m depth

Monochrome, snow-bridge depth is 4.0 m

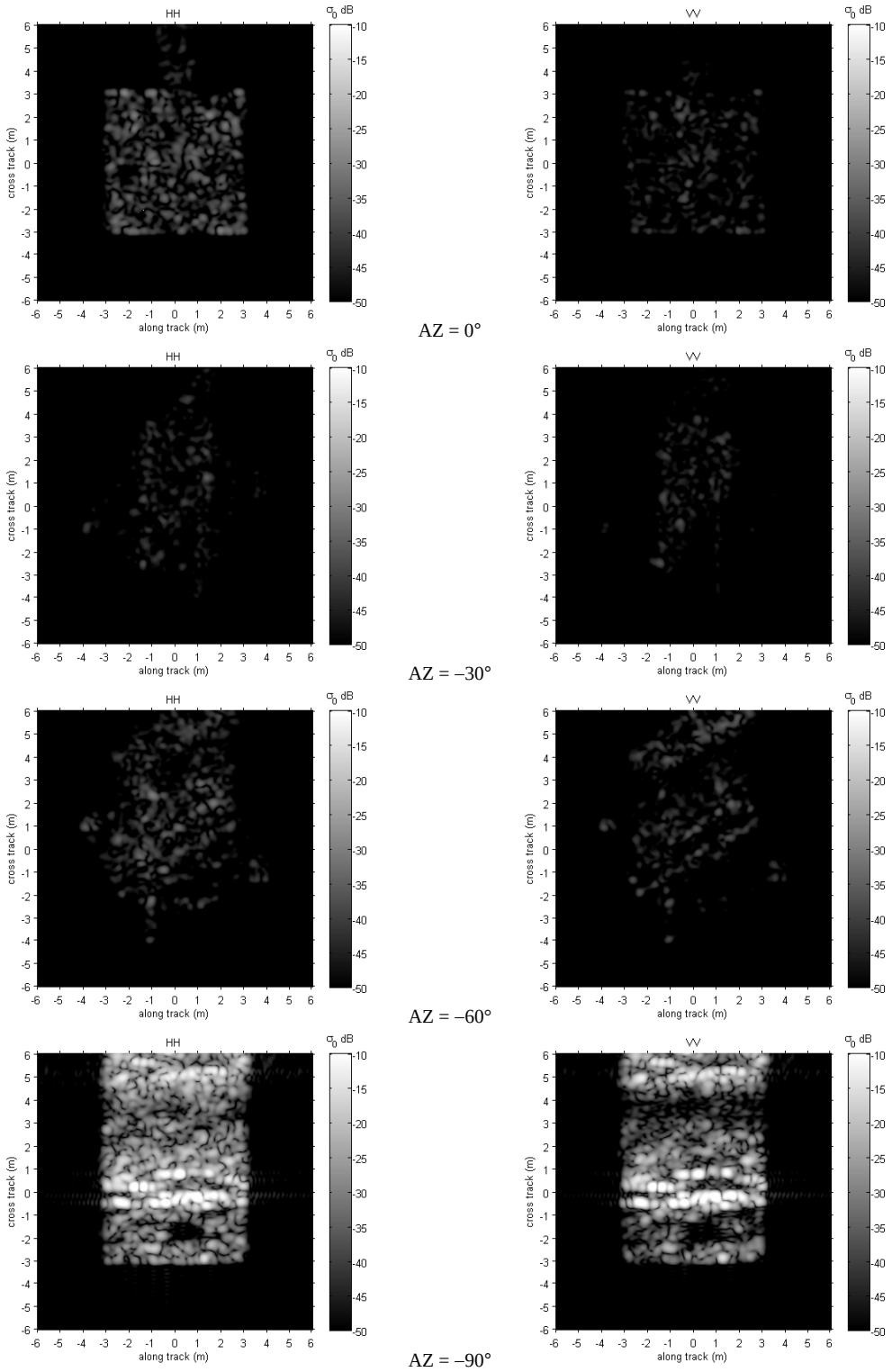

Figure V-73 Snow bridge only, 4-m depth, 8-inch resolution, $f_c = 9.5$ GHz *, 15° depression angle.*

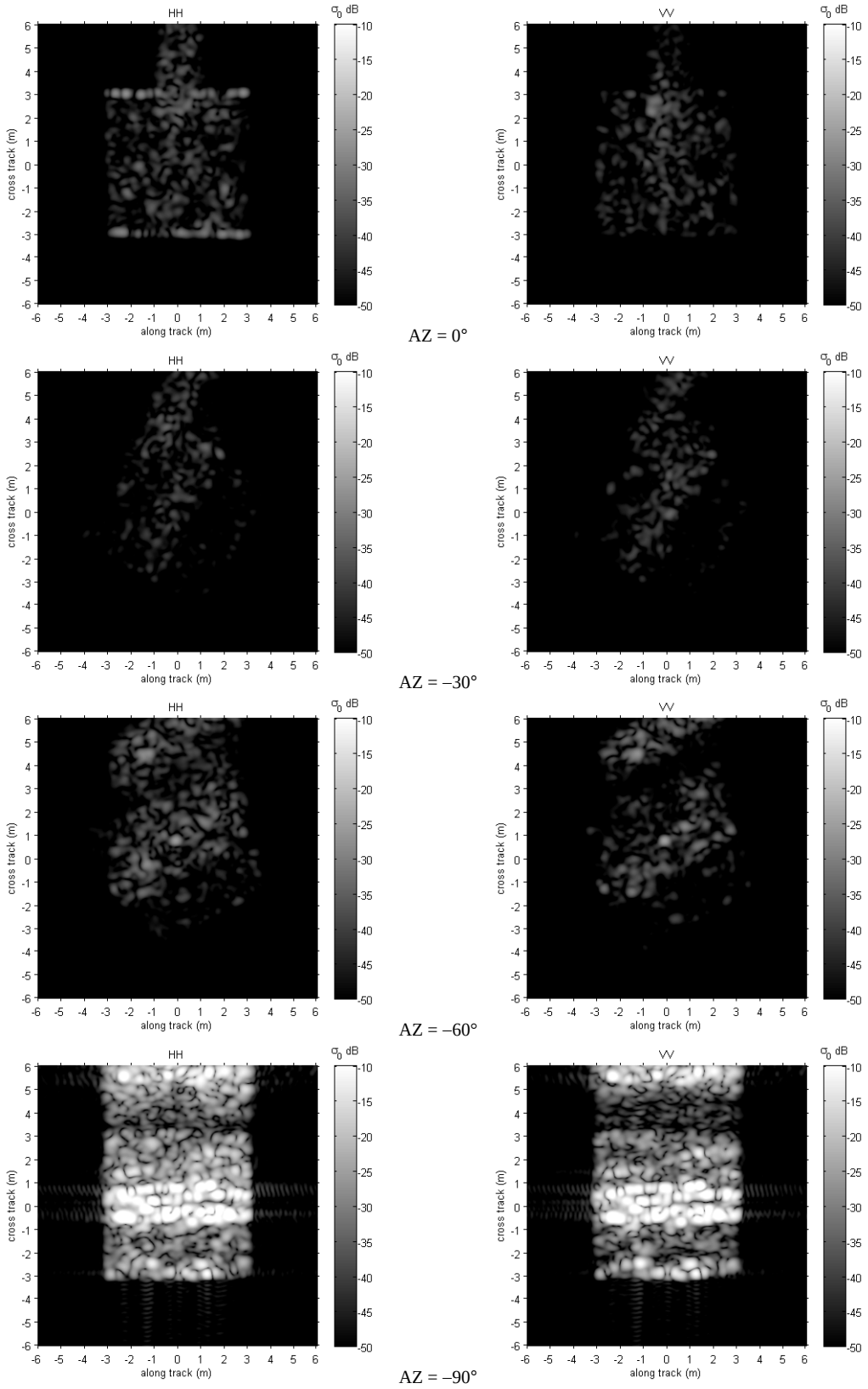

Figure V-74 Snow bridge only, 4-m depth, 8-inch resolution, $f_c = 9.5$ GHz *, 30° depression angle.*

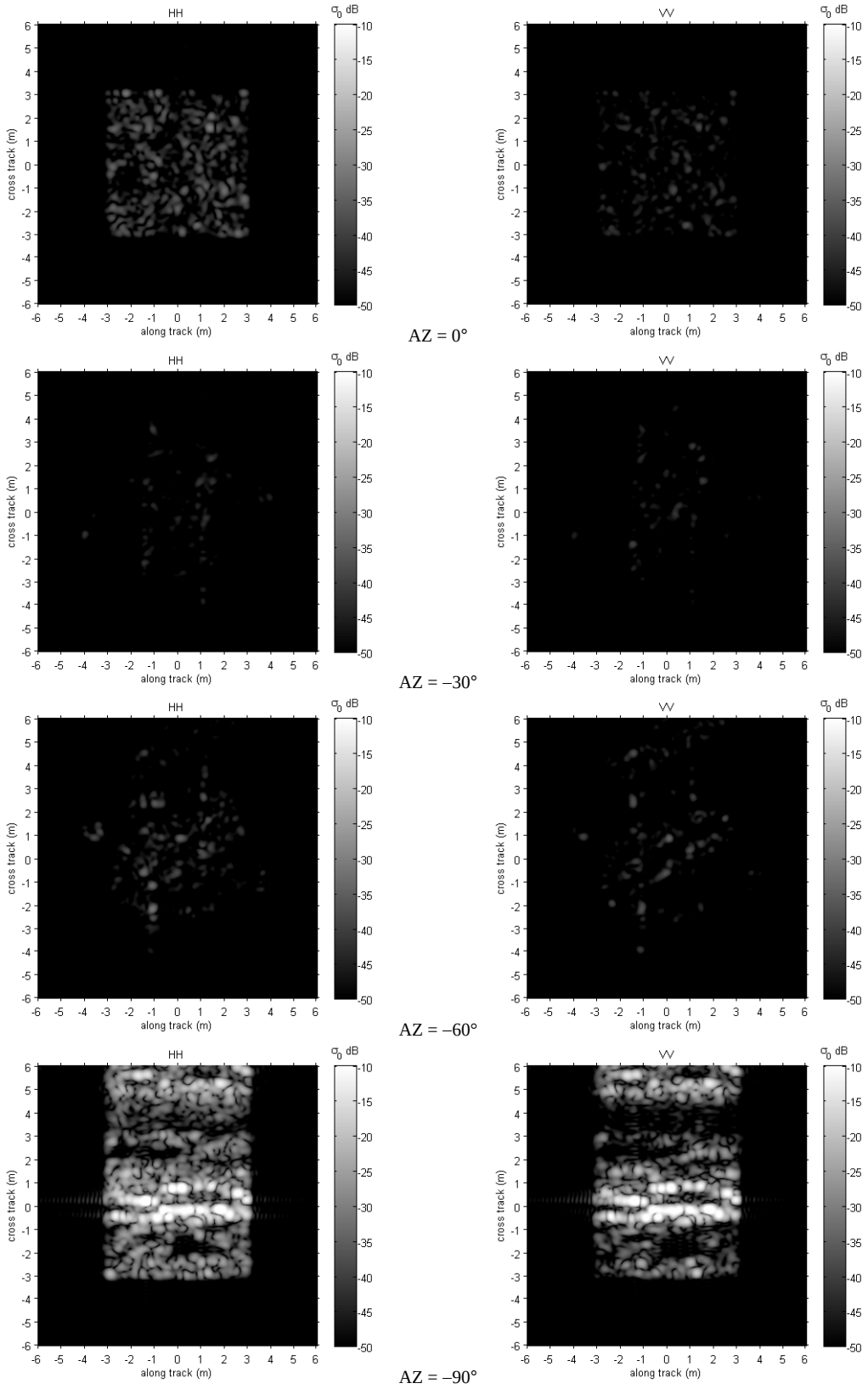

Figure V-75 Snow bridge only, 4-m depth, 8-inch resolution, $f_c = 16.8$ GHz *, 15° depression angle.*

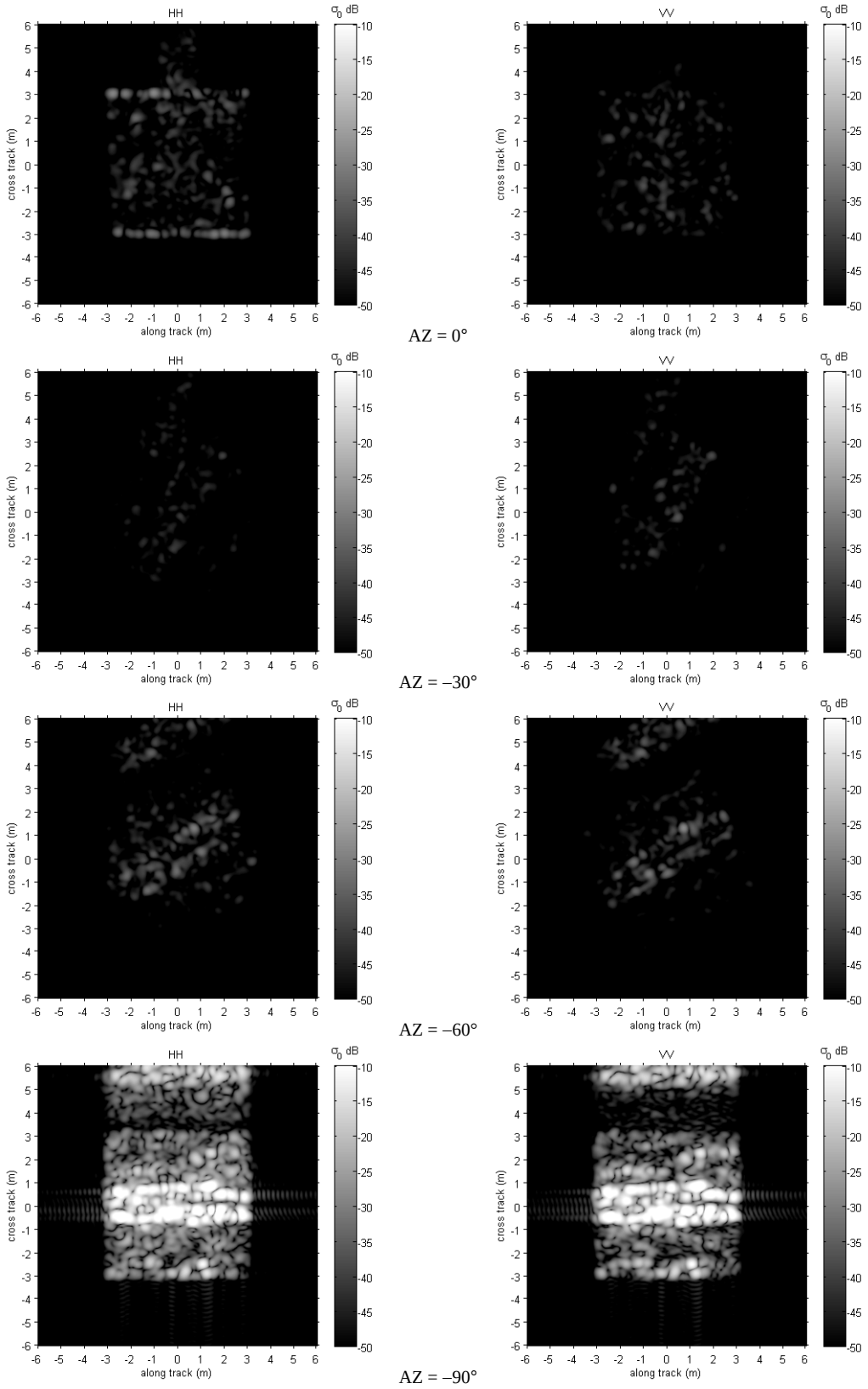

Figure V-76 Snow bridge only, 4-m depth, 8-inch resolution, $f_c = 16.8$ GHz *, 30° depression angle.*

Square root of magnitude (4th root of power), snow bridge only, 4-m depth

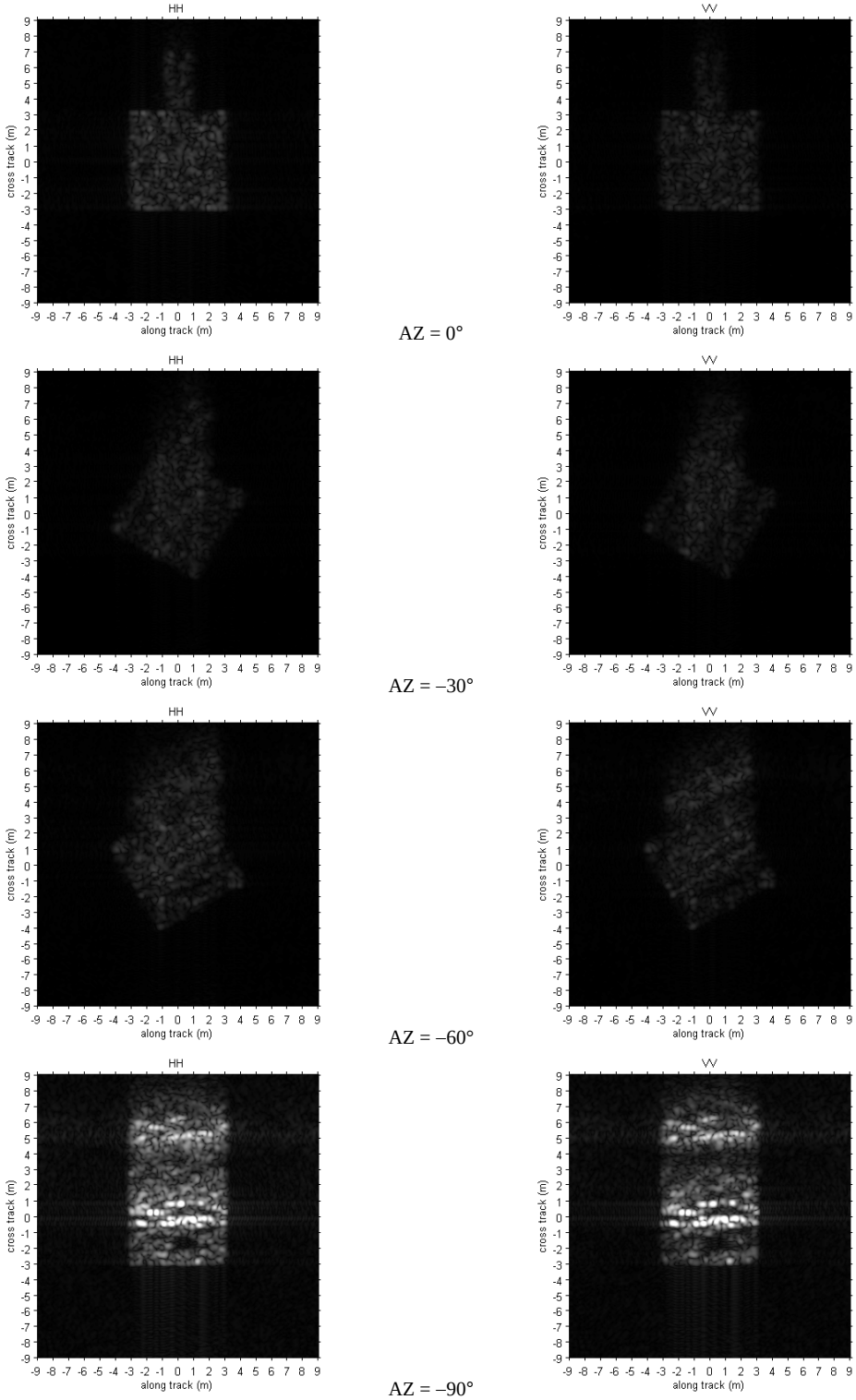

Figure V-77 Snow bridge only, 4-m depth, 8-inch resolution, $f_c = 9.5$ GHz *, 15° depression angle.*

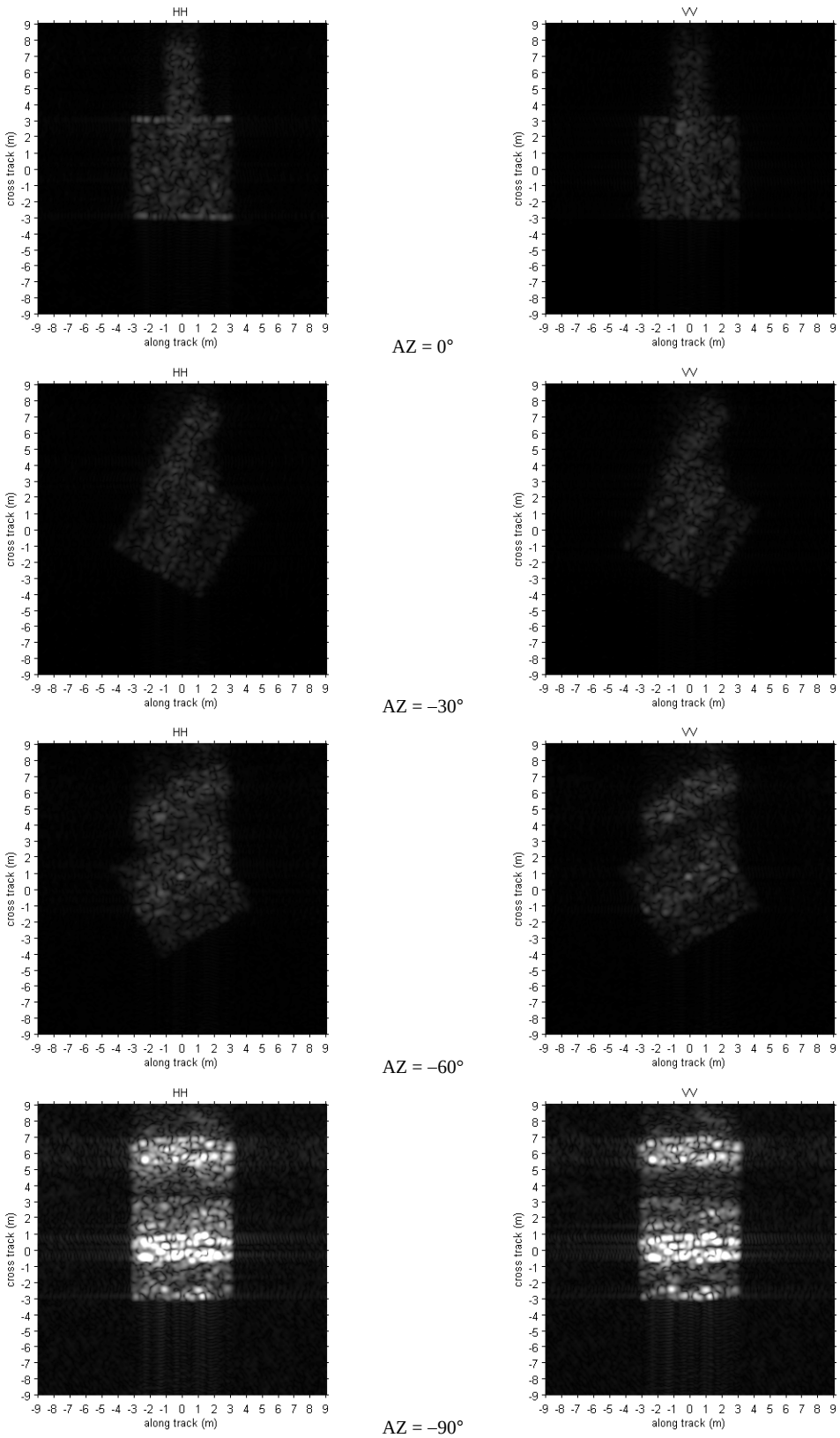

Figure V-78 Snow bridge only, 4-m depth, 8-inch resolution, $f_c = 9.5$ GHz *, 30° depression angle.*

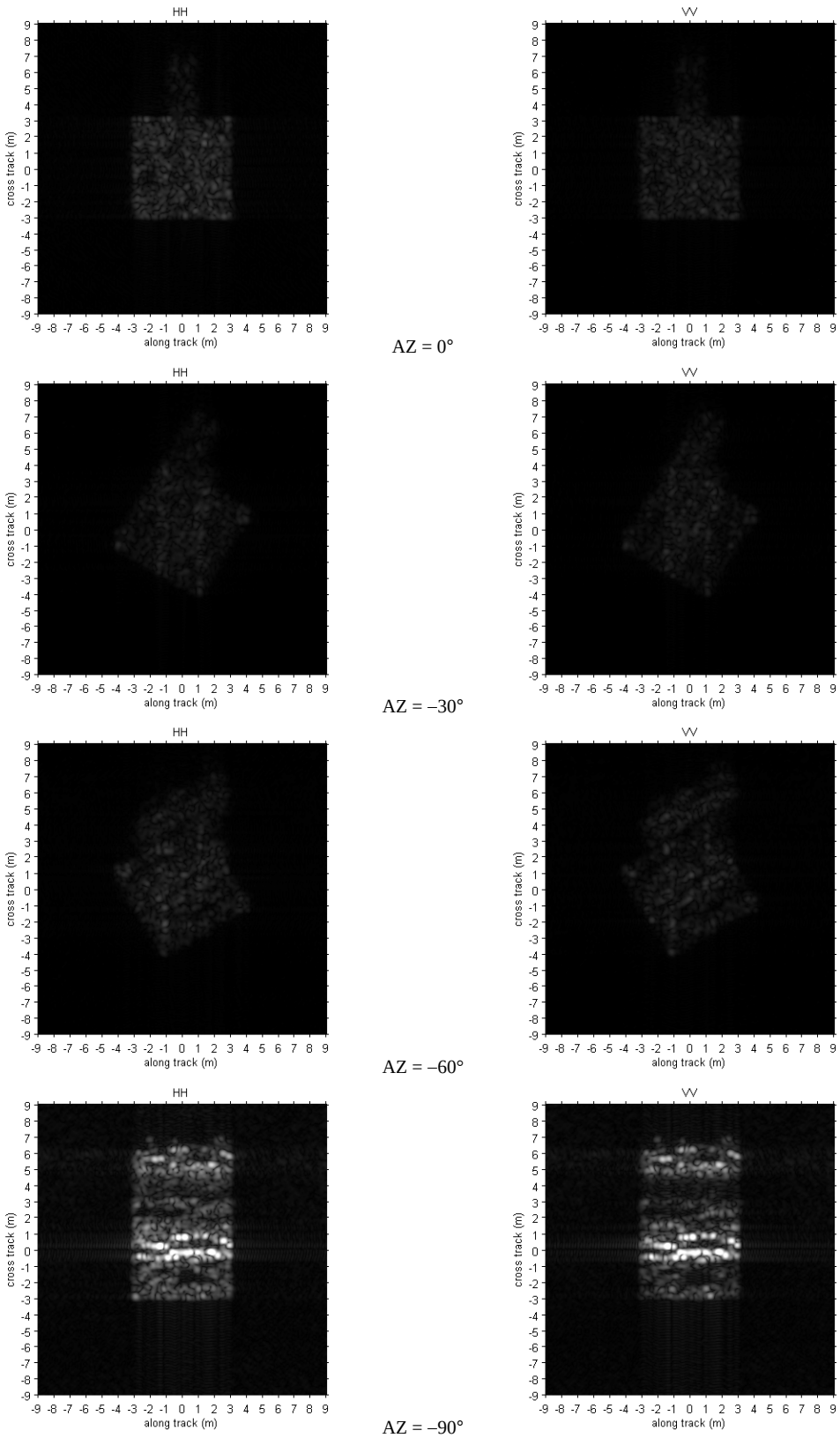

Figure V-79 Snow bridge only, 4-m depth, 8-inch resolution, $f_c = 16.8$ GHz *, 15° depression angle.*

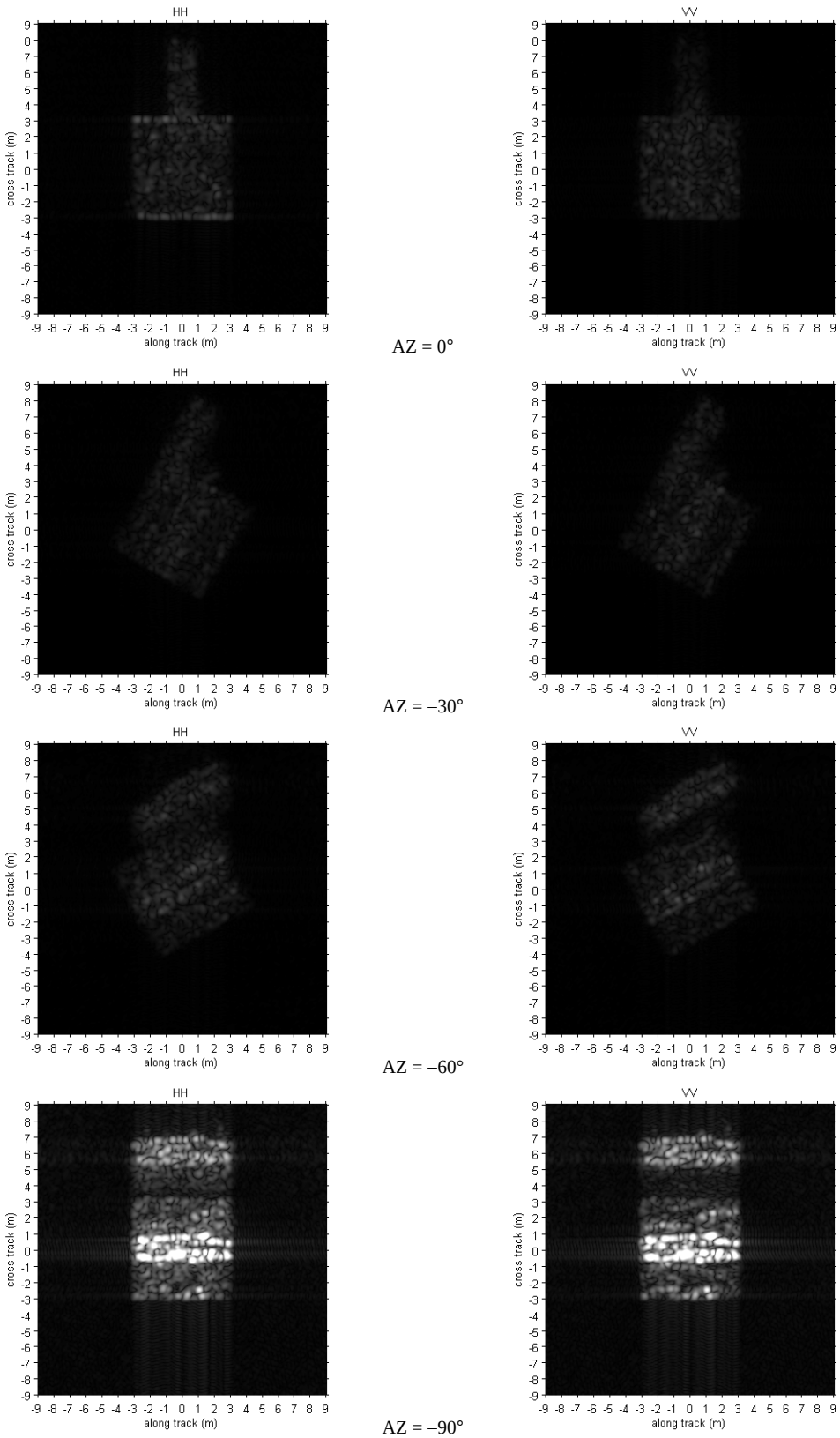

Figure V-80 Snow bridge only, 4-m depth, 8-inch resolution, $f_c = 16.8$ GHz *, 30° depression angle.*

Color, snow-bridge depth is 4.0 m

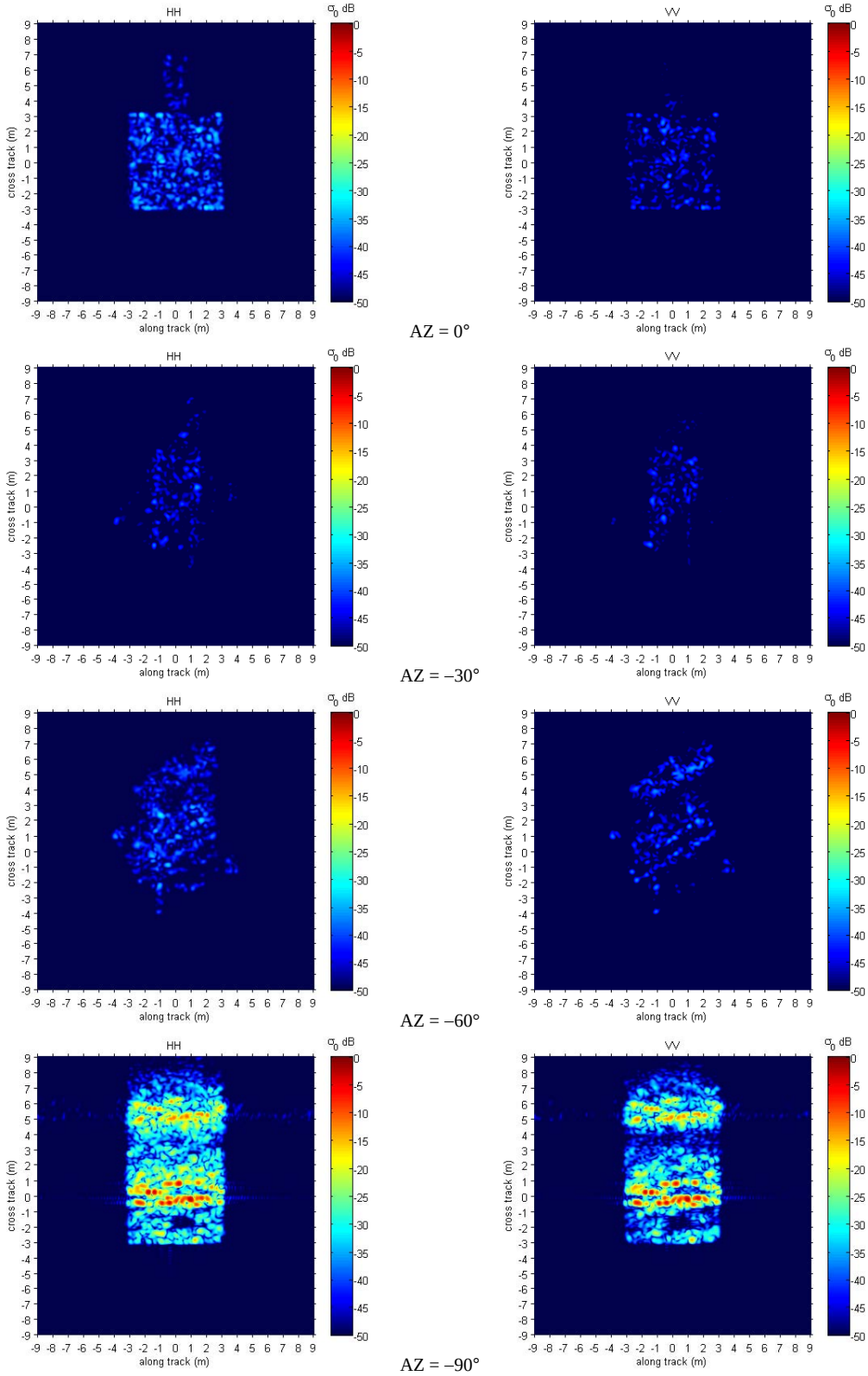

Figure V-81 Snow bridge only, 4-m depth, 8-inch resolution, $f_c = 9.5$ GHz *, 15° depression angle.*

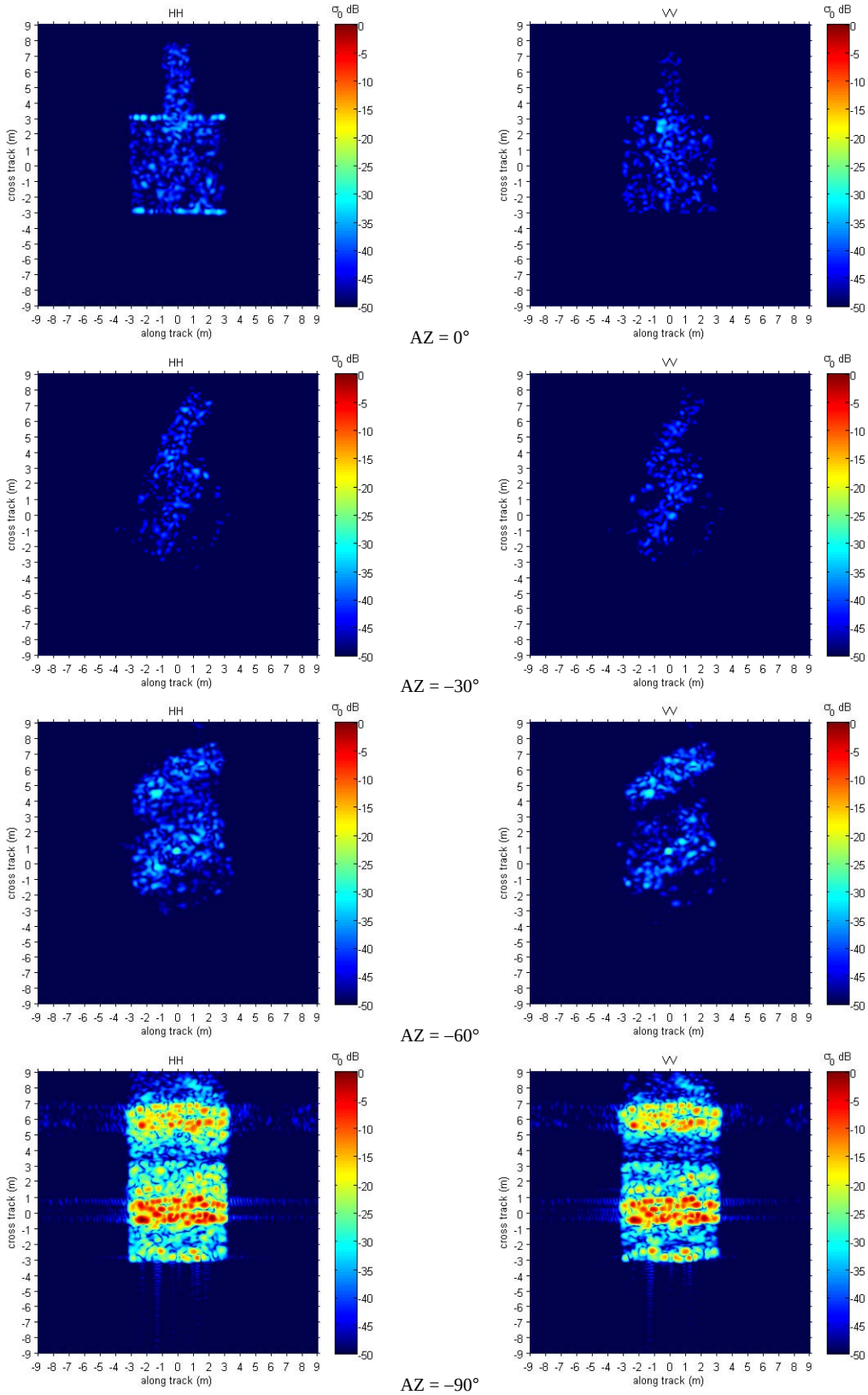

Figure V-82 Snow bridge only, 4-m depth, 8-inch resolution, $f_c = 9.5$ GHz *, 30° depression angle.*

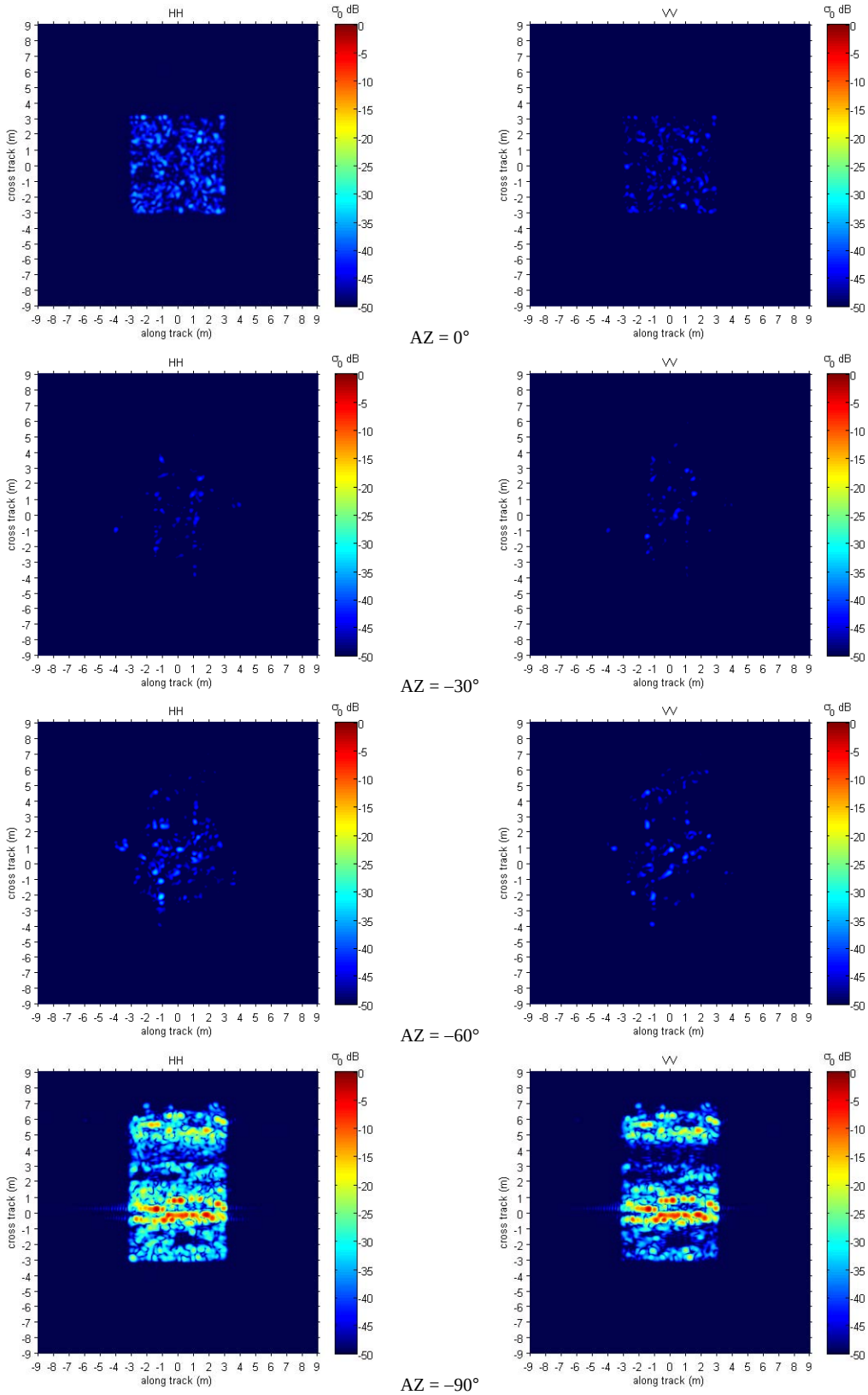

Figure V-83 Snow bridge only, 4-m depth, 8-inch resolution, $f_c = 16.8$ GHz *, 15° depression angle.*

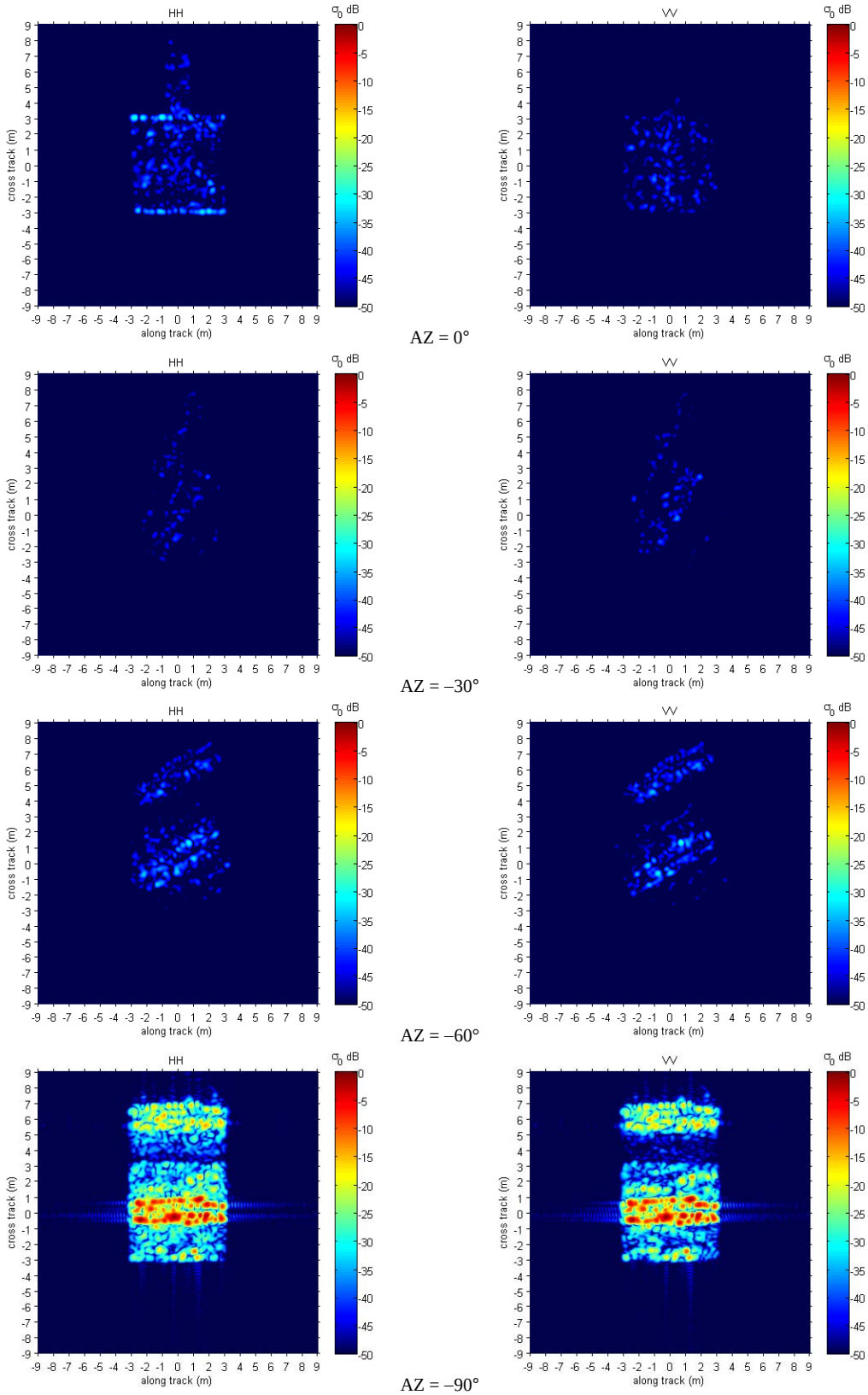

Figure V-84 Snow bridge only, 4-m depth, 8-inch resolution, $f_c = 16.8$ GHz *, 30° depression angle.*

Snow bridge only, Newall Glacier model, 4-m depth

Monochrome, snow-bridge depth is 4.0 m

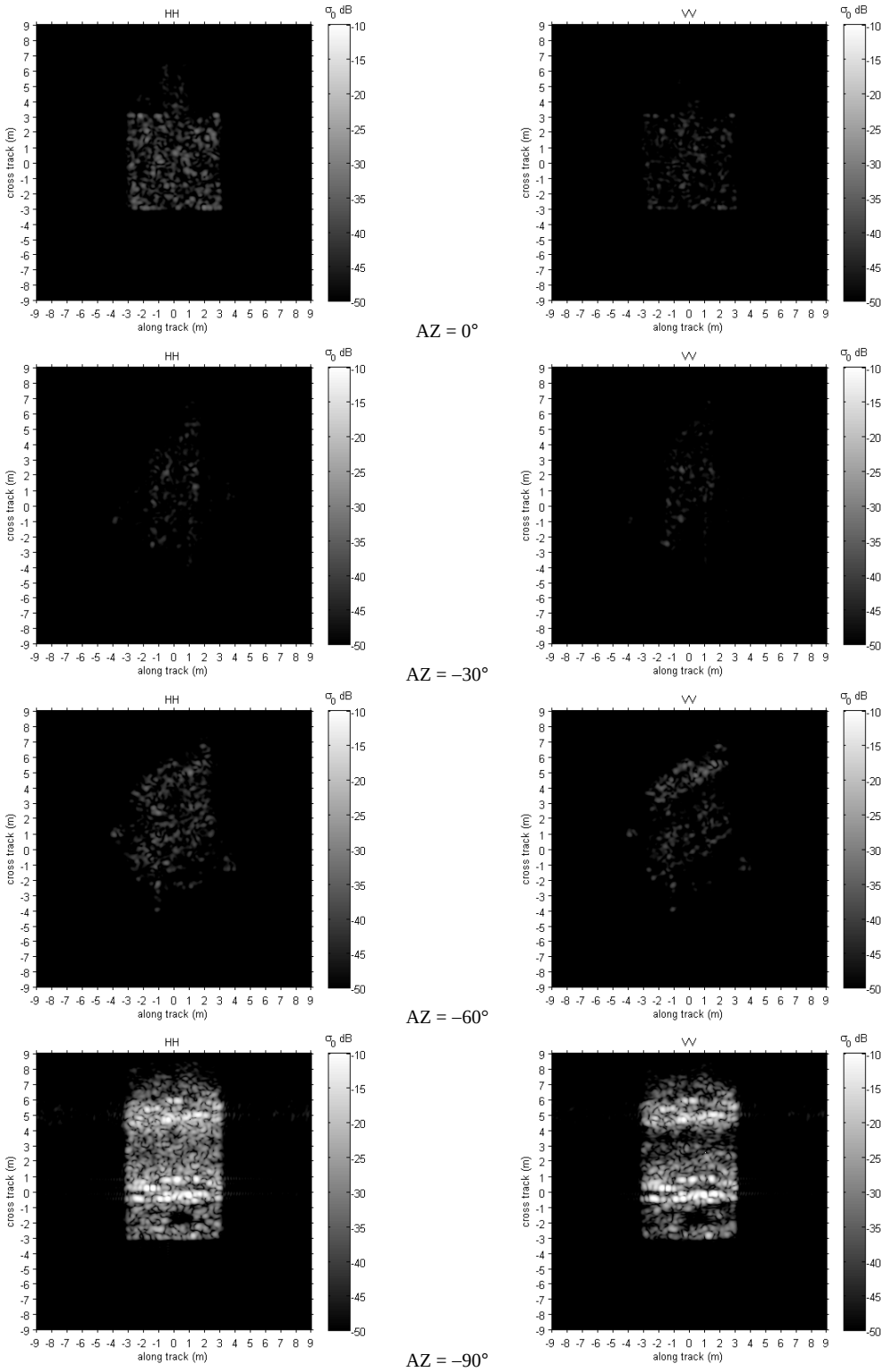

Figure V-85 Snow bridge only, 4-m depth, 8-inch resolution, $f_c = 9.5$ GHz *, 15° depression angle.*

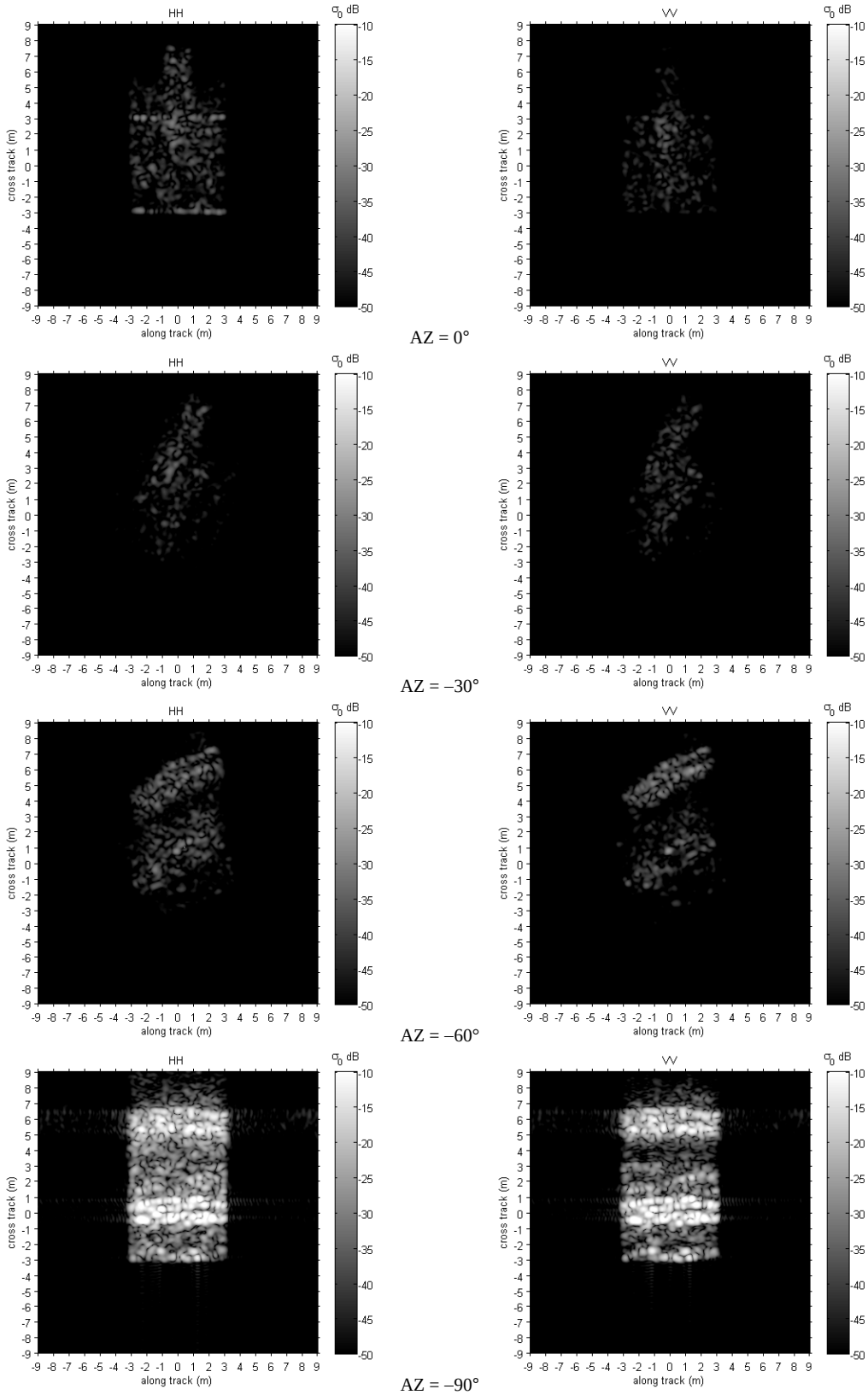

Figure V-86 Snow bridge only, 4-m depth, 8-inch resolution, $f_c = 9.5$ GHz *, 30° depression angle.*

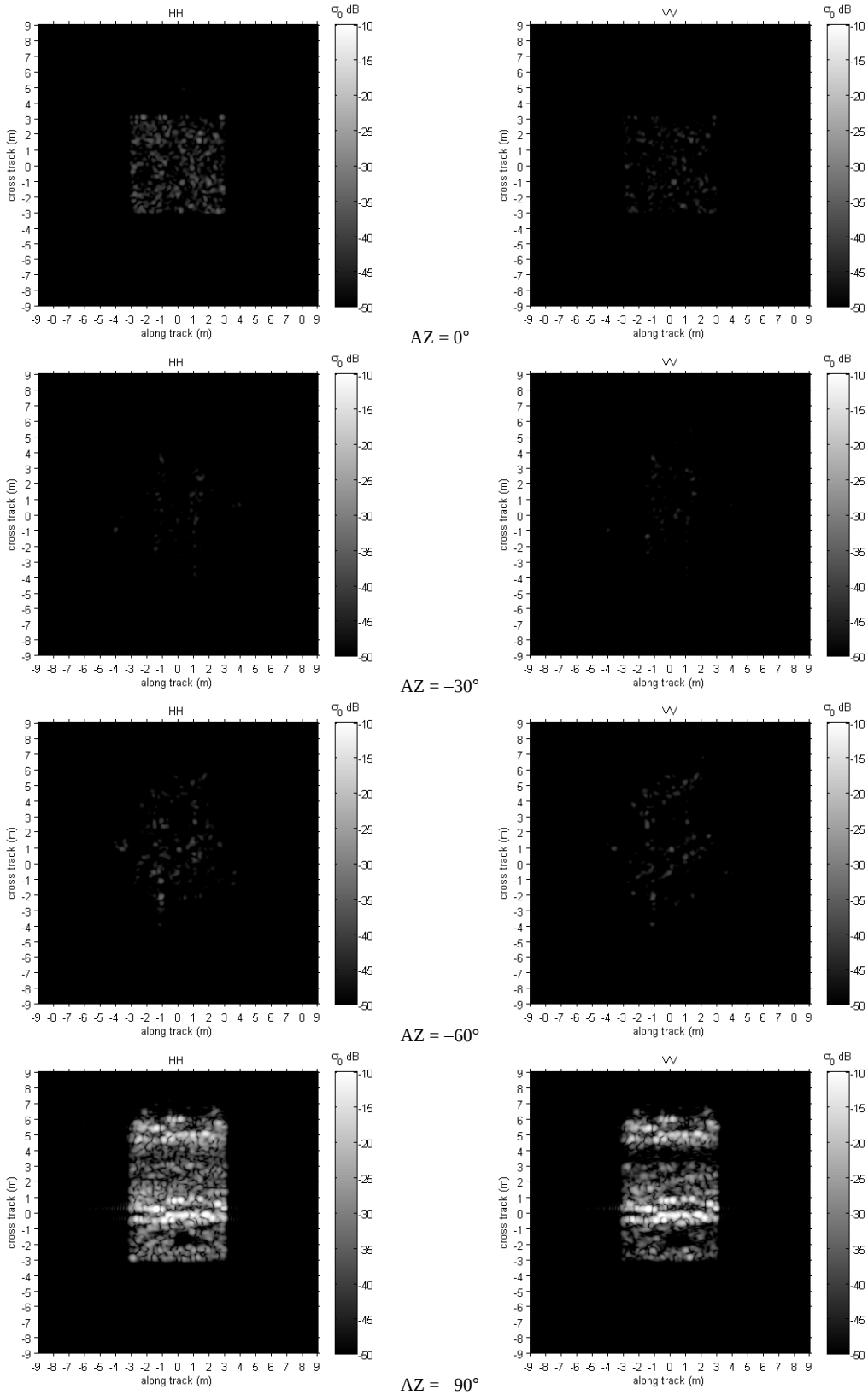

Figure V-87 Snow bridge only, 4-m depth, 8-inch resolution, $f_c = 16.8$ GHz *, 15° depression angle.*

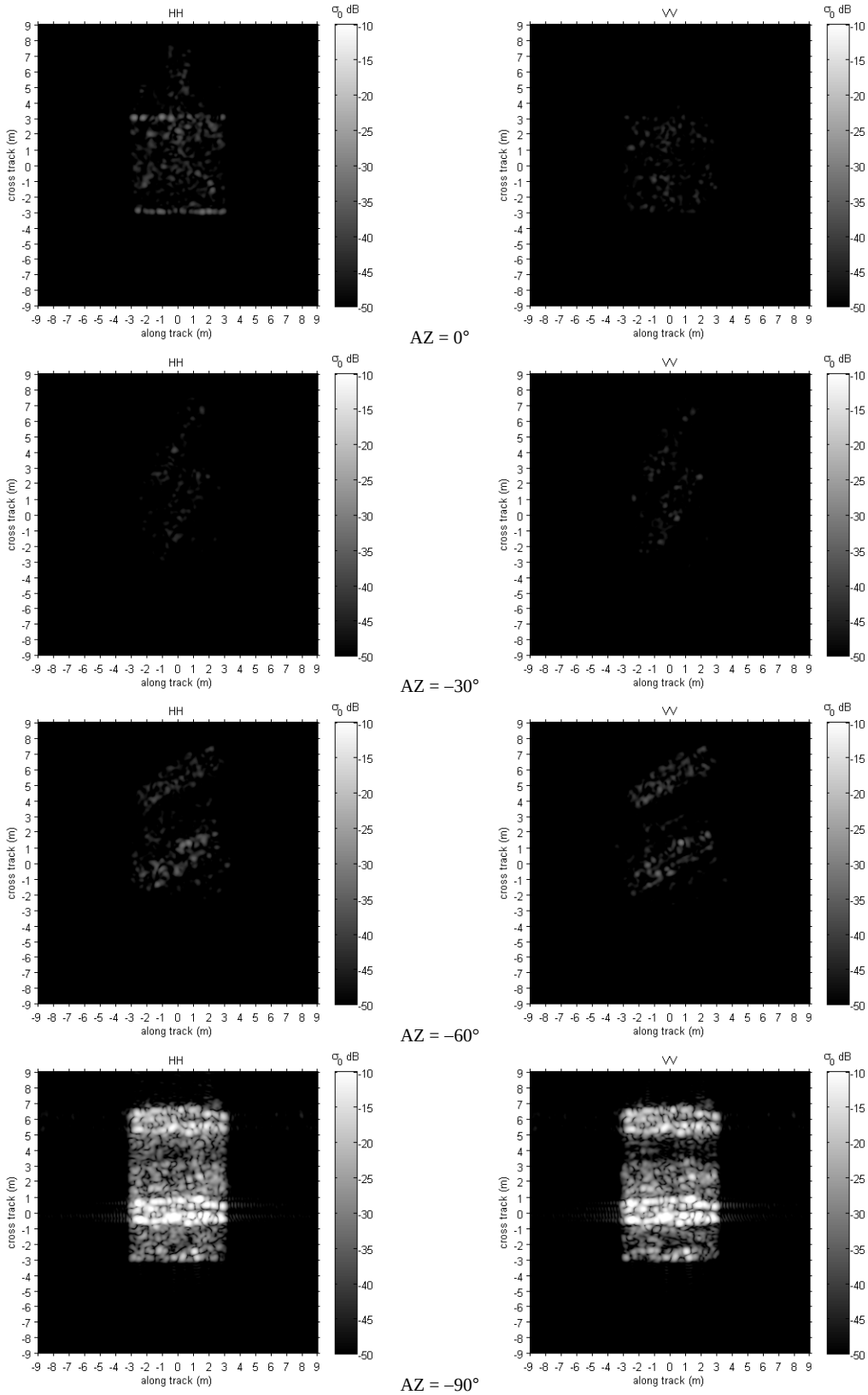

Figure V-88 Snow bridge only, 4-m depth, 8-inch resolution, $f_c = 16.8$ GHz *, 30° depression angle.*

Square root of magnitude (4th root of power), snow bridge only, 4-m depth

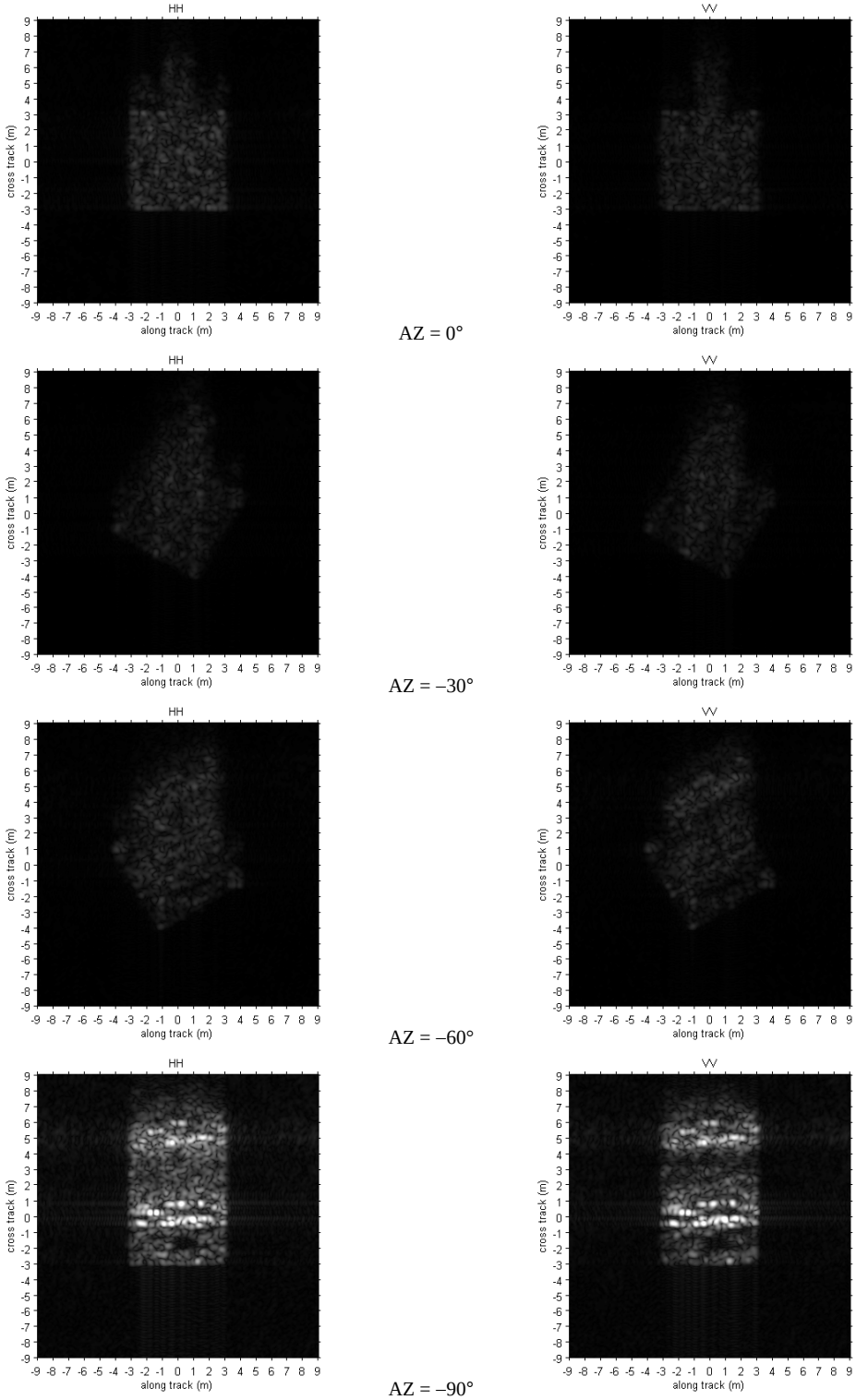

Figure V-89 Snow bridge only, 4-m depth, 8-inch resolution, $f_c = 9.5$ GHz *, 15° depression angle.*

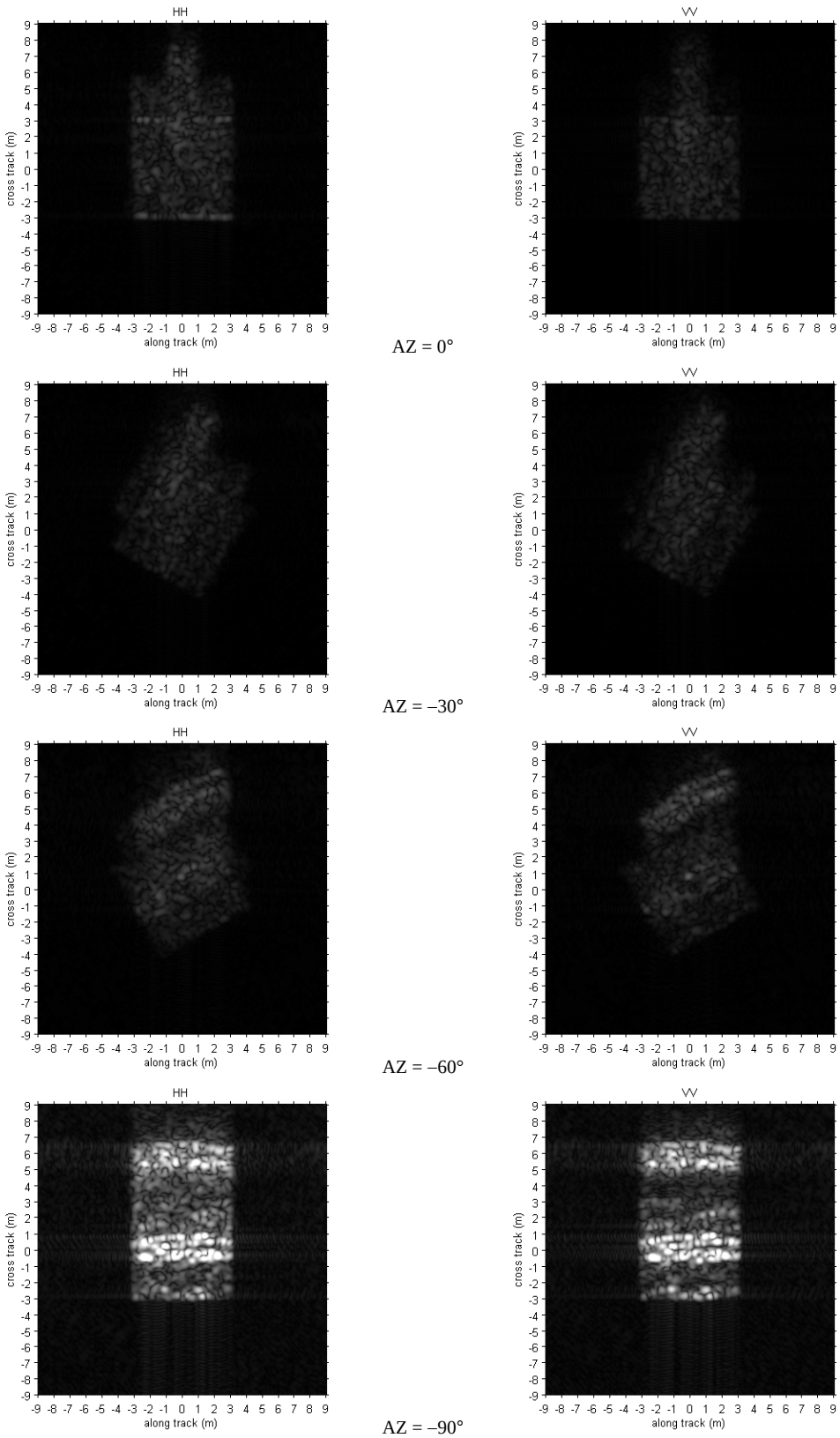

Figure V-90 Snow bridge only, 4-m depth, 8-inch resolution, $f_c = 9.5$ GHz *, 30° depression angle.*

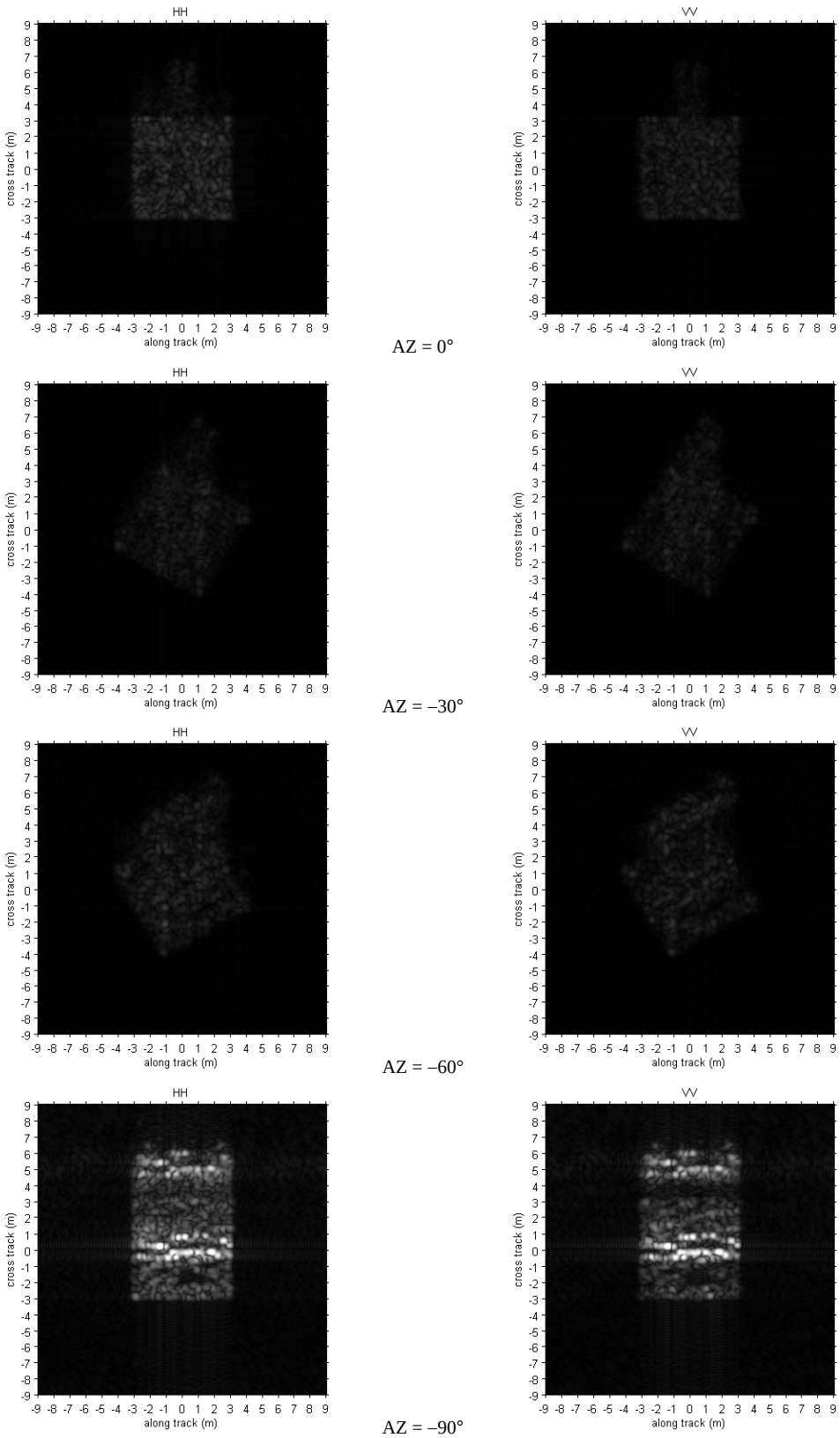

Figure V-91 Snow bridge only, 4-m depth, 8-inch resolution, $f_c = 16.8$ GHz *, 15° depression angle.*

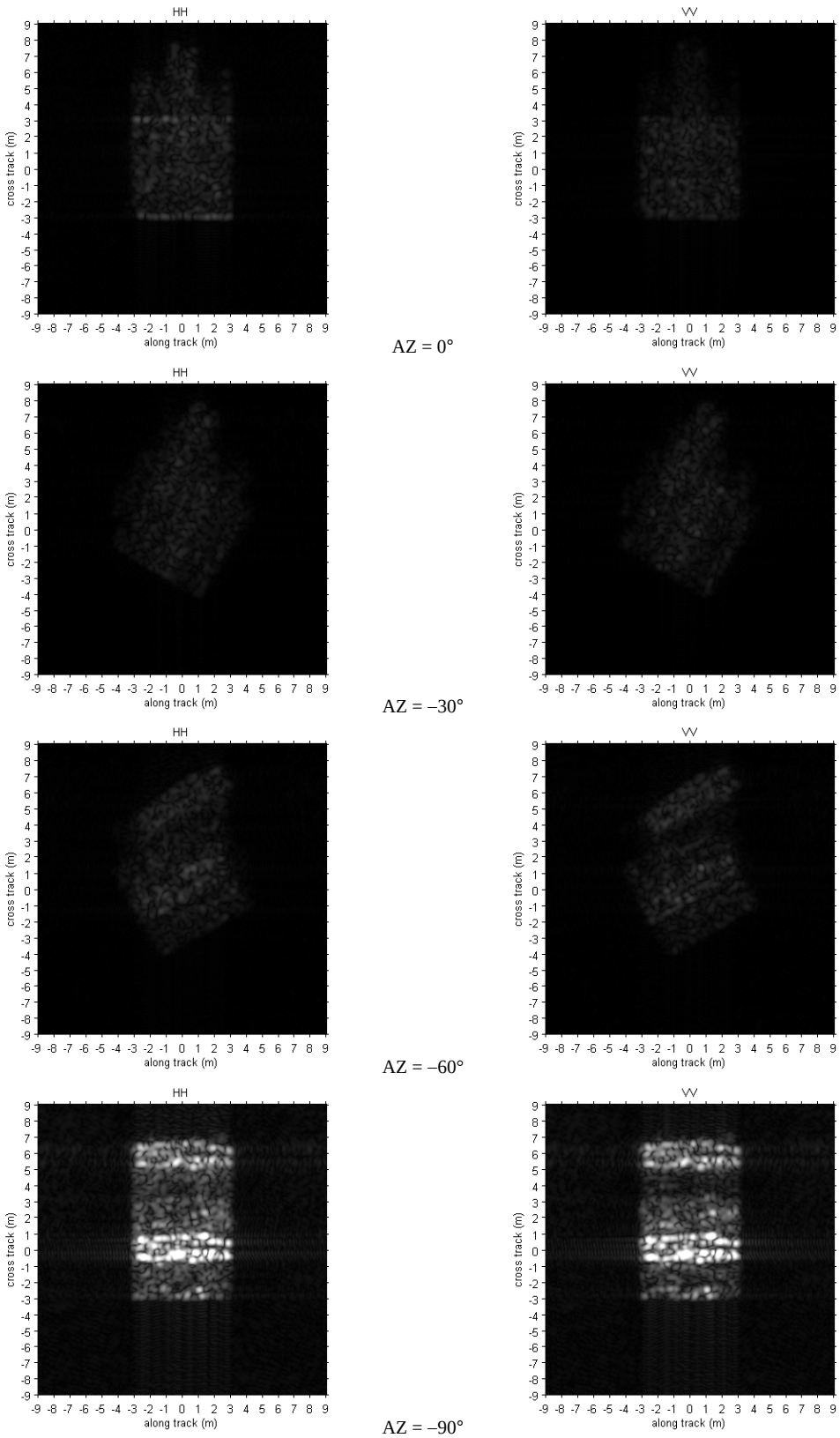

Figure V-92 Snow bridge only, 4-m depth, 8-inch resolution, $f_c = 16.8$ GHz *, 30° depression angle.*

Color, snow-bridge depth is 4.0 m

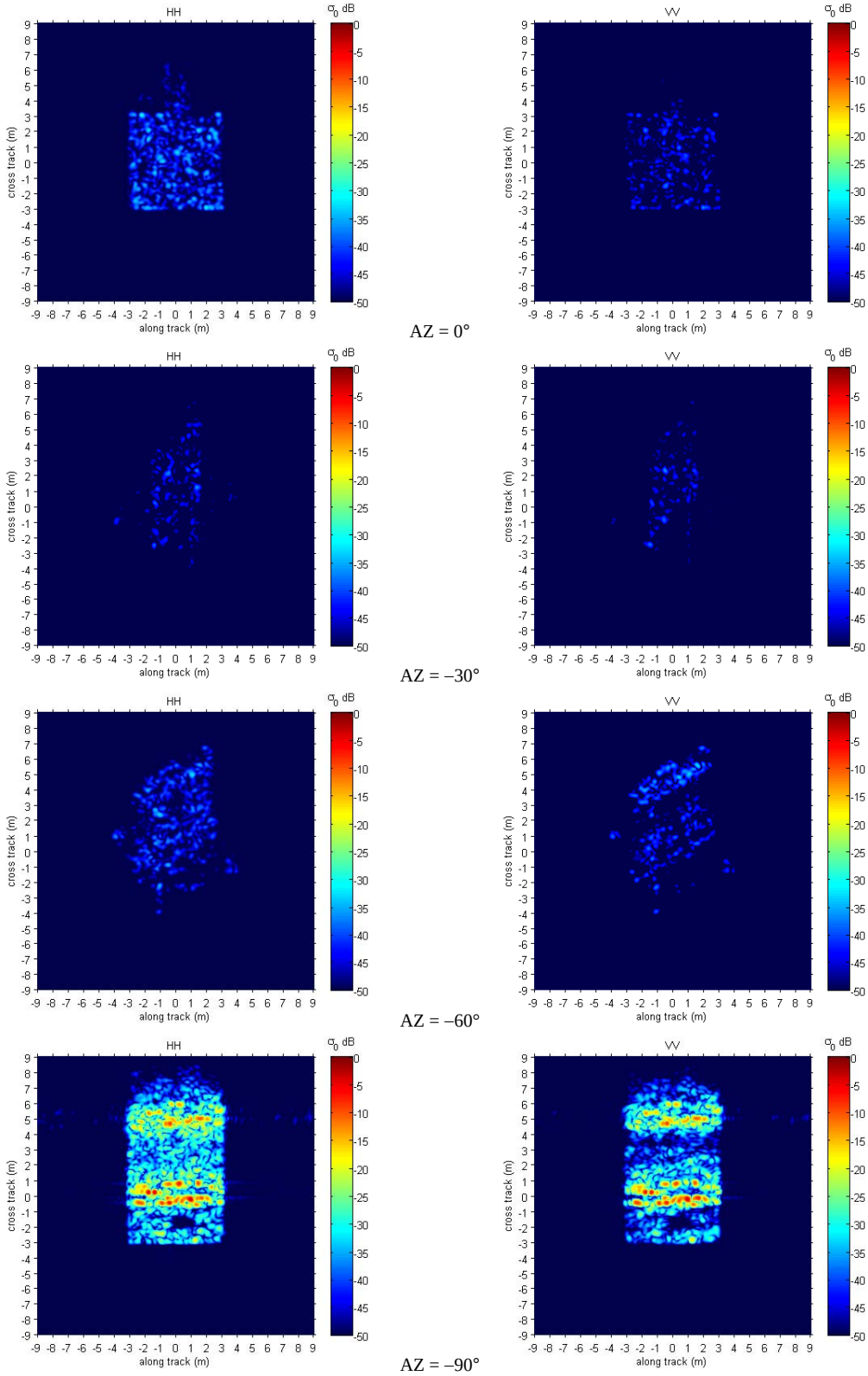

Figure V-93 Snow bridge only, 4-m depth, 8-inch resolution, $f_c = 9.5$ GHz *, 15° depression angle.*

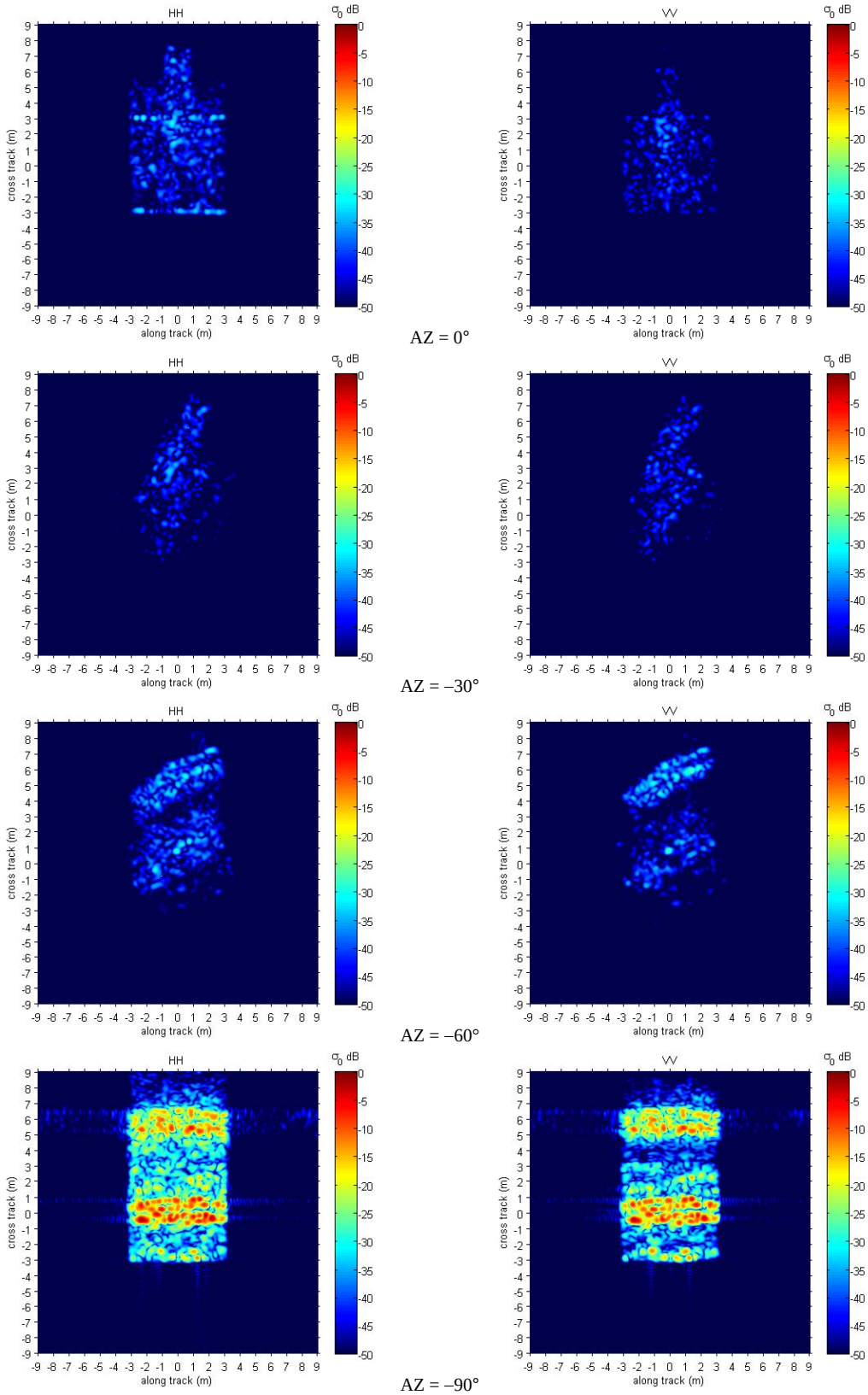

Figure V-94 Snow bridge only, 4-m depth, 8-inch resolution, $f_c = 9.5$ GHz *, 30° depression angle.*

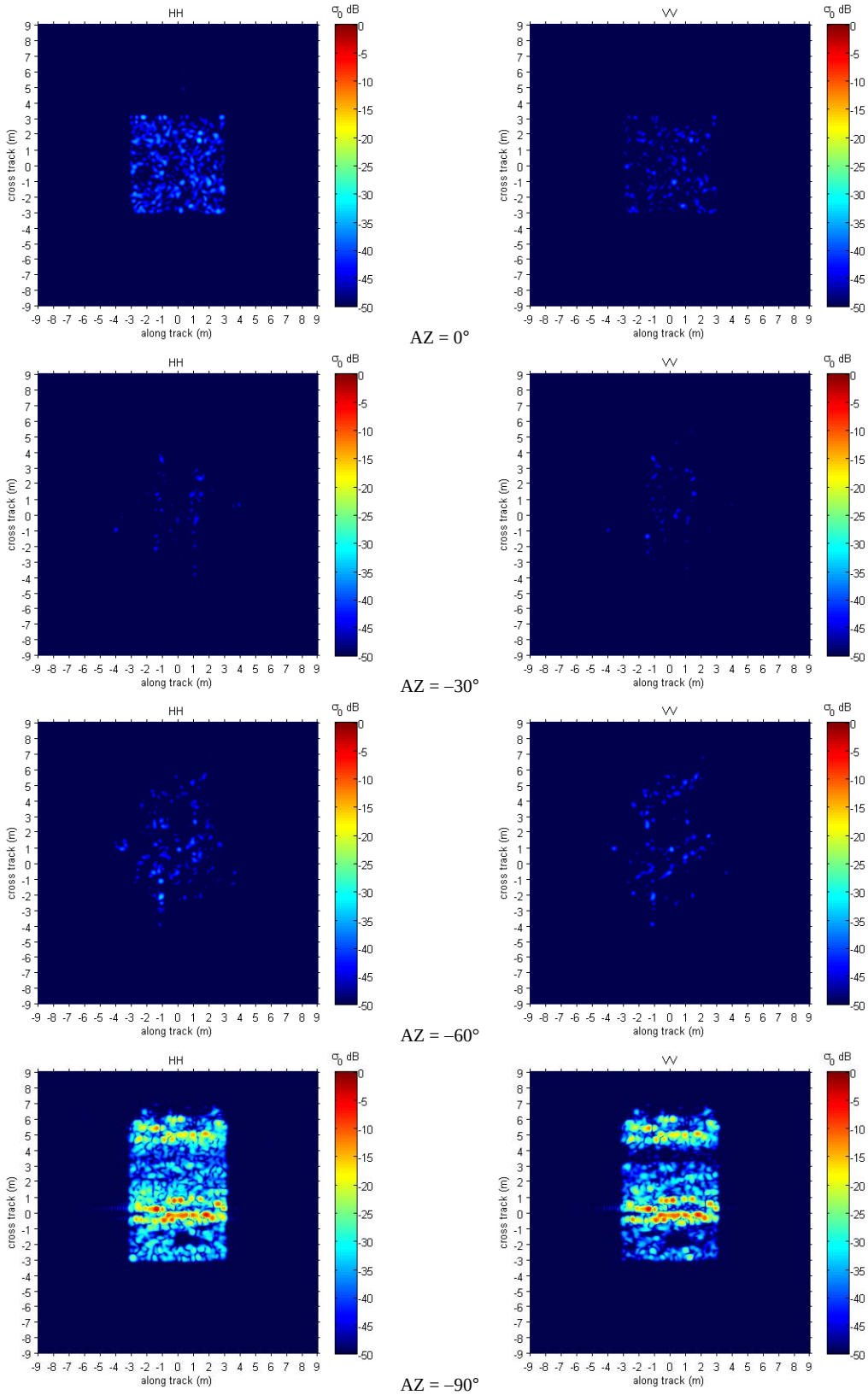

Figure V-95 Snow bridge only, 4-m depth, 8-inch resolution, $f_c = 16.8$ GHz *, 15° depression angle.*

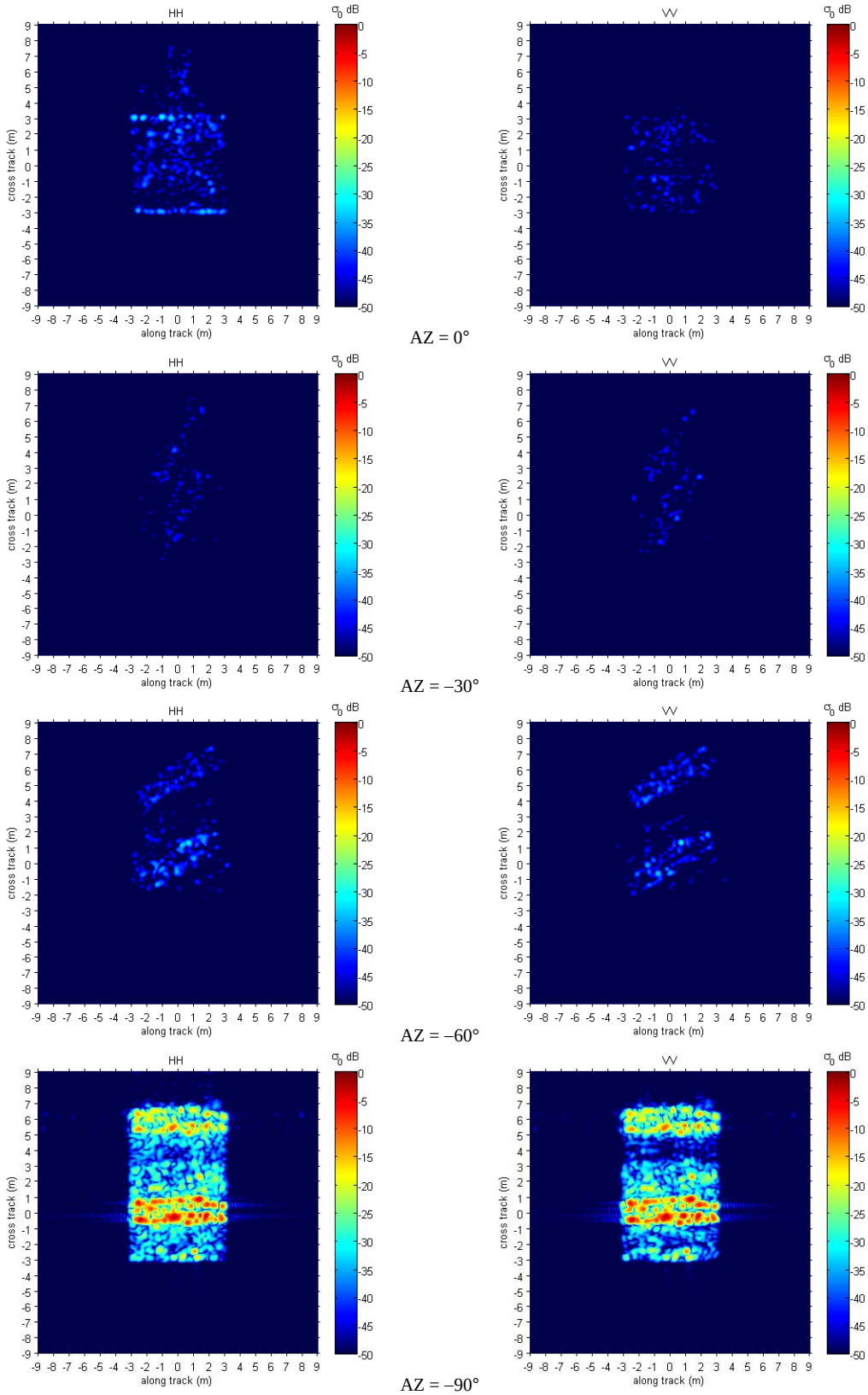

Figure V-96 Snow bridge only, 4-m depth, 8-inch resolution, $f_c = 16.8$ GHz *, 30° depression angle.*

This Page Intentionally Blank

References

[1] H. Ling, R. Chou, S. Lee, "Shooting and bouncing rays: Calculating RCS of an arbitrary cavity", *Digest of the IEEE Antennas and Propagation Society 1986 International Symposium*, Vol. 24, June 1986, pp 293-296.

[2] A. M. Marzougui, S. J. Franke, "Scattering from rough surfaces using the `shooting and bouncing rays' (SBR) technique and comparison with the method of moments solutions", *IEEE Antennas and Propagation Society International Symposium, 1990, AP-S Digest 'Merging Technologies for the 90's'*, vol.4, 7-11 May 1990 pp 1540-1543.

[3] Rajan Bhalla and Hao Ling, "A Fast Algorithm for Signature Prediction and Image Formation Using the Shooting and Bouncing Ray Technique", *IEEE Transactions On Antennas And Propagation*, Vol. 43, No. 1, July 1995, pp 727-731.

[4] John C. Cook, "An Electrical Crevasse Detector", *Geophysics*, vol. XXI, No. 4, October, 1956, pp. 1055-1070.

[5] Curt H. Davis and Vladimir I. Poznyak , "The Depth of Penetration in Antarctic Firn at 10 GHz", *IEEE Transactions on Geoscience and Remote Sensing*, vol. 31, No. 5. September 1993, pp 1107-1111.

[6] Mark Fahnestock, Robert Bindschadler, Ron Kwok, and Ken Jezek, "Greenland Ice Sheet Surface Properties and Ice Dynamics from ERS-1 SAR Imagery", *Science*, vol. 262, December 3, 1993, pp 1530-1534.

[7] E.G. Josberger, M.A. True, and R.A. Shuchman, "Determination of Surface Features on Glaciers in Alaska from ERS-1 SAR Observations", *International Geoscience and Remote Sensing Symposium 1994 (IGARSS '94)*, Vol. 4, 8-12 Aug. 1994, pp 2398 – 2400.

[8] A. J. Delaney, S. A. Arcone, A. O'Bannon, J. Wright, "Crevasse detection with GPR across the Ross Ice Shelf, Antarctica", *Tenth International Conference on Ground Penetrating Radar*, Delft, The Netherlands, June, 2004.

[9] Grant J. Sander, Douglas L. Bickel, Antarctica X-Band MiniSAR Crevasse Detection Radar: Final Report, Sandia National Laboratories Report, SAND2007-3526, Unclassified Unlimited Release, September 2007.

[10] Arthur R. Von Hippel, ed., *Dielectric Materials and Applications*, The Technology Press of M.I.T and John Wiley & Sons, Inc., New York, 1954.

[11] David R. Lide, editor-in-chief, *CRC Handbook of Chemistry and Physics, 88th Edition*, a CRCnetBASE product, CRC Press, Boca Raton, 2008.

[12] Christian Mätzler, "Microwave Permittivity of Dry Snow", *IEEE Transactions on Geoscience and Remote Sensing*, Vol. 34, No. 2, March 1996, pp 573-581.

[13] D. Polder and J. H. van Santen, "The Effective Permeability of Mixtures of Solids", *Physica* XII, no. 5, August 1946, pp 257-271.

[14] S. Koizumi, K. Sato, T. Sato, M. Shimba, "Dielectric Characteristics Of Snow", *Electronic Letters* Vol.22 No. 15, 17th July 1986.

[15] Martti E. Tiuri, Ari H. Sihvola, Ebbe G. Nyfors, Martti T. Hallikaiken, "The Complex Dielectric Constant of Snow at Microwave Frequencies", *IEEE Journal of Oceanic Engineering*, Vol. OE-9, No. 5, December 1984, pp 377-382.

[16] Georgi S. Bordonski, Sergei D. Krylov, "Loss-Factor Behavior of Freshwater Ice at 13.5 and 37.5 GHz", *IEEE Transactions on Geoscience and Remote Sensing*, Vol. 36, No. 2, March 1998, pp 678-680.

[17] *The United States Frequency Allocations, the Radio Spectrum*, U.S. Department of Commerce, National Telecommunications and Information Administration, Office of Spectrum Management, October 2003. Available: http://www.ntia.doc.gov/osmhome//allochrt.PDF .

[18] *Landsat Image Mosaic of Antarctica overview map*, produced by the British Antarctic Survey, Natural Environment research Council, in collaboration with the U.S. Geological Survey and the National Aeronautic and Space Administration. Available on Jan. 20, 2009: http://lima.usgs.gov/

[19] Gregg W. Lamorey, *Siple Shallow Core Density Data*, WAISCORES, National Snow and Ice Data Center (NSIDC), Boulder, Colorado, 2003. Available on Jan. 20, 2009: http://nsidc.org/data/nsidc-0129.html

[20] Sallie Whitlow, Paul Mayewski, *Newall Glacier Ice Core Data*, Institute for the Study of Earth, Oceans and Space, Glacier Research Group, University of New Hampshire, Durham, New Hampshire, 1988-1989. Available on Jan. 20, 2009: http://www.ncdc.noaa.gov/paleo/icecore/antarctica/newall/newall.html

[21] Paul Mayewski, *Dominion Range Ice Core Data*. International Ice Core Data Cooperative. IGBP Pages/World Data Center-A for Paleoclimatology, NOAA/NGDC Paleoclimatology Program, Boulder CO, USA, 1998. Available on Jan. 20, 2009: ftp://ftp.ncdc.noaa.gov/pub/data/paleo/icecore/antarctica/dominion/

[22] Personal communication from Lt. Col. Mark A Armstrong, New York Air National Guard, 109th Airlift Wing.

[23] Michiel van den Broeke, "Depth and Density of the Antarctic Firn Layer", *Arctic, Antarctic, and Alpine Research*, Vol. 40, No. 2, 2008, pp 432-438.

[24] *Landsat Image Mosaic of Antarctica*, National Landsat Archive Processing System, Landsat Image Mosaic of Antarctica (LIMA) Project**.** Available on Jan. 20, 2009: http://lima.usgs.gov/

[25] *Xpatch Advanced EM Topics*, *Xpatch*® code suite, ver. 4.7, SAIC / DEMACO, a division of Science Applications International Corporation.

[26] Constantine A. Balanis, *Advanced Engineering Electromagnetics*, John Wiley & Sons, New York, 1989.

[27] *Xpatch*® code suite, ver. 4.7, SAIC / DEMACO, a division of Science Applications International Corporation.

[28] D. Andersh, *et al*, "XPATCH 4: The Next Generation in High Frequency Electromagnetic Modeling and Simulation Software", *The Record of the IEEE 2000 International Radar Conference*, 7-12 May 2000, pp 844-849.

[29] CST Design Studio Suite™, CST Microwave Studio®, electromagnetic solver software from CST Computer Simulation Technology, Bad Nauheimer Str. 19, D-64289 Darmstadt, Germany (2007, June). Available: http://www.cst.com .

[30] C. Lu and S. W. Lee, *Documents of Computer Code SAF: Volume 1, User Manual of SAF, Version 3.1*, SAIC/DEMACO, Champaign, October, 2005.

[31] *NVIDIA Tesla GPU Computing Solutions For Workstations*, NVIDIA Corporation, Santa Clara, California, December 2009. Available: http://www.nvidia.com/object/personal_supercomputing.html

Distribution

5	Mark A. Armstrong, Lt Col, NYANG Commander 109th Communications Flight 1 ANG Road Scotia, New York 12302			
5	Walter Hallman NGB/A5RM (SRG) 3500 Fetchet Ave Andrews AFB, MD 20762			
2	Dr. Mark A. Sletten Naval Research Laboratory Code 7264 4555 Overlook Ave. SW Washington DC 20375			
1	MS 0501	R. M. Bugos	5343	
1	MS 0501	M. C. Dowdican	5338	
1	MS 0509	M. G. Knoll	5300	
1	MS 0509	K. D. Meeks	5350	
10	MS 0519	T. J. Mirabal	5341	
1	MS 0519	D. L. Bickel	5354	
1	MS 0519	C. L. Smithpeter	5354	
1	MS 0519	L. C. Velasquez	10653	
1	MS 0529	S. E. Allen	5345	
1	MS 0529	K. Coperich Branch	5345	
5	MS 0529	B. C. Brock	5345	
1	MS 0529	G. K. Froehlich	5345	
1	MS 0529	H. Loui	5345	
1	MS 0529	B. Strassner	5345	
1	MS 1330	J. J. Hudgens	5340	
1	MS 1330	B. L. Burns	5340	
1	MS 1330	S. D. Bensonhaver	5342	
1	MS 1330	A. W. Doerry	5342	
1	MS 1330	D. Harmony	5342	
1	MS 1330	W. H. Hensley	5342	
1	MS 1330	M. S. Murray	5342	
1	MS 1330	R. Riley	5342	
1	MS 1330	D. F. Dubbert	5345	
1	MS 1330	F. E. Heard	5345	
1	MS 1330	G. R. Sloan	5345	
1	MS 1330	K. W. Sorensen	5345	
1	MS 1330	S. M. Becker	5348	
1	MS 1330	A. D. Sweet	5348	
1	MS 1330	M. E. Thompson	5348	
1	MS 1330	S. A. Hutchinson	5349	
1	MS 1332	T. P. Bielek	5342	
1	MS 1332	J. D. Bradley	5342	
1	MS 1332	J. A. Hollowell	5342	
10	MS 1332	G. J. Sander	5342	
1	MS 0899	Technical Library	9536	(electronic copy)

Sandia National Laboratories